

ABSTRACT

Title of Dissertation: MODELING MOISTURE TRANSPORT IN ASPHALT
PAVEMENTS

Muhammed Emin Kutay, Doctor of Philosophy, 2005

Dissertation directed by: Assistant Professor Ahmet H. Aydilek
Department of Civil and Environmental Engineering

Many of the pavement distresses such as pot holes and surface cracks are caused by moisture damage, which is due to the destruction of adhesive bond between aggregate and the binder in the presence of moisture. These distresses can cause excessive pavement roughness that might necessitate replacement of the entire pavement layer. Hydraulic conductivity has traditionally been used to characterize the moisture transport in asphalt pavements. However, laboratory or field measured unidirectional hydraulic conductivity only provides information about the flow in one direction and does not represent flow in other directions. Numerical modeling of fluid flow within the pores of asphalt pavements is a viable alternative to characterize the directional hydraulic conductivity as well as pore pressures and viscous shear stresses.

Three-dimensional lattice Boltzmann (LB) fluid flow models were developed and validated using analytical solutions and laboratory experiments. An excellent agreement

was observed with second order accuracy. Three-dimensional real pore structures of the specimens were generated using X-ray CT technique and used as an input in the LB models. Numerous steady and unsteady fluid flow simulations were conducted on different asphalt specimens to study the moisture transport characteristics. Analysis of hydraulic conductivity tensor indicated that the asphalt specimens are isotropic comparing two horizontal directions and anisotropic comparing horizontal and vertical directions. Therefore, it is recommended that a new field testing standard be developed to account for this anisotropy. Analysis of hydraulic conductivity at different depths revealed a rapid decrease in the hydraulic conductivity as the analysis depth was increased. The decrease was more pronounced when compaction effort was increased; therefore, the field compaction effort could be adjusted to control the depth of water penetration. Local pressure gradients and shear stresses at constrictions during steady fluid flow were up to one order of magnitude higher than their average values. Unsteady flow simulations revealed that dynamic hydraulic conductivities of asphalt specimens were relatively close to their steady values. The pressure gradients and viscous shear stresses due to dynamic flow were much higher at the surface as compared to their steady values and the dynamic effect decreased with increasing depth.

MODELING MOISTURE TRANSPORT IN ASPHALT PAVEMENTS

by

Muhammed Emin Kutay

Dissertation submitted to the Faculty of the Graduate School of the
University of Maryland, College Park in partial fulfillment
of the requirements for the degree of
Doctor of Philosophy
2005

Advisory Committee:

Professor Ahmet H. Aydilek, Chair
Professor Deborah J. Goodings
Professor Charles W. Schwartz
Professor M. Sherif Aggour
Professor Elias Balaras
Professor Ugo Piomelli

©Copyright by

Muhammed Emin Kutay

2005

DEDICATION

To my wife Asiye, our son Salih Mirat, and my mother Nezahat.

ACKNOWLEDGEMENT

I am forever indebted to my advisor Professor Ahmet H. Aydilek for his great support and help on all stages of my research. I would like to extend appreciation to Tom Harman, Material and Construction Team Leader at the FHWA's Turner-Fairbank Highway Research Center for his wonderful supervision and guidance. The funding support of FHWA's Eisenhower Research Fellowship program is also gratefully acknowledged.

CHAPTER 1 INTRODUCTION.....	1
CHAPTER 2 LITERATURE REVIEW	6
2.1 LATTICE BOLTZMANN METHOD IN MODELING FLUID FLOW	6
2.2 SEMI-ANALYTICAL AND NUMERICAL METHODS FOR CHARACTERIZATION OF MOISTURE TRANSPORT IN ASPHALT PAVEMENTS.....	8
2.3 UNSTEADY (DYNAMIC) FLOW MODELING IN POROUS MEDIA.....	12
2.4 SYNTHESIS OF THE PREVIOUS WORK AND MOTIVATION FOR THE CURRENT STUDY	13
CHAPTER 3 LATTICE BOLTZMANN METHOD	16
3.1 BASIC THEORY: FROM BOLTZMANN EQUATION TO LATTICE BOLTZMANN METHOD	22
3.2 STEPS OF THE LATTICE BOLTZMANN ALGORITHM	25
3.2.1 Phase I-Initialization	27
3.2.2 Phase II-Propagation of Fluid to the Neighboring Nodes and Calculation of Distribution Function, Density and Velocity at Each Node	27
3.2.3 Phase III- Boundary Conditions and Calculation of the New Equilibrium Distribution Functions.....	30
3.3 BOUNDARY CONDITIONS	30
3.3.1 Boundary Conditions near Solid Nodes	30
3.3.1.1 No-Slip Boundary Condition	30
3.3.1.2 Slip Boundary Condition	32
3.3.1.3 Extrapolation.....	32
3.3.2 Boundary Conditions at Domain Boundaries.....	34
3.3.3 Other Techniques to Create Flow in LB Models	37
3.3.3.1 Density Gradient	37
3.3.3.2 Body Force.....	39
CHAPTER 4 DEVELOPMENT AND VALIDATION OF THE LB ALGORITHM	40
4.1 ALGORITHM DEVELOPMENT	40
4.2 VALIDATION OF TWO DIMENSIONAL D2Q9 MODEL.....	43
4.2.1 Flow between parallel plates	43
4.2.2 Wannier Flow.....	46
4.3 VALIDATION OF THE D3Q19 LB MODEL.....	49
4.3.1 Poiseuille Flow.....	49
4.4 LABORATORY HYDRAULIC CONDUCTIVITY TESTS.....	51
CHAPTER 5 IMAGE ACQUISITION AND ANALYSIS.....	56
5.1 X-RAY COMPUTED TOMOGRAPHY IMAGING	56
5.2 IMAGE ANALYSIS ALGORITHMS	62

5.2.1	Porosity Algorithm (<i>POROSITYFIND</i>)	62
5.2.2	Pore Connectivity Algorithm (<i>PORECON</i>)	63
5.2.3	Specific Surface Area Algorithm (<i>SSA</i>)	63
5.2.4	Tortuosity Algorithm (<i>TORT3D</i>)	66
CHAPTER 6 PORE STRUCTURE CHARACTERIZATION AND LABORATORY HYDRAULIC CONDUCTIVITY OF ASPHALT PAVEMENTS		69
6.1	MATERIAL PROPERTIES	69
6.1.1	Laboratory Compacted Specimens	69
6.1.2	Field Cores	74
6.2	ANALYSIS OF PORE STRUCTURE OF ASPHALT SPECIMENS	74
6.2.1	Porosity Variations within Each Specimen	74
6.2.2	Effect of Compaction Energy and Gradation Shape on the Total Porosity of the Specimens	87
6.3	METHODS OF LABORATORY HYDRAULIC CONDUCTIVITY TESTS.....	90
6.4	EFFECT OF PORE GEOMETRY AND MIXTURE CHARACTERISTICS ON THE HYDRAULIC CONDUCTIVITY OF ASPHALT SPECIMENS	95
6.4.1	Effect of Porosity on the Hydraulic Conductivity.....	95
6.4.2	Effect of Specific Surface Area on the Hydraulic Conductivity	97
6.4.3	Effect of Tortuosity on the Hydraulic Conductivity	99
6.4.4	Effect of Mix Design Parameters on the Hydraulic Conductivity	99
CHAPTER 7 NUMERICAL MODELING OF FLUID FLOW THROUGH ASPHALT PAVEMENTS USING LATTICE BOLTZMANN METHOD		104
7.1	SIMULATION OF LABORATORY HYDRAULIC CONDUCTIVITY TEST	104
7.1.1	Geometry Input	104
7.1.2	Boundary Conditions	107
7.1.3	Calculation of Hydraulic Conductivity Tensor	107
7.1.4	Results of Simulations and Comparison with the Experimental Measurements	109
7.2	DIRECTIONAL HYDRAULIC CONDUCTIVITY OF ASPHALT PAVEMENTS	121
7.2.1	Method of Calculating Components of the Hydraulic Conductivity Tensor.....	121
7.2.2	Relationship between Vertical and Horizontal Hydraulic Conductivities.....	127
7.2.3	Effect of Constrictions on the Hydraulic Conductivity Tensor.....	130
7.2.4	The Relationship between the Normal and Shear Components of the Hydraulic Conductivity Tensor.....	131
7.3	CHANGE IN HYDRAULIC CONDUCTIVITY WITH DEPTH.....	136
7.4	PORE WATER PRESSURE AND SHEAR STRESS VARIATIONS AT THE PORE-SOLID INTERFACE.....	140
7.4.1	Pore Pressure Variation.....	140
7.4.2	Shear Stress Variation.....	145

CHAPTER 8 DYNAMIC FLOW SIMULATIONS IN ASPHALT PAVEMENTS.....	156
8.1 VALIDATION OF LB ALGORITHMS FOR DYNAMIC (UNSTEADY) FLOW	156
8.2 DYNAMIC FLOW SIMULATIONS IN ASPHALT PAVEMENTS	157
8.2.1 Boundary Conditions	157
8.2.2 Calculation of Dynamic Hydraulic Conductivity.....	160
8.2.3 Results of Simulations	162
8.2.3.1 Effect of Amplitude of Pressure Gradient.....	162
8.2.3.2 Effect of Wavelength of Pressure Gradient on the Dynamic Hydraulic Conductivity.....	163
8.2.3.3 Dynamic Hydraulic Conductivities versus (steady) Hydraulic Conductivity Relationship	165
8.2.3.4 Comparison of Pressure Gradients in Steady and Dynamic Flow Conditions...	168
8.2.3.5 Comparison of Shear Stresses in Steady and Dynamic Flow Conditions	170
CHAPTER 9 CONCLUSIONS AND RECOMMENDATIONS	176
9.1 SUMMARY AND CONCLUSIONS	176
9.2 PRACTICAL IMPLICATIONS OF THE FINDINGS.....	185
9.3 RECOMMENDATIONS FOR FURTHER RESEARCH	186
APPENDIX A CALCULATION OF UNKNOWN COMPONENTS OF THE DISTRIBUTION FUNCTION.....	188
APPENDIX B ALGORITHMS	193
<i>LB-D2Q9</i> ALGORITHM.....	193
<i>LB-D3Q19</i> ALGORITHM.....	197
<i>IMAGETHRESHOLD</i> ALGORITHM.....	208
<i>POROSITYFIND</i> ALGORITHM.....	210
<i>PORECON</i> ALGORITHM	211
<i>SSA</i> ALGORITHM	214
<i>TORT3D</i> ALGORITHM.....	215
<i>RADIALPORE</i> ALGORITHM.....	216
APPENDIX C WANNIER'S ANALYTICAL SOLUTION OF STOKES FLOW AROUND A CIRCULAR CYLINDER IN THE VICINITY OF A MOVING PLATE	218
APPENDIX D PROCEDURES TO CONDUCT HYDRAULIC CONDUCTIVITY TESTS USING THE BUBBLE TUBE CONSTANT HEAD PERMEAMETER.....	220
APPENDIX E THE VARIATION IN PORE CROSS-SECTIONAL AREA IN THREE DIFFERENT DIRECTIONS FOR ALL SPECIMENS.....	225
APPENDIX F PORE PRESSURE AND PRESSURE GRADIENT VARIATION IN DIFFERENT DIRECTIONS	235
APPENDIX G VARIATION OF SHEAR STRESS TENSOR COMPONENTS OF ALL SPECIMENS	254

APPENDIX H PRESSURE GRADIENT VARIATION IN Z-DIRECTION FOR STEADY AND DYNAMIC FLOW CONDITIONS	273
APPENDIX I THE VARIATION OF SHEAR STRESS COMPONENTS IN Z-DIRECTION FOR STEADY (STRAIGHT LINES) AND DYNAMIC (DASHED LINES) FLOW CASES	276
NOMENCLATURE.....	280
REFERENCES.....	283

CHAPTER 1 INTRODUCTION

Hydraulic conductivity of an asphalt pavement is one of the most important parameters that have a direct influence on its design life. Moisture damage caused by the destruction of cohesive bond within the asphalt binder or the destruction of the adhesive bond between the aggregate and the asphalt binder decreases the life of asphalt pavements. Stripping of the aggregates from the binder as a result of moisture damage can cause cracks, and excessive deflections that might necessitate replacement of the entire pavement layer. There are numerous studies that indicated the susceptibility of asphalt pavements to moisture damage (McCann et al. 2005, Castelblanco et al. 2005). Understanding the relationship between pore structure and fluid transport is critical in determination of moisture damage in asphalt pavements.

Hydraulic conductivity has been commonly used to characterize the fluid transport properties of asphalt pavements. Laboratory or field measured unidirectional hydraulic conductivity is usually assumed to be constant in all directions. Since asphalt pavements usually have an anisotropic and heterogeneous internal pore structure (Masad et al. 1999), measured unidirectional hydraulic conductivity may not accurately provide the three-dimensional moisture transport characteristics in the field. Furthermore, it is impractical to measure the longitudinal (x-direction) and transverse (y-direction) hydraulic conductivities due to the difficulties associated with the specimen preparation and the cost of operation. There are several semi-analytical equations exist (Kozeny-Carman 1956, Walsh and Brace 1984, Al-Omari et al. 2002) for estimation of the hydraulic conductivity of porous media and they are generally applicable to isotropic pore structures. Derivations of these analytical models are usually based on the approximation

of pore structure with simpler geometries, such as tubes and cones, and often the accuracy of these models is questionable. Additionally, these techniques do not consider pore channel shape and connectivity, which are critical in fluid flow modeling and the estimation of hydraulic conductivity in asphalt pavements. Numerical modeling of fluid flow within the pores of asphalt pavements with the aid of X-ray Computed Tomography (CT) imaging technique is a viable alternative to characterize the directional hydraulic conductivity. X-ray CT technique can be used to acquire real three-dimensional pore structures of the asphalt specimens eliminating the potential errors that might stem from idealized pore structure assumptions used by past researchers (Pilotti 2003, Wang 2003).

Considerable progress has been made in the area of computational fluid dynamics in recent years and one of the most reliable methods, the lattice Boltzmann (LB) approach, have been increasingly used in various engineering applications in modeling the flow of both single and multi-component fluids (Rothman and Zaleski 1998, Chopard and Droz 1998, Kandhai et al. 1999, Chen and Doolen 2001, Succi 2001, Hazi 2003). The main advantages of the LB method include easy implementation of boundary conditions and computational efficiency by allowing parallel computing. The method also accommodates boundary conditions such as a pressure drop across the interface between two fluids and wetting effects at the fluid-solid interface (Martys et al. 2001). It has proven to be very accurate in simulating isothermal, incompressible flow at low Reynolds numbers (Succi 2001); however, information is lacking about its application to granular geomaterials used in civil engineering construction, such as asphalt pavements.

The objectives of this research can be summarized as follows:

- To investigate the characteristics of internal pore structure parameters (e.g. porosity, pore connectivity, specific surface area and tortuosity) of different asphalt mixtures by using their three dimensional X-ray CT images.
- To investigate the influence of different pore structure and mix design parameters on the unidirectional laboratory hydraulic conductivity of asphalt pavements.
- To evaluate the accuracy of semi-analytical hydraulic conductivity equations developed for homogeneous porous structures in predicting hydraulic conductivity of asphalt pavements.
- To develop a three dimensional image-based LB model that is capable of simulating single-phase, Newtonian and incompressible fluid flow within any pore geometry and confirm its accuracy in predicting hydraulic conductivity of asphalt pavements.
- To investigate the hydraulic conductivity of asphalt pavements in three different directions; longitudinal (k_{xx}), transverse (k_{yy}) and vertical (k_{zz}).
- To study the relation between vertical hydraulic conductivity (k_{zz}), and longitudinal (k_{xx}) and transverse (k_{yy}) hydraulic conductivities.
- To investigate the hydraulic conductivity variation in different depths of asphalt pavements, which is expected to characterize the vulnerability of different zones within asphalt pavements to moisture damage.
- To study of the pore constrictions in asphalt pavements and their relation to the hydraulic conductivity in different directions.

- To investigate the pore pressure and viscous shear stress variation during a steady-state fluid flow in pore structures of asphalt pavements, which may potentially have a direct influence on the binder stripping problem.
- To study the effect of dynamic (pulsatile) vehicle loading on the moisture transport characteristics of asphalt pavements.
- To investigate the (frequency dependent) dynamic hydraulic conductivity of asphalt pavements and its relation to (steady) hydraulic conductivity.

To meet these objectives, two- and three-dimensional fluid flow models were developed using the LB technique. The models were validated using well-known analytical equations and laboratory experiments on granular materials. Three dimensional pore structures of the specimens were generated using X-ray CT technique and used as an input in the LB models. The geometrical parameters of the specimens, i.e. porosity, pore connectivity, specific surface area and tortuosity were determined using image analysis algorithms developed as a part of this study. The relation of these parameters to the laboratory hydraulic conductivities of asphalt specimens was investigated. Numerous steady and unsteady (pulsatile) fluid flow simulations were conducted on different asphalt specimens to study a number of moisture transport characteristics such as hydraulic conductivity tensor, pore pressure and viscous shear stresses.

A detailed literature review about the LB method and existing analytical and numerical methods of estimating hydraulic conductivity of asphalt pavements are presented in Chapter 2. Chapter 3 provides a detailed explanation of the theory of LB method. Validation of both two- and three- dimensional LB models is presented in Chapter 4. Chapter 5 describes the theory of operation of X-ray CT technique and the

developed image analysis algorithms. Chapter 6 discusses the measured pore structure parameters of different asphalt mixtures and their relation to laboratory measured hydraulic conductivities. The results of three-dimensional fluid flow simulations in different asphalt specimens are presented in Chapter 7. Chapter 8 includes the results of pulsatile flow simulations on asphalt pavements. Summary and conclusions are given in Chapter 9.

CHAPTER 2 LITERATURE REVIEW

2.1 LATTICE BOLTZMANN METHOD IN MODELING FLUID FLOW

Among various techniques in fluid flow modeling, lattice Boltzmann (LB) method has been gaining wide acceptance due to its ease of implementation of boundary conditions and numerical stability in wide variety of flow conditions with various Reynolds numbers. It has evolved from the Lattice Gas Automata (LGA) (Buick 1997). Various difficulties experienced in LGA were overcome by the introduction of the LB method. It was first introduced by McNamara and Zanetti (1988) to eliminate the statistical noise in the LGA. Since then, it has been implemented and improved by various researchers in variety of disciplines. Early applications of the LB method to porous media largely focused on the feasibility of the method. Succi et al. (1989) used LB method to simulate flow through random pack of blocks and demonstrated the adherence to Darcy's law. Various researchers (Maier et al. 1996, Zou and He 1997, Guo et al. 2002, La Fuente et al. 2003) improved the LB method by introducing a variety of new boundary conditions for the solid boundaries. Some of selected boundary conditions for the solid walls are described in detail in Chapter 3.

Maier et al. (1997) implemented a three dimensional LB model (D3Q19) to simulate flow through bead packs and compared with the Kozeny-Carman prediction for the sphere packing. Kim (2002) utilized a two dimensional (D2Q9) LB method to simulate flow through rock fractures and compared with the analytical equations that assumes the rock fracture composed of set of parallel plates. Martys et al. (2002) successfully applied LB method to simulate a multiphase flow through Fontainebleau

sandstone. The hydraulic conductivities determined from the model were compared with those based on laboratory measurements.. Hornero et al. (2004) measured the performance of a two dimensional LB model for simulating soil flow in a simple erosion model and compared the results to those predicted by an analytical solution. Tang et al. (2004) successfully implemented LB method to simulate gas flow through microchannels.

Flow through fibrous materials such as papers, random fiber webs and woven fabrics also have been the interest of researchers using LB method. Koponen et al. (1998) modeled the hydraulic conductivity of three-dimensional random fiber webs using LB method and found a good agreement with the experimental measurements. Filippova (1997) used a three-dimensional LB method to model gas-particle flow through filters and successfully simulated filtration phenomenon. Clague (2000) modeled hydraulic conductivity of bounded and unbounded fibrous media using the LB method.

Artoli et al. (2002) presented a detailed analysis on the accuracy of the LB method in simulating pulsatile flow in a 2D channel and a 3D tube. They studied the accuracy of the lattice Boltzmann BGK method in recovering the Womersley solution for pulsatile flow in a rigid tube with a sinusoidal pressure gradient. They concluded that the LB method successfully predicts the velocity profiles in parallel plates and circular tubes subjected to oscillating pressure gradients.

2.2 SEMI-ANALYTICAL AND NUMERICAL METHODS FOR CHARACTERIZATION OF MOISTURE TRANSPORT IN ASPHALT PAVEMENTS

Hydraulic conductivity has traditionally been the only parameter for characterization of moisture transport in asphalt pavements. Various models were developed to estimate hydraulic conductivity of asphalt pavement, most of which were semi-analytical. These semi-analytical models are usually based on the approximation of the pore structure into simpler geometries such as tubes and cones, where it is possible to derive an analytical solution from main differential equations of fluid flow (Navier-Stokes Equations). Kozeny-Carman equation is one of the commonly used semi-analytical equations to estimate the hydraulic conductivity of porous structures which has also been used to estimate hydraulic conductivity of asphalt pavements. The derivation of the Kozeny-Carman equation is based on the assumption that the pore structure of a material can be represented by capillary tubes and the hydraulic radius theory applies. The equation can be written as follows;

$$k = \frac{\gamma}{\mu} \frac{C n_e^3}{(1 - n_e^2) S_a^2} \quad (2.1)$$

where k is the hydraulic conductivity, C is a shape factor (= 1/180 for spherical particles), S_a is the specific surface area defined as the ratio of the surface area of the pores to the total volume of the specimen, n_e is the effective porosity, γ is the unit weight of the fluid (water at 20°C), and μ is fluid viscosity and is equal to 10^{-3} kg/(m-s) for water.

Walsh and Brace (1984) also defined an semi-analytical equation for estimation of hydraulic conductivity of porous structures. It has more sophisticated structure than the Kozeny-Carman equation, and includes tortuosity, which is a measure of the tortuous pathways that the fluid travels. The equation has the following form:

$$k = \frac{\gamma}{\mu} \frac{n_e^3}{bT^2} \frac{1}{S_a^2} \quad (2.2)$$

where k is the hydraulic conductivity, n_e is the effective porosity, γ and μ are the unit weight and viscosity of fluid, respectively, b is a constant given as 2 for perfectly circular pore structure and 3 for rough texture on the pore surface, T is the tortuosity defined as the ratio of the total length of path followed by a fluid particle to the shortest distance from inflow to the outflow, and S_a is the specific surface area. It should be noted that, all the pore parameters (n_e , T and S_a) in this equation are calculated for only interconnected (effective) pores. Isolated pores are not considered.

Al-Omari et al. (2002) proposed an empirical formula based on their laboratory studies on asphalt mixes, which can be written as follows:

$$k = \frac{\gamma}{\mu} \frac{V_a^m}{3S_a^2} \quad (2.3)$$

where k is the hydraulic conductivity, V_a is the percent total air voids in an asphalt mix, γ and μ are the unit weight and viscosity of water, respectively, S is the specific surface area, and m is a regression coefficient.

Masad et al. (2003) proposed a revised version of Equation (2.3) where they replaced the specific surface area with the surface area of aggregates. Their equation has following form:

$$k = \frac{\gamma}{\mu} \frac{V_a^m}{c S_{agg}^t} \quad (2.4)$$

where S_{agg} is the surface area of the aggregates in an asphalt mixture and c , m and t are regression coefficients that were determined by statistical data fitting to the laboratory measurements of hydraulic conductivity. Their statistical analysis revealed that the constant m ranged from 4 to 6.9 in different asphalt mixtures, and constants c and t found to be 5 and 1, respectively. They concluded that the constant m was significantly affected by the method of hydraulic conductivity measurement.

There has been attempts to use commercially available finite-element and finite difference softwares (such as SEEP/W and FLAC) to estimate the macroscopic fluid flow patterns within asphalt pavements (Masad et al. 2003, Hunter and Airey 2005). These modeling approaches usually assumed the asphalt pavement as a homogeneous and isotropic media with a constant hydraulic conductivity value in all directions. Masad et al. (2003) utilized a two-dimensional finite-element model (SEEP/W) to investigate the influence of the vertical gradient of porosity on water flow patterns. They divided the pavement thickness into 10 mm sublayers and assigned a hydraulic conductivity value to each sub-layer. The hydraulic conductivity of each sub-layer was calculated using Equation 2.4 using the different porosity values obtained from the X-ray CT images of an asphalt specimen. They assumed that the hydraulic conductivity of each layer to be

constant in both x- and y-directions. Their analysis concluded that the hydraulic conductivity decreased in the vertical direction, and as a result, most the fluid flow occurred in the horizontal direction.

Hunter and Airey (2005) utilized a finite difference model to investigate the validity of the assumption that the flow is vertical during hydraulic conductivity measurements in the field permeameters. They indicated that this assumption is inaccurate and the magnitude of error in the hydraulic conductivity value depends on the depth of the pavement layer and the diameter of the field permeameter. They concluded that the error exceeds one order of magnitude when the diameter of the permeameter is small (e.g. 50 mm) and the pavement layer is thick (e.g. >250 mm).

Little work has been done on the microscopic fluid flow modeling within pores of the asphalt pavements. Al-Omari and Masad (2004) utilized a semi-implicit method for pressure-linked equations (SIMPLE) finite difference scheme to estimate the hydraulic conductivity of asphalt pavements. They compared their vertical hydraulic conductivity estimations based on their numerical model with the Kozeny-Carman equation (Equation 2.1) and found reasonably good agreement.

More recently, Kringos and Scarpas (2005) introduced a modeling technique to understand the physical processes and mechanics causing debonding of the mastic from the aggregates due to the fluid flow in asphalt pavements. In their preliminary analysis, they included the diffusion, desorption and dispersion as the fundamental processes causing raveling. A two dimensional idealized circular aggregate coated with a mastic film was utilized in their study. Then the diffusion of water into the mastic film and desorption of mastic from the aggregate was modeled. They assumed arbitrary diffusion

and desorption coefficients for asphalt mastic film and indicated that there is an ongoing experimental research for more realistic values of these coefficients.

2.3 UNSTEADY (DYNAMIC) FLOW MODELING IN POROUS MEDIA

Unsteady flow has been in the interest of many researchers due its importance in human health (McDonald 1974). Cardiovascular diseases are considered as the main causes of death throughout the world and it is believed that understanding the viscous shear stresses due to the dynamic blood flow play a dominant role in diagnosis and treatment of such diseases (Artoli et al. 2002). Therefore, there has been tremendous effort in modeling unsteady flow in arteries (McDonald 1974). On the other hand, there has been relatively less attempts in modeling dynamic flow in porous media encountered in engineering. Sheng and Zhou (1988) presented the frequency dependent permeability in porous media for a variety of microstructures. They showed that when the dynamic permeability is scaled by its static value and the applied angular velocity scaled by a characteristic angular velocity particular to the microstructure, the resulting function exhibits universal behavior. Sheng and Zhou (1989) further evaluated the dynamic permeability constant and derived formulations for the dynamic permeability of circular tubes. They extended their analyses by studying different idealized pore throat (constriction) shapes in which they investigated effect of the characteristic length (i.e., constriction diameter) and porosity on the dynamic permeability behavior. Their analysis was limited to symmetrical geometries such as uniformly packed glass beads and did not include random or anisotropic pore geometries. Duarte et al. (1992) studied the dynamic permeability of relatively more complex porous media where they placed circular obstacles of a given size between two parallel plates and modeled dynamic flow using a

two-dimensional cellular automata model. They found that increasing number of circles significantly increased the number of time steps for stabilization.

2.4 SYNTHESIS OF THE PREVIOUS WORK AND MOTIVATION FOR THE CURRENT STUDY

The lattice Boltzmann method has emerged as a versatile alternative to traditional finite element and finite difference Navier-Stokes solvers in variety of flow conditions. It has proven to be very accurate in modeling isothermal, incompressible flow at low Reynolds numbers (Succi 2001) especially in the case of flow through porous media. It was summarized in Section 2.1 that several studies utilized LB method to model fluid flow. However, information is lacking about its application to granular geomaterials, such as asphalt pavements.

Several efforts have been made in recent years to estimate the hydraulic conductivity of asphalt pavements (Al-Omari et al. 2002, Masad et al. 2003, and Masad et al. 2004). Most of these studies utilized empirical analytical equations to relate certain pore parameters such as porosity to the hydraulic conductivity. The analytical equations utilized in previous studies were primarily developed for a relatively homogeneous and isotropic media such as cohesionless soils. Therefore, the calculated hydraulic conductivity value was naturally assumed to be constant in any direction in the field. However, majority of asphalt pavements have an anisotropic and heterogeneous internal pore structure (Masad et al. 1999), which has a direct influence on the magnitude of the hydraulic conductivities in different directions. Macro-scale numerical studies (Masad et al. 2003, Hunter and Airey 2005) concluded that the most of fluid flow is in horizontal direction in asphalt pavements. Therefore, the magnitude of horizontal hydraulic

conductivities (i.e., longitudinal (k_{xx}) and transverse (k_{yy}) hydraulic conductivity) may have significant effect on moisture transport through asphalt pavements. Directional hydraulic conductivity of porous structures has been studied by several researchers (Latini 1967, Moore 1979); however, their analyses were limited to cohesionless soils. Information is lacking on the horizontal hydraulic conductivity of asphalt pavements primarily due to the difficulties associated with field and laboratory measurements.

Most of the previous studies utilized only the hydraulic conductivity value as a mean to characterize the moisture induced damage in asphalt pavements. Pore pressure and shear stress distributions at the pore-solid interfaces in an asphalt pore structure due to the fluid flow, which could have significant negative contribution to binder stripping problem, have never been investigated. Furthermore, the variation in pore pressure and shear stress due to unsteady fluid flow caused by the repeated tire loading on the saturated pavement needs to be well understood in order to accurately characterize the moisture damage in the field. The critical values of shear stresses and pore pressures caused by both steady state and dynamic flow are also very important parameters that should be included as an input for microscale raveling studies characterizing the debonding of mastic from the aggregate (e.g., Kringos and Scarpas 2005).

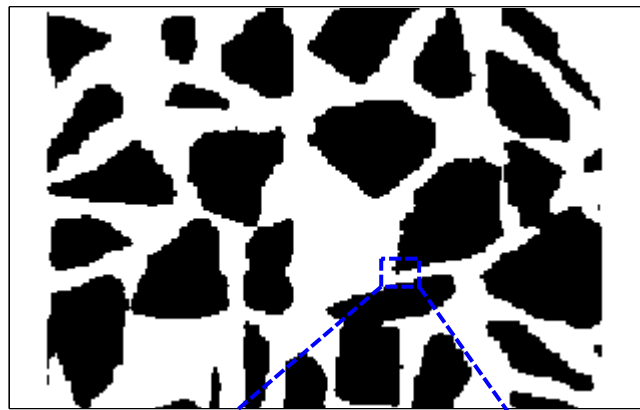
To respond this need, three-dimensional lattice Boltzmann (LB) fluid flow models were developed to study the moisture transport characteristics of asphalt pavements such as hydraulic conductivity tensor, pore pressure and viscous shear stress. Numerous steady and unsteady fluid flow simulations were conducted on different asphalt specimens to study these characteristics. The analyses of asphalt pavements included field cores and laboratory prepared specimens that were fabricated to study a number of mixture

variables which are likely to affect the pore structure (e.g., NMAS, aggregate gradation and compaction effort). Three-dimensional real pore structures of the specimens were generated using X-ray CT technique and used as an input in the LB models.

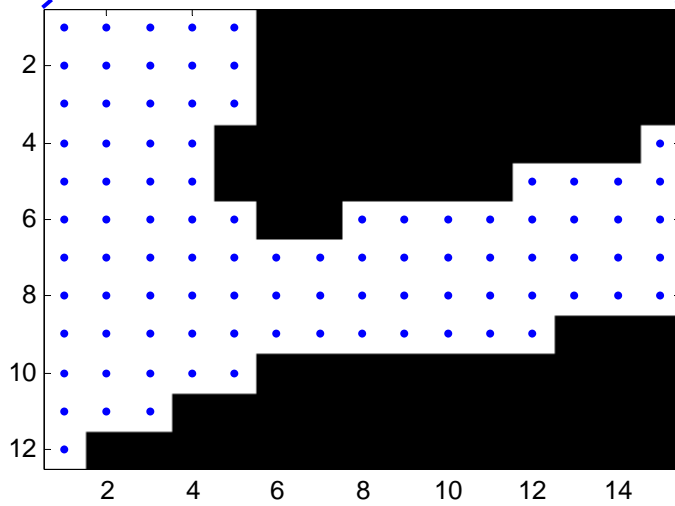
CHAPTER 3 LATTICE BOLTZMANN METHOD

The lattice Boltzmann (LB) method is a numerical method for simulation of viscous fluid flow. The LB method approximates the continuous Boltzmann equation by discretizing a physical space with lattice nodes and velocity space on a set of microscopic velocity vectors (Maier et al. 1997). A lattice corresponds to a set of nodes that represents the discrete phase of a physical space, where each node corresponds to either a void or a solid. The binary image of an aggregate structure is given in Figure 3.1a as an example to present the discretization of the physical space with black and white pixels. The lattice nodes are created at the center of each pixel as shown in Figure 3.1b. In the LB method, fluid particles travel on these nodes following the main LB equations, which ultimately satisfy the Navier-Stokes equations.

Conventional simulations of fluid flow such as finite difference, finite element, finite volume and spectral methods generally start from the nonlinear partial difference equations (Navier-Stokes equations) and solve these equations by using various numerical methods. This type of approach is called '*top-down*' approach (Figure 3.2) (Wolf-Gladrov 2000). On the other hand, LB method utilizes a '*bottom-up*' approach to reach the solution of differential equations. It has been shown by performing Chapman-Enskog expansion that LB method evolves according to the Navier-Stokes equations (Chin et al. 2002). Error resulting from truncation of Taylor series when going from differential to finite difference, and numerical instabilities are some of the disadvantages experienced in the former '*top-down*' approach. These problems were not experienced in the '*bottom-up*' approach. The studies conducted by numerous researchers



(a)



(b)

Figure 3.1 (a) Binary image of aggregates, black area representing aggregates and white area representing the pores, (b) creation of lattice nodes at the center of each white pixel

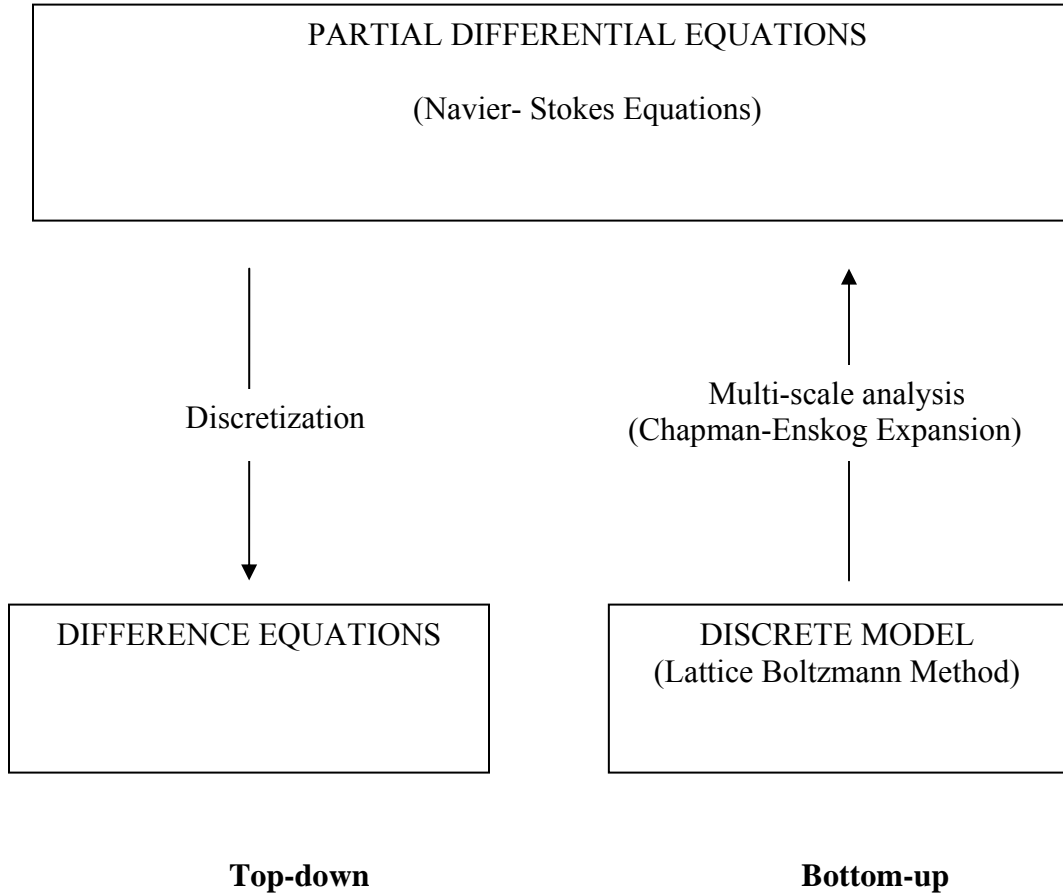


Figure 3.2 Top-down versus bottom-up approach in fluid flow simulation.

(Yoshino et al. 2004) comparing these two approaches concluded that LB method is comparable to traditional methods in relatively high Reynolds numbers and superior in low Reynolds numbers especially in the case of flow through porous media.

The basic idea of LB method comes from the kinetic theory of fluids. LB method considers a representative volume element of fluid (a node in the lattice) composed of particles that are defined in terms of a particle velocity distribution function, $F_i(\mathbf{x}, t)$ (Martys and Hagedorn 2002). This function is a discrete function that has Q number of components, where Q is the number of microscopic velocity directions (\mathbf{e}_i) around a lattice node (Figure 3.3). Each component of the function ($F_i, i= 1, 2 \dots Q$) represents a fraction of the total number of particles at each node with a microscopic velocity \mathbf{e}_i (Figure 3.3). The fluid particles travel on the lattice nodes through the use of distribution function which determine the macroscopic flow parameters, i.e., density and macroscopic velocity of fluid at each lattice node.

Various LB models exist for numerical solution of various fluid flow scenarios, where each model has different way of characterizing microscopic movement of the fluid particles. The LB models are usually denoted as D_xQ_y where x and y corresponds to the number of dimensions and number of microscopic velocity directions (\mathbf{e}_i), respectively (Table 3.1). For example, D2Q9 represents a two-dimensional geometry with nine microscopic velocity directions. Figure 3.3 shows microscopic velocity directions of D2Q9 and D3Q19 LB models which were implemented in this study.

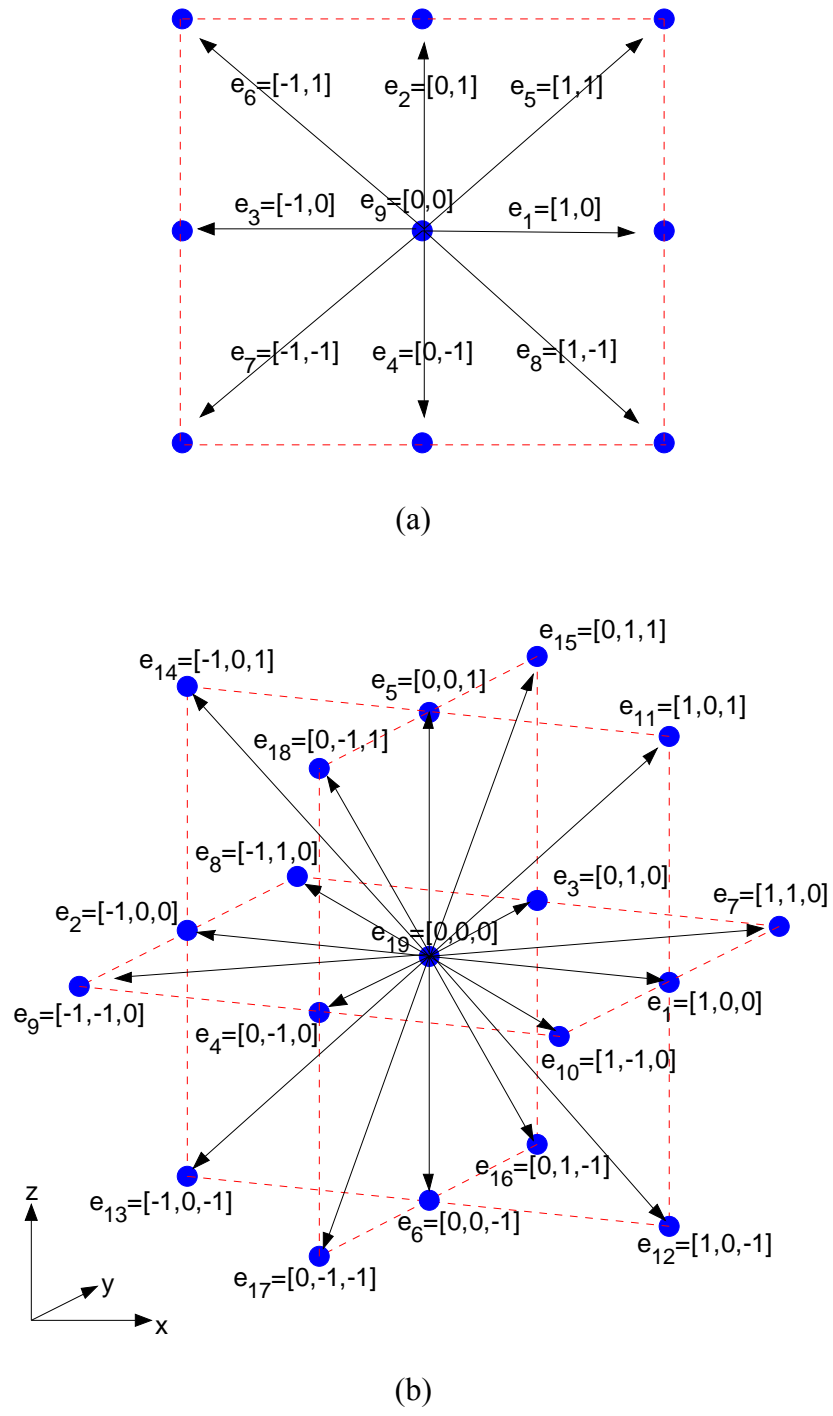
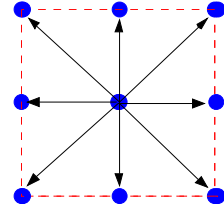
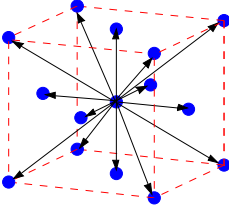
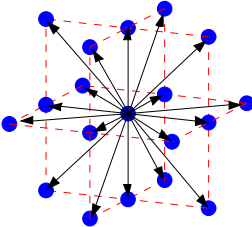


Figure 3.3 (a) D2Q9 and (b) D3Q19 lattice microscopic velocity directions.

Table 3.1 Properties of various LB models

Model Name	Lattice Speed of Sound, (c_s^2)	Weight Factors	Velocity Directions
D1Q3	1/3	4/6 ⁽¹⁾ 1/6 ⁽²⁾	
D1Q5	1	6/12 ⁽¹⁾ 2/12 ⁽²⁾ 1/12 ⁽²⁾	
D2Q9	1/3	16/36 ⁽¹⁾ 4/36 ⁽²⁾ 1/36 ⁽³⁾	
D3Q15	1/3	16/72 ⁽¹⁾ 8/72 ⁽²⁾ 1/72 ⁽³⁾	
D3Q19	1/3	12/36 ⁽¹⁾ 2/36 ⁽²⁾ 1/36 ⁽³⁾	

Note: Weight factors for; ⁽¹⁾ rest particle, ⁽²⁾ face-connected neighbors, ⁽³⁾ edge-connected neighbors

3.1 BASIC THEORY: FROM BOLTZMANN EQUATION TO LATTICE BOLTZMANN METHOD

Generalized form of Boltzmann equation is given as (Chapman and Cowling 1970, Cercignani 1975):

$$\frac{\partial f}{\partial t} + \mathbf{u} \cdot \frac{\partial f}{\partial \mathbf{x}} + \mathbf{F} \cdot \frac{\partial f}{\partial \mathbf{u}} = \Omega(f) \quad (3.1)$$

where f is the distribution function, \mathbf{u} is the velocity, \mathbf{F} is the body force per unit mass, \mathbf{x} is the vector coordinates of the fluid molecule and $\Omega(f)$ is the collision function. Collision function is given in an integral form, which transforms the incoming velocities into outgoing velocities of the fluid particles (Succi 2000) through a collision operation. Due to its complex structure, integral form of the collision function will not be presented here. Instead, a discrete form of the simplified collision function is given in the following paragraphs. The distribution function, f , is a statistical function from which that the macroscopic properties of the fluid can be found. The complexity of Boltzmann equation makes it impractical to be solved directly for macroscopic flow problems. To simplify it, physical space is discretized into a set of uniformly spaced nodes (lattice) that represents the voids and the solids (Figure 3.1) and discrete set of (microscopic) velocities are defined for each node (Figure 3.3). A common way of accomplishing the discrete phase of physical space is the utilization of centers of pixels obtained from its digital image as seen in Figure 3.1b. Then, discrete velocity directions are defined such that each direction points to a neighboring node as seen in Figure 3.3a and Figure 3.3b, for two dimensional and three dimensional cases, respectively. The discrete form of Boltzmann equation can be written for each discrete (microscopic) velocity direction (\mathbf{e}_i), as follows:

$$\frac{\partial f_i}{\partial t} + \mathbf{e}_i \cdot \frac{\partial f_i}{\partial \mathbf{x}} + \mathbf{F} \cdot \frac{\partial f}{\partial \mathbf{e}_i} = \Omega_i \quad (3.2)$$

where f_i is the distribution function in the i^{th} microscopic velocity direction and Ω_i is the collision function.

The relation of the time derivative of f_i , measured at a fixed position (i.e., using Eulerian variables) with the one measured while following the particle (i.e., using Lagrangian variables) can be defined by using the substantial derivative as follows (Panton 1996):

$$\frac{Df_i}{Dt} = \frac{\partial f_i}{\partial t} + \mathbf{e}_i \cdot \frac{\partial f_i}{\partial \mathbf{x}} \quad (3.3)$$

Note that, left hand side (LHS) of Equation (3.3) is in Lagrangian viewpoint, whereas, right hand side (RHS) is in Eulerian viewpoint. Discrete phase of substantial derivative in Lagrangian viewpoint (i.e. as measured while on a moving particle) can be written in the following form after integrating over time and neglecting higher order terms (He and Luo 1997):

$$\frac{DF_i}{Dt} = F_i(\mathbf{x} + \mathbf{e}_i, t+1) - F_i(\mathbf{x}, t) \quad (3.4)$$

Combining equations (3.2), (3.3) and (3.4) for discrete space (lattice) reveals:

$$F_i(\mathbf{x} + \mathbf{e}_i, t+1) = F_i(\mathbf{x}, t) + \Omega_i - B_F \quad (3.5)$$

where F_i is the (discrete) particle distribution function at lattice node \mathbf{x} , at time t , and B_F is the body force. Note that, the third component of the LHS of Equation (3.1) is referred

to as B_F in here for simplicity. Among the various forms of B_F , the following form (Martys et al. 1998) was used in this study:

$$B_F = -\frac{w_i}{c_s^2}(\mathbf{e}_i \cdot \nabla \mathbf{p}) \quad (3.6)$$

where w_i is the weight factor for each direction around a node, \mathbf{e}_i are the lattice velocity directions, c_s^2 is a constant called *lattice speed of sound* (see Table 3.1) and $\nabla \mathbf{p}$ is the pressure gradient. Weight factors vary in different LB methods as seen in Table 3.1. For example, weight factors (w_i) for D2Q9 LB method are: $w_0=4/9$ for rest particle, $w_i=1/9$ ($1 \leq i \leq 4$) for particles streaming to the face-connected neighbors and $w_i=1/36$ ($5 \leq i \leq 8$) for particles streaming to the edge-connected neighbors.

The collision function, Ω_i , can be simplified by assuming that the distribution functions relax to their equilibrium state at a constant rate (also called Bhatnagar-Gross-Krook (BGK) approximation (Bhatnagar et al. 1954)). Then the collision function takes the following form:

$$\Omega_i = -\frac{F_i - F_i^{eq}}{\tau} \quad (3.7)$$

where F_i^{eq} is the equilibrium distribution function and τ is the relaxation time which is a function of viscosity of the fluid. Equilibrium distribution functions for different models were derived by He and Luo (1997). The function is given in the following form for D2Q9 and D3Q19 models:

$$F_i^{eq} = w_i \rho \left[1 + \frac{\mathbf{e}_i \cdot \mathbf{u}}{c_s^2} + \frac{(\mathbf{e}_i \cdot \mathbf{u})^2}{2c_s^4} - \frac{(\mathbf{u} \cdot \mathbf{u})}{2c_s^2} \right] \quad (3.8)$$

where F_i^{eq} is the equilibrium distribution function, ρ is the density, \mathbf{u} is the macroscopic velocity of the node. The relaxation time relates to viscosity of fluid (ν) as follows:

$$\nu = c_s^2 \left(\tau - \frac{1}{2} \right) \quad (3.9)$$

The macroscopic properties, density and velocity, of the nodes are calculated using the following relations:

$$\rho = \sum_{i=1}^Q F_i \quad (3.10)$$

$$\mathbf{u} = \frac{\sum_{i=1}^Q F_i \mathbf{e}_i}{\rho} \quad (3.11)$$

where ρ and \mathbf{u} are the macroscopic density and velocity of the fluid each node of lattice.

3.2 STEPS OF THE LATTICE BOLTZMANN ALGORITHM

There are three basic phases in a typical LB algorithm. Figure 3.4 summarizes the sequence of the algorithm implemented in this study. In the first phase, initial conditions of the simulation were set. The second phase was the propagation of fluid particles to the neighboring nodes followed by the calculation of new density and macroscopic velocity of each node for the next time step. The third phase involved prescribing boundary conditions and calculation of new equilibrium distribution functions.

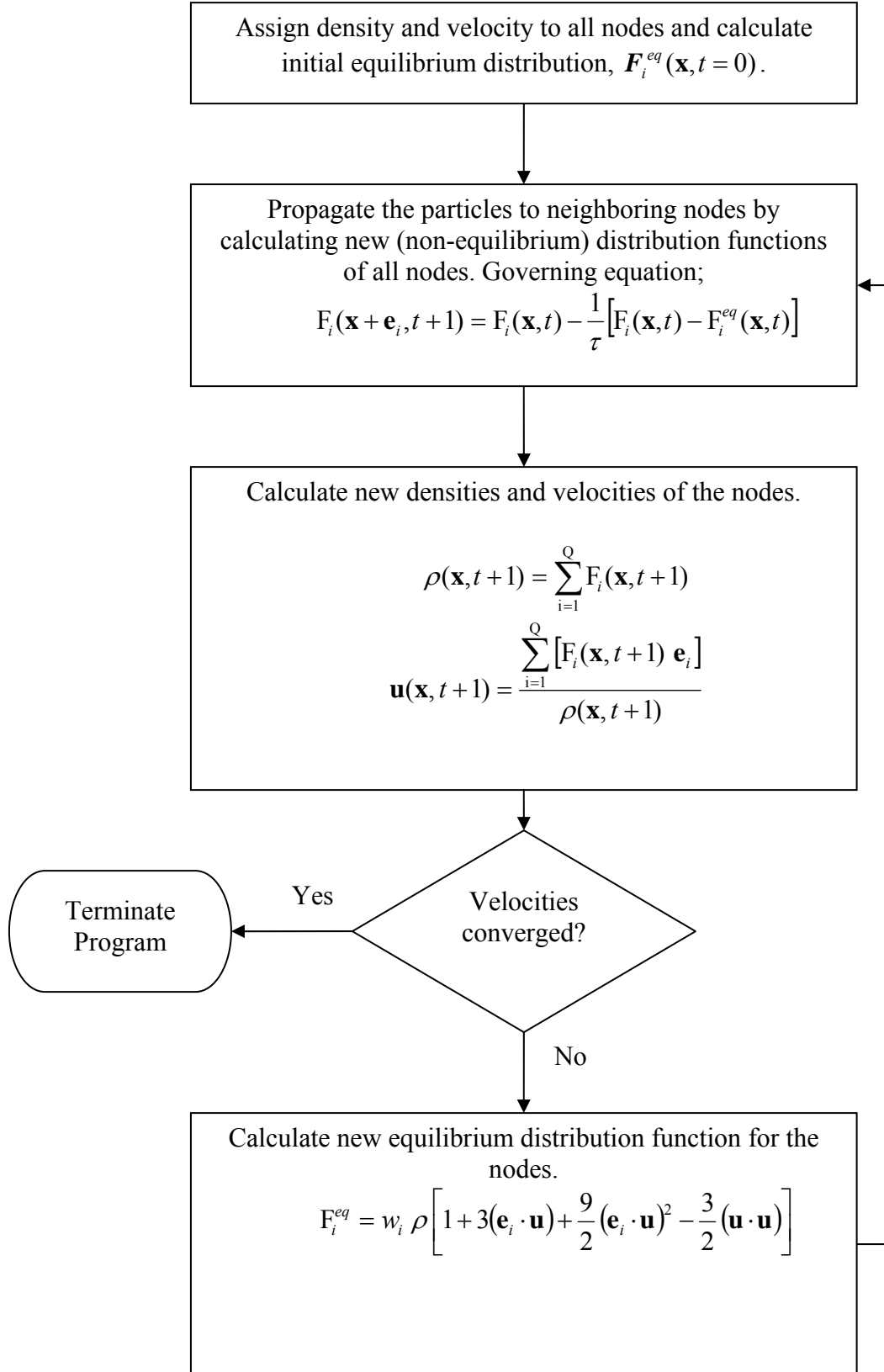


Figure 3.4 Flow chart of LB algorithm implemented in this study.

The phases two and three were repeated until the difference in average velocities of the domain calculated in the previous time and current time steps was less than a threshold value, which confirmed the onset of steady-state flow.

3.2.1 Phase I-Initialization

As a part of the first phase, densities and velocities of the lattice nodes were set to an initial value. Then, initial equilibrium distribution functions of all nodes were calculated by using the following equation:

$$F_i^{eq} = w_i \rho \left[1 + 3(\mathbf{e}_i \cdot \mathbf{u}) + \frac{9}{2} (\mathbf{e}_i \cdot \mathbf{u})^2 - \frac{3}{2} (\mathbf{u} \cdot \mathbf{u}) \right] \quad (3.12)$$

where $F_i^{eq} = F_i^{eq}(\mathbf{x}, t = 0)$ is the equilibrium distribution function; $\rho = \rho(\mathbf{x}, t = 0)$ and $\mathbf{u} = \mathbf{u}(\mathbf{x}, t = 0)$ are initial density and macroscopic velocity of the node \mathbf{x} , respectively; \mathbf{e}_i is the lattice velocity direction, and w_i is the weight factor for the component i . The microscopic velocity directions and weight factors vary for different LB models, as seen in Table 3.1. The non-equilibrium distribution function (F_i) was initially set to be equal to the equilibrium distribution function:

$$F_i(\mathbf{x}, t = 0) \leftarrow F_i^{eq}(\mathbf{x}, t = 0) \quad (3.13)$$

3.2.2 Phase II-Propagation of Fluid to the Neighboring Nodes and Calculation of Distribution Function, Density and Velocity at Each Node

Figure 3.5a shows the orientation of the equilibrium distribution function components at time= t ($F_i^{eq}(\mathbf{x}, t)$), where each component points towards a microscopic velocity direction, \mathbf{e}_i . These components at each node propagate to the neighboring nodes

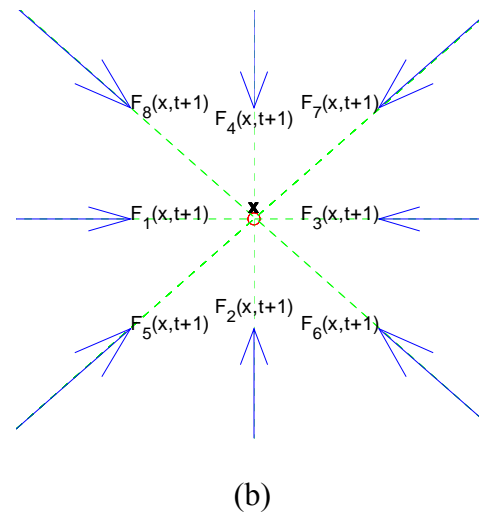
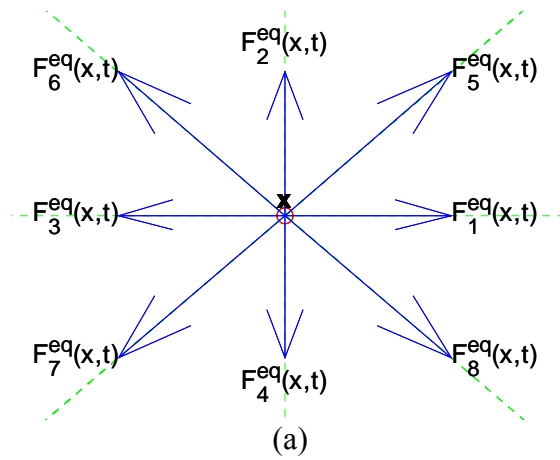


Figure 3.5 (a) Orientation of components of equilibrium distribution function calculated in the previous time step, (b) illustration of non-equilibrium distribution function calculated in Step II.

and produce the non-equilibrium distribution function for the next time step of the neighboring node ($F_i(\mathbf{x} + \mathbf{e}_i, t+1)$). The propagation was performed using the following equation:

$$F_i(\mathbf{x} + \mathbf{e}_i, t+1) = F_i(\mathbf{x}, t) - \frac{1}{\tau} [F_i(\mathbf{x}, t) - F_i^{eq}(\mathbf{x}, t)] \quad (3.14)$$

where $F_i(\mathbf{x}, t)$ and $F_i(\mathbf{x} + \mathbf{e}_i, t+1)$ are the non-equilibrium distribution functions in the i^{th} lattice direction at node \mathbf{x} , at time t , and at node $\mathbf{x} + \mathbf{e}_i$ at time $t+1$, respectively; τ is the relaxation time which is a function of viscosity of the fluid ($\hat{\nu} = (2\tau - 1)/6$), and $F_i^{eq}(\mathbf{x}, t)$ is the equilibrium distribution function. Undefined components of the distribution function at the solid wall boundaries and at inlet and outlet were calculated using appropriate boundary conditions which are described in Boundary Conditions section.

To increase the computational efficiency, Equation 3.14 was further simplified into the following form by setting the relaxation time to unity (i.e., $\tau=1$):

$$F_i(\mathbf{x} + \mathbf{e}_i, t+1) = F_i^{eq}(\mathbf{x}, t) \quad (3.15)$$

Figure 3.5b illustrates how non-equilibrium distribution function components migrate from neighboring nodes and accumulate at the center node. After colliding at the center node, these components define the density and macroscopic velocity of the node.

$$\rho(\mathbf{x}, t + 1) = \sum_{i=1}^Q F_i(\mathbf{x}, t + 1) \quad (3.16)$$

$$\mathbf{U}(\mathbf{x}, t + 1) = \sum_{i=1}^Q [F_i(\mathbf{x}, t + 1) \mathbf{e}_i] \quad (3.17)$$

where $\rho(\mathbf{x}, t + 1)$ and $\mathbf{U}(\mathbf{x}, t + 1)$ are the density and the momentum of node \mathbf{x} , at time $t + 1$. Macroscopic velocity ($\mathbf{u}(\mathbf{x}, t + 1)$) of each node was calculated using the following relation:

$$\mathbf{u}(\mathbf{x}, t + 1) = \frac{\mathbf{U}(\mathbf{x}, t + 1)}{\rho(\mathbf{x}, t + 1)} \quad (3.18)$$

3.2.3 Phase III- Boundary Conditions and Calculation of the New Equilibrium Distribution Functions

In this phase of the algorithm, boundary conditions were imposed at the boundaries of the domain. Then, the new values of the equilibrium distribution function were computed for each lattice node at time step $t + 1$ using Equation 3.12. The phases II and III were repeated until the steady state flow conditions were satisfied.

3.3 BOUNDARY CONDITIONS

3.3.1 Boundary Conditions near Solid Nodes

3.3.1.1 No-Slip Boundary Condition

In particle propagation step of the algorithm, all components of non-equilibrium distribution function were computed at each node except at nodes neighboring to solid nodes (Figure 3.6a). At those nodes, certain components of the distribution function that

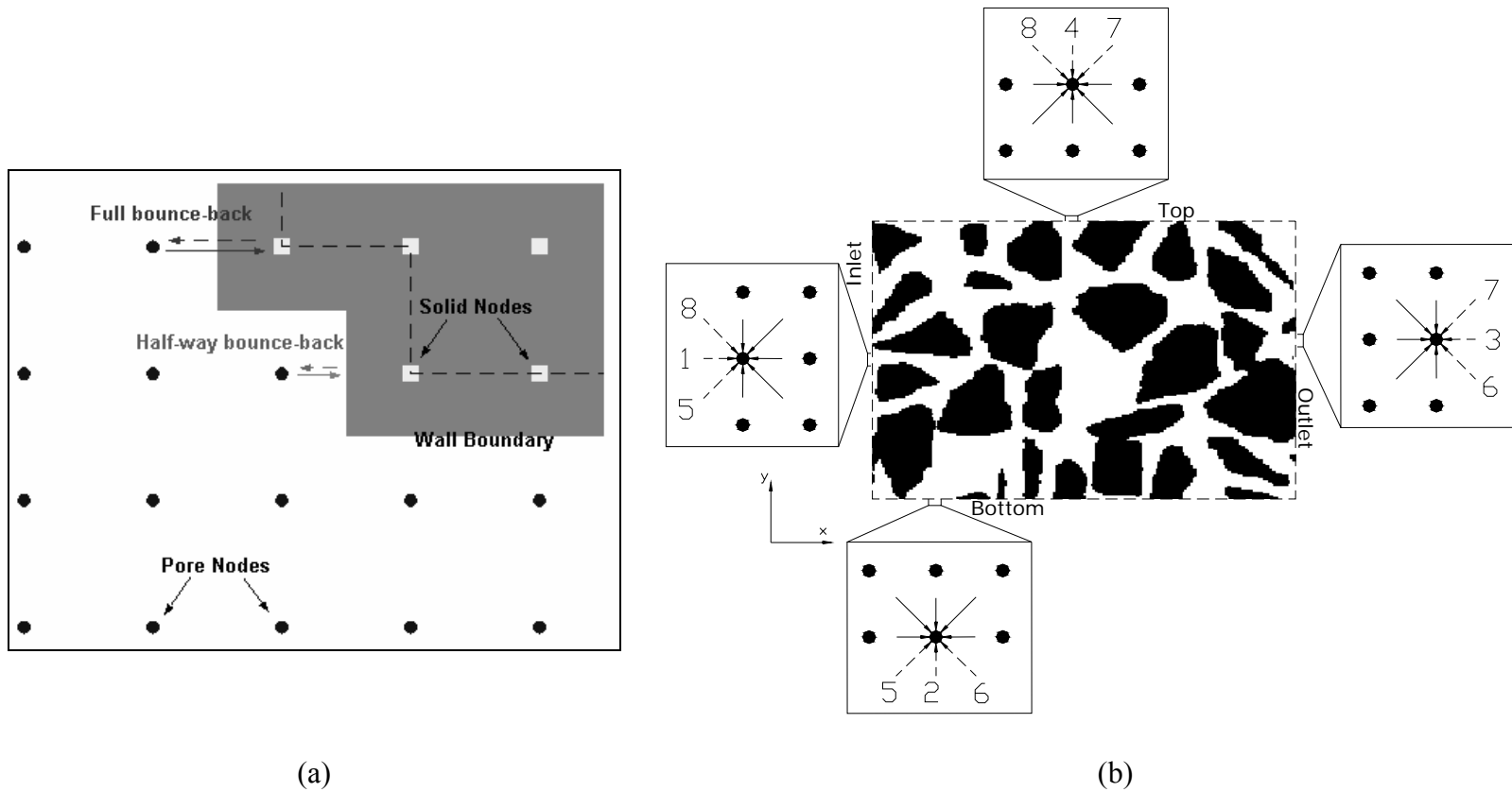


Figure 3.6 Illustration of (a) two types of no-slip boundary conditions; full bounce back and half-way bounce back, and (b) unknown components of the distribution function streaming from outside the boundaries

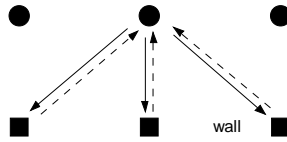
are expected to be migrating from the solid node were unknown. In this case, a wall boundary condition was used to calculate the missing components. Most commonly used technique for scattering of the distribution function at nodes located near the solid nodes is the no-slip boundary condition (Maier et al. 1996). It is also referred to as the *bounce-back* scheme, in which the distribution function components heading towards the solid nodes scatter directly back to the node. Two kinds of no-slip boundary conditions exist as illustrated in Figure 3.6a. The first one, named as *full bounce-back*, assumes that the wall is located at the solid nodes whereas the second one, named as *half-way bounce-back*, assumes that the wall is located half-way between the pore and solid nodes. The solid and dashed lines in Figure 3.6a show the wall boundaries for full bounce-back and half-way bounce-back scheme, respectively. It has been shown that full bounce-back provides a first order accuracy, whereas, half-way bounce-back provides a second order accuracy (Ziegler 1993). Second-order accurate half-way bounce back wall boundary condition was used in the current simulations to calculate the missing components of the distribution function at nodes neighboring to solid walls.

3.3.1.2 Slip Boundary Condition

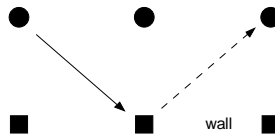
Slip boundary condition is applicable only to extremely smooth surfaces where negligible friction is applied to the fluid (Succi 2001). A comparison of no-slip and slip boundary conditions is illustrated in Figures 3.7a and 3.7b, respectively.

3.3.1.3 Extrapolation

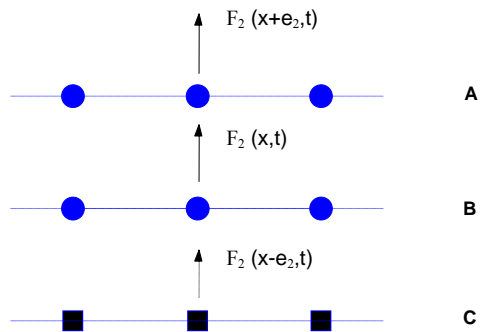
Extrapolation scheme was first proposed by Chen et al. (1996). It is assumed that there is one additional imaginary layer of sites at the wall nodes (filled squares in Figure 3.7c). At



(a)



(b)



(c)

Figure 3.7 Comparison of three different boundary conditions at solid nodes: (a) No-slip boundary condition, (b) slip boundary condition, and (c) extrapolation scheme.

each time step, before the particle propagation (step II of algorithm), the distribution functions emanating from the imaginary layer (layer C in Figure 3.7c) are calculated using a second order extrapolation, based on the value of the distribution function on the layer A and layer B. The following condition is enforced to calculate the components of the distribution function at wall nodes streaming into the fluid nodes:

$$F_i^C = 2F_i^B - F_i^A \quad (3.19)$$

where superscripts, A , B and C represents the layers shown in Figure 3.7c. For example, the 2nd component of the distribution function emanating from the solid node is calculated as follows (Figure 3.7c):

$$F_2(x - e_2, t) = 2F_2(x, t) - F_2(x + e_2, t) \quad (3.20)$$

3.3.2 Boundary Conditions at Domain Boundaries

In addition to the nodes near solid nodes, certain components of distribution function of the nodes located at the boundaries of the domain; i.e. inlet, outlet, top and bottom nodes are also unknown as seen in Figure 6b. These components (e.g. F_1, F_5, F_8 at inlet nodes) can be calculated from the known components (e.g. F_9, F_2, F_4, F_3, F_6 and F_7 at inlet nodes) and by setting at least two constraints such as prescribing two components of macroscopic velocity (i.e., u_x, u_y). Another set of alternative constraints can also be the density and one component of the macroscopic velocity (i.e., ρ, u_x) at those nodes. This approach creates a continuous momentum at the boundaries which is transported throughout the domain generating the flow. For example, given the two components of the macroscopic velocity, the density and unknown distribution function components at those nodes can be calculated using the relationships given in Table 3.2. These

Table 3.2 Relations for the unknowns at the boundaries for D2Q9 model.

Boundary Nodes	Known Components	Unknown Components	Relations
Inlet	$u_x, u_y,$ F_9, F_2, F_4 $F_3, F_6,$ F_7	$\rho,$ $F_1, F_8,$ F_5	$\rho_{in} = \frac{1}{1 - u_{x(in)}} [F_9 + F_2 + F_4 + 2(F_3 + F_6 + F_7)]$ $F_1 = F_3 + \frac{2}{3} \rho u_x$ $F_8 = F_6 + \frac{1}{2} (F_2 - F_4) + \frac{1}{6} \rho u_x - \frac{1}{2} \rho u_y$ $F_5 = F_7 - \frac{1}{2} (F_2 - F_4) + \frac{1}{6} \rho u_x + \frac{1}{2} \rho u_y$
Outlet	$u_x, u_y,$ $F_9, F_2,$ $F_4,$ $F_1, F_5,$ F_8	$\rho,$ $F_3, F_6,$ F_7	$\rho_{out} = \frac{1}{1 + u_{x(out)}} [F_9 + F_2 + F_4 + 2(F_3 + F_6 + F_7)]$ $F_3 = F_1 - \frac{2}{3} \rho u_x$ $F_6 = F_8 - \frac{1}{2} (F_2 - F_4) - \frac{1}{6} \rho u_x + \frac{1}{2} \rho u_y$ $F_7 = F_5 + \frac{1}{2} (F_2 - F_4) - \frac{1}{6} \rho u_x - \frac{1}{2} \rho u_y$
Bottom	$u_x, u_y,$ F_9, F_1, F_3 F_4, F_7, F_8	$\rho,$ $F_2, F_6,$ F_5	$\rho_{bottom} = \frac{1}{1 - u_{y(bottom)}} [F_9 + F_1 + F_3 + 2(F_4 + F_7 + F_8)]$ $F_2 = F_4 + \frac{2}{3} \rho u_y$ $F_6 = F_8 + \frac{1}{2} (F_1 - F_3) + \frac{1}{6} \rho u_y - \frac{1}{2} \rho u_x$ $F_5 = F_7 - \frac{1}{2} (F_1 - F_3) + \frac{1}{6} \rho u_y + \frac{1}{2} \rho u_x$
Top	$u_x, u_y,$ F_9, F_1, F_3 $F_2, F_6,$ F_5	$\rho,$ F_4, F_7, F_8	$\rho_{top} = \frac{1}{1 + u_{y(top)}} [F_9 + F_1 + F_3 + 2(F_2 + F_6 + F_5)]$ $F_4 = F_2 - \frac{2}{3} \rho u_y$ $F_8 = F_6 - \frac{1}{2} (F_1 - F_3) - \frac{1}{6} \rho u_y + \frac{1}{2} \rho u_x$ $F_7 = F_5 + \frac{1}{2} (F_1 - F_3) - \frac{1}{6} \rho u_y - \frac{1}{2} \rho u_x$

Table 3.3 Relations for the unknowns at the boundaries for D3Q19 model.

Boundary	Known Components	Unknown Components	Relations
Inlet	$\rho, u_x=0,$ $u_y=0,$ $F_{19}, F_1, F_2,$ $F_3, F_4, F_6,$ $F_7, F_8, F_9,$ $F_{10}, F_{12}, F_{13},$ F_{16}, F_{17}	$u_z,$ $F_5,$ $F_{11},$ $F_{14},$ $F_{15},$ $F_{18},$	$u_{z(in)} = 1 - \frac{F_{19} + \sum_{i=1}^4 F_i + \sum_{i=7}^{10} F_i + 2(F_6 + F_{12} + F_{13} + F_{16} + F_{17})}{\rho_{in}}$ $F_5 = F_6 + \frac{1}{3}\rho u_z$ $F_{15} = F_{17} - \frac{1}{4}(F_3 - F_4) + \frac{1}{6}\rho u_z$ $F_{18} = F_{16} + \frac{1}{4}(F_3 - F_4) + \frac{1}{6}\rho u_z$ $F_{11} = F_{13} - \frac{1}{4}(F_1 - F_2) + \frac{1}{6}\rho u_z$ $F_{14} = F_{12} + \frac{1}{4}(F_1 - F_2) + \frac{1}{6}\rho u_z$
Outlet	$\rho, u_x=0,$ $u_y=0,$ $F_{19}, F_1, F_2,$ $F_3, F_4, F_7,$ $F_8, F_9, F_{10},$ $F_5, F_{11}, F_{14},$ $F_{15}, F_{18},$	$u_z,$ $F_6,$ $F_{12},$ $F_{13},$ $F_{16},$ F_{17}	$u_{z(out)} = -1 + \frac{F_{19} + \sum_{i=1}^4 F_i + \sum_{i=7}^{10} F_i + 2(F_5 + F_{11} + F_{14} + F_{15} + F_{18})}{\rho_{out}}$ $F_6 = F_5 - \frac{1}{3}\rho u_z$ $F_{17} = F_{15} + \frac{1}{4}(F_3 - F_4) - \frac{1}{6}\rho u_z$ $F_{16} = F_{18} - \frac{1}{4}(F_3 - F_4) - \frac{1}{6}\rho u_z$ $F_{13} = F_{11} + \frac{1}{4}(F_1 - F_2) - \frac{1}{6}\rho u_z$ $F_{12} = F_{14} - \frac{1}{4}(F_1 - F_2) - \frac{1}{6}\rho u_z$

relationships were derived using density (Eq. 3.16) and momentum (Eq. 3.17) equations, and their derivations are provided in Appendix A. The unknown components of the distribution function given in Table 3.2 were calculated by assuming that the bounce-back scheme is valid for the non-equilibrium part of the particle distribution function (Zou and He 1997).

Since the cylindrical asphalt specimens tested in the laboratory for this study were confined by the membranes, only the unknown distribution functions at the inlet and the outlet were of interest. Therefore, relations similar to the ones given in Table 3.2 for D2Q9 model were derived for the three dimensional D3Q19 model only for inlet and outlet faces and provided in Table 3.3. It should be noted that the relations given in Table 3.3 are derived based on the given constraints that velocity parallel to the inlet and outlet face are zero (i.e., $u_x=0$ and $u_y=0$) and density at these nodes are known.

Use of periodic boundary conditions is another technique to eliminate unknown components of the distribution function of the nodes at the boundaries of the domain. In this case, components of the distribution function exiting from outlet nodes are treated as entering from the inlet nodes as illustrated in Figure 3.8. This way there is not any missing component of the distribution function at those boundary nodes.

3.3.3 Other Techniques to Create Flow in LB Models

3.3.3.1 Density Gradient

Practical laboratory flow experiments employ constraints such as fixed pressure at inlet and outlet to create flow (e.g. constant head permeability test). This kind of flow experiments can easily be simulated by using LB model. A very important characteristic

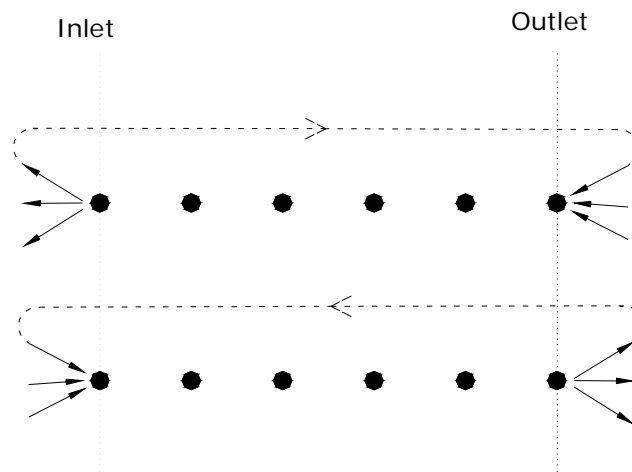


Figure 3.8 Illustration of periodic boundary conditions where components exiting from one end of the boundary are treated as entering from the other end.

of LB models is that the pressure is proportional to the density which is defined by the equation of state (Maier et al. 1997, Zou and He 1997):

$$P = c_s^2 \rho \quad (3.21)$$

where P and ρ are pressure and density, respectively, and c_s is a constant called *lattice speed of sound*. Therefore, the flow can be triggered in a LB model by setting certain densities at the inlet and outlet nodes to produce a density gradient which is consistent with the desired pressure gradient. This method creates flow from high density (pressure) inlet nodes towards low density (pressure) outlet nodes.

3.3.3.2 Body Force

A different approach to trigger the flow is the application of a constant force at each node along with the periodic boundary conditions. This force, referred to as body force, is added to the main propagation equation as follows:

$$F_i(\mathbf{x} + \mathbf{e}_i, t + 1) = F_i(\mathbf{x}, t) - \frac{1}{\tau} [F_i(\mathbf{x}, t) - F_i^{eq}(\mathbf{x}, t)] - g_i \quad (3.22)$$

where g_i is the body force term for i^{th} component. Among the various forms of body force term, the following form given by Martys and Hagedorn (2002) was utilized in this study.

$$g_i = -3w_i(\mathbf{e}_i \cdot \nabla \mathbf{p}) \quad (3.23)$$

where w_i and \mathbf{e}_i are the weight factor and microscopic velocity, respectively, and $\nabla \mathbf{p}$ is the pressure gradient.

CHAPTER 4 DEVELOPMENT AND VALIDATION OF THE LB ALGORITHM

4.1 ALGORITHM DEVELOPMENT

LB algorithms were implemented using Matlab programming language and named as *LB-D2Q9* and *LB-D3Q19*, for 2D and 3D models, respectively. An innovative way of programming was developed in Matlab which utilized only matrix manipulations without using loops, taking advantage of the fact that Matlab is very powerful in matrix manipulations. Traditional LB programs generally use a series of “for loops” which visit every node in the lattice and perform the lattice Boltzmann operations such as particle propagation, density and velocity calculation, equilibrium distribution function calculation, and applying boundary conditions. A different approach was used in this study to fully utilize the Matlab’s build-in functions, most of which are optimized for the best performance (least expensive in terms of computational time and least computer memory usage). The algorithms were implemented in such a way that geometry of the domain of interest can directly be input to the algorithm by reading the digital image of the domain for 2D analysis or reading the image stacks of the domain for 3D analysis. This allows the three dimensional D3Q19 LB algorithm to more easily handle X-ray Computed Tomography image stacks of a geomaterial in 3D flow simulations. The algorithms *LB-D2Q9* and *LB-D3Q19* are given in Appendix B and their sequence are as follows:

- I. The image of the domain is read and a coordinate matrix, \mathbf{X} , of size $N \times 2$ in *LB-D2Q9* and $N \times 3$ in *LB-D3Q19* is created where N is the total number of lattice points corresponding to pores. First and second columns represent the x , y coordinates in

both *LB-D2Q9* and *LB-D3Q19* algorithms and third column in *LB-D3Q19* represent the z coordinate of each pore point.

- II. The row indices of the conjugate nodes for each microscopic velocity direction are computed using coordinate matrix \mathbf{X} . Conjugate of a node herein corresponds to a neighboring node that is one microscopic velocity direction (\mathbf{e}_i) away from the node.
- III. A velocity matrix, \mathbf{V} , of size $N \times 2$ in *LB-D2Q9* and $N \times 3$ in *LB-D3Q19* is created. For example for 3D geometry; first, second and third columns of any given row correspond to u_x , u_y and u_z , respectively, of the pore that has the coordinates given in the same row of coordinate matrix, \mathbf{X} .
- IV. A density matrix, p , of size $N \times 1$ is created where each row has the density value of pore point whose coordinates is given in the same row in the coordinate matrix, \mathbf{X} .
- V. Initial velocity and density values are assigned based on the desired initial boundary conditions.
- VI. A matrix, F_{eq} , defining the equilibrium distribution function of each node is created. It has the size of $N \times 9$ in *LB-D2Q9* and $N \times 19$ in *LB-D3Q19* algorithm. Each row in this matrix has the equilibrium distribution function values of the point whose coordinates given in the same row of coordinate matrix. Each column in a given row represents the equilibrium distribution function value of a microscopic velocity direction (Figure 4.1a). Then initial equilibrium distribution function values are computed using Equation 3.12.

$$F_{\text{eq}} = \begin{pmatrix} \mathbf{e}_1 & \mathbf{e}_2 & \mathbf{e}_3 & \cdots & \mathbf{e}_9 \\ F_{\text{eq}}^1(x_1, y_1) & F_{\text{eq}}^2(x_1, y_1) & F_{\text{eq}}^3(x_1, y_1) & \cdots & F_{\text{eq}}^9(x_1, y_1) \\ F_{\text{eq}}^1(x_2, y_2) & F_{\text{eq}}^2(x_2, y_2) & F_{\text{eq}}^3(x_2, y_2) & \cdots & F_{\text{eq}}^9(x_2, y_2) \\ F_{\text{eq}}^1(x_3, y_3) & F_{\text{eq}}^2(x_3, y_3) & F_{\text{eq}}^3(x_3, y_3) & \cdots & F_{\text{eq}}^9(x_3, y_3) \\ F_{\text{eq}}^1(x_4, y_4) & F_{\text{eq}}^2(x_4, y_4) & F_{\text{eq}}^3(x_4, y_4) & \cdots & F_{\text{eq}}^9(x_4, y_4) \\ \vdots & \vdots & \vdots & \cdots & \vdots \\ F_{\text{eq}}^1(x_N, y_N) & F_{\text{eq}}^2(x_N, y_N) & F_{\text{eq}}^3(x_N, y_N) & \cdots & F_{\text{eq}}^9(x_N, y_N) \end{pmatrix}$$

$$F = \begin{pmatrix} \mathbf{e}_1 & \mathbf{e}_2 & \mathbf{e}_3 & \cdots & \mathbf{e}_9 \\ F^1(x_1, y_1) & F^2(x_1, y_1) & F^3(x_1, y_1) & \cdots & F^9(x_1, y_1) \\ F^1(x_2, y_2) & F^2(x_2, y_2) & F^3(x_2, y_2) & \cdots & F^9(x_2, y_2) \\ F^1(x_3, y_3) & F^2(x_3, y_3) & F^3(x_3, y_3) & \cdots & F^9(x_3, y_3) \\ F^1(x_4, y_4) & F^2(x_4, y_4) & F^3(x_4, y_4) & \cdots & F^9(x_4, y_4) \\ \vdots & \vdots & \vdots & \cdots & \vdots \\ F^1(x_N, y_N) & F^2(x_N, y_N) & F^3(x_N, y_N) & \cdots & F^9(x_N, y_N) \end{pmatrix}$$

Figure 4.1 Equilibrium and nonequilibrium distribution function matrices

- VII. A matrix, F , defining the non-equilibrium distribution function of each node is created as the F_{eq} . Initial values of the non-equilibrium distribution function are assumed to be the same of F_{eq} .
- VIII. Particle propagation step is carried out by replacing the cells of matrix F with the new values computed for the next time step. For each column in matrix F , which represents one microscopic velocity direction (\mathbf{e}_i), the non-equilibrium distribution function value in each row is replaced by its new value computed using Equation 3.14. This is accomplished by using the corresponding row indices (computed in step II) of a node and its conjugate node for a given microscopic velocity direction (\mathbf{e}_i).
- IX. New density and velocity matrices are calculated using Equations 3.16 and 3.17.
- X. Boundary conditions are imposed by replacing density or velocity values wherever necessary, and computing unknown components of the non-equilibrium distribution function at boundaries.
- XI. New equilibrium distribution function values are computed using Equation 3.12.
- Steps VIII, IX, X and XI are repeated using a “while loop” until the steady state flow is achieved.

4.2 VALIDATION OF TWO DIMENSIONAL D2Q9 MODEL

4.2.1 Flow between parallel plates

First and simplest level of verification of a fluid flow model is to compare it with the analytical solution of velocity profile of a fluid flowing between infinitely long parallel plates. The analytical solution of a parabolic velocity profile of flow between parallel plates is given as:

$$u_x = \frac{\nabla P_x}{2\mu} y(B - y) \quad (4.1)$$

where u_x is the velocity in the direction of pressure gradient, ∇P_x = pressure gradient, μ = dynamic viscosity, B is the width of channel, and y is the distance from the bottom plate as shown in Figure 4.2a. To verify the accuracy of the D2Q9 LB model and its sensitivity to the number of lattice sites (i.e. spatial resolution), flow between two parallel plates separated with a distance of 5 mm was modeled using four different number of lattice points (N_y): 5, 10, 20 and 40 pixels. A pressure gradient of $6.4 \times 10^{-7} \text{ g}/(\text{mm}^2 \text{ sec}^2)$ was applied in the x-direction to create a flow field with a corresponding Reynolds number of 0.01. A body force together with the periodic boundary conditions in x direction was used to apply pressure gradient. Half-way bounce back boundary condition is used at the walls. The velocity profiles computed from LB simulations at different number of lattice sites (given as N_y in figure) together with the analytical solution (Equation 4.1) are presented in Figure 4.2a. An excellent agreement between the analytical solution and LB simulations is clearly visible in all lattice resolutions. The LB algorithm successfully modeled the flow even at very low resolutions (e.g. $N_y = 5$). An error analysis was performed to evaluate the magnitude of the error and the order of accuracy of the current LB model. The error, measuring the difference between analytical and LB model was computed in two ways as follows:

$$RMS = \left(\frac{1}{N_y} \sum_{i=1}^{N_y} (u_x^A - u_x^{LB})^2 \right)^{0.5} \quad (4.2)$$

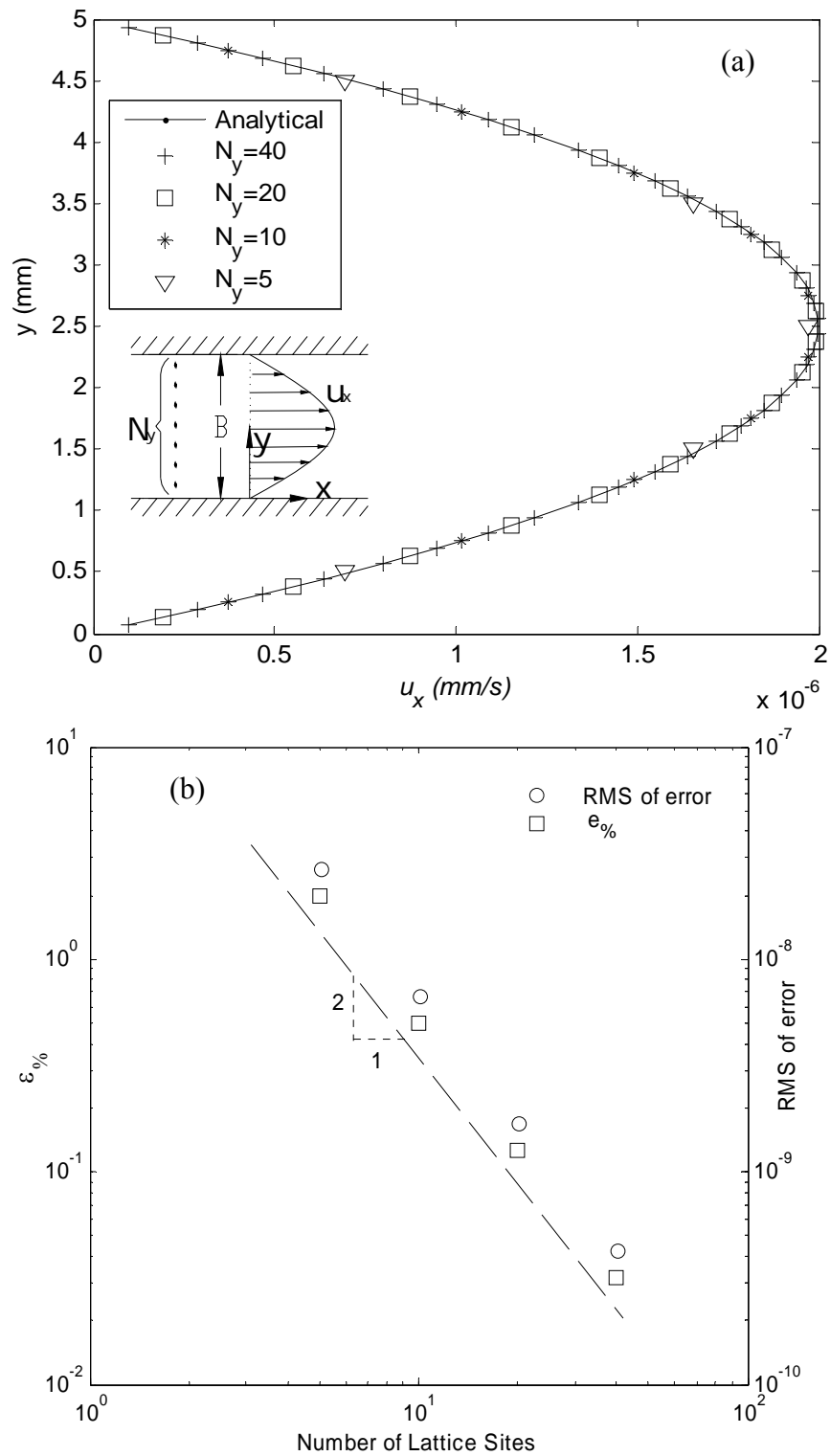


Figure 4.2 (a) Velocity profiles computed by LB simulation using different number of lattice sites, (b) error analysis: Square represents percent error, and circles represent the RMS of error.

$$\varepsilon_{\%} = \left\langle \frac{u_x^A - u_x^{LB}}{u_x^A} \right\rangle \times 100 \quad (4.3)$$

where RMS and $\varepsilon_{\%}$ are the root mean square error and the percent error, respectively, N_y is the number of lattice sites, u_x^A and u_x^{LB} are velocities calculated from analytical equation and LB model, respectively. The bracket $\langle \rangle$ represents the mean value. Figure 4.2b shows the RMS of error (circles, right axis) and percent difference (squares, left axis) between analytical and LB model results in four different resolutions. As seen in Figure 4.2b, the error ranges from 0.03 % (RMS of 0.0042×10^{-7} mm/s) to 2 % (RMS of 0.2668×10^{-7} mm/s). Furthermore, the error decreases four times as the number of lattice sites increased twice, illustrating the second order accuracy of the $LB-D2Q9$ algorithm.

4.2.2 Wannier Flow

Accuracy of the D2Q9 model was also verified by comparing with the analytical solution of Stokes flow around a circular cylinder in the vicinity of a moving plate. An analytical solution for this flow case was derived by Wannier (1950). A cylinder of 20 mm diameter was placed 35 mm from the moving plate as seen Figure 4.3a. Streamlines and velocity vectors were calculated from the analytical equation given by Wannier (1950) for a window of 70 mm by 70 mm around the cylinder. Analytical solution for the streamlines has given in Appendix C. Herein, a streamline is defined as a line that is tangent to the velocity vectors everywhere in space.

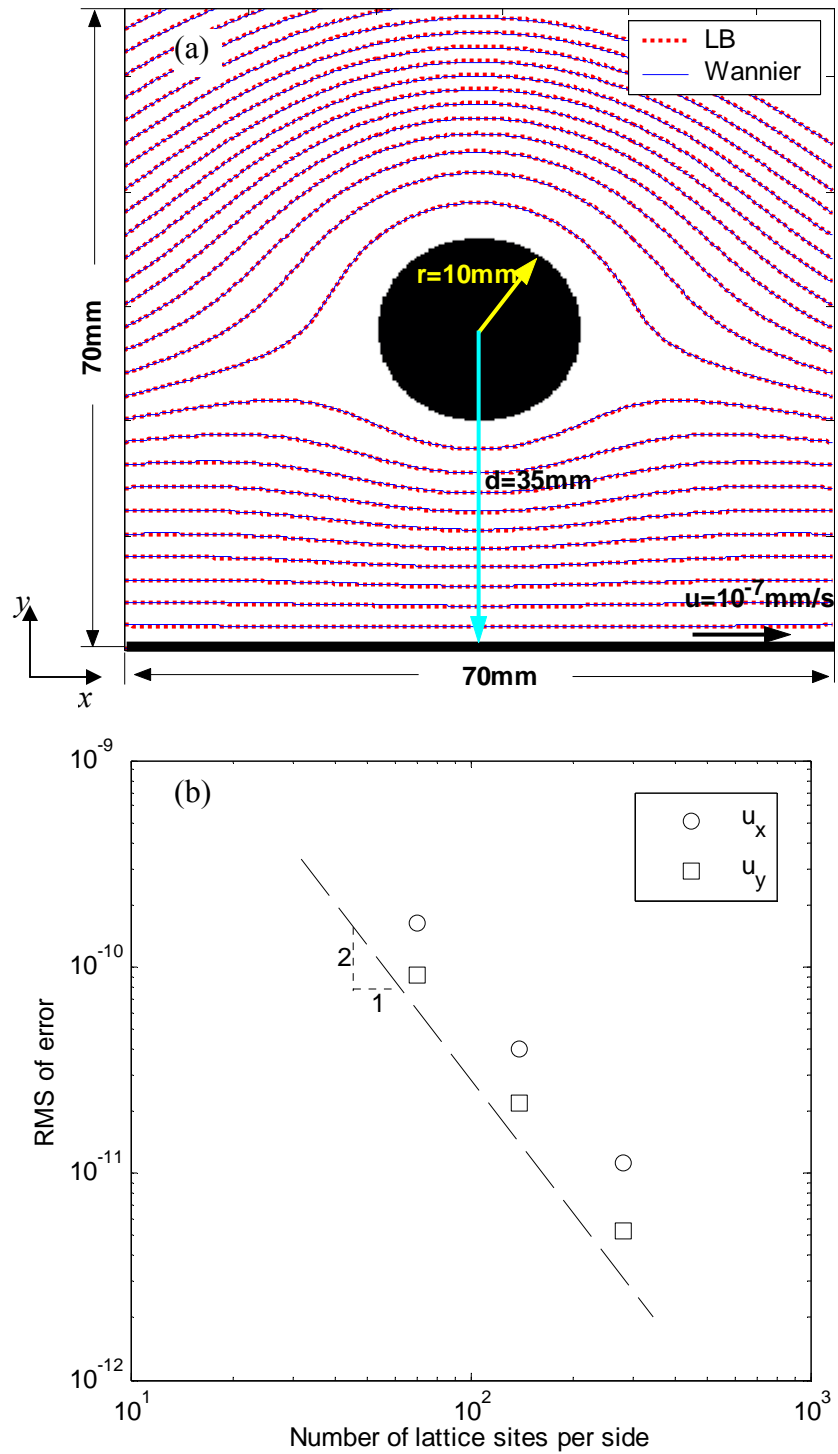


Figure 4.3 (a) Streamlines computed by the LB simulation and analytical solution, (b) error analysis; square points represent RMS of error in vertical velocity, and circles represent the RMS of error in horizontal velocity.

Three separate simulations were carried out with a varying number of lattice nodes: 70x70 ($\Delta x=1$), 140x140 ($\Delta x=0.5$), and 280x280 ($\Delta x=0.25$), to demonstrate the effect of number of lattice points on the accuracy of the LB model. A velocity of $u_x=10^{-7}$ mm/s was prescribed at the bottom boundary. In all other boundaries, analytical solution of the velocity was prescribed. Missing components at the boundaries were calculated using the relations given in Table 3.2.

Figure 4.3a compares the streamlines computed from the LB simulations using 280x280 lattice resolution with the streamlines computed from the Wannier (1950) analytical equation. The figure clearly indicates that an excellent agreement exists between the analytical solution and the LB-based results, which confirms the validity of the D2Q9 model for predicting a well-known flow scheme. To investigate the order of accuracy of the LB model, an error analysis was performed for the three lattice resolutions. The error, measuring the difference between analytical and a LB model solution was computed as follows:

$$RMS \text{ of error in } u_x = \left(\frac{1}{N_x N_y} \sum_{i=1}^{N_x N_y} (u_x^{LB} - u_x^{wannier})^2 \right)^{0.5} \quad (4.4)$$

$$RMS \text{ of error in } u_y = \left(\frac{1}{N_x N_y} \sum_{i=1}^{N_x N_y} (u_y^{LB} - u_y^{wannier})^2 \right)^{0.5} \quad (4.5)$$

where *RMS* is the root mean square error, N_x and N_y are the horizontal and vertical number of lattice sites, respectively, u_x and u_y are the velocities in horizontal and vertical directions, respectively. Figure 4.3b shows the results of error analysis where error

decreases four times as the number of lattice sites increased twice, illustrating the second order accuracy of the present methodology.

4.3 VALIDATION OF THE D3Q19 LB MODEL

4.3.1 Poiseuille Flow

Assuming laminar flow of water, the velocity of flow through a single circular tube can be calculated using Poiseuille's Law. The analytical solution of the velocity distribution in a circular tube with diameter D is given by the following equation:

$$u_z = \frac{\nabla P_z}{\mu} \left(\frac{D^2}{16} - \frac{r^2}{4} \right) \quad (4.6)$$

where u_z is the velocity in the vertical direction (z-direction), ∇P_z is the pressure gradient, μ is the dynamic viscosity, D is the diameter of the tube, and r is the distance from the centerline of the tube in radial direction. Flow through a 10 mm diameter circular tube was simulated using the D3Q19 LB model. A pressure gradient of 10^{-6} g/mm²-sec² was applied to the system to trigger the flow using the technique described in section 3.3.3.1. Velocity values at the inlet and outlet were computed using relations given in Table 3.3. Simulations were carried out at three different resolutions: 10, 20, and 40 lattice points along the diameter (N_D). Figure 4.4a shows the velocity profiles computed using Equation 4.6 and the velocities based on the LB simulations. Figure 4.4a clearly indicates that an excellent agreement exists between the results based on Poiseuille's Law and the D3Q19 model. In addition to the *RMS* of error, a second parameter was introduced for the error analysis:

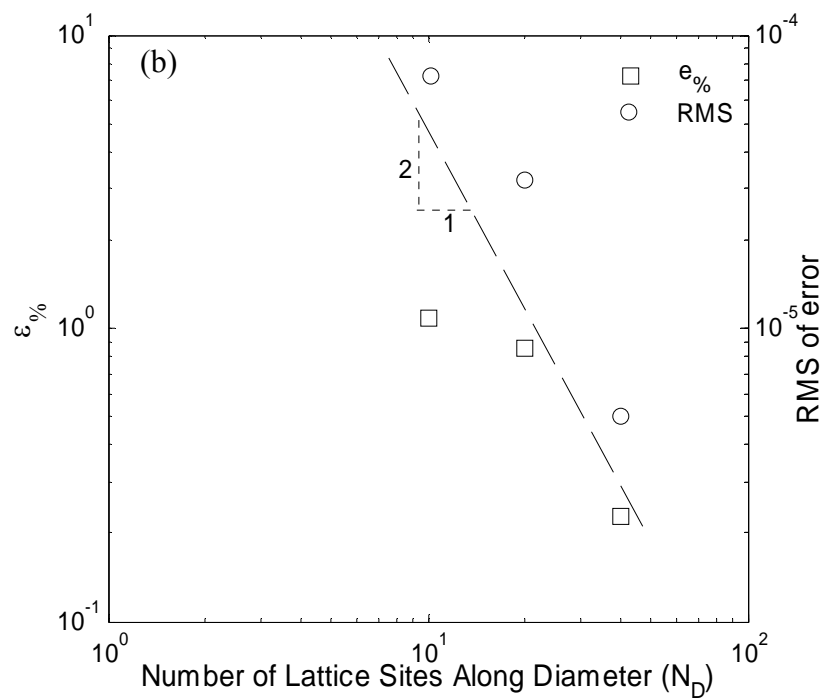
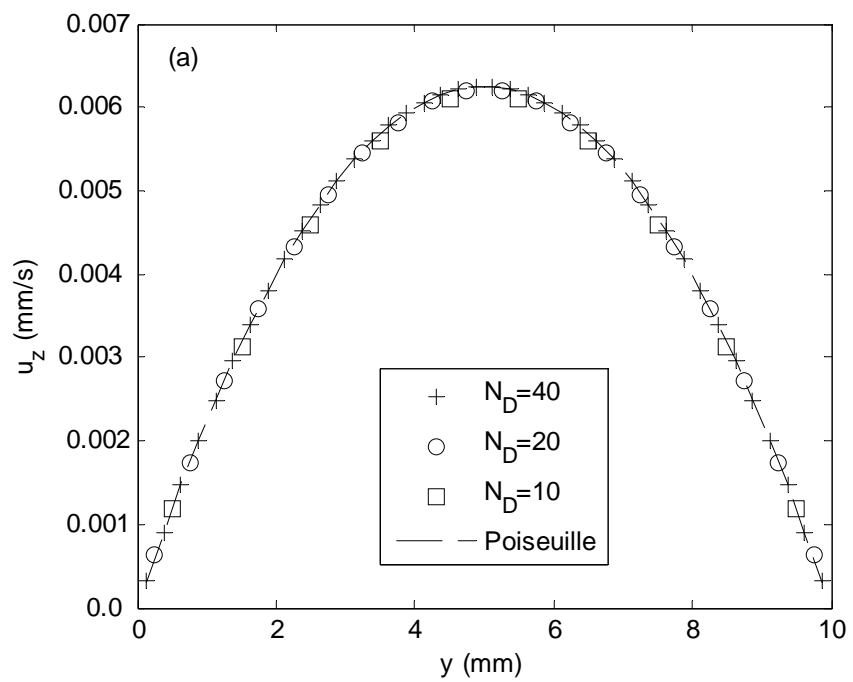


Figure 4.4 Flow in a circular tube: (a) Velocity profiles computed with different resolutions (b) error analysis.

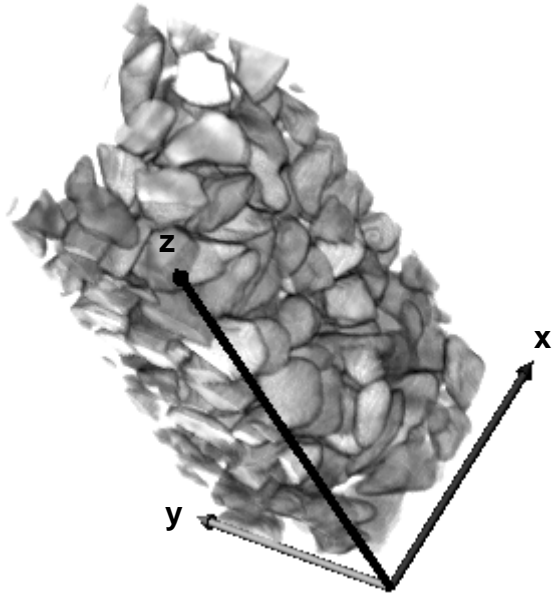
$$\varepsilon_{\%} = \left\langle \frac{u_z^A - u_z^{LB}}{u_z^A} \right\rangle \times 100 \quad (4.7)$$

where $\varepsilon_{\%}$ is the percent error, and u_z^A and u_z^{LB} are the velocities in the z-direction computed from Equation 4.6 and from LB simulations, respectively. As seen in Figure 4.4b, the *RMS* and $\varepsilon_{\%}$ are quite low and range from 5×10^{-6} to 7.5×10^{-5} and 0.2 to 1%, respectively. Both parameters decrease with increasing resolution (number of lattice nodes). These comparisons confirm the validity of the three-dimensional LB technique (D3Q19 model) for predicting tubular flow.

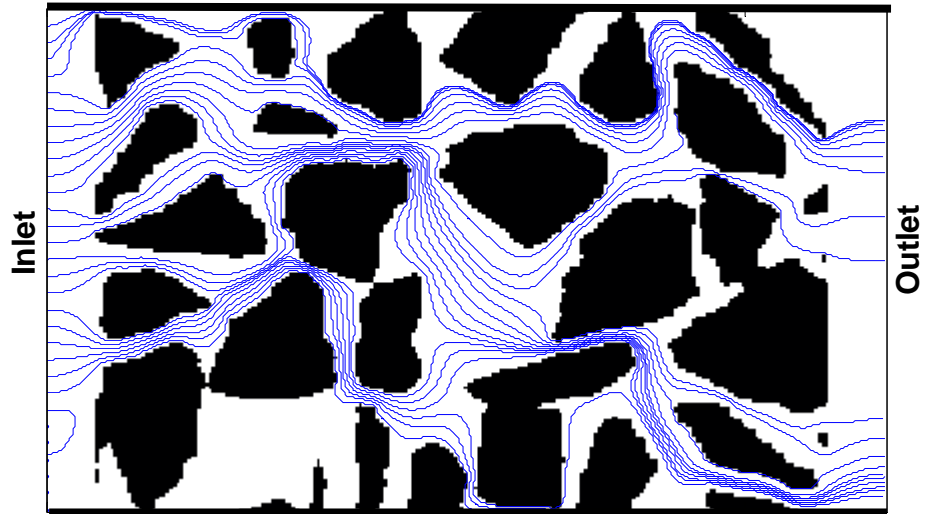
4.4 LABORATORY HYDRAULIC CONDUCTIVITY TESTS

A series of laboratory hydraulic conductivity tests were conducted on compacted geomaterials to further confirm the validity of the D3Q19 lattice Boltzmann model in simulating the three-dimensional flow. Aggregates with average equivalent diameters of 9.5 mm, 4.75 mm and 2.36 mm were selected as the geomaterials and named as AG1, AG2 and AG3, respectively. The aggregates were placed in specially fabricated molds of 100 mm in diameter and 130 mm in height and subjected to hydraulic conductivity tests using the constant head method in accordance with ASTM D 2434.

Before the hydraulic conductivity tests, the three-dimensional images of the aggregates placed in the molds were captured using the X-ray Computed Tomography (CT). The X-ray CT is a powerful non-destructive imaging technique to analyze the interior structure of materials, using their X-ray attenuation characteristics. Chapter 5



(a)



(b)

Figure 4.5 (a) 3D reconstructed X-ray CT image of AG1, (b) streamlines of a vertical section computed by D3Q19 LB model.

provides more detailed description of the X-ray CT technique. Figure 4.5a presents the three-dimensional structure of AG1 generated using X-Ray CT technique. Grayscale images of the aggregates were converted to binary images by morphological thresholding, where black areas (pixel values of 0) represent solid and white areas (pixel values of 1) represent voids. In image processing, selecting the appropriate threshold value to create a binary image in complex geometries is generally cumbersome; however since the X-ray CT technique is based on the density differences within the material, the discrimination of the pores from the solid phase was not difficult (i.e., air has a very low density as opposed to aggregates). After obtaining the binary images, lattice nodes were generated at the centers of each pixel. A pressure gradient in the range of 5.34×10^{-3} to $3.6 \times 10^{-5} \text{ g/mm}^2\text{-sec}^2$ was applied to the system to initiate the flow during the LB simulations. The velocities at the inlet and outlet nodes were calculated using the Equations 10 and 11, respectively.

Streamlines of a random section within AG1 computed by LB method is presented in Figure 4.5b, where the flow path of the fluid particles from inlet to outlet is clearly visible. After the simulations, hydraulic conductivities of the specimens were calculated using Darcy's law:

$$k = \frac{q}{i_h A} \quad (4.8)$$

where k is the hydraulic conductivity, q is the average flow rate computed from LB simulations, i_h is the applied hydraulic gradient ($i_h = \nabla P / \gamma$), and A is the specimen cross sectional area perpendicular to the direction of pressure gradient. The hydraulic conductivities of the aggregates based on LB simulations and laboratory measurements is

plotted in Figure 4.6. A relatively good agreement was observed between the two sets of data. The laboratory-based hydraulic conductivities are 1.4 to 1.9 times lower than those predicted by the lattice Boltzmann technique. The difference can be attributed to the difficulty of achieving a complete saturation due to presence of air bubbles which may have blocked the flow pathways within the pores. Another reason could have been due to the difficulty experienced while maintaining very low hydraulic gradients during the laboratory tests since the aggregates had very high hydraulic conductivity values. This might have affected the assumption that the flow regime was laminar during the LB simulations.

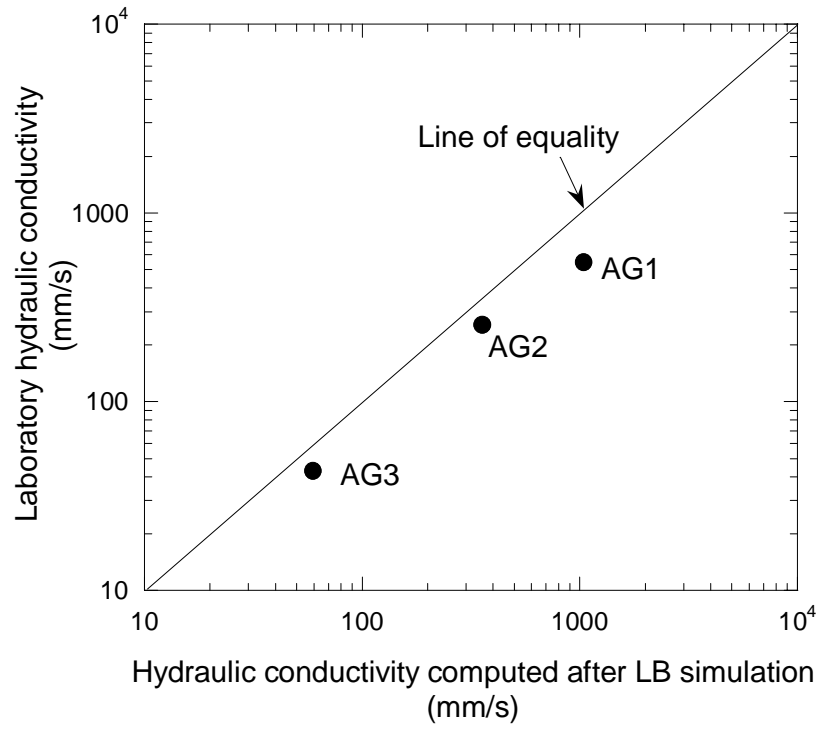
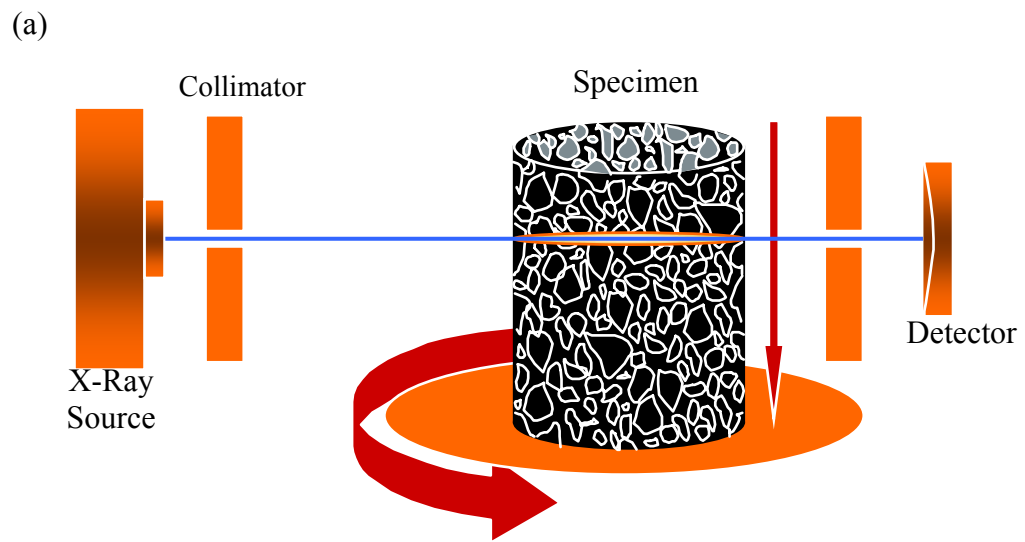


Figure 4.6 The hydraulic conductivities of the aggregates based on LB simulations and laboratory measurements

CHAPTER 5 IMAGE ACQUISITION AND ANALYSIS

5.1 X-RAY COMPUTED TOMOGRAPHY IMAGING

X-ray computed tomography (CT) is a completely nondestructive technique for visualizing features in the interior of opaque solid objects to obtain digital information on their 3-D geometry and properties. It is also known as computerized axial tomography, computed assisted tomography, or CAT scanning. An illustration of a typical X-ray CT system is given in Figure 5.1. The system is composed of an X-ray source, a collimator (window), and a detector. The system specifications of the X-ray CT system used in this study is provided in Table 5.1. In principle, planar X-rays are directed towards the specimen, and the specimen absorbs some portion of the X-rays. Unabsorbed portion is detected by an array of detector cells in the detector. The ratio of unabsorbed X-rays to the X-rays coming from the source gives a CT number (Figure 5.1b). As the specimen is rotated, CT numbers are collected from various different directions. After a full 360-degree rotation, a set of CT numbers collected for all directions generates an image slice. Then, the specimen is shifted vertically by a certain amount and entire process is repeated to obtain additional slices. The amount of vertical shift was determined by the thickness of the detector aperture, t_d ; i.e. the specimen is shifted at an interval of t_d so the image of the entire specimen can be captured. As a result, the total number of image slices for a specimen is the height of the specimen divided by t_d . A three dimensional image of the specimen can be generated by stacking these image slices (Figure 5.2). The dimensions of the images are directly related to the number of detector cells in the detector. For example, a detector with 512 detector cells (also called detector channels)



(b) Top view

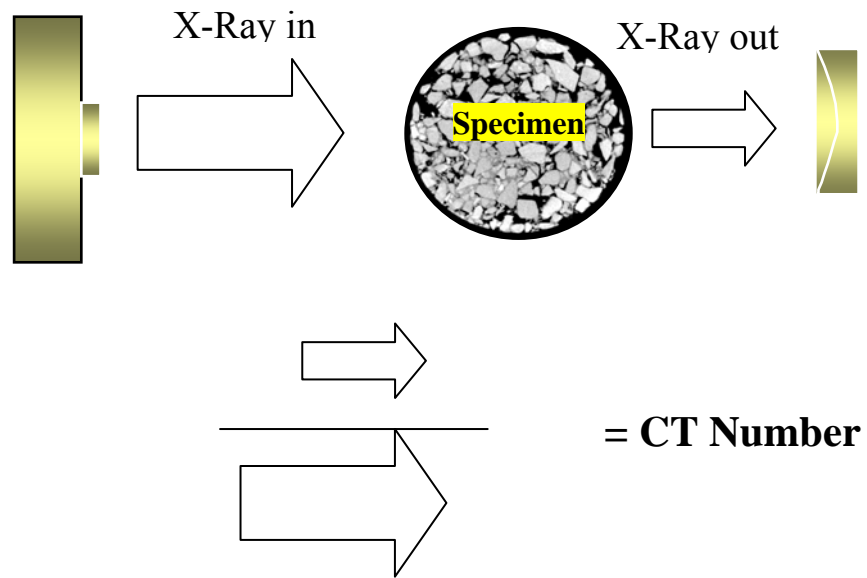
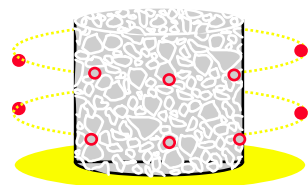


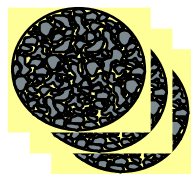
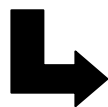
Figure 5.1 Illustration of (a) a typical X-Ray CT system, and (b) acquiring CT number.

Table 5.1 The Specifications of the X-Ray CT System used in this study

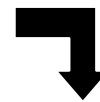
X-RAY SOURCE	420 keV continuous source
X-RAY DETECTOR	512 channels linear array detector
SLICE THICKNESS	0.1 mm – 5mm
IMAGE SIZE	256 x 256, 512 x 512, or 1024 x 1024 pixels
RESOLUTION	50 μm for small specimens 200 μm for large specimens



Tomography



2-D Images



Rendering Algorithms



3-D Image

Figure 5.2 Illustration of generation of 3D structure from X-Ray CT

produces an image slice of 512 by 512 pixels. Larger images can be generated from the X-ray CT equipment; however, those images are generated by interpolation of the original 512 by 512 data and do not represent the exact image resolution.

The spatial calibration, i.e., finding the resolution of the X-ray CT images is relatively straightforward. The number of pixels is counted for a known distance (e.g., the diameter of the specimen in Figure 5.3) and dimensions of each pixel (i.e. the resolution) were determined by ratio of the known distance in units of millimeters to the number of pixels counted from the image.

The pixel intensities of an X-ray CT image are directly related to the X-ray absorption characteristics of the material located at each pixel. This usually depends on the density and/or atomic number of the material. In principle, dense regions in the specimen are represented by bright pixels in the image. The 8-bit grayscale images have a range of pixel intensities from 0 (pure black) to 255 (pure white). A sample image slice of a concrete specimen is shown in Figure 5.3 to present this phenomenon, where high-density aggregates have brighter color than the cement mortar. The air voids in the image are shown in pure black (pixel intensity of 0), since they have much lower densities compared to the solid regions (asphalt mastic).

The magnitude of X-rays sent to the specimen should be carefully selected during scanning. If too much X-rays are sent to a low density material, CT number shown in Figure 5.1b will be very high, i.e., most of the X-rays will pass through the material. This may lead to poor contrast within different regions in a test specimen. Therefore, before scanning the entire specimen, preliminary scans were conducted at different X-ray levels until the best contrast was achieved.

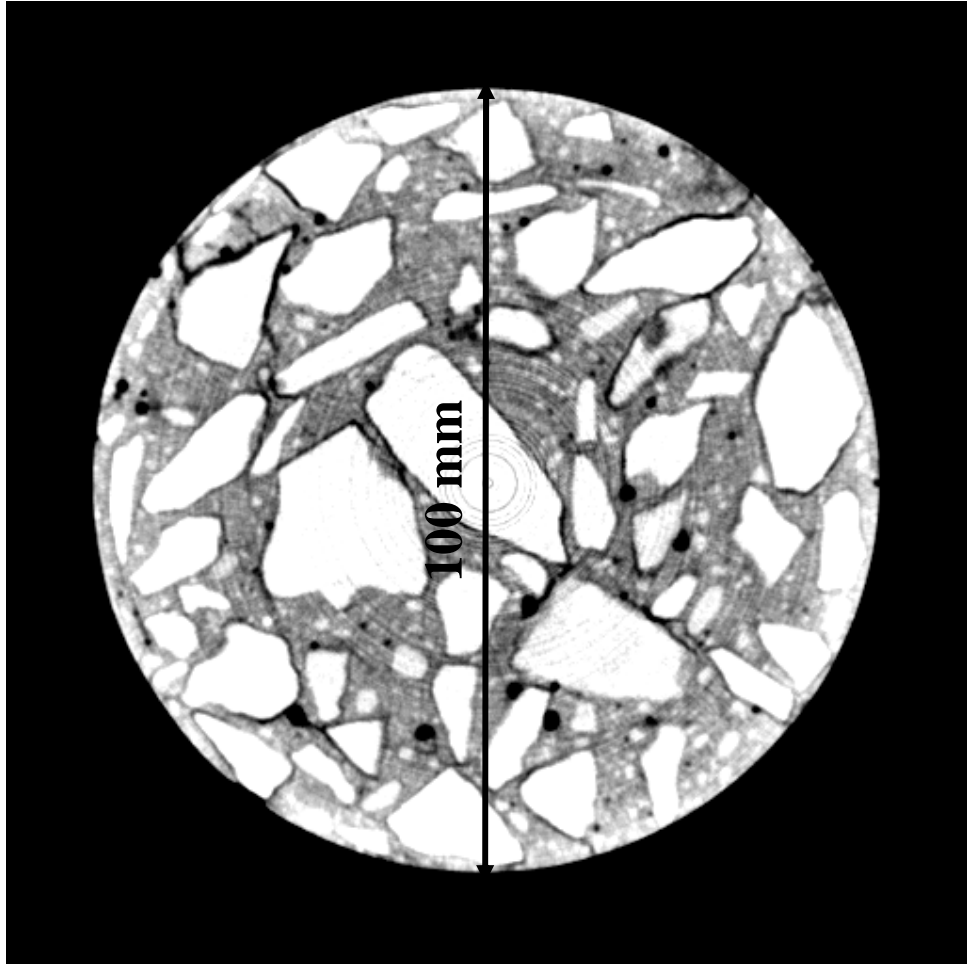


Figure 5.3 Calibration of an X-ray CT image

5.2 IMAGE ANALYSIS ALGORITHMS

The geometrical properties of the specimens (i.e., porosity, pore connectivity, specific surface area and tortuosity) were determined using different image analysis algorithms developed in Matlab. The 3D binary (black and white) images of the specimens that are necessary for those algorithms were processed using morphological thresholding technique. The developed algorithm (*IMAGETHRESHOLD*) is given in Appendix B.

5.2.1 Porosity Algorithm (*POROSITYFIND*)

This algorithm calculates the porosity of each specimen. After obtaining the binary images of the grayscale X-ray CT images, the number of white pixels was counted which gives the pore volume in voxels. Then this number was converted to the world units as follows;

$$V_p = \hat{V}_p \Delta x \Delta y \Delta z \quad (5.1)$$

where V_p and \hat{V}_p are pore volume in world units (mm^3) and lattice units (voxels), respectively, and Δx , Δy and Δz are the resolutions (in mm/pixel) in x, y and z directions respectively. It should be noted that Δx and Δy usually have the same value since the X-ray CT images have the same number of pixels in both directions (usually 512 by 512). Then the porosity was calculated by dividing V_p by the total volume of the specimen.

5.2.2 Pore Connectivity Algorithm (*PORECON*)

The algorithm *PORECON* groups the interconnected pores. Algorithm first labels the interconnected white pixels by using a build-in connected components function which is embedded in Image Processing Toolbox of Matlab. Connected components function basically groups the connected pixels based on a neighborhood criteria. Neighborhood criteria can be 4 or 8 in 2D and can be 6, 18 or 26 in 3D. For example, a neighborhood criterion of 4 (also called four-connected neighborhood) suggests that only four neighboring pixels which are above, below, right and left of a pixel should be considered connected. An example of grouping pixels using a four-connected neighborhood criterion is illustrated in Figure 5.4. In the 3D asphalt images captured in this study, 18 connected neighborhood criterion was used during labeling. After the labeling was complete, the labeled groups that are not connected to both ends of specimen (top and bottom) were eliminated. This produced a pore channel that has a connection to both ends of the specimen.

5.2.3 Specific Surface Area Algorithm (*SSA*)

Specific surface area is another pore geometry characteristic which is defined as the ratio of the surface area of the pores to the total volume of the specimen (Walsh and Brace, 1984) and defined as follows:

$$S_a = \frac{A_s}{V} \quad (5.2)$$

where S_a is the specific surface area, A_s is the total surface area of the pores and V is the total volume of the specimen. The surface area of the pores of a specimen was calculated

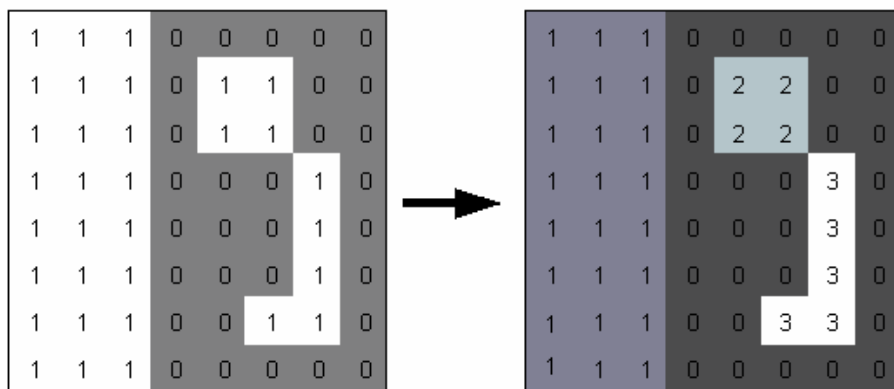


Figure 5.4 Labeling of white pixels based on the four-connected neighborhood criterion

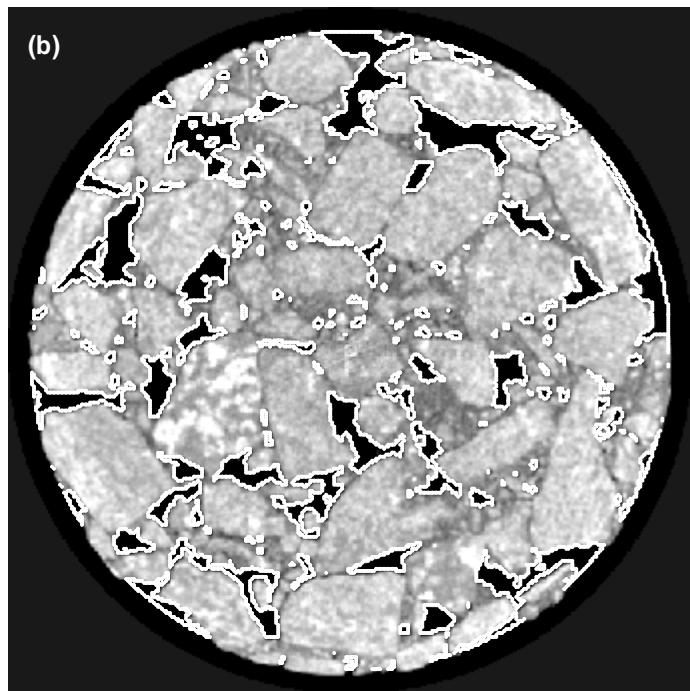
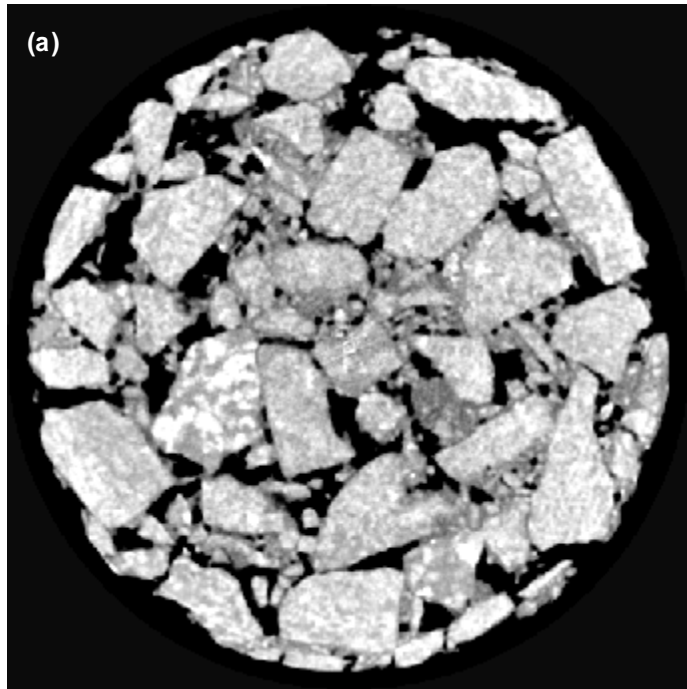


Figure 5.5 (a) Original image of specimen 25C75 and (b) same image with perimeters of pores are shown

by first calculating the perimeter of pores in each image slice. A build-in function of Matlab, “bwperim”, was utilized to obtain the perimeter. An illustration of perimeter pixels is given in Figure 5.5. After calculating the total perimeter of the pores in each slice (\hat{P}_i) in terms of pixels, surface area (A_i) was determined as follows:

$$A_i = (\hat{P}_i \Delta x) (\Delta z) \quad (5.3)$$

where Δx and Δz are horizontal and vertical resolutions, respectively. Cumulative summation of A_i over all slices of the specimen yielded the total surface area of the pores:

$$A_s = \sum_{i=1}^N A_i \quad (5.4)$$

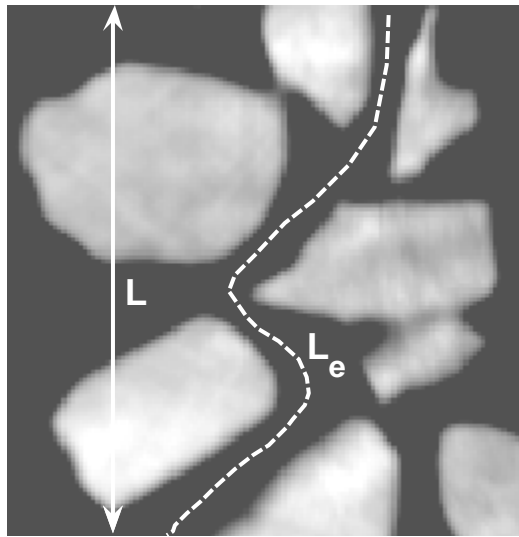
where A_s and N are the total surface area of the pores and the number of image slices, respectively.

5.2.4 Tortuosity Algorithm (*TORT3D*)

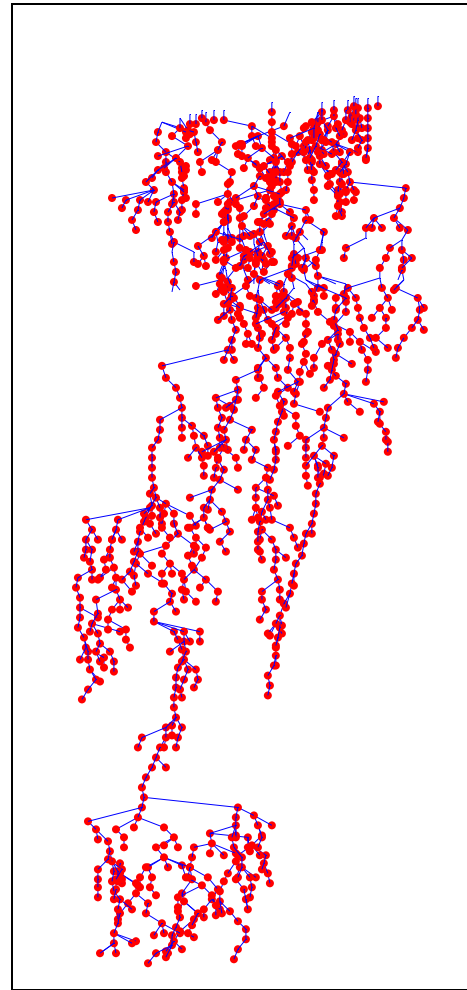
Tortuosity is defined as the ratio of the longest path traveled by the fluid particles (L_e) to the shortest distance between two ends of a specimen (L), i.e.

$$T = \frac{L_e}{L} \quad (5.5)$$

where T is the tortuosity and L_e and L are shown in Figure 5.6a. Although Figure 5.6a illustrates the tortuosity in a very simplistic manner, it is usually very difficult to



(a)



(b)

Figure 5.6 (a) Illustration of the longest flow path and shortest distance for tortuosity calculation, (b) various flow paths estimated by the *TORT3D* algorithm in the pore structure of an asphalt specimen.

calculate the tortuosity of pore geometry without conducting a tracer test (Walsh and Brace, 1984). In a 3D pore space, there are various possible paths that fluid can travel. These paths were estimated as follows: After obtaining the interconnected pore structure using *PORECON*, isolated pore cross sections were grouped in each image slice and centroid of each group was connected to the centroid of the closest pore cross sectional area in the next image slice. For each line connecting two pore cross sections, a tortuosity was calculated by dividing the length of the connecting line to the vertical distance between two slices. Lines illustrating the various possible flow paths estimated by the *TORT3D* algorithm in the pore structure of an asphalt specimen are provided in Figure 5.6b. After obtaining a set of tortuosity values for each consecutive image slice, an average tortuosity was calculated for the whole specimen.

CHAPTER 6 PORE STRUCTURE CHARACTERIZATION AND LABORATORY HYDRAULIC CONDUCTIVITY OF ASPHALT PAVEMENTS

6.1 MATERIAL PROPERTIES

6.1.1 Laboratory Compacted Specimens

A set of laboratory specimens of different asphalt mix designs was prepared to investigate the moisture transport characteristics of different asphalt pavements. Specimens were fabricated to study a number of mixture variables that are likely to affect the pore structure. The selected variables included NMAS (Nominal Maximum Aggregate Size), compaction energy (number of gyrations in the gyratory compactor) and gradation shape. Of the 36 specimens prepared for this study, 24 were Superpave mixtures and 12 were SMA (Stone Matrix Asphalt) mixtures. For the Superpave mixtures, two different gradations from NMASs of 9.5 mm, 12.5 mm, 19 mm and 25 mm were selected. SMA gradations were selected from three different NMASs: 9.5 mm, 12.5 mm and 19 mm. Figures 6.1 and 6.2 shows the aggregate gradations used in this study. Mix designs of Superpave mixtures were performed according to the AASHTO PP28-03 “Standard Practice for Superpave Volumetric design for Hot-Mix Asphalt (HMA)”. Gyration level for mix design was selected as 100, as it covers a wide range of traffic categories in the AASHTO PP28-03. Table 6.1 and 6.2 shows mix design properties of the Superpave and SMA mixtures, respectively.

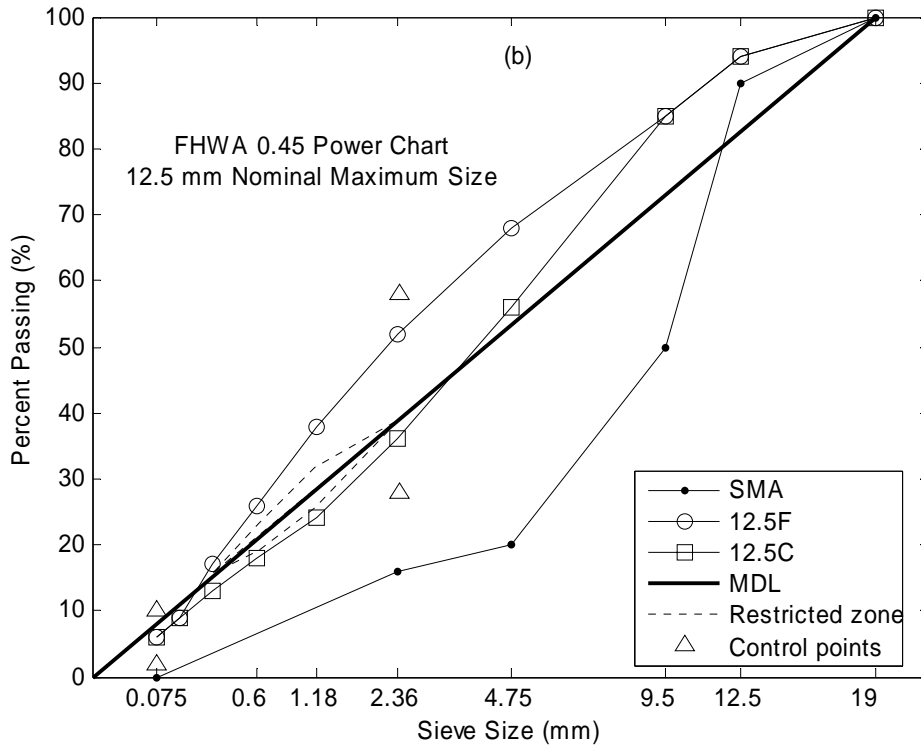
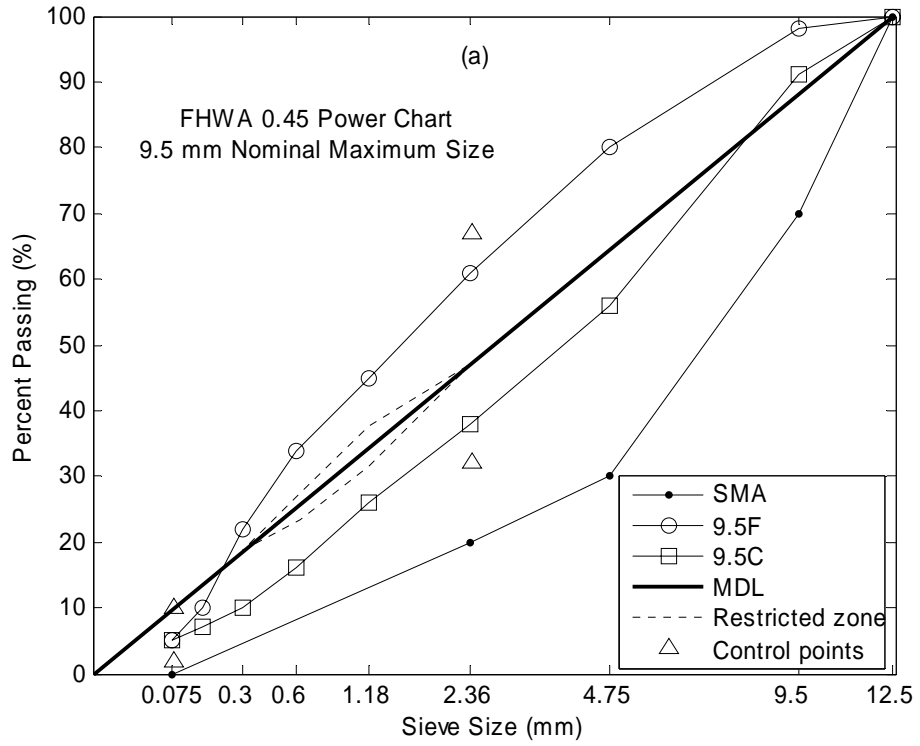


Figure 6.1 Gradations of (a) NMA 9.5 mm and (b) NMA 12.5. MDL= Maximum Density Line

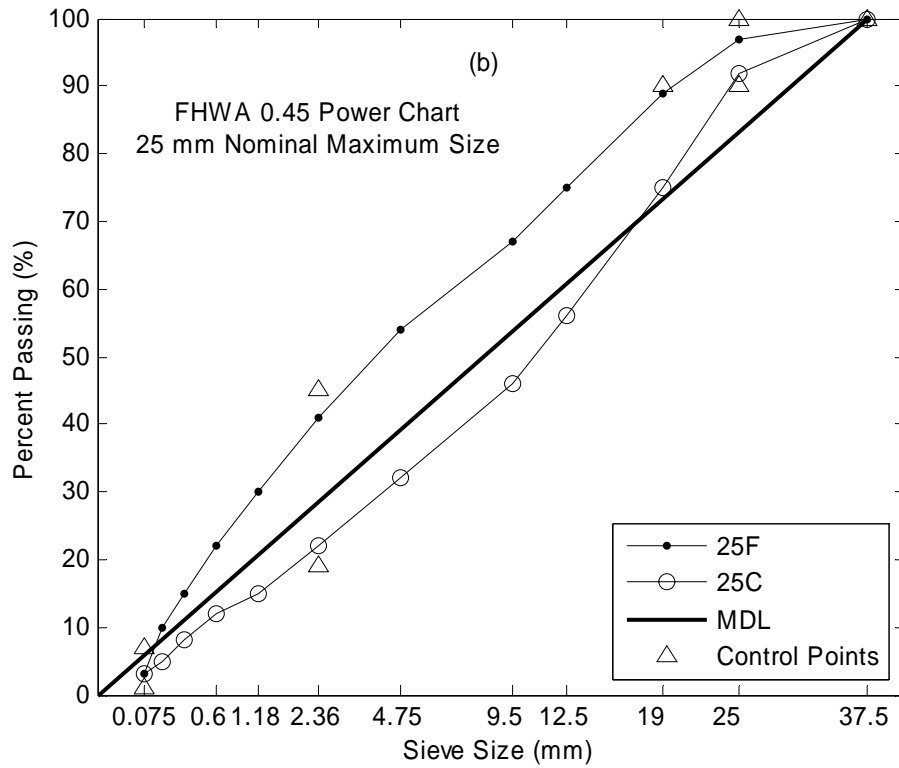
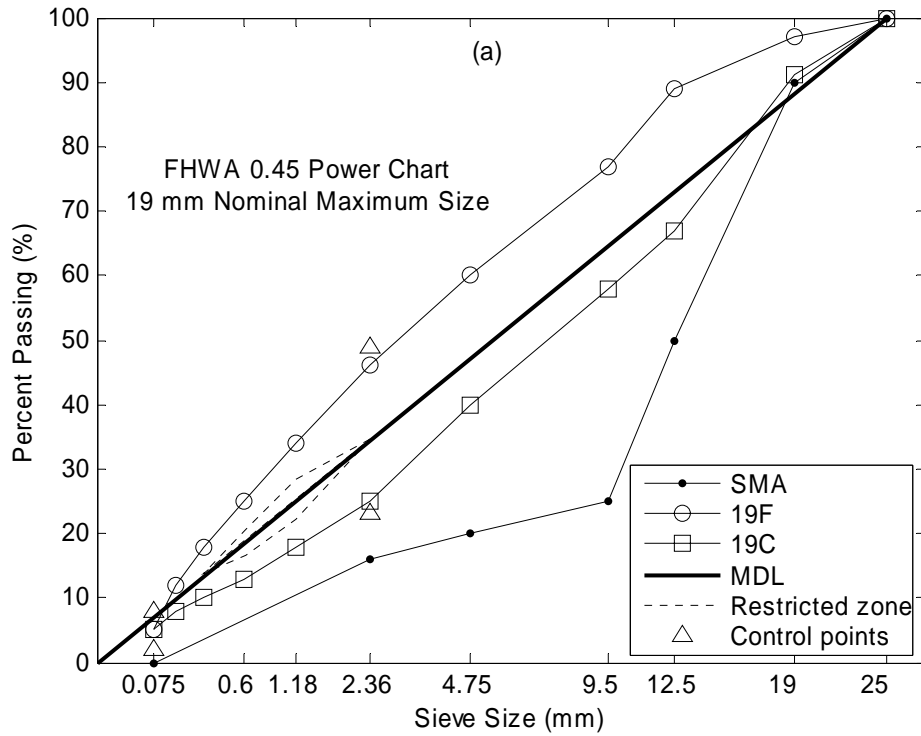


Figure 6.2 Gradations of (a) NMAS 19 mm and (b) NMAS 25. MDL= Maximum Density Line

Table 6.1 Properties of the dense asphalt specimens

Specimen No	Specimen ID	NIMAS (mm)	Number of Gyration	Gradation	Opt. Binder Content (%)	Max Specific Gravity of Mix	Bulk Specific Gravity of Mix	Porosity
						(G _{max}) (g/cm ³)	(G _{mm}) (g/cm ³)	(CoreLok) (%)
1	9.5F25	9.5	25	Fine	4.85	2.72	2.47	9.19%
2	9.5C25			Coarse	4.76	2.72	2.42	10.88%
3	9.5F50		50	Fine	4.85	2.72	2.50	8.28%
4	9.5C50			Coarse	4.76	2.72	2.53	7.05%
5	9.5F75		75	Fine	4.85	2.72	2.57	5.71%
6	9.5C75			Coarse	4.76	2.72	2.58	5.32%
7	12.5F25	12.5	25	Fine	4.75	2.73	2.58	5.41%
8	12.5C25			Coarse	5.32	2.71	2.55	5.75%
9	12.5F50		50	Fine	4.75	2.73	2.61	4.2%
10	12.5C50			Coarse	5.32	2.71	2.57	5.12%
11	12.5F75		75	Fine	4.75	2.73	2.64	2.77%
12	12.5C75			Coarse	5.32	2.71	2.61	3.61%
13	19F25	19	25	Fine	4.51	2.74	2.52	8.11%
14	19C25			Coarse	4.85	2.74	2.43	11.35%
15	19F50		50	Fine	4.51	2.74	2.55	6.79%
16	19C50			Coarse	4.85	2.74	2.51	8.34%
17	19F75		75	Fine	4.51	2.74	2.69	1.7%
18	19C75			Coarse	4.85	2.74	2.60	5.0%
19	25F25	25	25	Fine	4	2.76	2.50	9.45%
20	25C25			Coarse	4.63	2.75	2.43	11.89%
21	25F50		50	Fine	4	2.76	2.57	6.81%
22	25C50			Coarse	4.63	2.75	2.50	9.35%
23	25F75		75	Fine	4	2.76	2.60	5.74%
24	25C75			Coarse	4.63	2.75	2.48	9.91%

Note: NIMAS=Nominal Maximum Aggregate Size.

Table 6.2 Properties of the SMA specimens

Sample No	Sample ID	NMAS (mm)	Number of Gyration	Binder Content (%)	Porosity (%)
1	9.5SMA-A1	9.5	50	5.5	14.7
2	9.5SMA-A2			5.5	16.3
3	9.5SMA-B1		25	5.5	21.6
4	9.5SMA-B2			5.5	16.8
5	12.5SMA-A1	12.5	75	5.5	16.2
6	12.5SMA-A2			5.5	22.4
7	12.5SMA-B1		50	5.5	12.5
8	12.5SMA-B2			5.5	18.5
9	19SMA-A1	19	25	5.5	14.7
10	19SMA-A2			5.5	16.6
11	19SMA-B1		75	5.5	14.0
12	19SMA-B2			5.5	18.1

Note: NMAS=Nominal Maximum Aggregate Size.

6.1.2 Field Cores

Field cores were obtained from the current testing sections of the Accelerated Loading Facility (ALF) at the Turner Fairbank Highway Research Center (TFHRC) of Federal Highway Administration (FHWA). There are currently 12 test sections at the ALF site and 150 mm diameter specimens were collected from the sections 1 to 7. Mix design of each lane is provided in Table 6.3 and aggregate gradations used in the lanes are given in Figure 6.3.

6.2 ANALYSIS OF PORE STRUCTURE OF ASPHALT SPECIMENS

6.2.1 Porosity Variations within Each Specimen

Inhomogeneities in the geometry of an asphalt specimen not only affect its hydraulic conductivity, but affect its long term field performance as well. Segregation of both aggregates and air voids might lead to poor performance. In this study, the air void segregation was analyzed since the segregation of aggregates in asphalt pavements was beyond the scope of this project. In order to investigate the air void segregation during laboratory compaction by gyratory compactor and during field compaction by roller compactor, air void distribution of the specimens were analyzed using their X-Ray CT images. The percentage of air voids in the specimens is equal to using porosity (n), which is defined as:

Table 6.3 Mix design properties of ALF lanes

Lane(s)	Binder Designation	Binder PG	Gradation ⁽¹⁾	Binder Content (%)	Design Air Voids (%)
1	AZ-CR	60-28	B	7.1	5.5
2	PG 70-22	73-23	A	5.3	5
3	Air Blown	75-28	A	5.3	4.1
4	SBS LG	71-29	A	5.3	4.2
5	TX-TBCR	77-28	A	5.3	4.6
6	Terpolymer	76-30	A	5.3	4.9
7	Polyester Fiber	73-23	A	5.3	4.8

Note : ⁽¹⁾ Gradations A and B are provided in Figure 6.3. PG=performance grade.

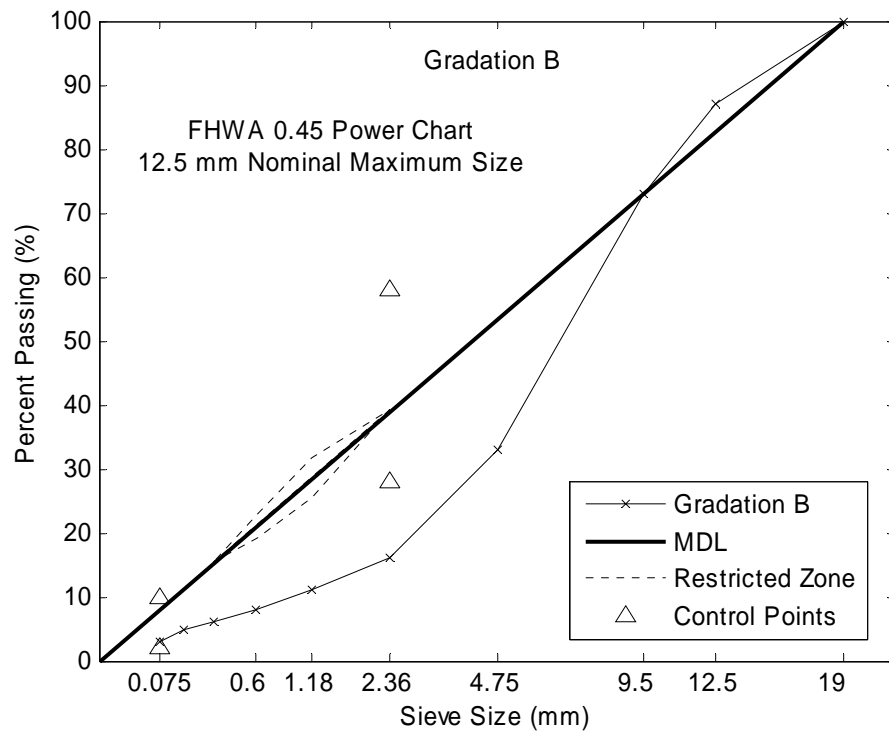
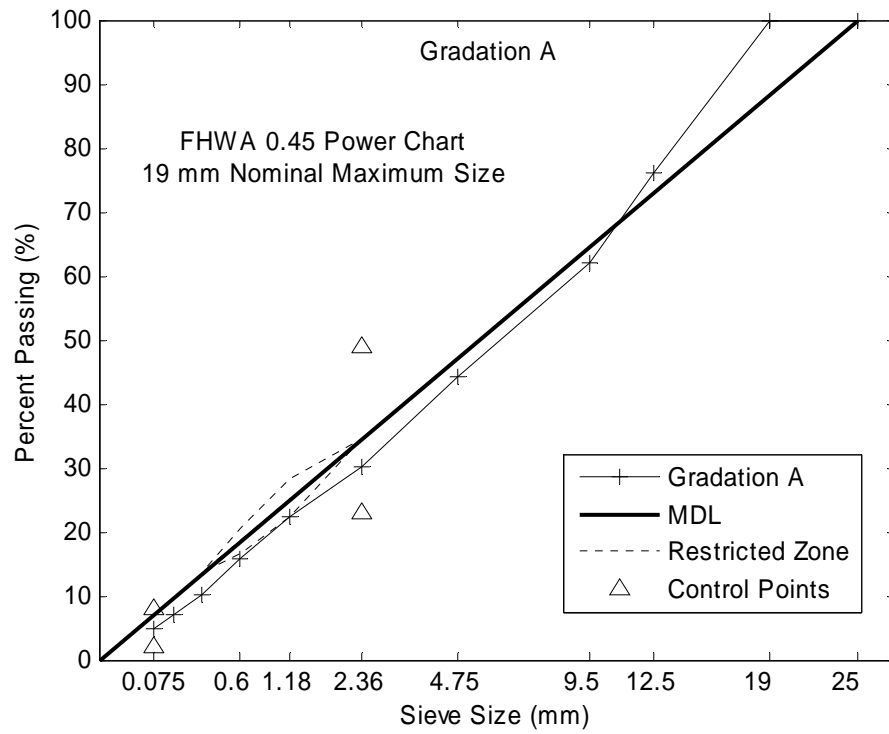


Figure 6.3 Two gradations used in the current testing sections in the Accelerated Loading Facility (ALF) of FHWA

$$n = \frac{V_p}{V} \quad (6.1)$$

where V_p and V are the volume of the air voids (pores) and total volume of the specimen, respectively.

First, change in porosity with depth was analyzed. As mentioned in Chapter-5, X-ray CT provides (cross sectional) slice images of the specimens. Figure 6.4 illustrates a sample image stack constructed by stacking slice images of the same specimen. Each slice has a thickness of 1 mm which is the aperture of the linear detector of the X-Ray CT equipment. Before computing porosity, grayscale images were converted to binary (black and white) images by morphological thresholding, where black areas (pixel values of 0) represent solid and white areas (pixel values of 1) represent air voids. Porosity of each slice was computed using a simple image analysis algorithm written in Matlab (*POROSITYFIND* in Appendix B) which computes the fraction of the white pixels in the binary image. Figures 6.5 through 6.7 present the porosity versus depth relationship of the all specimens. It can clearly be observed from the figures that the porosity values are higher at the two ends of the specimen. This indicates that the air voids are segregated at the two ends, which is consistent with the findings of previous studies (Masad et al. 2000). The porosities at the surface and the bottom of the specimens ranged from 20 to 30 %, whereas this value ranged from 1 to 10% in the mid-depths for the coarse gyratory specimens (Figure 6.5). In fine graded specimens, the porosities in the mid-zone were

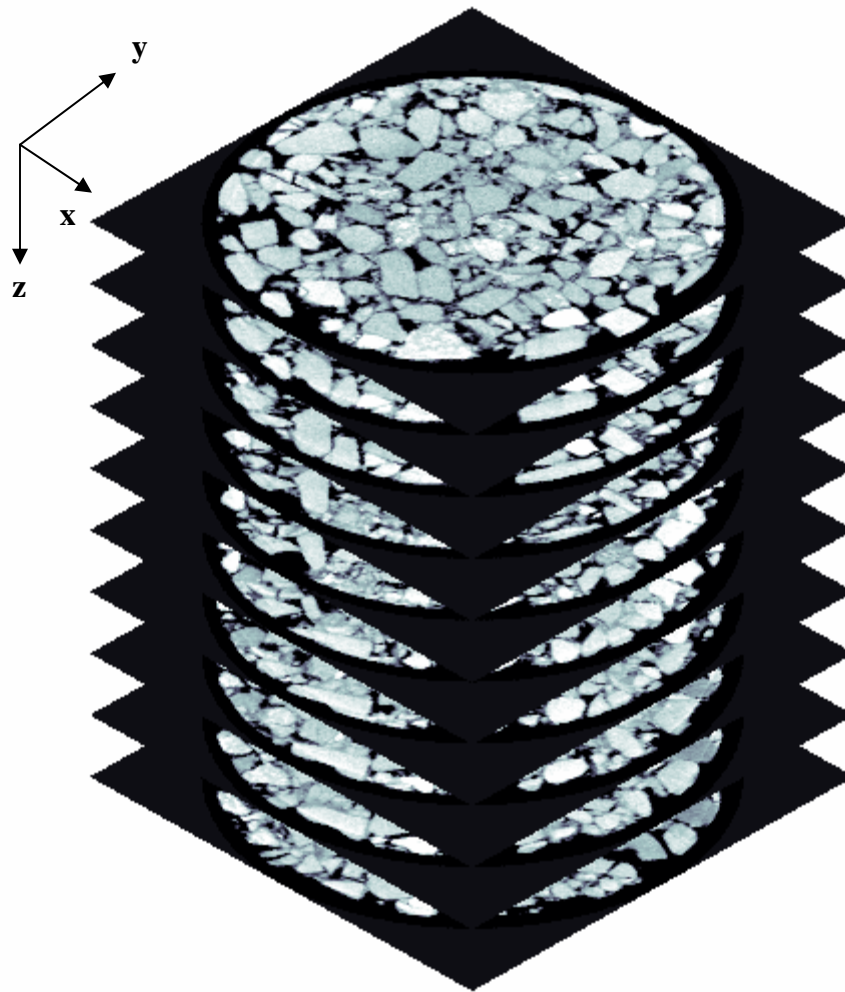


Figure 6.4 Image stacks of 25C75 obtained from X-Ray CT.

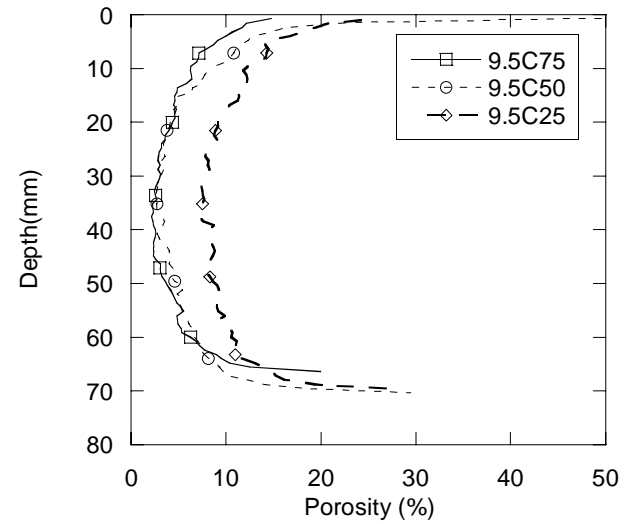
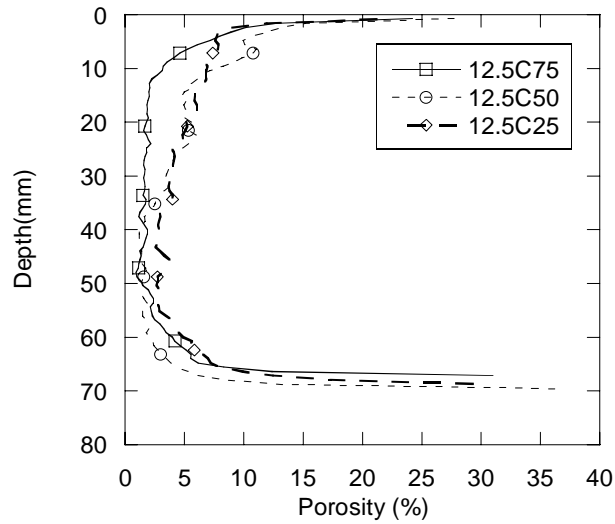
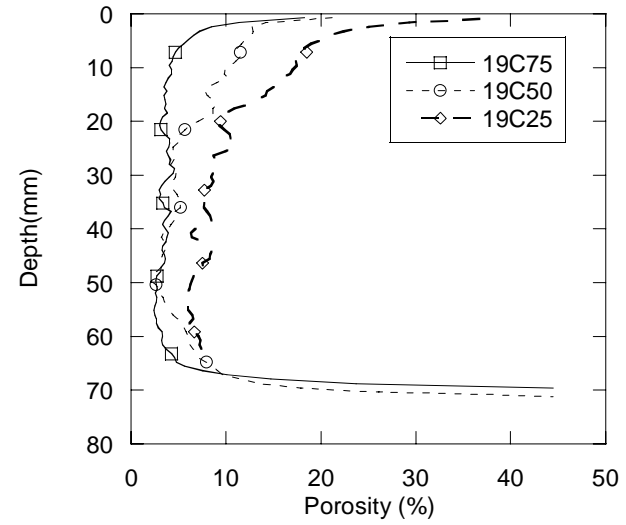
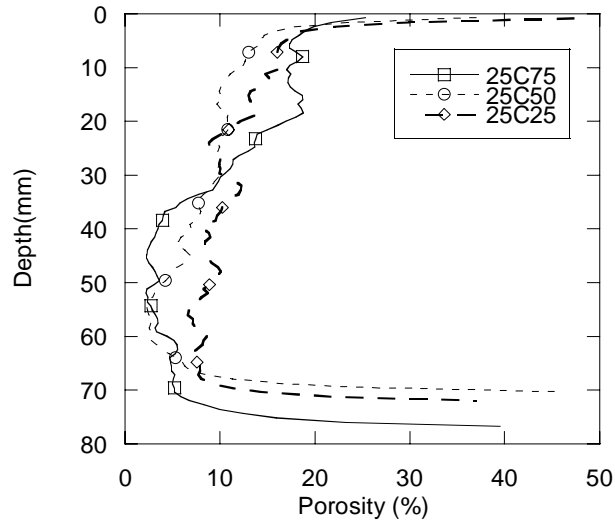


Figure 6.5 Porosity versus depth relationships of coarse Superpave mixtures

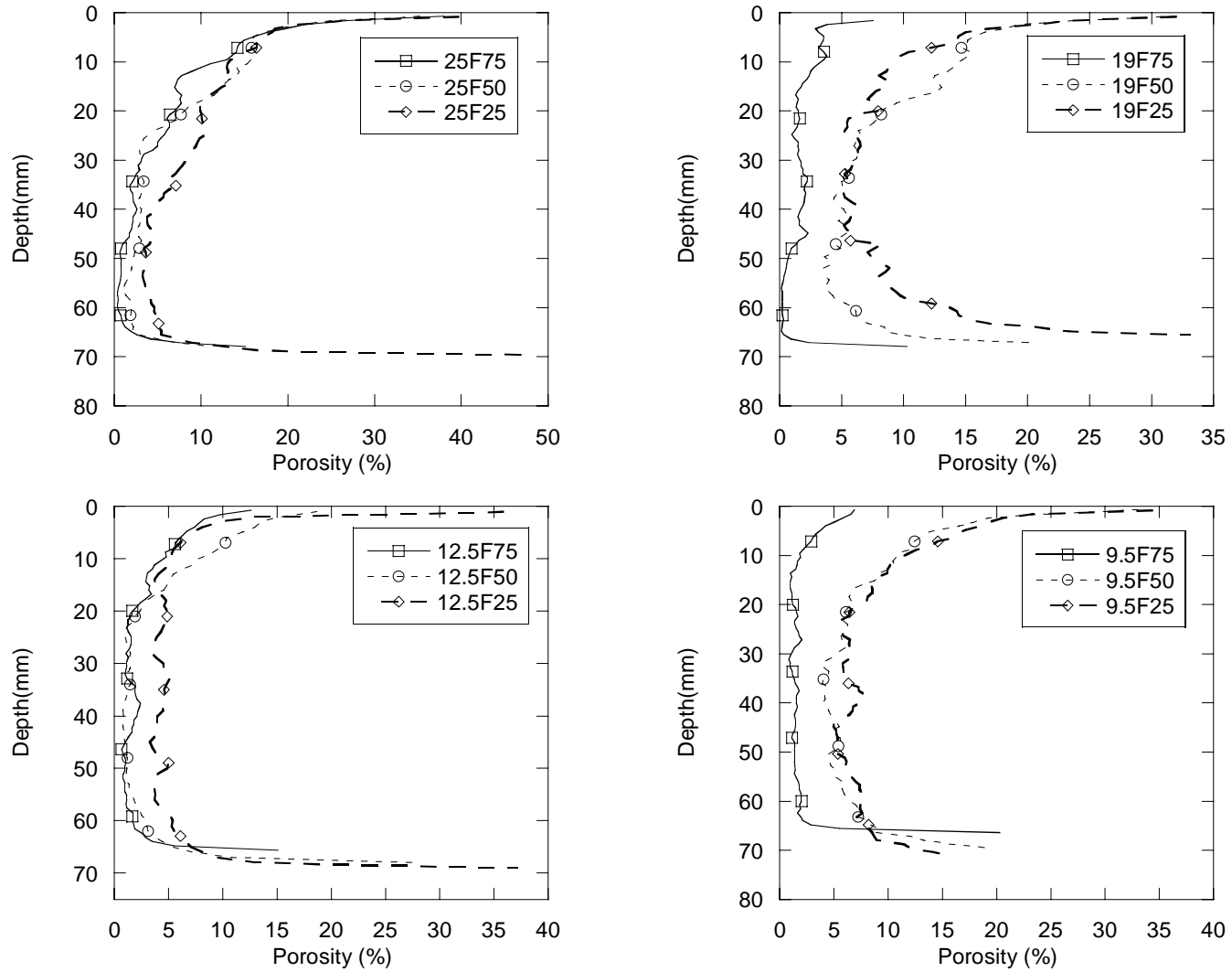


Figure 6.6 Porosity versus depth relationships of fine Superpave mixtures

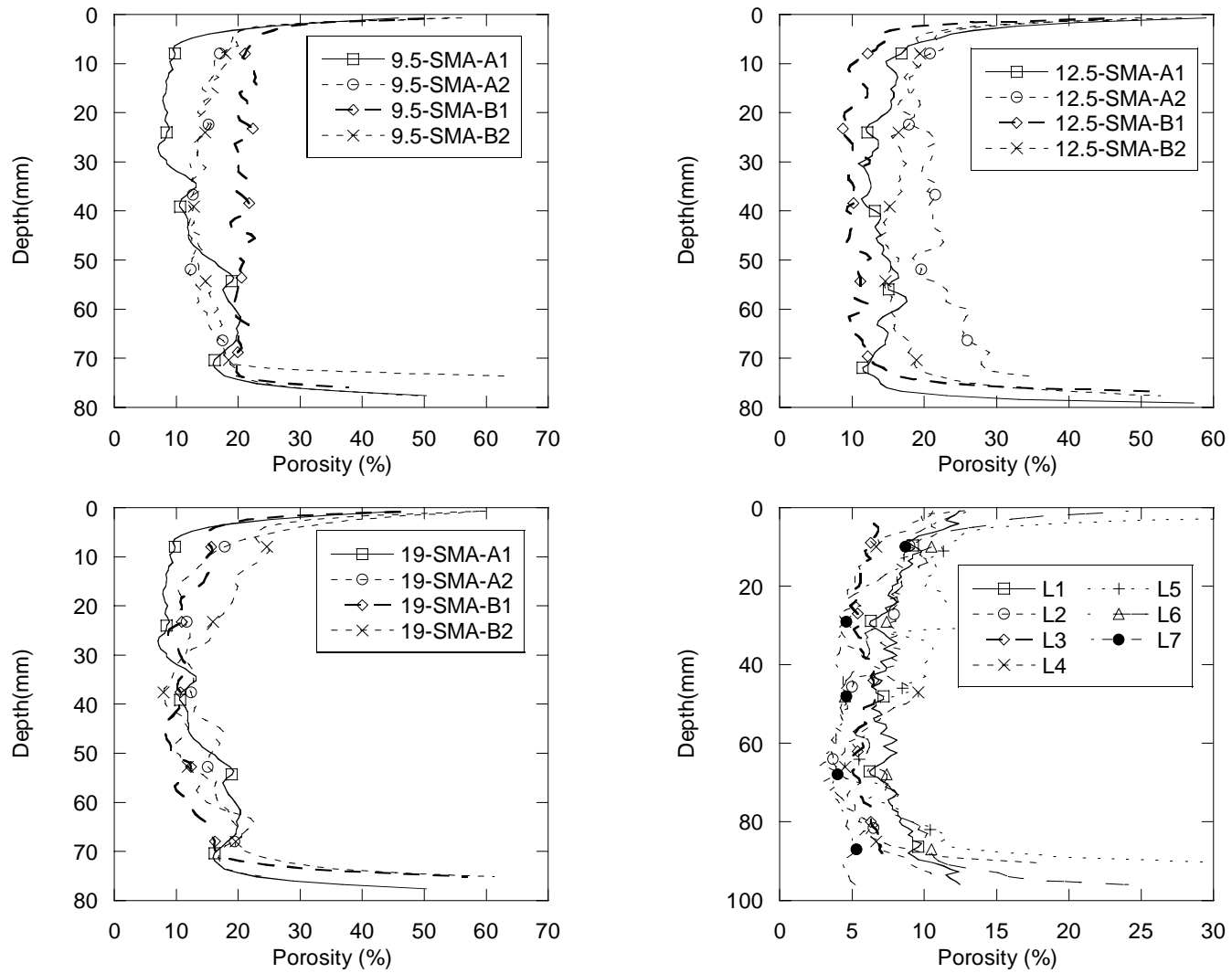
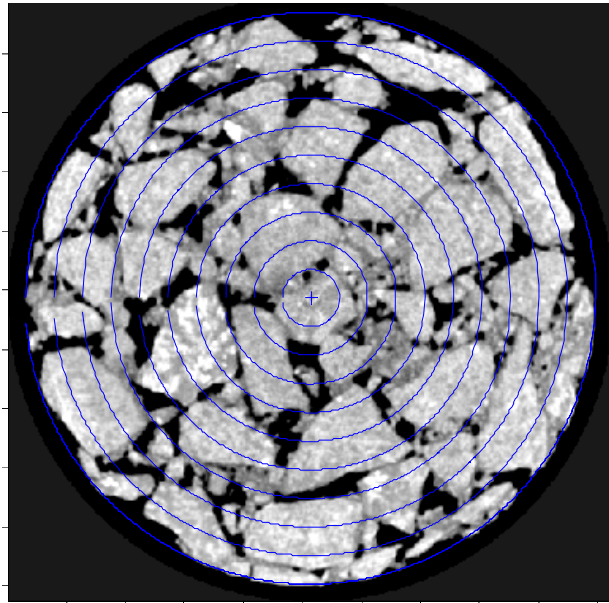


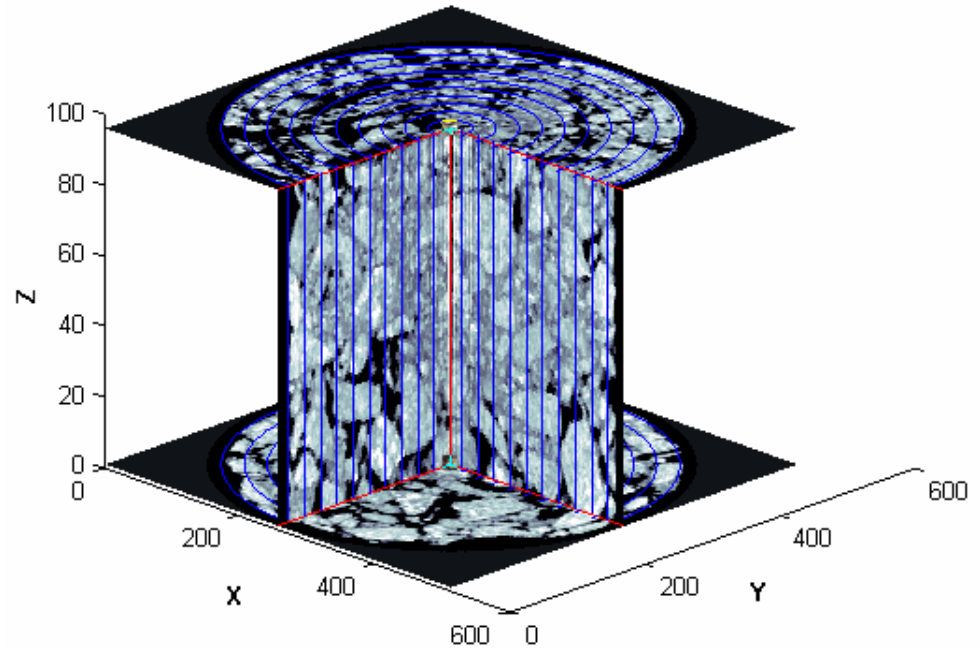
Figure 6.7 Porosity versus depth relationships of SMA specimens and field core

smaller where it ranged from 0.5 to 7% (Figure 6.6), whereas the surface and bottom porosities were similar in magnitude to the coarse graded specimens. The porosities of the SMA specimens were much higher than the fine and coarse graded gyratory specimens (Figure 6.7). Minimum porosities in the mid-zone ranged from 8 to 20%, and the porosities at the surface and bottom of the specimens ranged from 40 to 60%. The porosity variation in field cores was similar to the porosity variation of coarse graded gyratory specimens. The mid-zone porosities were ranged between 4 and 8%, and surface and bottom porosities ranged from 12 to 25%. The Figures 6.5 and 6.6 also indicates the effect of compaction energy on the porosity distribution of the specimens. The specimens compacted at larger number of gyrations (higher compaction effort) generally exhibited smaller porosities along the depth than the ones compacted at lower number of gyrations. This phenomenon is visible in depths between 10 and 60 mm.

In order to investigate the porosity variation in horizontal direction, porosities in radial variation were determined. The image stack of each specimen was divided into concentric cylinders with varying diameters, as illustrated in Figure 6.8. The diameters of the cylinders were 150, 135, 120, 105, 90, 75, 60, 45 and 30 mm. The total porosity of each cylindrical section was calculated using an image processing algorithm developed in Matlab (*RADIALPORE* in Appendix B). The algorithm starts with the largest diameter (150 mm) which covers the whole specimen and calculates its porosity. Then, the algorithm goes to the next smaller diameter and clears all the pores outside the cylinder of that given diameter and calculates the porosity of the inner part of cylindrical boundary. This procedure is repeated for ten different selected diameters. Porosities calculated for each diameter were plotted in Figures 6.9 through 6.11 for all laboratory



(a)



(b)

Figure 6.8 (a) Plan view and (b) perspective view of 25C75 that shows the cylindrical sections for radial porosity analysis

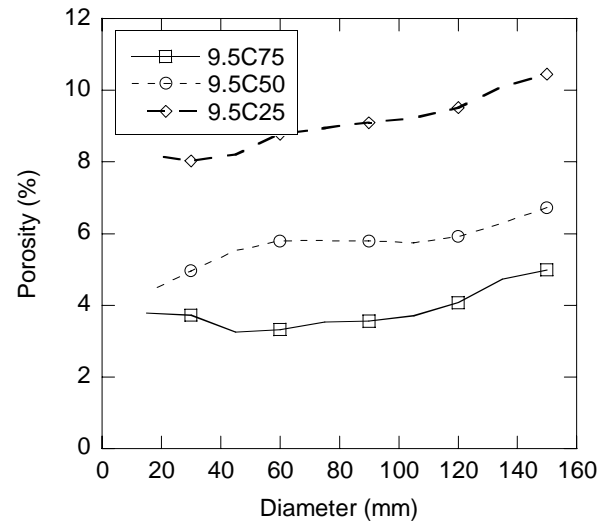
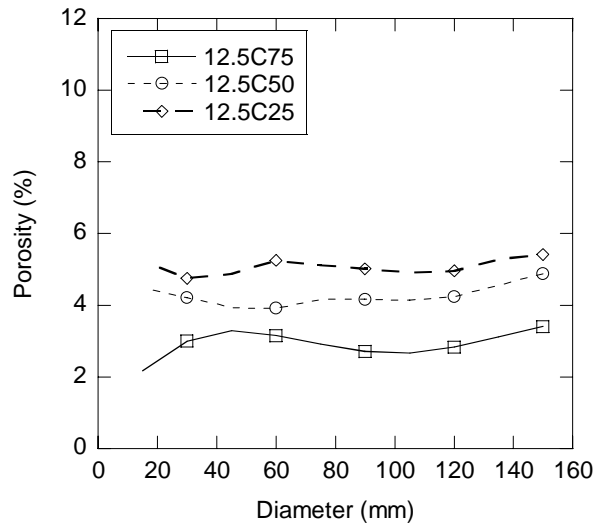
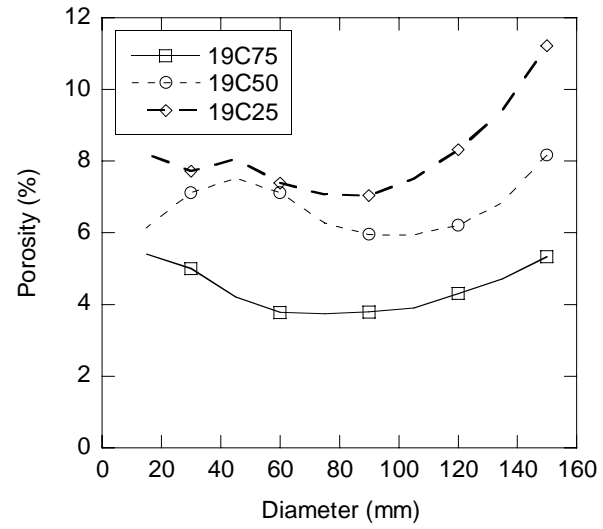
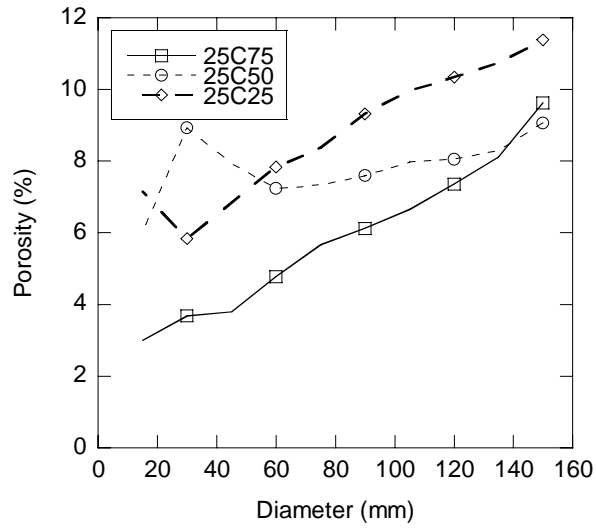


Figure 6.9 Porosity change in radial direction for coarse laboratory mixtures

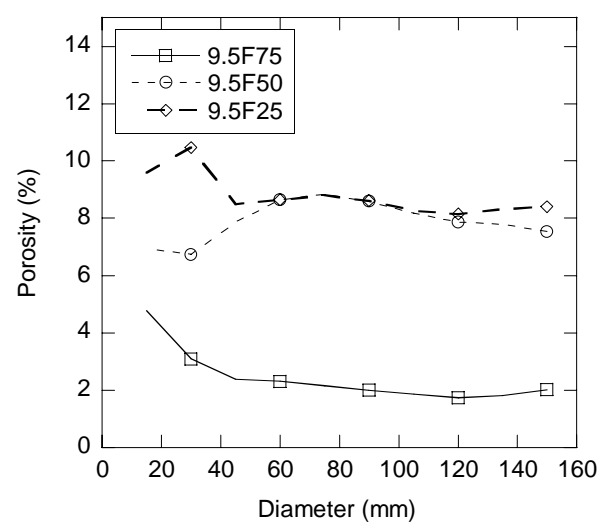
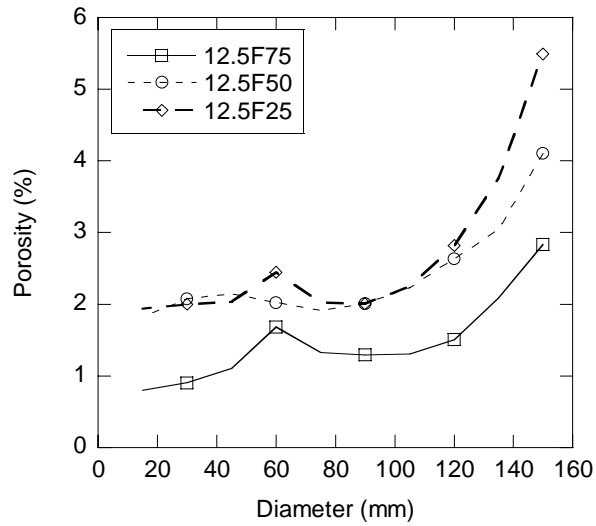
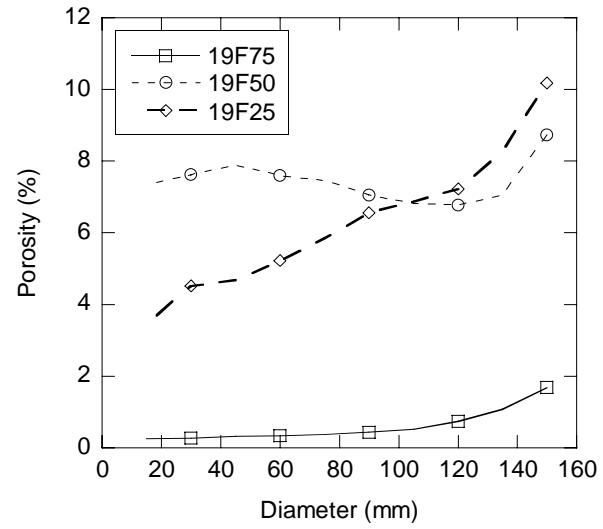
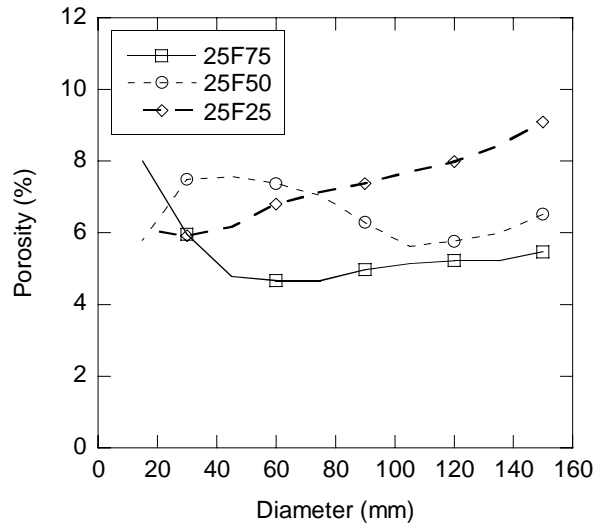


Figure 6.10 Porosity change in radial direction for fine laboratory mixtures

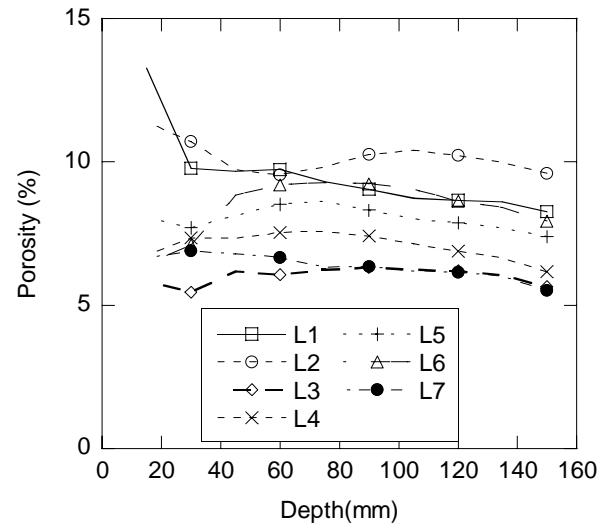
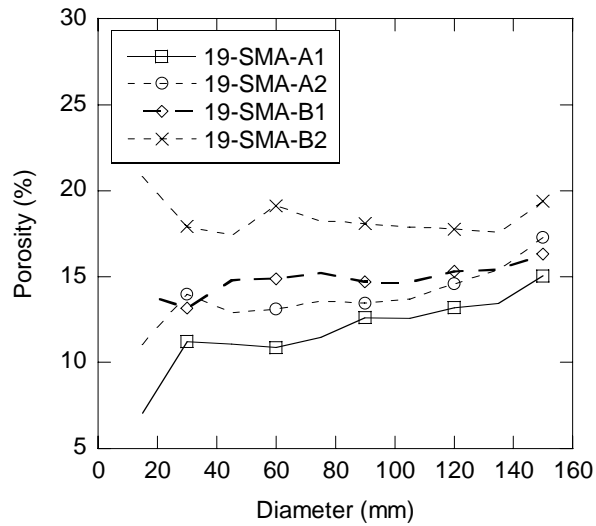
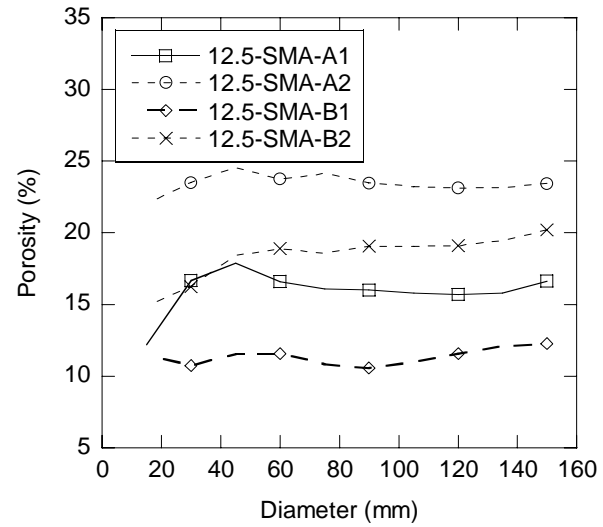
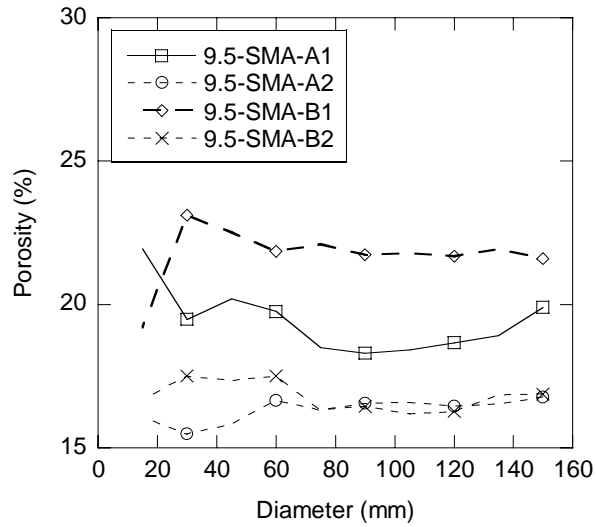


Figure 6.11 Porosity change in radial direction for SMA specimens and field core

prepared asphalt specimens and for the field cores. The figures indicate that most of the specimens did not exhibit significant change in porosity in the radial direction. The exceptions to this were the specimens 25C25, 25C50, 25C75, 12.5F25, 12.5F50, 12.5F75 and 25F25, for which an increase in porosity was observed with increasing diameter. This means that, in those specimens, most of the air voids were accumulated at the outer edges. Unlike the variation in porosity with depth (higher values at the two ends of the specimens) a consistent trend is not evident in the radial direction. Increase in porosity in radial direction for some of the specimens can be attributed to the inhomogeneous mixing in the laboratory before placing into the compaction mold. The relatively small variation of porosity in radial direction indicates that, unlike the vertical direction (z-direction, in Figure 6.4), the specimens may be considered homogeneous throughout the horizontal direction (x- and y- directions).

6.2.2 Effect of Compaction Energy and Gradation Shape on the Total Porosity of the Specimens

The total porosities of the specimens were calculated using Eq. 6.1. Figure 6.12, which shows the total porosity of each specimen compacted at different number of gyrations (compaction levels) clearly indicates that the compaction level affects the total porosity of the specimens. In most of the specimens, the porosity decreases as the number of gyrations increased, except in the 25C75 (75 gyrations), which has slightly higher porosity than the 25C50 (50 gyrations). Two possible reasons might have led to higher porosity in 25C75. First, the large aggregates (with sizes greater than 25mm) in 25C75 might have been stacked on the top of each other preventing efficient compaction.

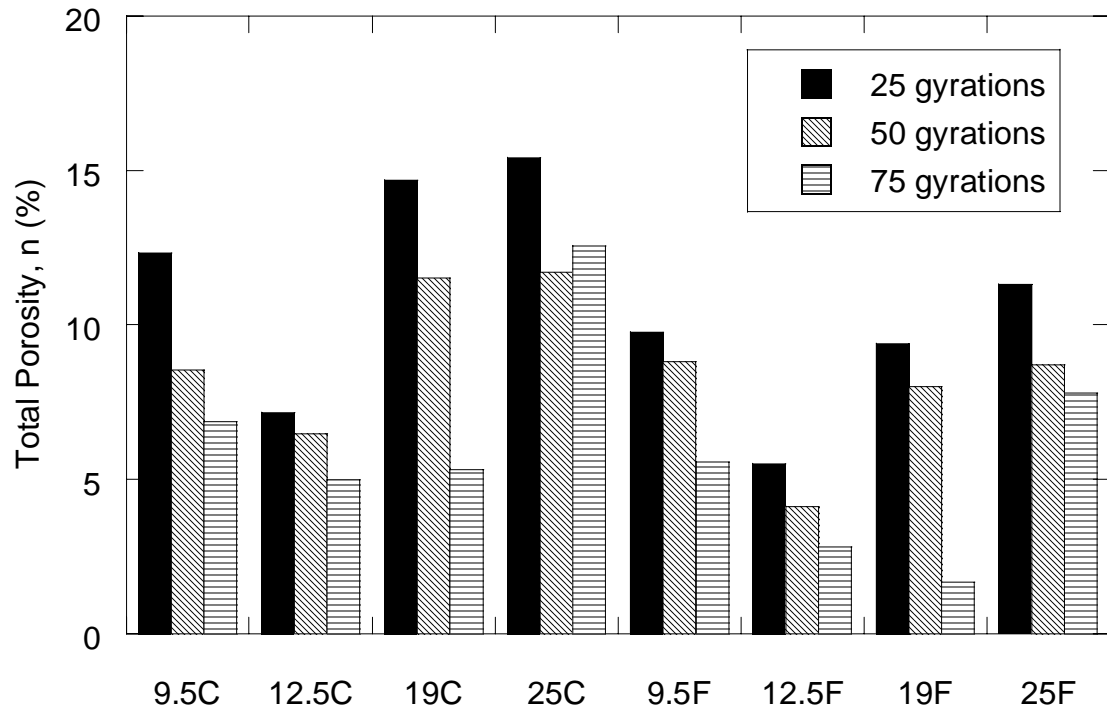


Figure 6.12 Total porosities of laboratory mixtures grouped based on the compaction efforts and NMAS

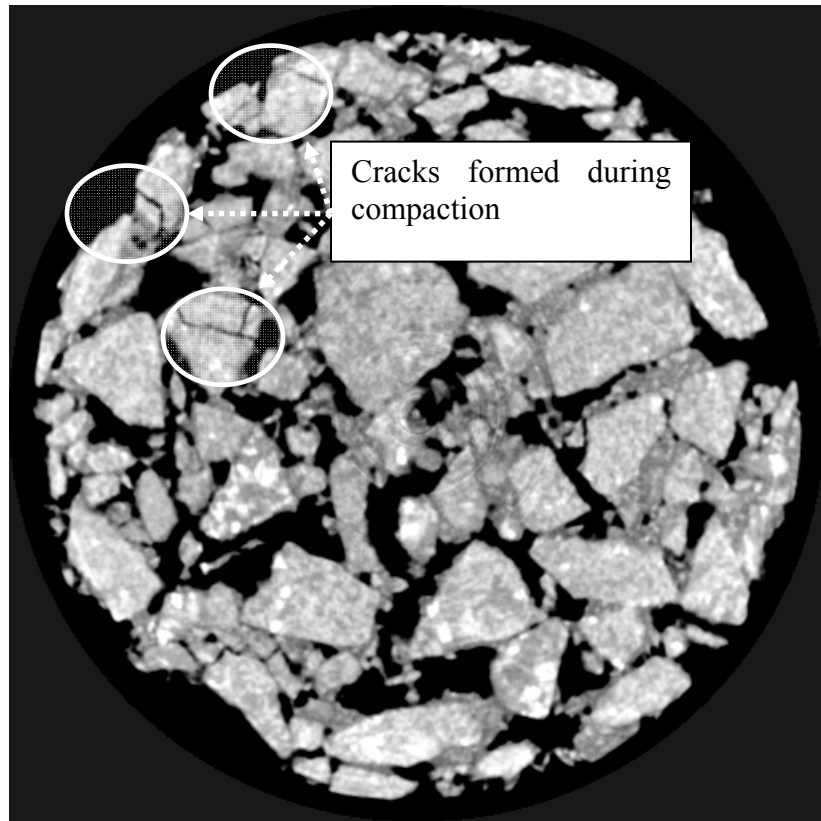


Figure 6.13 Illustration of cracks formed in 25C75 during compaction in gyratory compactor.

Second, the stacked large aggregates might have cracked due to the high forces exerted by the gyratory compactor. Figure 6.13 shows the cracks observed in 25C75 as an evident of the compaction force effect. It is believed that a combination of both factors affected the porosity change in 25C75.

Figure 6.12 also indicates the differences in the total porosities between the coarse graded (e.g., 25C) and fine graded specimens (e.g., 25F). Comparing the ones that has same NMAAS and gyration level (e.g., 25C75 versus 25F75), larger porosities were observed for coarse specimens as compared to the fine specimens.

6.3 METHODS OF LABORATORY HYDRAULIC CONDUCTIVITY TESTS

A number of devices have been developed to measure the hydraulic conductivity of geomaterials. These devices are usually classified based on the type of specimen confinement (such as rigid wall and flexible wall permeameters) and based on the flow boundary conditions (such as constant head and falling head tests). For asphalt pavements, specially designed field falling head permeameters have been generally used (Mogawer et al. 2002, Gogula et al. 2003). These permeameters are usually placed directly on the pavements and infiltration of water into the pavement is measured by noting the differences in the water elevations in the reservoirs of the permeameters. A hydraulic conductivity value is computed using the Darcy's well-known falling head permeability equation. The computed hydraulic conductivity value is assumed to represent the hydraulic conductivity in all directions. As a result, asphalt pavements are assumed to be homogeneous and isotropic. This assumption is highly questionable as the pore structure of the asphalt pavements may significantly vary in different directions, especially in z-direction (i.e., with depth) as shown in previous section. Similar

observations on pore structure heterogeneity were also made by Masad et al. (1999). Furthermore, falling head hydraulic conductivity equation assumes that the flow is occurring in one direction. However, in the field, water can move in any direction after it exits from the permeameter. Other potential problems of field permeameters include the uncontrolled saturation and boundary conditions. Therefore, the comparisons of field measured hydraulic conductivities are generally poorly correlated to the hydraulic conductivity measured in the laboratory (Gogula et al. 2003).

Many laboratory permeameters are designed to measure hydraulic conductivity of sandy soils (e.g., rigid wall permeameter) or clayey soils (e.g., flexible wall permeameter). Their applicability to asphalt pavements is questionable as their structures differ from the commonly encountered geomaterials. Preliminary work was required to find the appropriate permeameter for asphalt specimens. Initial tests conducted in rigid-wall permeameters using a constant-head approach produced unreasonably high hydraulic conductivity values primarily due to the sidewall leakage. Another shortcoming of the rigid-wall permeameter was that it was not possible to apply very low hydraulic gradients to keep the flow laminar in highly permeable specimens. Another set of tests were conducted using a flexible wall permeameter. However, the flexible wall permeameter also did not perform well for the highly permeable asphalt specimens used in this study. The flexible wall permeameters are mainly designed to measure the hydraulic conductivity of clayey and dense graded geomaterials ($k < 10^{-4}$ mm/s) and as a result the diameters of their inflow and outflow tubes are very small. Therefore, hydraulic conductivity measurements can greatly be affected by these connections. When highly

porous asphalt specimens were placed in these devices unreasonably low hydraulic conductivities were observed.

In order to overcome the problems mentioned above, a flexible wall permeameter was specially designed for measuring hydraulic conductivity of 150 mm diameter asphalt specimens. Figure 6.14 shows the schematic drawing of the so called “Bubble Tube Constant Head Permeameter”. It was designed to accommodate high flow rates associated with testing highly permeable asphalt specimens. The unique design eliminates the use of valves, fittings and smaller diameter tubings, all which contribute to head losses that interfere with the test measurements. As shown in Figure 6.14, permeameter was placed in a tub, which was used to maintain constant tail water elevation. The tub rim is located a few millimeters above the specimen top. As water flows out of the reservoir tube through the specimen, air bubbles emerge from the bottom of the bubble tube. The total head difference through the specimen (H), which is constant during the test, is the height difference between the bottom of the bubble tube and the top of the tub (Figure 6.14). The hydraulic gradient is calculated as follows:

$$i_h = \frac{H}{L} \quad (6.2)$$

where i_h is the hydraulic gradient, H is shown in Figure 6.14 and L the length of the specimen. Then the hydraulic conductivity was calculated using Eq. 4.8. The total flow rate through the specimen (i.e., q) was determined by noting the water elevation drop in the reservoir tube and multiplying it with the inner area of the reservoir tube minus the outer area of the bubble tube. A photograph of the Bubble Tube Constant Head Permeameter is given in Figure 6.15.

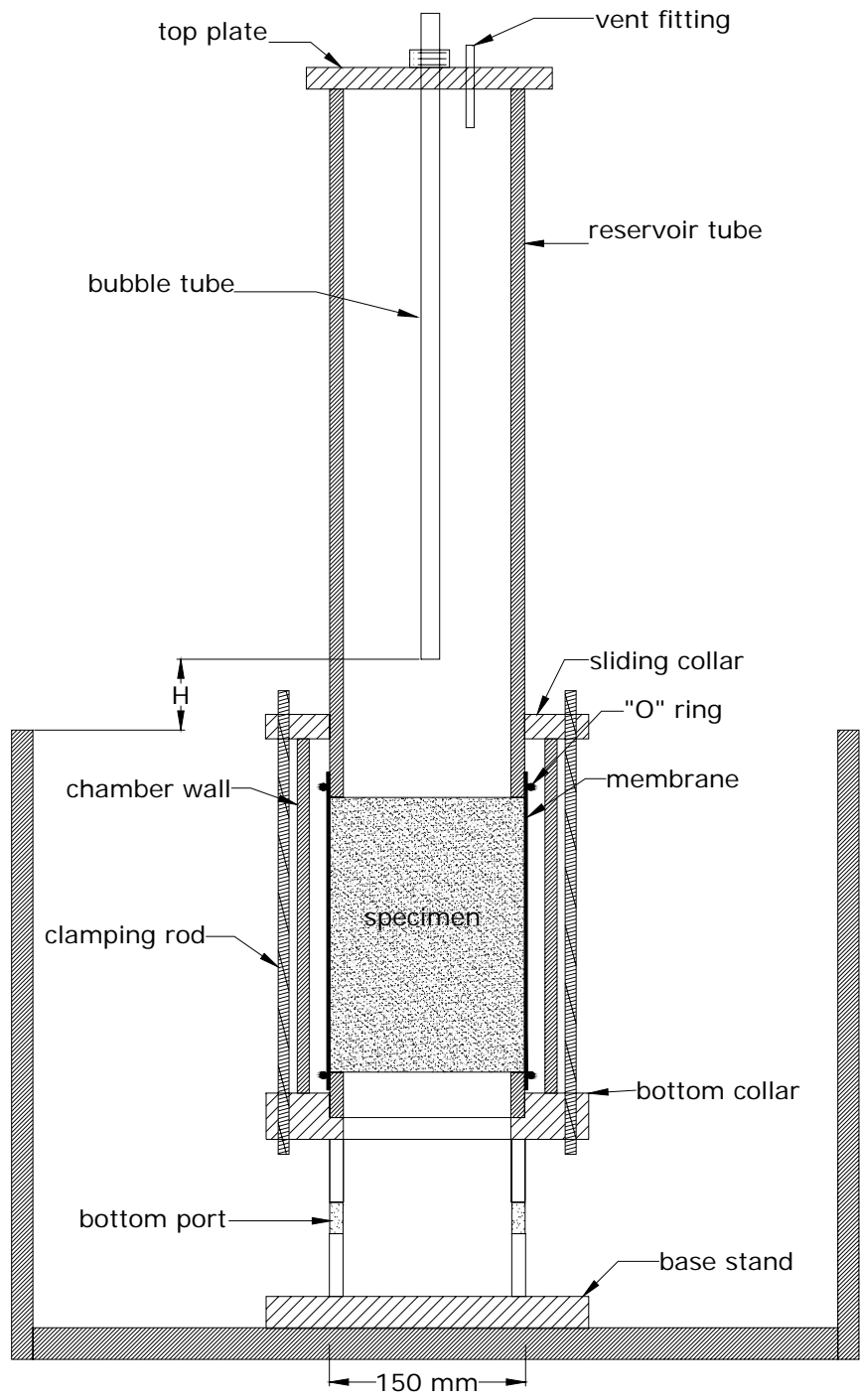


Figure 6.14 Bubble tube constant head permeameter



Figure 6.15 The photo of upper and lower portions of the bubble tube constant head permeameter

Advantages of the bubble tube constant head permeameter are: (1) very low hydraulic gradients can be applied, (2) high flow rates can be accommodated, (3) sidewall leakage is minimized due to the membrane and (4) almost no head loss exists in the inflow and outflow.

Procedures followed to conduct hydraulic conductivity tests using the bubble tube constant head permeameter are given in Appendix D.

6.4 EFFECT OF PORE GEOMETRY AND MIXTURE CHARACTERISTICS ON THE HYDRAULIC CONDUCTIVITY OF ASPHALT SPECIMENS

Analytical hydraulic conductivity prediction models usually use various pore geometry parameters, such as effective porosity, surface area of pores and tortuosity of the pore channels. These three parameters were determined for the asphalt specimens using digital image analysis and correlated to the laboratory based hydraulic conductivity measurements. The same parameters were also plotted against NMAS and the number of gyrations (compaction level) to investigate the effect of mixture characteristics on the hydraulic conductivity.

6.4.1 Effect of Porosity on the Hydraulic Conductivity

The total porosity and effective porosity versus hydraulic conductivity relationships of all specimens were plotted in Figures 6.16a and 6.16b, respectively. Effective porosity herein corresponds to the ratio of the volume of the pores that contributes to the fluid flow to the total volume of the specimen. It only includes the pores that are connected from top of the specimen to the bottom of the specimen (isolated pores were eliminated). Effective porosity was calculated using the *PORECON* algorithm described in Chapter

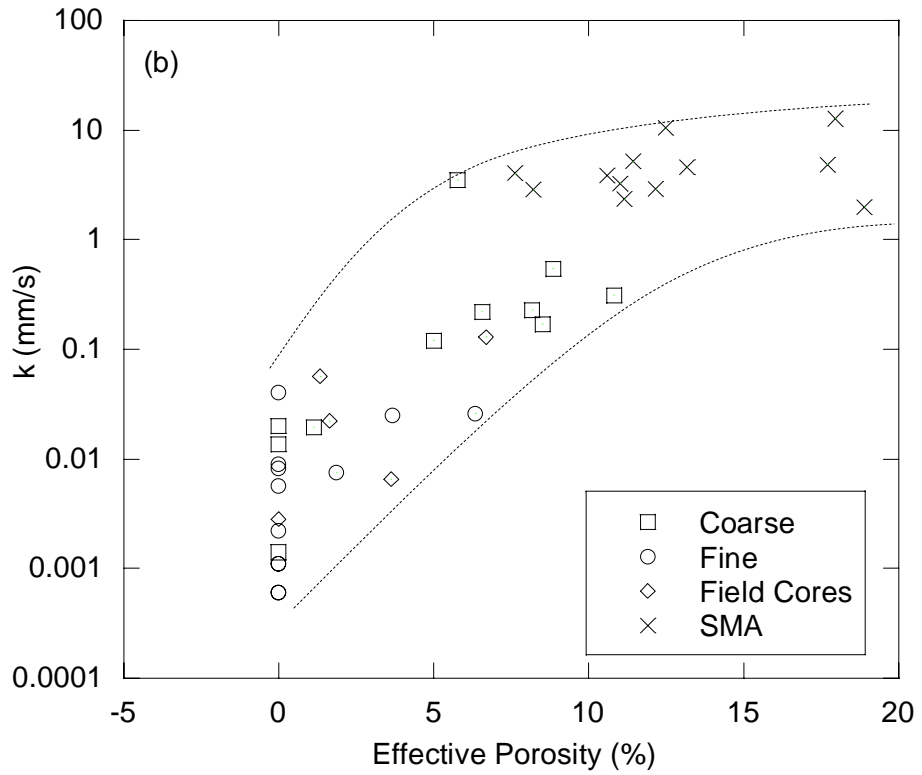
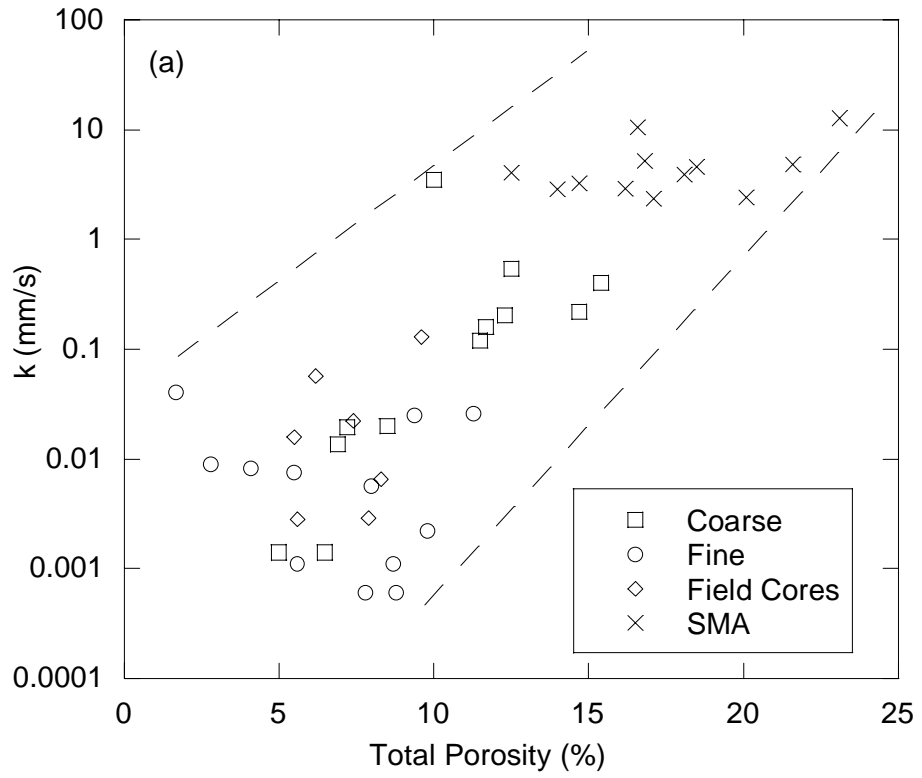


Figure 6.16 (a) Total porosity and (b) effective porosity versus hydraulic conductivity relationships.

5.2.2 which uses 3D binary images of the specimens obtained from the X-Ray CT. Even though fine-graded mixtures had total porosities in the range of 5.8% to 9.5%, only two of them (19F25 and 25F25) had interconnected pores, the rest of the specimens had very low effective porosities which were not within the detection limits of X-ray CT. The laboratory tests yielded low hydraulic conductivities (ranging from 6×10^{-4} to 8.9×10^{-3} mm/s) for the specimens which had very low effective porosity, which supported the image based observations. It should be noted that the resolution of the X-Ray CT images was 0.317 mm/pixel, i.e., it is not possible to detect the pores less than 0.317 mm in size, which can be referred to as the micro-scale pores. Low hydraulic conductivities of the fine-graded mixtures having very low effective porosity were possibly due to the flow in the micro-scale pores. Figures 6.16a and 6.16b shows that hydraulic conductivities increase in as both total and effective porosities increase, however, a better relationship (with less scatter in data) is seen between the effective porosity and hydraulic conductivity.

6.4.2 Effect of Specific Surface Area on the Hydraulic Conductivity

Specific surface area of each specimen was calculated using the *SSA* algorithm described in Section 5.2.3. Figure 6.17a presents the specific surface area versus hydraulic conductivity relationship for the specimens that have interconnected pore structure. There is a slight increase in hydraulic conductivity as the surface area increases. This is somewhat surprising since larger surface area indicates higher frictional shear stress that is applied to the fluid. However, larger surface area may also mean higher porosity which in turn indicates larger voids for fluid to travel. In order to

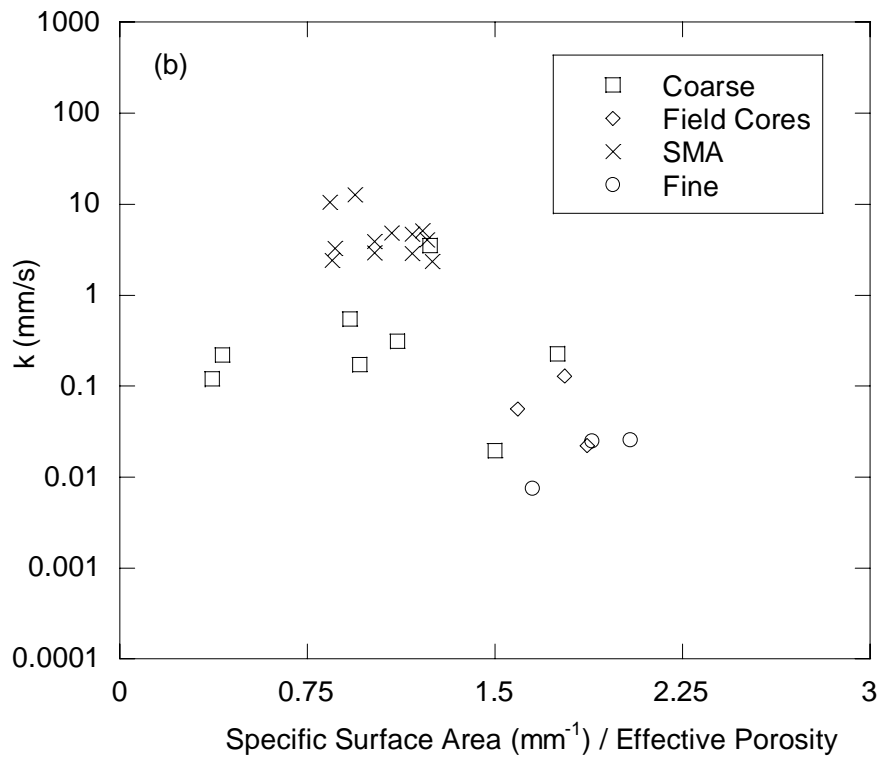
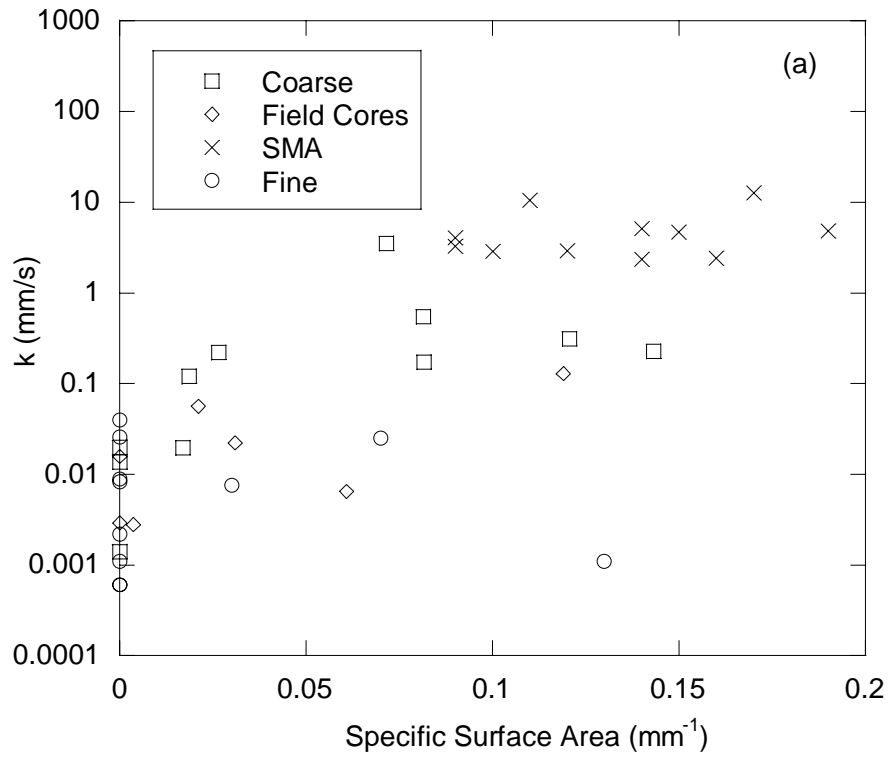


Figure 6.17 Relationships between hydraulic conductivity and (a) specific surface area and (b) specific surface area normalized by the effective porosity.

overcome this dual effect, specific surface area is normalized by the effective porosity and plotted against laboratory hydraulic conductivity data. The hydraulic conductivity generally decreases with the increasing normalized surface area.

6.4.3 Effect of Tortuosity on the Hydraulic Conductivity

Tortuosities of the specimens were calculated using the *TORT3D* algorithm described in Section 5.2.4. Figure 6.18 presents the relationship between hydraulic conductivity and the average tortuosity calculated within each specimen. As seen in Figure 6.18, hydraulic conductivity increases with the increasing tortuosity of the specimen, which is somewhat surprising, since one would expect that hydraulic conductivity should decrease as the tortuosity increases. Further research is needed to investigate this phenomenon.

6.4.4 Effect of Mix Design Parameters on the Hydraulic Conductivity

Figures 6.19a and 6.19b present the relationships between hydraulic conductivity and NMAAS and compaction level (number of gyrations), respectively. A clear trend was not observed between the hydraulic conductivity and these variables. In fact these variables along with the binder content and gradation shape determine the pore structure parameters (e.g. porosity and specific surface area). Therefore, the effects of NMAAS and compaction level on the asphalt hydraulic conductivity are embedded in the pore structure parameters.

The amount of fines (i.e., soil passing 2.36 mm sieve) in an asphalt mixture can have a direct effect on the reduction of pore space. Larger amount of fines, when mixed with binder, can quickly close the spaces between the larger aggregates. To investigate

the effect of fines on the hydraulic conductivity, fraction of the fines in each asphalt mixture were plotted against the laboratory measured hydraulic conductivity in Figure 6.20. The plots were created by grouping the specimens that were compacted at the same number of gyrations, as it could have a significant effect on the pore space reduction. Figure 6.20 clearly indicates that the hydraulic conductivity decreases exponentially as the percent fines increased, where the exponential best fit lines produced R^2 s of 0.45, 0.58 and 0.68, for 75, 50 and 25 number of gyrations. Best correlation was observed in the 25 gyrations, and the correlation decreased as the number of gyrations increased. This phenomenon was expected, because when the specimen is compacted more, the orientation and connectivity of pores can change and the effect of amount of fines on the pore structure can diminish.

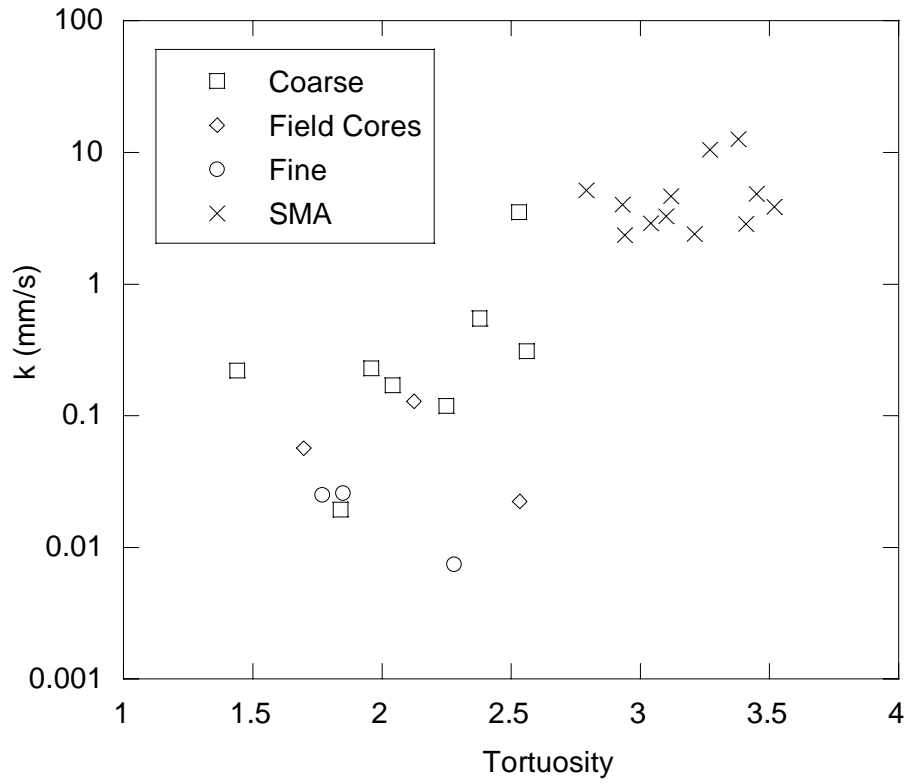


Figure 6.18 Relationship between hydraulic conductivity and tortuosity.

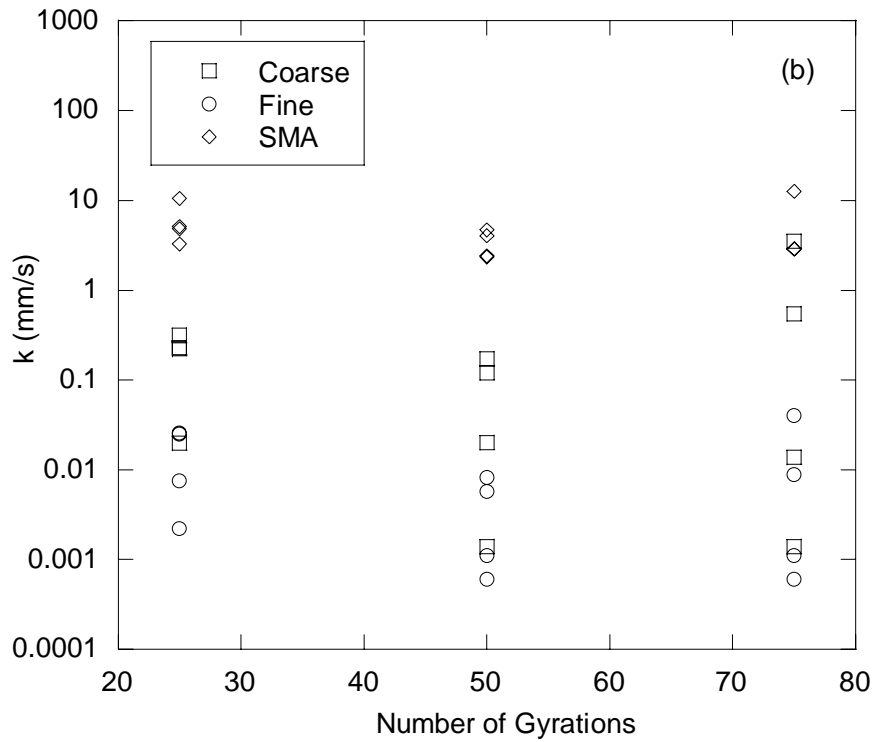
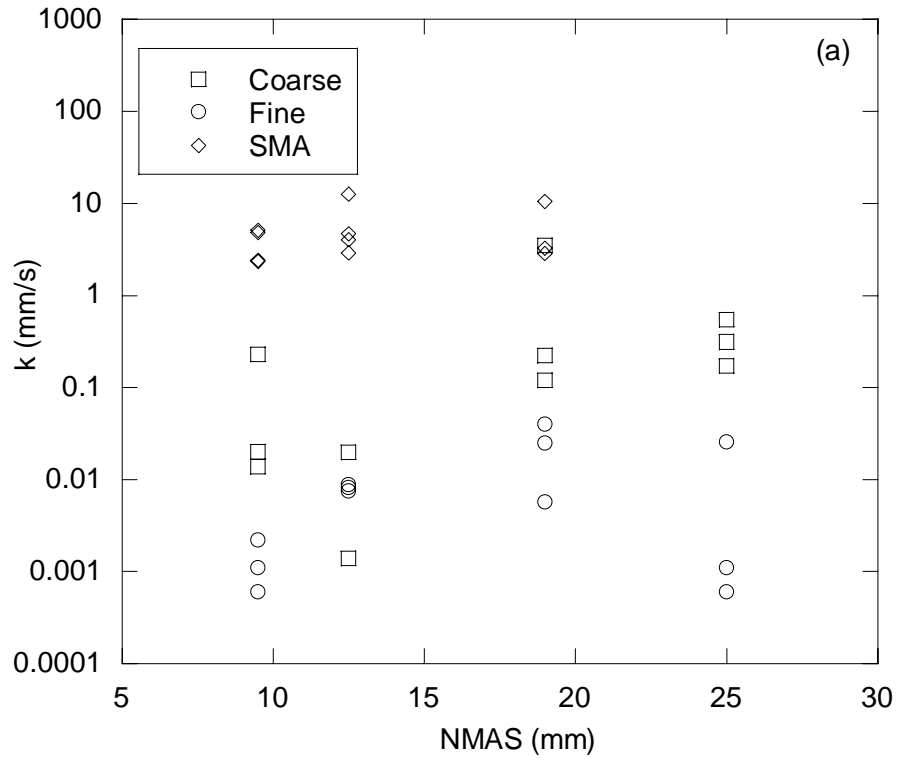


Figure 6.19 Relationship between hydraulic conductivity and (a) NMAS and (b) Number of gyrations

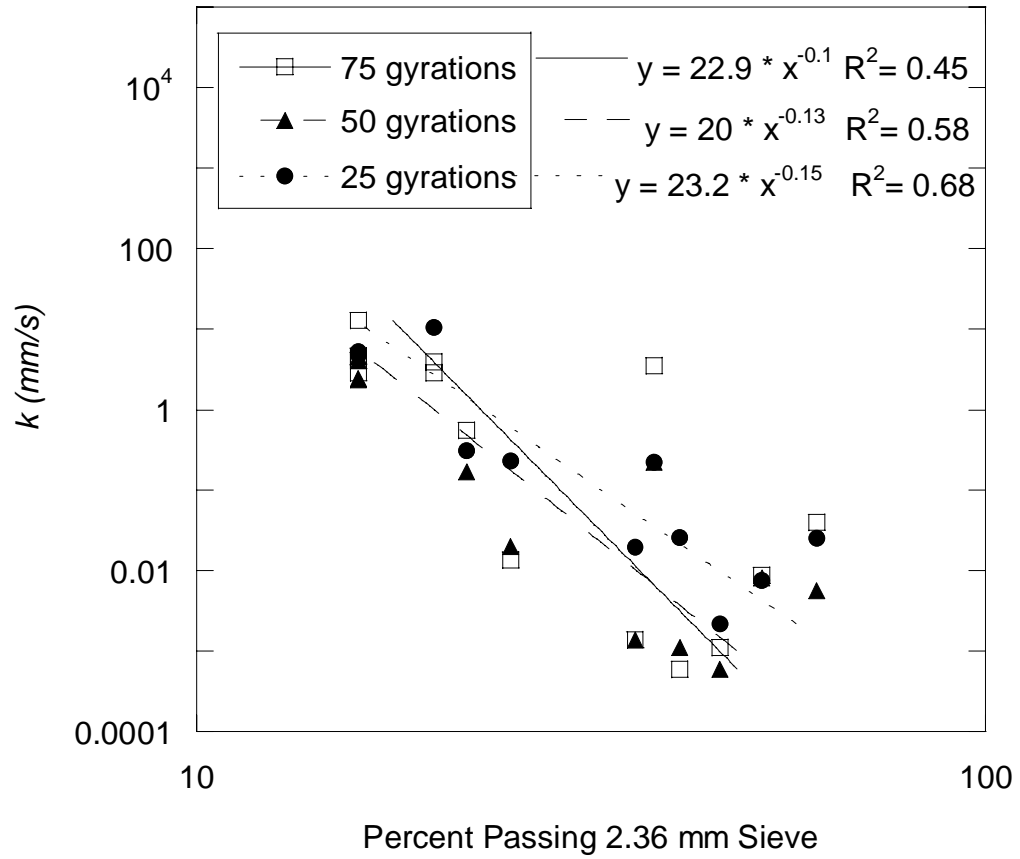


Figure 6.20 Effect of amount of fine graded soil in the mixture (% passing 2.36 mm sieve) on the hydraulic conductivity.

CHAPTER 7 NUMERICAL MODELING OF FLUID FLOW THROUGH ASPHALT PAVEMENTS USING LATTICE BOLTZMANN METHOD

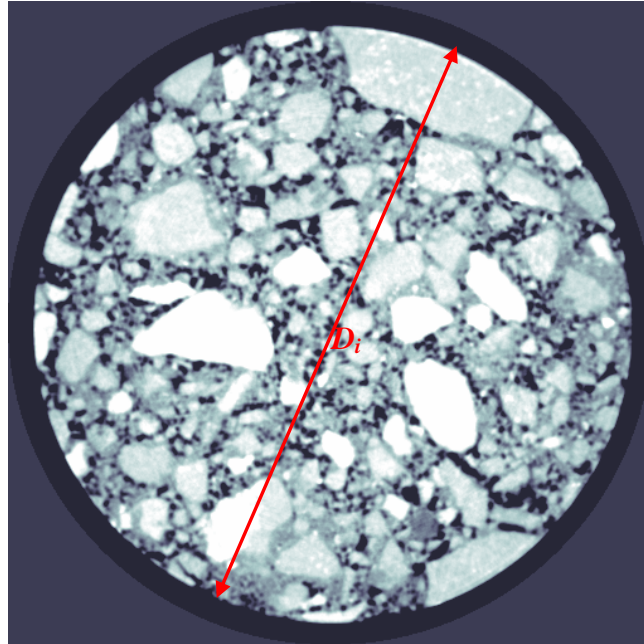
7.1 SIMULATION OF LABORATORY HYDRAULIC CONDUCTIVITY TEST

7.1.1 Geometry Input

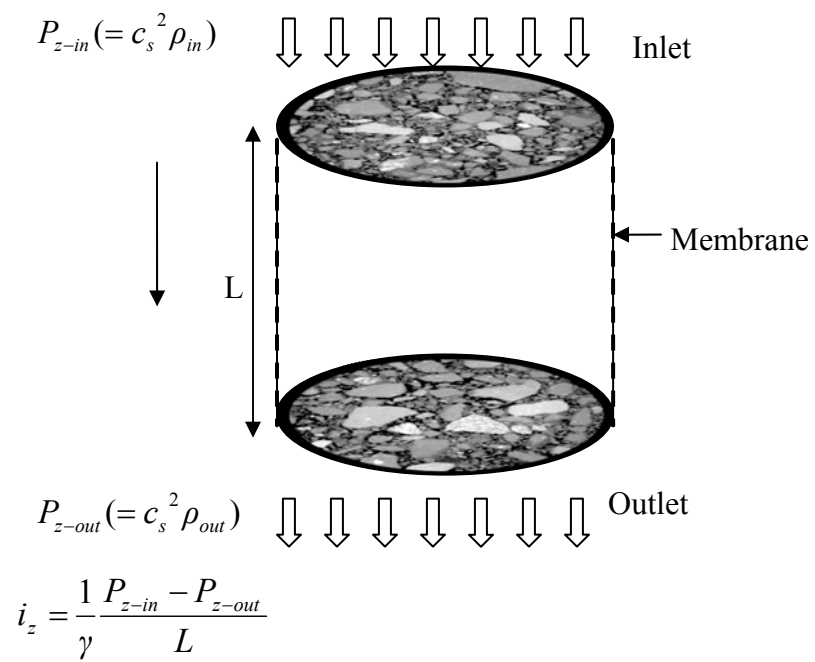
First input needed for the fluid flow simulation using LB method was the 3D geometry of the asphalt specimens. The 3D geometry of the asphalt specimens were generated from the X-ray CT images which were acquired at the radiography laboratory of Turner-Fairbank Highway Research Center (TFHRC) of FHWA. After obtaining the image slices of each specimen, an additional processing was needed to achieve a uniform pixel resolution in horizontal and vertical directions. Since the dimensions of acquired images were 512 by 512 pixels, the resolutions in two horizontal directions (Δx and Δy) were identical. These resolutions were determined using the known diameter of the specimens, whereas the vertical resolution (Δz) was always constant due to the constant thickness of the X-ray CT detector aperture. For example, Figure 7.1a shows an X-ray CT image slice of an asphalt specimen. Measuring the distance (in pixels) from the image, horizontal resolution was computed as follows:

$$\Delta x = \Delta y = \frac{D_w}{D_i} \quad (7.1)$$

where D_w is the diameter in units of millimeters. On the other hand, the vertical resolution of the images (i.e. slice thickness of each image) was registered by the aperture



(a)



(b)

Figure 7.1 (a) X-ray CT slice of an asphalt specimen, (b) illustration of inlet, outlet and the membrane confinement in LB simulations.

of the linear detector of the X-ray CT device, which is 0.8 mm. Therefore, the vertical resolution (Δz) was 0.8 mm/pixel in all specimens. To achieve a uniform resolution in all directions (x, y and z), image slices were resized by using bilinear interpolation so that the horizontal resolutions are equivalent to the vertical ones.

After achieving same resolution in all directions, images were converted to binary (black and white) images using morphological thresholding technique, where black areas (pixel values of 0) represent solid and white areas (pixel values of 1) represent air voids. Selection of appropriate threshold value is critical in correct determination of the pore structure. In principal, the lowest pixel values in an X-ray CT image should give the air voids as their density is the lowest. Therefore, a pixel intensity that is close to zero is generally used as the threshold value. However, in small isolated pores or the pore throats (constrictions) where the size of the pores are close to the resolution of the images, the built-in algorithm of the X-ray CT equipment may compute elevated pixel intensities of these pores. In those cases, higher threshold values are needed to capture these pores. However, selecting higher threshold value may also widen the boundaries of the larger pores in other locations. To minimize the possible errors due to this tradeoff, several trial threshold values were used at each specimen and a threshold value that includes most of the small pores without excessively widening the larger pores was visually determined. This relatively inaccurate technique may have caused slight deviations from the actual pore structure and the LB simulation results should be interpreted accordingly.

After obtaining the three dimensional pore geometry defined by the white voxels, isolated pores were eliminated using the *PORECON* algorithm, producing a 3D image of the interconnected pore structure. It is important to mention that this step is not required

for the LB simulations; however, the isolated pores were eliminated solely to speed up the simulation at each time step. Furthermore, decreasing the number of nodes reduced the total number of time steps to reach steady state flow condition. Finally, lattice nodes were generated at the center of each voxel (3D equivalent of a pixel) within the 3D image.

7.1.2 Boundary Conditions

To simulate the pressure boundary conditions of the laboratory bubble tube constant head hydraulic conductivity test, certain pressure (i.e., density) values were set at the inlet and the outlet of the specimen during the LB simulations. The curved face of the cylindrical specimens was confined by the solid walls, which simulates the membrane confinement around the specimen, as shown in Figure 7.1b. Applied pressure gradient, densities and the resolution of each specimen are provided in Table 7.1. The densities of all nodes were initially assigned to such values that the magnitude of the density decreases linearly from inlet nodes to the outlet nodes. Lastly, the macroscopic velocities at all nodes were set to zero.

7.1.3 Calculation of Hydraulic Conductivity Tensor

Hydraulic conductivity is usually computed using the Darcy's well-known equation given in Eq. 6.3, which can be rewritten in the following form:

$$k_{zz} = \frac{(Q_z / A)}{i_z} \quad (7.2)$$

where k_{zz} is the hydraulic conductivity, Q_z is the measured flow rate, i_z is the applied hydraulic gradient ($i_z = \nabla P_z / \gamma$) in z-direction shown in Figure 7.1b, and A is the specimen cross sectional area perpendicular to the direction of pressure gradient. Another form of the Eq. 7.2 can be obtained by replacing Q_z/A with the Darcy's velocity (u_z^c) and replacing the hydraulic gradient (i_z) with $\nabla P_z / \gamma$

$$u_z^c = k_{zz} \nabla P_z / \gamma \quad (7.3)$$

Equation 7.3 is a simplified form of the Darcy's equation. The general form of the Darcy's equation for any pore structure has a more complicated structure and given as (Dullien, 1992):

$$\begin{bmatrix} u_x \\ u_y \\ u_z \end{bmatrix} = -\frac{1}{\mu} \begin{bmatrix} K_{xx} & K_{xy} & K_{xz} \\ K_{yx} & K_{yy} & K_{yz} \\ K_{zx} & K_{zy} & K_{zz} \end{bmatrix} \begin{bmatrix} \nabla P_x \\ \nabla P_y \\ \nabla P_z \end{bmatrix} \quad (7.4)$$

where the tensor K_{ij} is called the intrinsic permeability tensor, μ is the dynamic viscosity, u_x , u_y and u_z are the average (seepage) velocities in x-, y- and z-directions, respectively and ∇P_x , ∇P_y and ∇P_z are the pressure gradients in x-, y- and z-directions, respectively.

In laboratory hydraulic conductivity test, the pressure gradient is usually applied only in z-direction (i.e. $\nabla P_x = 0$ and $\nabla P_y = 0$), which reduces Eq. 7.4 to the following:

$$u_x = - (K_{xz} \nabla P_z / \mu) \quad (7.5)$$

$$u_y = - (K_{yz} \nabla P_z / \mu) \quad (7.6)$$

$$u_z = - (K_{zz} \nabla P_z / \mu) \quad (7.7)$$

Darcy's velocity vector (\mathbf{u}^c) in Eq. 7.2 relates to the seepage velocity vector (\mathbf{u}) as follows (Das, 2001):

$$\mathbf{u}^c = \mathbf{u} n_{eff} \quad (7.8)$$

where n_{eff} is the effective porosity of the medium. Combining Equations 7.3, 7.5-7.7 and 7.8 reveal the following set of equations for the hydraulic conductivity tensor:

$$k_{xz} = - \gamma n_{eff} (u_x / \nabla P_z) \quad (7.9)$$

$$k_{yz} = - \gamma n_{eff} (u_y / \nabla P_z) \quad (7.10)$$

$$k_{zz} = - \gamma n_{eff} (u_z / \nabla P_z) \quad (7.11)$$

7.1.4 Results of Simulations and Comparison with the Experimental Measurements

The LB fluid flow simulations were run until a steady-state flow condition was achieved. The steady-state flow criterion was set such that the difference in the overall mean velocity in z -direction (u_z) between two consecutive time steps is less than a threshold value. This threshold was selected as the 0.001% of the mean velocity of the current time step. Figure 7.2 shows a typical change in mean velocity over time steps

Table 7.1 The input that are used in LB simulations of laboratory hydraulic conductivity test.

Specimen ID	LB Method	Flow Method	Lattice Resolution (Δx) (mm/pixel)	Length of the Specimen (mm)	Pressure Gradient (∇P_z) ($\text{g}/\text{mm}^2\text{-s}^2$)
9.5C25	D3Q19	DG	0.4	70.4	8.79E-04
12.5C25	D3Q19	DG	0.4	68.8	1.00E-06
19C25	D3Q19	DG	0.8	74	1.00E-03
19C50	D3Q19	DG	0.8	73.6	1.00E-03
19C75	D3Q19	DG	0.8	71	1.00E-03
25C25	D3Q19	DG	0.8	72	1.37E-04
25C50	D3Q19	DG	0.8	70.4	1.00E-06
25C75	D3Q19	DG	0.8	76.8	1.37E-05
19F25	D3Q19	DG	0.8	70.1	1.00E-03
25F25	D3Q19	DG	0.8	72.3	1.00E-03
9.5SMA-A1	D3Q19	DG	0.8	80	1.00E-03
9.5SMA-A2	D3Q19	DG	0.8	80	1.00E-03
9.5SMA-B1	D3Q19	DG	0.8	79.5	1.00E-03
9.5SMA-B2	D3Q19	DG	0.8	79	1.00E-03
12.5SMA-A1	D3Q19	DG	0.8	81	1.00E-03
12.5SMA-A2	D3Q19	DG	0.8	77.5	1.00E-03
12.5SMA-B1	D3Q19	DG	0.8	81	1.00E-03
12.5SMA-B2	D3Q19	DG	0.8	81	1.00E-03
19SMA-A1	D3Q19	DG	0.8	81	1.00E-03
19SMA-A2	D3Q19	DG	0.8	78	1.00E-03
19SMA-B1	D3Q19	DG	0.8	76	1.00E-03
19SMA-B2	D3Q19	DG	0.4	77	1.00E-03
L2	D3Q19	DG	0.4	47	9.97E-07
L4	D3Q19	DG	0.4	47	9.97E-07
L5	D3Q19	DG	0.4	35	1.00E-06

Note: 9.5C25 represents the specimen with an NMAS of 9.5mm and compacted at 25 gyration level. L2 is the field core taken from lane 2 of accelerated loading facility at the TFHRC. DG=density gradient. D3Q19= three dimensional LB model with 19 microscopic velocity directions.

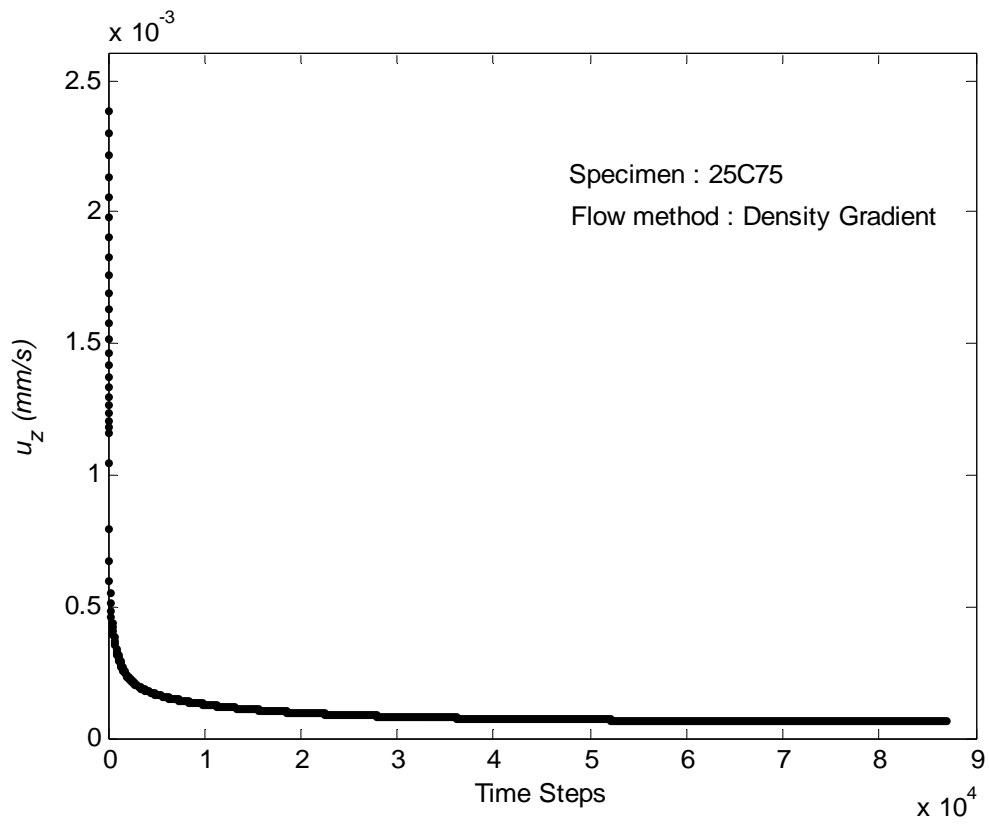


Figure 7.2 Change in mean velocity over time steps during LB fluid flow simulation in specimen 25C75.

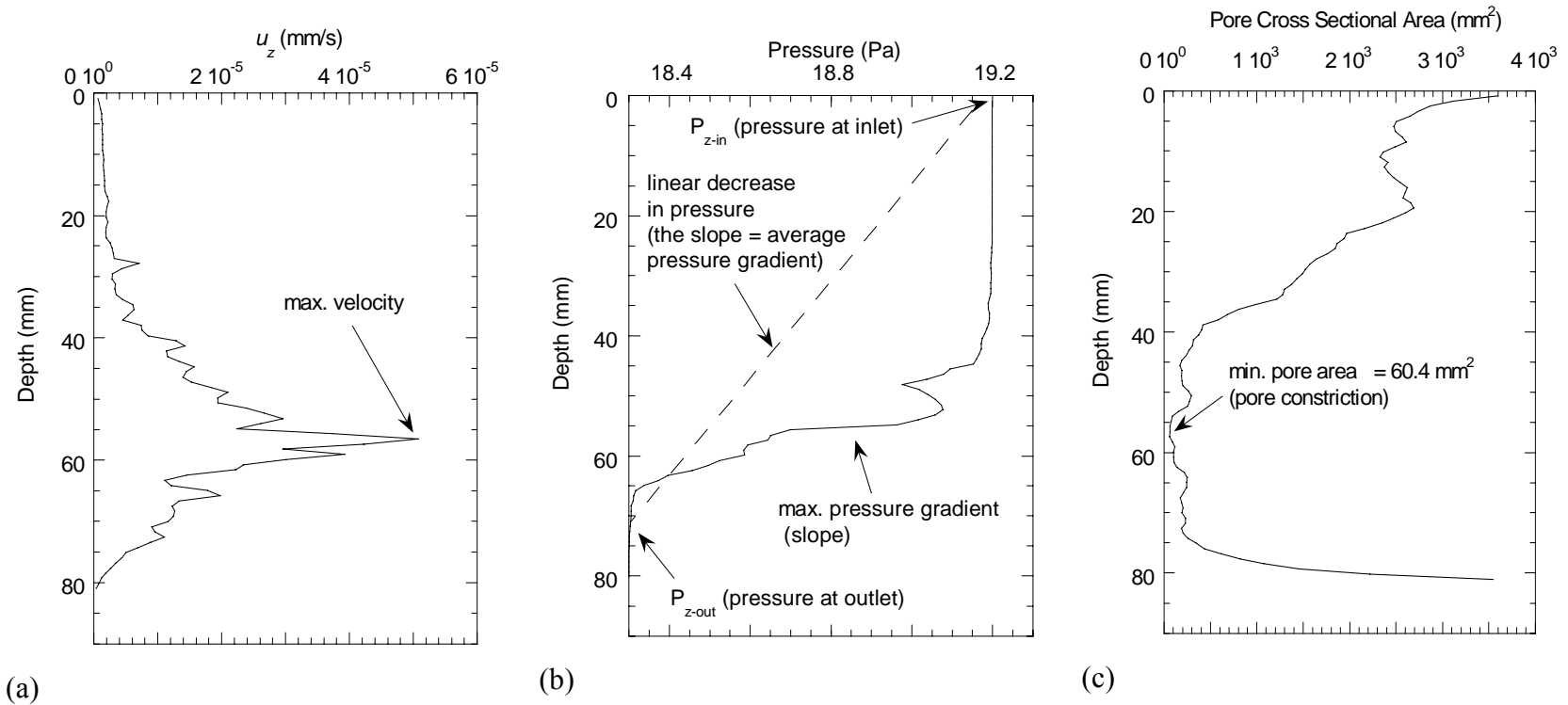


Figure 7.3 Change in (a) mean velocity, (b) pressure and (c) pore cross sectional area with depth.

during a LB simulation. In this particular case (specimen 25C75), the steady state flow is observed after approximately 52,000 time steps. It was observed that the number of time steps required for flow stabilization varied from 1000 to 150,000, depending on the angularity of the internal pore structure. Less number of time steps was required for system stabilization for specimens with less angular pore-solid interface. Similar observations were also reported by Duarte et al. (1992) in their 2D Cellular Automata (CA) based model of flow through cylindrical obstacles placed between parallel plates.

A typical velocity and pore water pressure profile at the end of a LB simulation is provided in Figure 7.3a and Figure 7.3b, respectively. Each data point in Figures 7.3a and 7.3b corresponds to the mean velocity and mean pressure at a given depth, respectively. In addition, the change of pore cross sectional area with depth was also provided in Figure 7.3c. As seen in Figure 7.3, the maximum velocity and pressure gradient occur at a depth of 58 mm. This depth also corresponds to a point where the pore cross sectional area reaches its lowest value (i.e. the constriction). Furthermore, the pressure gradient (slope of the curve in Figure 7.3b) observed at the constriction zone is significantly higher than the overall average pressure gradient. This may lead to high shear stresses at the constriction zone, which in turn might cause stripping of the binder from the aggregate and damage to the asphalt matrix. Further discussions on shear stresses at constrictions are given in Section 7.4.2. Figure 7.4 shows the streamlines computed at the end of LB simulation for specimen 25C75. Flow streamlines in Figure 7.4 clearly indicates the preferential flow pathways, where only a portion of the pores are utilized in the flow after certain depth.

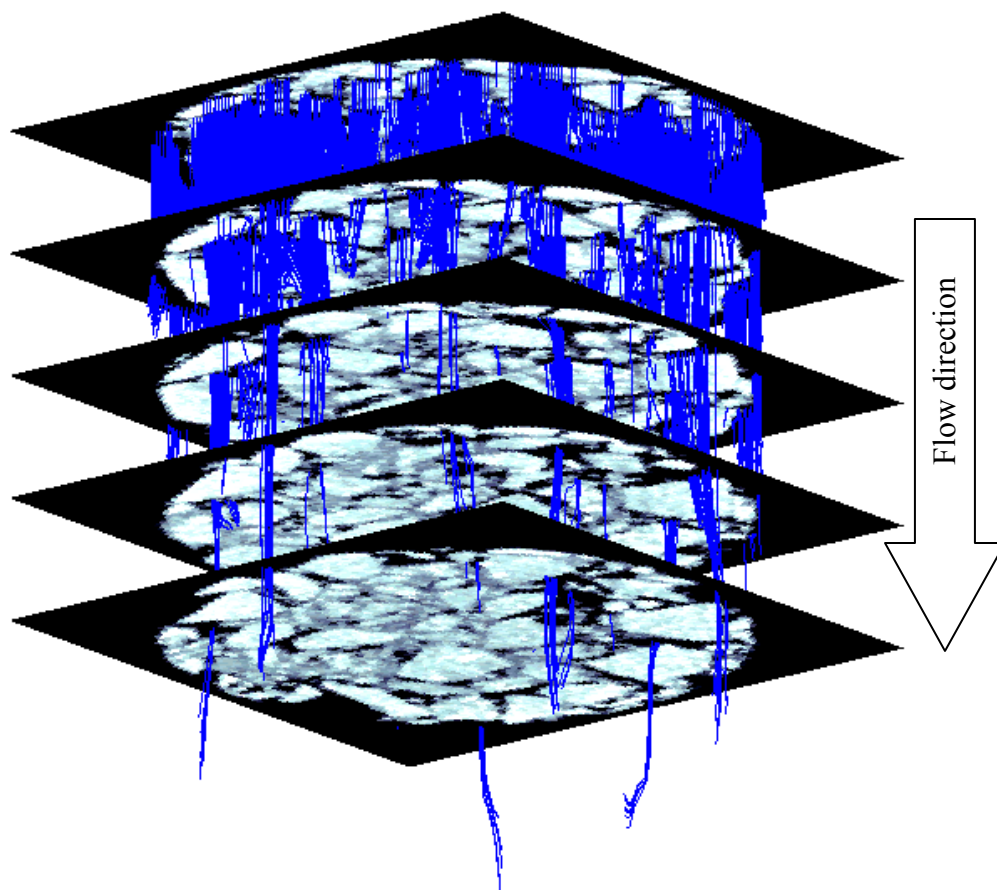


Figure 7.4 Streamlines computed at the end of LB simulation for specimen 25C75.

Table 7.2 Summary of the hydraulic conductivities based on laboratory measurements and based on LB simulations.

Sample No	Identification	Sample ID	Total Porosity, n (%)	Effective Porosity, n_{eff} (%)	k_{zz} (mm/s)	
					Laboratory Test	Lattice Boltzmann Model
1	Coarse Graded Gyrotory Specimens	9.5C25	12.3	8.18	0.2290	0.3560
2		9.5C50	8.5	NA	0.0200	NC
3		9.5C75	6.9	NA	0.0137	NC
4		12.5C25	7.2	1.13	0.0195	0.0300
5		12.5C50	6.5	NA	0.0014	NC
6		12.5C75	5.0	NA	0.0014	NC
7		19C25	14.7	6.56	0.2200	0.2785
8		19C50	11.5	5.00	0.2210	0.4000
9		19C75	10.0	5.78	3.5000	7.1300
10		25C25	15.4	10.82	0.3100	0.2800
11		25C50	11.7	8.51	0.1700	0.1750
12		25C75	12.5	8.85	0.5450	0.3600
13	Fine Graded Gyrotory Specimens	9.5F25	9.8	NA	0.0022	NC
14		9.5F50	8.8	NA	0.0006	NC
15		9.5F75	5.6	NA	0.0011	NC
16		12.5F25	5.5	NA	0.0075	NC
17		12.5F50	4.1	NA	0.0082	NC
18		12.5F75	2.8	NA	0.0089	NC
19		19F25	9.4	3.67	0.0250	0.100
20		19F50	8.0	NA	0.0057	NC
21		19F75	1.7	NA	0.0400	NC
22		25F25	11.3	6.35	0.0258	0.0225
23		25F50	8.7	NA	0.0011	NC
24		25F75	7.8	NA	0.0006	NC

Note: NC refers to the specimens with no interconnected macro pores (i.e. minimum size greater than 0.3 mm) between two opposite faces of a specimen. NA: Effective porosity was not available due to lack of interconnected pore structure. The hydraulic conductivities observed in these specimens are possibly due to the flow in micro pores whose size is less than 0.3 mm. This size is not observable by the X-ray CT technique.

Table 7.2 (cont'd) Summary of the hydraulic conductivities based on laboratory measurements and based on LB simulations.

Sample No	Identification	Sample ID	Total Porosity, n (%)	Effective Porosity, n_{eff} (%)	k_{zz} (mm/s)		
					Laboratory Test	Lattice Boltzmann Model	
25	SMA Mixtures	9.5SMA-A1	20.1	18.90	2.4233	3.408	
26		9.5SMA-A2	17.1	11.16	2.3600	4.86	
27		9.5SMA-B1	21.6	17.70	4.8300	11.5	
28		9.5SMA-B2	16.8	11.44	5.1650	3.1100	
29		12.5SMA-A1	16.2	12.17	2.9000	3.25	
30		12.5SMA-A2	23.1	17.97	12.6700	20.3600	
31		12.5SMA-B1	12.5	7.63	4.0300	4.260	
32		12.5SMA-B2	18.5	13.17	4.6400	5.48	
33		19SMA-A1	14.7	11.02	3.2600	7.5600	
34		19SMA-A2	16.6	12.48	10.5100	7.2000	
35		19SMA-B1	14.0	8.22	2.8600	3	
36		19SMA-B2	18.1	10.60	3.84	3.2500	
37		Field Cores	L1	8.3	NA	0.0065	NC
38			L2	9.6	6.70	0.1290	0.2100
39	L3		5.6	NA	0.0028	NC	
40	L4		6.2	1.33	0.0567	0.0380	
41	L5		7.4	1.653	0.0223	0.0210	
42	L6		7.9	NA	0.0029	NC	
43	L7		5.5	NA	0.0158	NC	

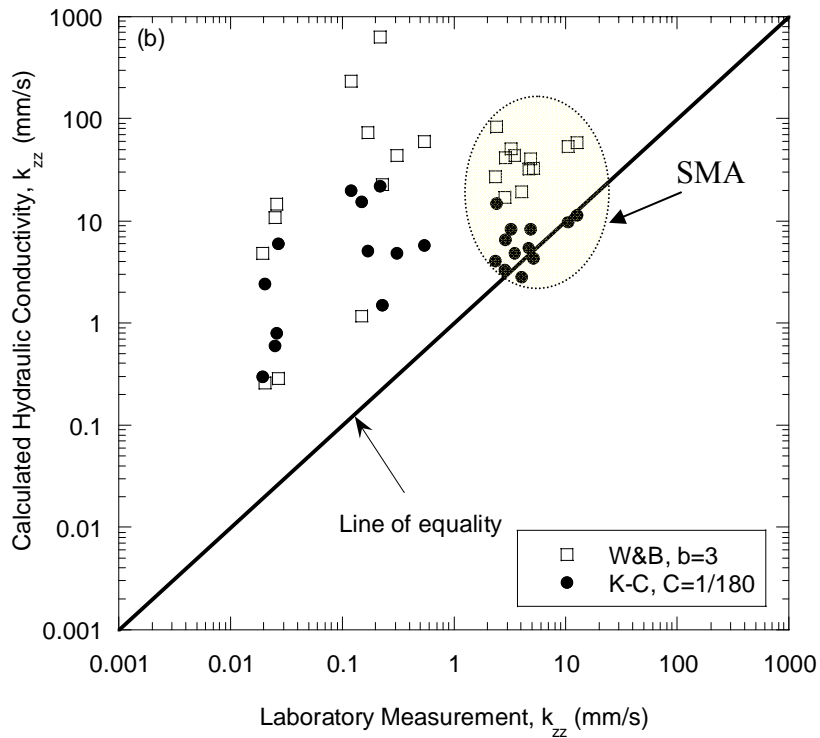
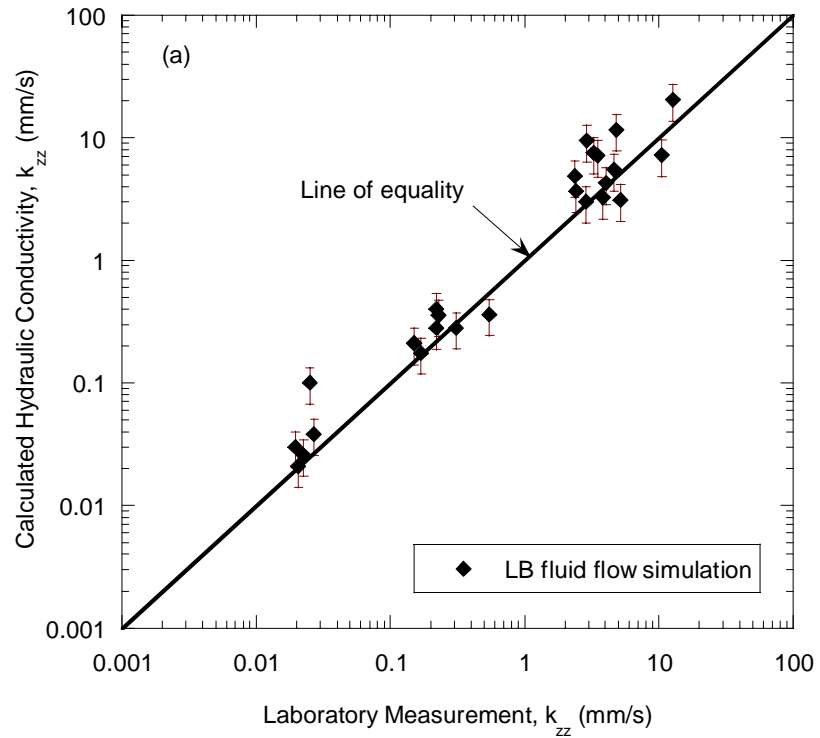


Figure 7.5 Comparison of laboratory-based hydraulic conductivity with those produced by (a) the LB method and (b) two analytical equations.

A summary of the hydraulic conductivities based on LB simulations and laboratory measurements is given in Table 7.2. Table 7.2 also includes the total and effective porosities of the 43 specimens employed in the testing program. It should be recalled that the effective porosities were calculated using the image analysis algorithm *PORECON*. The analyses revealed that 18 specimens had no interconnected macro pores (i.e. minimum size greater than 0.3 mm) between two opposite faces of a specimen. Therefore, the effective porosities of those specimens are denoted with “NA”. The magnitudes of the laboratory-based hydraulic conductivities in those specimens are one to three orders of magnitude lower as compared to the specimens with positive effective porosities. The low hydraulic conductivities measured in the laboratory were possibly due to the flow in micro pores whose size is less than 0.3 mm. It should be noted that the best resolution that can be obtained by the X-ray CT technique for a 150 mm diameter specimen was 0.3 mm/pixel. Therefore, X-ray CT technique was not able to capture the micro pores in the specimens. For the specimens with interconnected macro pores, the hydraulic conductivities were higher which is usually governed by the macro pores. Therefore, LB fluid flow simulations were performed on the specimens who have pores connected to their two opposite faces. After LB simulations, the computed steady-state velocities were used to calculate the hydraulic conductivities of the specimens using Eq. 7.11. Computed hydraulic conductivities based on LB simulations were plotted against the hydraulic conductivities based on laboratory measurements in Figure 7.5a. Figure 7.5a clearly indicates that estimations of LB simulations are in a very good agreement with the laboratory based results. Most of the specimens were within the variability limits indicated by the error bars. The error bars were computed based on the variations in the

Table 7.3 Permeability predictions of two analytical models compared with the laboratory measurements.

Specimen ID	S_a (mm ⁻¹)	T	n_e (%)	k_{zz} (mm/s)		
				Kozeny-Carman (Eq. 2.1) b=3	Walsh & Brace (Eq. 2.2) C=1/180	Laboratory Test
9.5C25	0.14	1.96	8.2	1.5	22.8	0.2290
12.5C25	0.02	1.84	1.1	0.3	4.8	0.0195
19C25	0.03	1.44	6.6	21.8	626.3	0.2200
19C50	0.02	2.25	5.0	19.6	231.4	0.1200
19C75	0.07	2.53	5.78	4.8	43.6	3.5000
25C25	0.12	2.56	10.8	4.8	43.6	0.3100
25C50	0.08	2.04	8.5	5.1	72.9	0.1700
25C75	0.08	2.38	8.9	5.7	60.3	0.5450
19F25	0.07	1.77	3.7	0.6	10.7	0.0250
25F25	0.13	1.85	6.4	0.8	14.5	0.0258
9.5SMA-A1	0.16	3.21	18.9	14.8	83.2	2.4233
9.5SMA-A2	0.14	2.94	11.2	4.0	27.1	2.3600
9.5SMA-B1	0.19	3.45	17.7	8.3	40.7	4.8300
9.5SMA-B2	0.14	2.79	11.4	4.3	32.7	5.1650
12.5SMA-A1	0.12	3.04	12.2	6.5	41.4	2.9000
12.5SMA-A2	0.17	3.38	18.0	11.4	58.2	12.6700
12.5SMA-B1	0.09	2.93	7.6	2.8	19.2	4.0300
12.5SMA-B2	0.15	3.12	13.2	5.4	32.5	4.6400
19SMA-A1	0.09	3.10	11.0	8.2	50.4	3.2600
19SMA-A2	0.11	3.27	12.5	9.7	53.7	10.5100
19SMA-B1	0.096	3.4059	8.2	3.3	17.0	2.8600
19SMA-B2	0.11	3.52	10.6	5.6	26.7	3.8400
L2	0.12	2.35	6.7	15.4	1.161	0.1500
L4	0.02	1.53	1.3	6.0	0.287	0.027
L5	0.031	2.16	1.7	2.4	0.257	0.0205

Note: S_a is the specific surface area, T is the tortuosity and n_e is the effective porosity.

laboratory test, where multiple tests were conducted on various specimens and average variability was computed as 31%. This variability was attributed to the saturation problems during testing and problems associated with the membrane confinement. A tradeoff existed on selection of appropriate magnitude of cell pressure applied on the membrane. Applying too little cell pressure caused sidewall leakage, whereas applying too much pressure caused the membrane fill in the voids connected to the surface which might have caused flow reduction.

The estimations of two commonly used analytical hydraulic conductivity equations (Kozeny-Carman, Eq. 2.1 and Walsh & Brace, Eq. 2.2) were plotted against the laboratory based measurements in Figure 7.5b. The pore structure parameters (i.e., S_a , T and n_e) of the asphalt specimens, which were used in the analytical equations, are summarized in Table 7.3. It can be seen from Figure 7.5b that the estimations of analytical equations were relatively accurate at high hydraulic conductivities (i.e., $k_{zz} > 1$ mm/s), whereas, at low hydraulic conductivities (i.e., $k_{zz} < 1$ mm/s), their estimations were up to two order of magnitude higher than the laboratory measurements. In general Kozeny-Carman performed better than the Walsh & Brace's equation. It should be noted that the constants C and b in Equations 2.1 and 2.2 can have a significant affect on the estimation of hydraulic conductivity. Using the reported values of these constants (i.e. $C=1/180$ and $b=3$) revealed a biased estimation at low hydraulic conductivities. These empirical constants can be adjusted to for a better estimation; however, the new constants do not necessarily represent all asphalt pavements. On the other hand, these equations can provide relatively good qualitative comparison between different asphalt specimens.

7.2 DIRECTIONAL HYDRAULIC CONDUCTIVITY OF ASPHALT PAVEMENTS

7.2.1 Method of Calculating Components of the Hydraulic Conductivity Tensor

Generalized Darcy's formula given in Eq. 7.4 can be rewritten by using the hydraulic conductivity tensor as follows:

$$\begin{bmatrix} u_x \\ u_y \\ u_z \end{bmatrix} = -\frac{1}{\gamma n_{eff}} \begin{bmatrix} k_{xx} & k_{xy} & k_{xz} \\ k_{yx} & k_{yy} & k_{yz} \\ k_{zx} & k_{zy} & k_{zz} \end{bmatrix} \begin{bmatrix} \nabla P_x \\ \nabla P_y \\ \nabla P_z \end{bmatrix} \quad (7.12)$$

Simple relations (Equations 7.9-7.11) were derived in Section 7.1.3 for the last column of the hydraulic conductivity tensor given in Eq. 7.12, by setting the pressure gradients in the horizontal directions to zero (i.e. $\nabla P_x=0$ and $\nabla P_y=0$). Simulations were performed by applying a pressure gradient only in z -direction to compute the three components of the hydraulic conductivity tensor (i.e. k_{xz} , k_{yz} , and k_{zz}). A similar approach was undertaken to compute the other components of the hydraulic conductivity tensor. Prior to the simulations, a cubical sample was extracted from the X-ray CT images of the cylindrical specimens as shown in Figure 7.6. Initially, a pressure gradient in x -direction was applied and the pressure gradients in other directions were set to zero (i.e. $\nabla P_z=0$ and $\nabla P_y=0$). The first column of the hydraulic conductivity tensor was computed using the following set of equations:

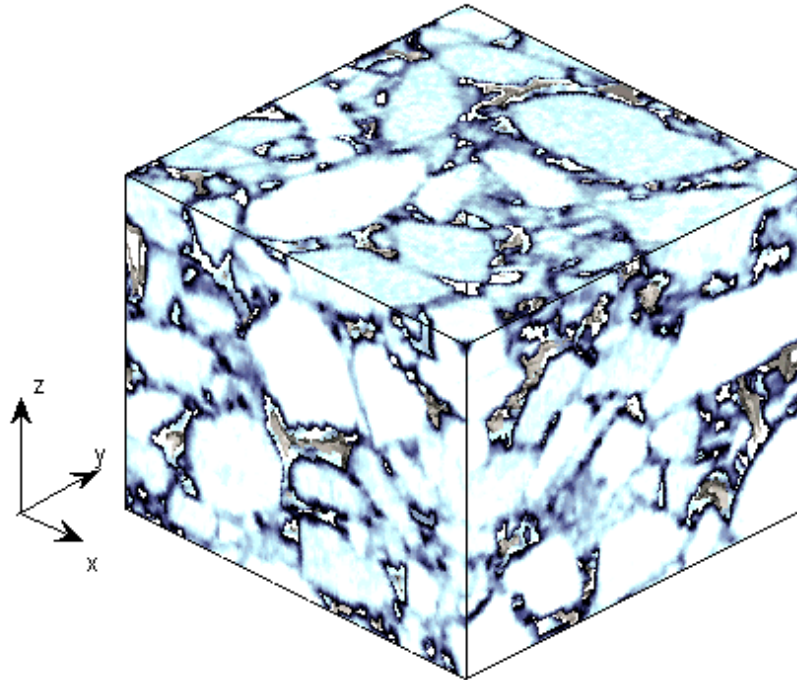


Figure 7.6 A typical 3D image extracted from X-ray CT image of a cylindrical asphalt concrete specimen.

$$k_{xx} = - \gamma n_{eff}(u_x / \nabla P_x) \quad (7.13)$$

$$k_{yx} = - \gamma n_{eff}(u_y / \nabla P_x) \quad (7.14)$$

$$k_{zx} = - \gamma n_{eff}(u_z / \nabla P_x) \quad (7.15)$$

Lastly, a pressure gradient in y -direction was applied while keeping pressure gradients in other directions zero (i.e. $\nabla P_z=0$ and $\nabla P_x=0$) and the second column of the hydraulic conductivity tensor was computed using the following equations:

$$k_{xy} = - \gamma n_{eff}(u_x / \nabla P_y) \quad (7.16)$$

$$k_{yy} = - \gamma n_{eff}(u_y / \nabla P_y) \quad (7.17)$$

$$k_{zy} = - \gamma n_{eff}(u_z / \nabla P_y) \quad (7.18)$$

Table 7.4 summarizes the simulations performed for calculating the hydraulic conductivity tensor components. Total 60 simulations were performed to compute all nine components of the hydraulic conductivity tensor. Each simulation provided three components; therefore at least three simulations were necessary for each specimen. Table 7.3 also includes the number of time steps required for steady-state flow condition which ranged from 1200 to 164000 time steps for different specimens.

Table 7.4 Summary of simulations performed for calculating the components of the hydraulic conductivity tensor

Simulation No	Specimen	Direction	Image Resolution (mm/pixel)	Applied Pressure Gradient $\text{g/mm}^2\text{-s}^2$	Number of Time Steps to reach Steady-State Flow	Computed Variables
1	9.5C25	x	0.4	1.00E-08	51618	k_{xx}, k_{yx}, k_{zx}
2		y	0.4	1.00E-08	50990	k_{xy}, k_{yy}, k_{zy}
3		z	0.4	1.00E-08	68400	k_{xz}, k_{yz}, k_{zz}
4	12.5C25	x	0.4	1.00E-08	163800	k_{xx}, k_{yx}, k_{zx}
5		y	0.4	1.00E-08	53100	k_{xy}, k_{yy}, k_{zy}
6		z	0.4	1.00E-08	9900	k_{xz}, k_{yz}, k_{zz}
7	19C25	x	0.8	1.00E-08	123300	k_{xx}, k_{yx}, k_{zx}
8		y	0.8	1.00E-08	117000	k_{xy}, k_{yy}, k_{zy}
9		z	0.8	1.00E-08	18980	k_{xz}, k_{yz}, k_{zz}
10	19C50	x	0.8	1.00E-08	152700	k_{xx}, k_{yx}, k_{zx}
11		y	0.8	1.00E-08	148800	k_{xy}, k_{yy}, k_{zy}
12		z	0.8	1.00E-08	75300	k_{xz}, k_{yz}, k_{zz}
13	19C75	x	0.8	1.00E-08	1340	k_{xx}, k_{yx}, k_{zx}
14		y	0.8	1.00E-08	1240	k_{xy}, k_{yy}, k_{zy}
15		z	0.8	1.00E-08	41400	k_{xz}, k_{yz}, k_{zz}
16	25C25	x	0.4	1.00E-08	18290	k_{xx}, k_{yx}, k_{zx}
17		y	0.4	1.00E-08	38090	k_{xy}, k_{yy}, k_{zy}
18		z	0.4	1.00E-08	11380	k_{xz}, k_{yz}, k_{zz}
19	25C50	x	0.4	1.00E-08	11000	k_{xx}, k_{yx}, k_{zx}
20		y	0.4	1.00E-08	11720	k_{xy}, k_{yy}, k_{zy}
21		z	0.4	1.00E-08	15170	k_{xz}, k_{yz}, k_{zz}
22	25C75	x	0.4	1.00E-08	42360	k_{xx}, k_{yx}, k_{zx}
23		y	0.4	1.00E-08	24300	k_{xy}, k_{yy}, k_{zy}
24		z	0.4	1.00E-08	63600	k_{xz}, k_{yz}, k_{zz}
25	9.5SMA-A1	x	0.8	1.00E-08	22200	k_{xx}, k_{yx}, k_{zx}
26		y	0.8	1.00E-08	27600	k_{xy}, k_{yy}, k_{zy}
27		z	0.8	1.00E-08	19200	k_{xz}, k_{yz}, k_{zz}
28	9.5SMA-A2	x	0.8	1.00E-08	31200	k_{xx}, k_{yx}, k_{zx}
29		y	0.8	1.00E-08	31200	k_{xy}, k_{yy}, k_{zy}
30		z	0.8	1.00E-08	25800	k_{xz}, k_{yz}, k_{zz}
31	9.5SMA-B1	x	0.8	1.00E-08	17700	k_{xx}, k_{yx}, k_{zx}
32		y	0.8	1.00E-08	18600	k_{xy}, k_{yy}, k_{zy}
33		z	0.8	1.00E-08	15600	k_{xz}, k_{yz}, k_{zz}

Note: 9.5C25 represents the specimen with an NMAS of 9.5mm and compacted at 25 gyration level. 9.5-SMA-A1 represents the SMA specimen with an NMAS of 9.5 mm.

Table 7.4 (cont'd) Summary of simulations performed for calculating the components of the hydraulic conductivity tensor

Simulation No	Specimen	Direction	Image Resolution (mm/pixel)	Applied Pressure Gradient $g/mm^2 \cdot s^2$	Number of Time Steps to reach Steady-State Flow	Computed Variables
34	9.5SMA-B2	x	0.8	1.00E-08	25500	k_{xx}, k_{yx}, k_{zx}
35		y	0.8	1.00E-08	25800	k_{xy}, k_{yy}, k_{zy}
36		z	0.8	1.00E-08	21000	k_{xz}, k_{yz}, k_{zz}
37	12.5SMA-A1	x	0.8	1.00E-08	27000	k_{xx}, k_{yx}, k_{zx}
38		y	0.8	1.00E-08	27600	k_{xy}, k_{yy}, k_{zy}
39		z	0.8	1.00E-08	22200	k_{xz}, k_{yz}, k_{zz}
40	12.5SMA-A2	x	0.8	1.00E-08	18000	k_{xx}, k_{yx}, k_{zx}
41		Y	0.8	1.00E-08	18300	k_{xy}, k_{yy}, k_{zy}
42		Z	0.8	1.00E-08	14700	k_{xz}, k_{yz}, k_{zz}
43	12.5SMA-B1	X	0.8	1.00E-08	48600	k_{xx}, k_{yx}, k_{zx}
44		y	0.8	1.00E-08	34200	k_{xy}, k_{yy}, k_{zy}
45		z	0.8	1.00E-08	42280	k_{xz}, k_{yz}, k_{zz}
46	12.5SMA-B2	x	0.8	1.00E-08	34200	k_{xx}, k_{yx}, k_{zx}
47		y	0.8	1.00E-08	35400	k_{xy}, k_{yy}, k_{zy}
48		z	0.8	1.00E-08	28800	k_{xz}, k_{yz}, k_{zz}
49	19SMA-A1	x	0.8	1.00E-08	33900	k_{xx}, k_{yx}, k_{zx}
50		y	0.8	1.00E-08	35400	k_{xy}, k_{yy}, k_{zy}
51		z	0.8	1.00E-08	27300	k_{xz}, k_{yz}, k_{zz}
52	19SMA-A2	x	0.8	1.00E-08	32700	k_{xx}, k_{yx}, k_{zx}
53		y	0.8	1.00E-08	34200	k_{xy}, k_{yy}, k_{zy}
54		z	0.8	1.00E-08	26700	k_{xz}, k_{yz}, k_{zz}
55	19SMA-B1	x	0.8	1.00E-08	87600	k_{xx}, k_{yx}, k_{zx}
56		y	0.8	1.00E-08	56100	k_{xy}, k_{yy}, k_{zy}
57		z	0.8	1.00E-08	33900	k_{xz}, k_{yz}, k_{zz}
58	19SMA-B2	x	0.8	1.00E-08	37800	k_{xx}, k_{yx}, k_{zx}
59		y	0.8	1.00E-08	123300	k_{xy}, k_{yy}, k_{zy}
60		z	0.8	1.00E-08	47100	k_{xz}, k_{yz}, k_{zz}

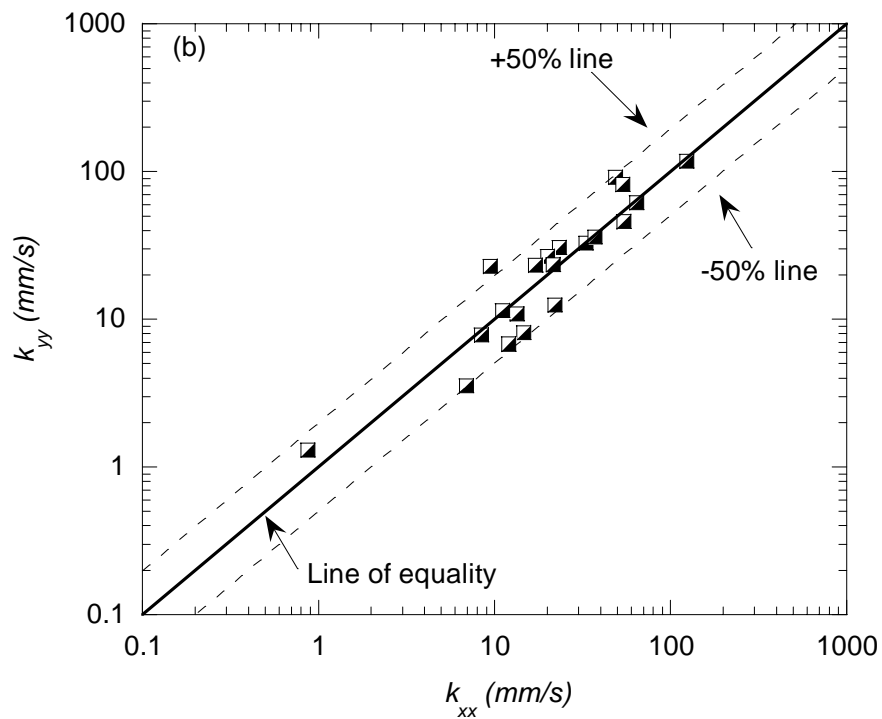
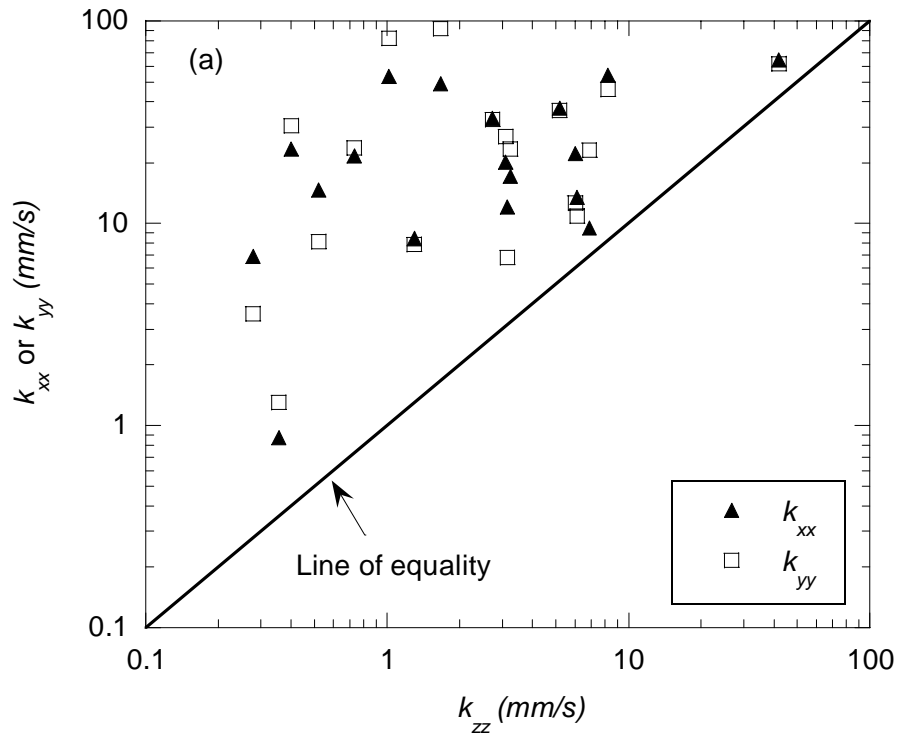


Figure 7.7 (a) The relationship between (a) vertical (i.e. k_{zz}) and horizontal (i.e., k_{xx} and k_{yy}) hydraulic conductivities, and (b) two horizontal hydraulic conductivities (i.e., k_{xx} versus k_{yy})

7.2.2 Relationship between Vertical and Horizontal Hydraulic Conductivities

It was mentioned in Chapter 2 that there are several semi-analytical formulas to estimate the hydraulic conductivity of asphalt pavements. These formulas are usually applicable to granular and sandy soils and assume that the pore structure is homogeneous and isotropic. The pore structure analyses of the different asphalt specimens in Chapter 6 raised some questions about the validity of these assumptions for asphalt pavements. It was shown that the porosity decreases with depth, which implied the possible existence of constrictions; whereas, the porosity did not significantly vary in the radial direction implying the isotropy in horizontal directions (i.e., x - and y - directions). The results of fluid flow simulations in various asphalt specimens supported the findings of the pore structure analyses performed in Chapter 6. In order to investigate the isotropy of asphalt specimens, the relationship between the vertical (i.e. k_{zz}) and horizontal (i.e., k_{xx} and k_{yy}) hydraulic conductivities was plotted in Figure 7.7a. It can clearly be seen that the horizontal hydraulic conductivities are higher than the vertical hydraulic conductivity, where, in some specimens, the difference is up to two orders of magnitude. Whereas, the ones in two horizontal (i.e., k_{xx} and k_{yy}) are close to each other. A plot of k_{xx} versus k_{yy} provided in Figure 7.7b confirms that the hydraulic conductivities in two horizontal directions are comparable within a 50% confidence interval. These observations indicated that the asphalt specimens are isotropic comparing two horizontal directions (x - and y - directions) and anisotropic comparing horizontal and vertical directions.

In order to further investigate the cause of the relatively lower hydraulic conductivity values in z -direction, the variation of pore cross-sectional area (PCSA) in three different directions was plotted in Figure 7.8 for specimen 25C75. The plots for the

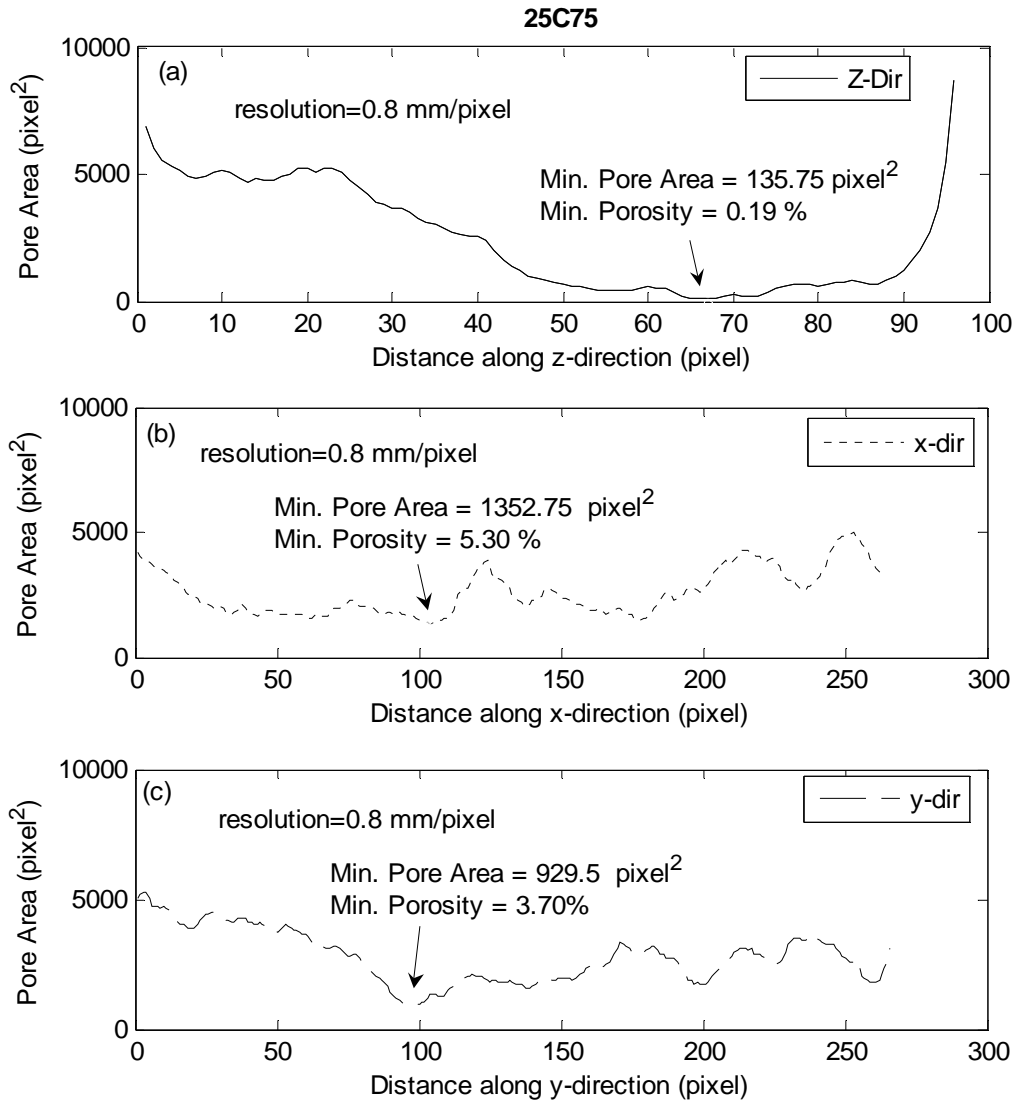


Figure 7.8 Variation in pore cross-sectional area in (a) z-, (b) x- and (c) y-directions in specimen 25C75

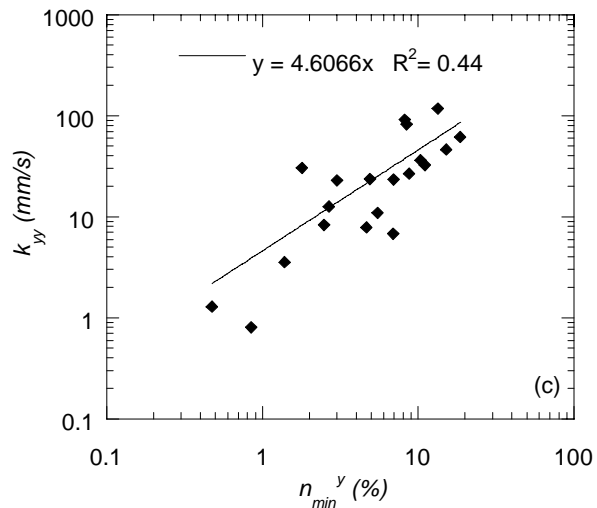
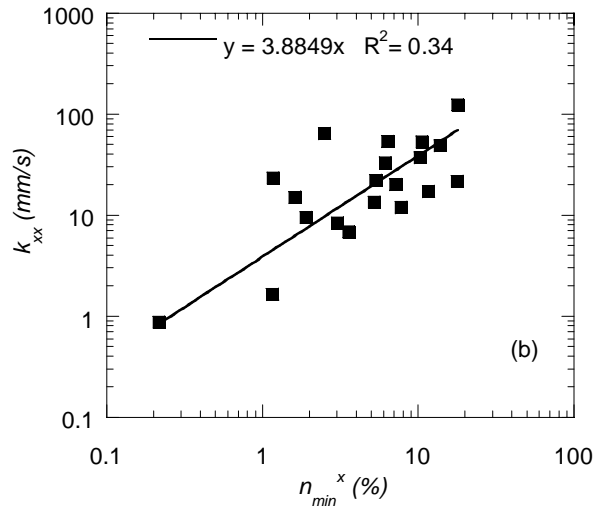
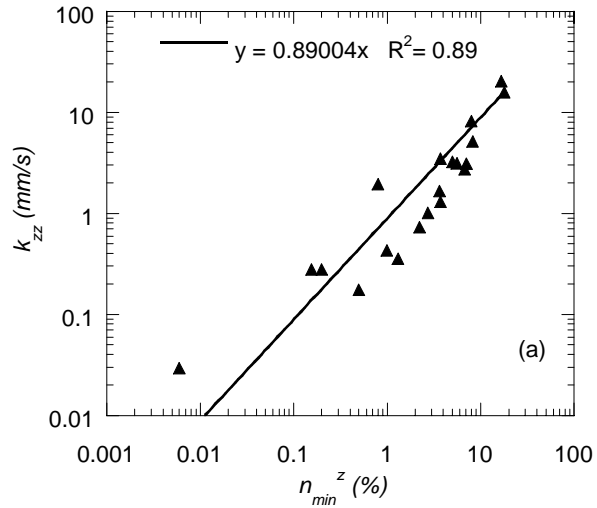


Figure 7.9 The relationship between the minimum porosity and the hydraulic conductivity for three different directions

rest of the specimens can be found in Appendix E. As seen in Figure 7.8a, the minimum PCSA in z -direction is about one order of magnitude less than that of the other directions (Figure 7.8b and 7.8c), which leads to a lower hydraulic conductivity in z -direction.

7.2.3 Effect of Constrictions on the Hydraulic Conductivity Tensor

The findings summarized in the previous subsection indicated that the constrictions (i.e., low PCSA) in the direction of flow have a profound effect on the hydraulic conductivity. In order to further investigate the effect of constrictions on the flow, minimum porosity on the plane perpendicular to the direction of applied pressure gradient are plotted in Figure 7.9 against the hydraulic conductivity in the same direction. The minimum porosity herein corresponds to the ratio of minimum PCSA to the total cross sectional area of the specimen. Figure 7.9 shows that the relationship between the minimum porosity and hydraulic conductivity varies in different directions. Relatively good relationship was observed (with an R^2 of 0.89) when the minimum porosity in z -direction (n_{\min}^z) was plotted against the hydraulic conductivity in the same direction (Figure 7.9a). However, the degrees of correlation between the horizontal hydraulic conductivities (i.e., k_{xx} and k_{yy}) and the minimum porosities in the two horizontal directions (i.e., n_{\min}^x and n_{\min}^y) were much lower ($R^2=0.34$ and 0.44 in x - and y -directions, respectively). This phenomenon was attributed to the differences in the pore structure variation in different directions, as shown in Figure 7.8. Figure 7.8 indicates that there is only one location where the PCSA is minimal in z -direction (at a depth of 66 pixels). The constriction controlling the hydraulic conductivity in that direction most likely located at this location. However, in x - and y - directions (Figures 7.8b and 7.8c), low PCSAs can be seen at different locations (e.g., at 50, 100 and 180 pixels in x -direction and at 100, 200

and 260 pixels in y-direction) where different constrictions might be located. Therefore, it is difficult to relate the hydraulic conductivity in x- and y-directions to only one variable.

7.2.4 The Relationship between the Normal and Shear Components of the Hydraulic Conductivity Tensor

Physical meaning of the hydraulic conductivity of a porous medium is that it relates the pore water pressure gradient to the resulting fluid velocity in the voids. For example, Eq. 7.11 simply implies that k_{zz} (herein called “normal component” in z -direction) is a ratio of the average velocity to the applied pressure gradient in z -direction. Similarly, the “shear components” (i.e., k_{xz} and k_{yz}) of the hydraulic conductivity tensor in z -direction relate the pressure gradient in z -direction to the velocities in other directions (Figure 7.10).

Figure 7.11 shows three field cases where components of the hydraulic conductivity tensor can be used to calculate the fluid velocities. Case-1 illustrates a pavement laying on a flat surface. In this case, the flow can be triggered by a rain event creating a pressure gradient in z -direction. The velocities in different directions can easily be computed by using only three components of the hydraulic conductivity tensor. Case-2 illustrates a pavement on a slope. In this case, the pressure gradients are present in two directions; therefore, six components of the hydraulic conductivity tensor are needed to calculate the fluid velocities. Case-3 illustrates a pavement on a curvature and going downhill, which could create pressure gradients in all three directions. In this case, all nine components of the hydraulic conductivity tensor are needed to compute the velocities. These three cases illustrates the significance of the components of the

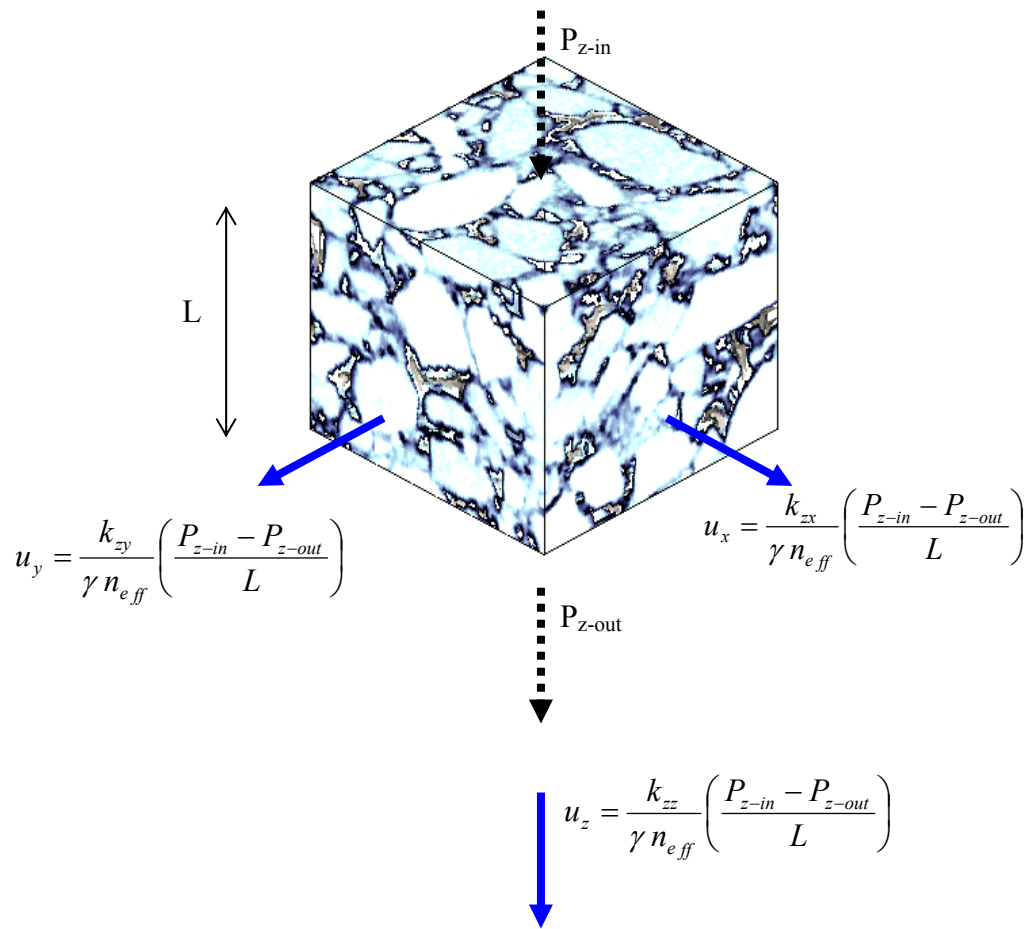
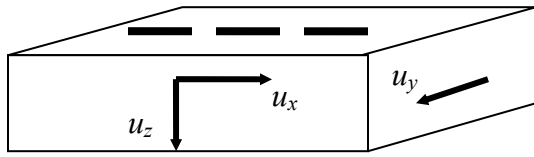


Figure 7.10 Illustration of physical meaning of the hydraulic conductivity tensor components.



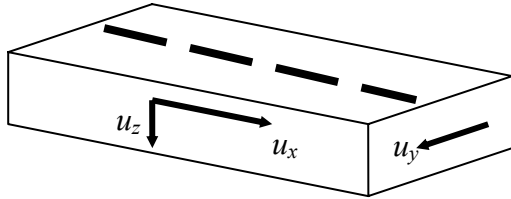
$$\nabla P_z > 0, \nabla P_x = 0, \nabla P_y = 0$$

$$u_x = -k_{xz} \nabla P_z / \gamma n_{eff}$$

$$u_y = -k_{yz} \nabla P_z / \gamma n_{eff}$$

$$u_z = -k_{zz} \nabla P_z / \gamma n_{eff}$$

Case-1: Gravity



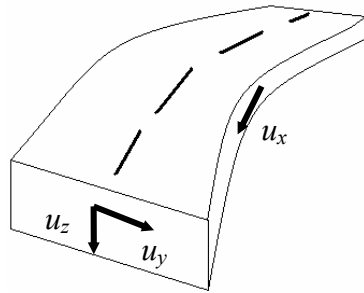
$$\nabla P_z > 0, \nabla P_x > 0, \nabla P_y = 0$$

$$u_x = -(k_{xx} \nabla P_x + k_{xz} \nabla P_z) / \gamma n_{eff}$$

$$u_y = -(k_{yx} \nabla P_x + k_{yz} \nabla P_z) / \gamma n_{eff}$$

$$u_z = -(k_{zx} \nabla P_x + k_{zz} \nabla P_z) / \gamma n_{eff}$$

Case-2: Gravity and slope



$$\nabla P_z > 0, \nabla P_x > 0, \nabla P_y > 0$$

$$u_x = -(k_{xx} \nabla P_x + k_{xy} \nabla P_y + k_{xz} \nabla P_z) / \gamma n_{eff}$$

$$u_y = -(k_{yx} \nabla P_x + k_{yy} \nabla P_y + k_{yz} \nabla P_z) / \gamma n_{eff}$$

$$u_z = -(k_{zx} \nabla P_x + k_{zy} \nabla P_y + k_{zz} \nabla P_z) / \gamma n_{eff}$$

Case-3: Gravity, slope and curve

Figure 7.11 Three different cases where the components of the hydraulic conductivity tensor are used in engineering design.

hydraulic conductivity tensor to calculate the fluid velocities in the pore structure of asphalt pavements.

Figure 7.12 shows the relationship between the normal and shear components of the hydraulic conductivity tensor in three different directions. In all three directions, the shear components (e.g., k_{xz} and k_{yz} for z -direction) of the hydraulic conductivity is one to three orders of magnitude lower than the normal components (e.g. k_{zz} for z -direction), however, the range of the difference varies for different directions. For example, in z -direction (Figure 7.12a) the data are closer to the line of equality than x - and y -directions, which indicates that the difference between the normal and shear components are less in z -direction. The shear components are generally expected to be significantly lower than the normal components, as the flow is forced in the direction of applied pressure gradient. However, in z -direction, the normal component was relatively close to shear components. This was attributed to the fact that, as a pressure gradient was applied in z -direction (e.g., Case-1 in Figure 7.11), the constrictions in that direction blocks the flow and forces fluid to move towards the other two directions (i.e., x and y), leading to relatively higher k_{xz} and k_{yz} . Therefore, it can be concluded that, for a pavement shown in Case-1 of Figure 7.11, flow velocities in x - and y -directions could be close to the velocity in z -direction, for given a pressure gradient applied in z -direction. This phenomenon was further supported by the shear components of the hydraulic conductivity in x - and y -directions. Figures 7.12b and 7.12c show that the shear components pointing z -direction (i.e. k_{zx} and k_{zy}) are in general lower than the shear components pointing other directions (i.e. k_{yx} and k_{xy}), indicating that flow is prevented in z -direction and diverted towards the other directions.

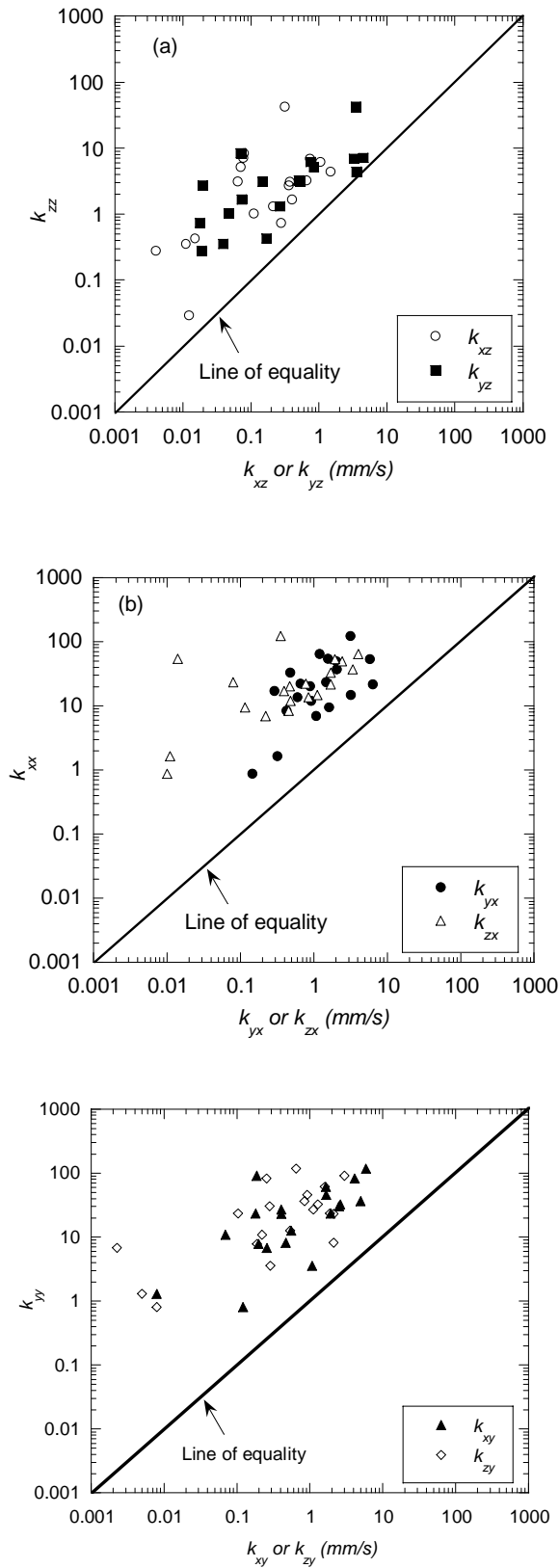


Figure 7.12 The relationship between the normal and shear components of the hydraulic conductivity tensor.

7.3 CHANGE IN HYDRAULIC CONDUCTIVITY WITH DEPTH

It may be imperative to know the variation of the hydraulic conductivity at different depths within asphalt pavements to predict the possible flow directions during a rain event. This would aid in estimation of depth of water penetration and in turn characterization of the vulnerability of different zones within the asphalt layer to the moisture damage. In order to investigate the hydraulic conductivity at different depths, the specimens were divided into four layers; top-10mm, top-20 mm, top 40 mm and the entire depth, as shown in Figure 7.13. It should be noted that all these layers are specified such that the depth of water penetration from the surface of the pavement could be characterized. They do not simulate a laboratory process where the specimens are cut into multiple layers and the hydraulic conductivity of each layer is tested independently. In such a process, each layer would exhibit different hydraulic conductivity values, as the pore connectivity of each layer may be different than that of the layers specified in Figure 7.13. Therefore, care should be taken while interpreting the hydraulic conductivity of the layers specified in Figure 7.13.

More than 100 LB fluid flow simulations were performed to compute the hydraulic conductivity of each layer of different specimens. The resulting hydraulic conductivities (k_{zz}) were plotted versus depth in Figures 7.14 and 7.15. A rapid decrease in the hydraulic conductivity was observed in most of the specimens. In most of the specimens shown in Figure 7.14a, the decrease was one order of magnitude when the analysis depth was doubled (e.g., k_{zz}^{10} versus k_{zz}^{20}). Figures 7.14 and 7.15 also show the effect of compaction effort on the change in the hydraulic conductivity with depth. The specimens compacted at higher compaction effort (i.e. higher number of gyrations) generally exhibited a more

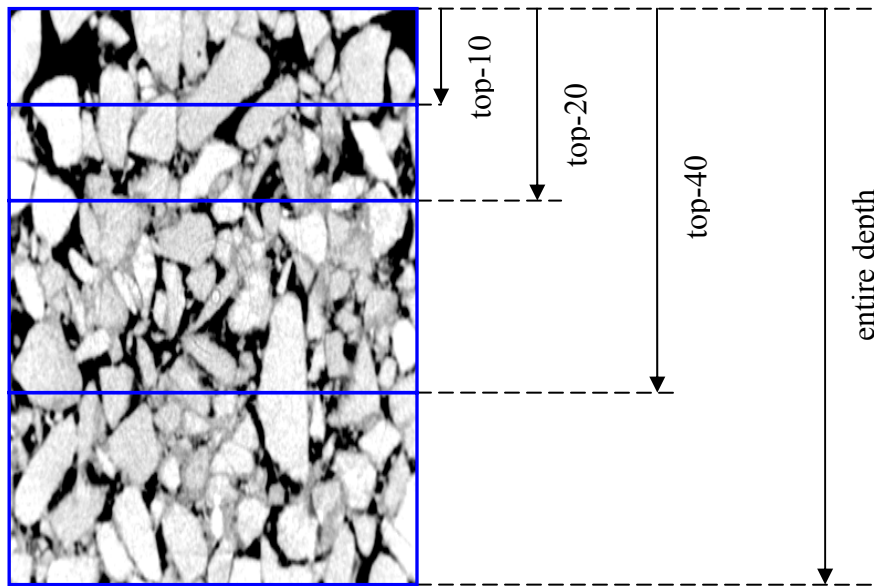


Figure 7.13 Imaginary sectioning of an asphalt specimen for analysis of hydraulic conductivity throughout the depths.

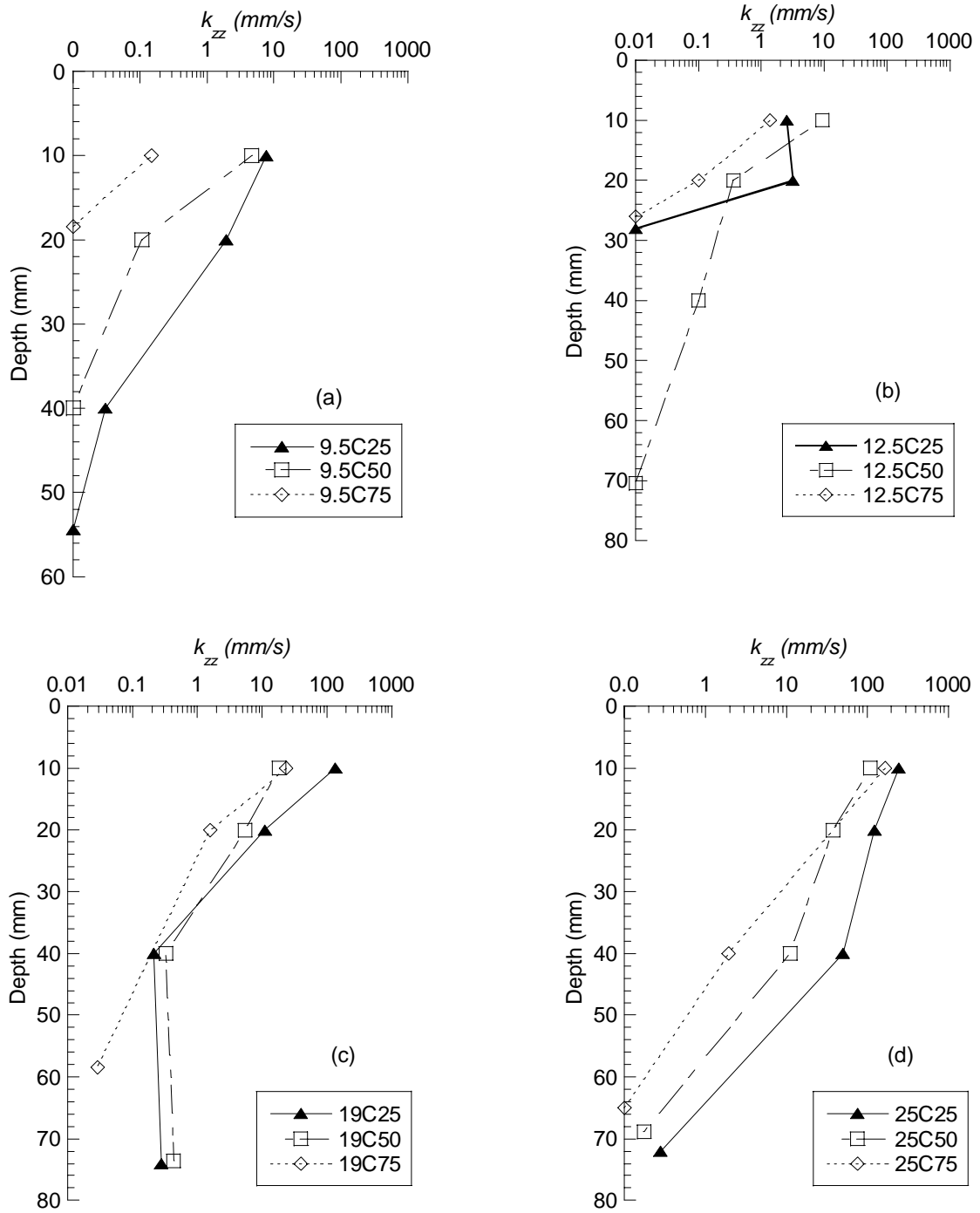


Figure 7.14 The variation of hydraulic conductivity with depth in z - direction for specimens with NMAs of (a) 9.5 mm, (b) 12.5 mm, (c) 19mm and (d) 25mm.

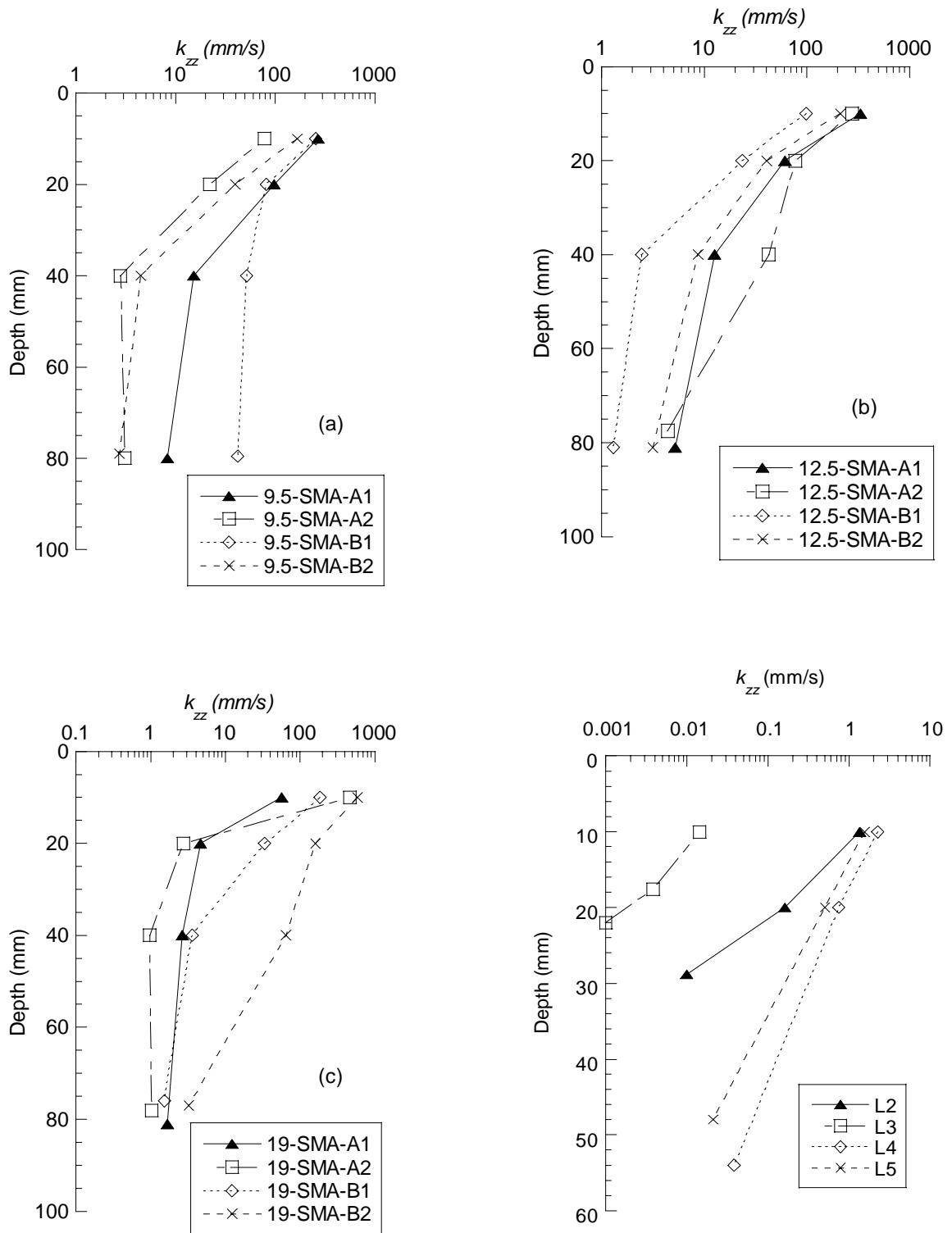


Figure 7.15 The variation of hydraulic conductivity with depth in z - direction for the SMA specimens with NMAs of (a) 9.5 mm, (b) 25 mm, (c) 19 mm and (d) field cores.

rapid decrease in hydraulic conductivity than those prepared with lower compaction effort (e.g. 9.5C75 versus 9.5C25). It can be concluded that increasing the compaction effort in the field can significantly reduce the depth to which the water can penetrate, thus limit the possible moisture damage only to the surface of the pavement. For example, in Figure 7.14a, the maximum depth that water can penetrate in specimen 9.5C75 (compacted with 75 gyrations) was approximately 19 mm; whereas, this value was about 55 mm for 9.5C25.

7.4 PORE WATER PRESSURE AND SHEAR STRESS VARIATIONS AT THE PORE-SOLID INTERFACE

7.4.1 Pore Pressure Variation

It should be noted that fluid flow in a porous structure is usually caused by a pressure difference (i.e. pressure gradient) applied between its two opposite boundaries. For a specimen with a homogeneous and isotropic pore structure (e.g. uniformly packed glass beads), the pressure decrease from one end to the other end is linear, as illustrated with a dashed line in Figure 7.16a. On the other hand, the pressure decrease curve is usually nonlinear in the case of asphalt specimens. In order to illustrate the observed phenomena, the trends for 9.5C50 are given in Figure 7.16a as an example. Pore water pressure stays relatively constant within the upper 45mm portion of the specimen. A sharp decrease in pressure was observed between 45 and 65mm, which was followed by a nearly constant pressure for the remaining depths.

In order to quantify the decrease in pressure throughout a direction, a local pressure gradient (slope of the pressure decrease line) was computed as follows:

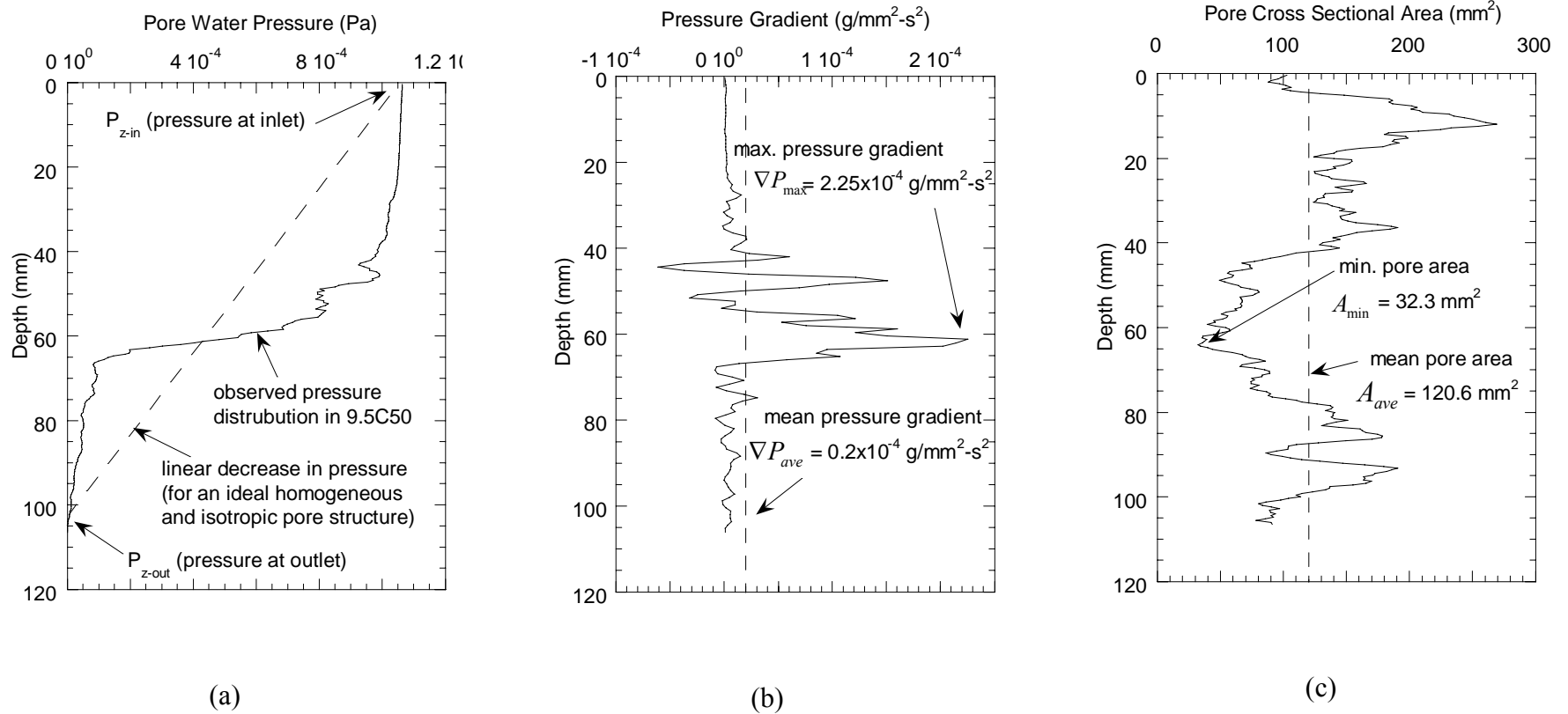


Figure 7.16 Variation of (a) pore water pressure, (b) pressure gradient and (c) porosity with depth for specimen 9.5C50

$$\nabla \bar{P}_i = -\frac{\bar{P}_{i+1} - \bar{P}_{i-1}}{2\Delta l} \quad (7.19)$$

where $\nabla \bar{P}_i$ is the local pressure gradient within the i^{th} slice, Δl is the slice thickness \bar{P}_{i-1} and \bar{P}_{i+1} are the mean pressure values of previous and next slices, respectively. Figure 7.16b shows the local pressure gradient variation within 9.5C50. In the previous sections, it was shown that the existence of pore constrictions in the direction of flow has a profound effect on the flow regime. Similarly, the constrictions also affected the variation of the local pressure gradient. The pore cross sectional area variation of specimen 9.5C50 is plotted in Figure 7.16c, which shows a constriction zone about 60 mm depth. At this depth, the local pressure gradient (Figure 7.16b) was much higher than the gradient at other depths as well as the overall average pressure gradient within the entire specimen. Considering the conservation of mass and momentum principles, high pressure gradient is meaningful at constrictions. For example, when fluid particles are forced to pass through a constriction where the area available for moving fluid particles decreases significantly, the velocities must be very high to conserve the mass and momentum between the inlet (large area) and outlet (small area) of the constriction (which looks like a funnel shape). These high velocities can only be created by large pressure gradients at this zone.

In order to further investigate the relation between the constriction zone and the local pressure gradient, two ratios were defined; (1) pressure gradient ratio (∇P_r) and (2) area ratio (A_r):

$$\nabla P_r = \frac{\nabla P_{\max}}{\nabla P_{\text{ave}}} \quad (7.20)$$

$$A_r = \frac{A_{\text{ave}}}{A_{\min}} \quad (7.21)$$

where A_{ave} and A_{\min} are the average and minimum pore cross sectional areas, respectively, and ∇P_{\max} and ∇P_{ave} are the maximum and average pressure gradients, respectively (see Figures 7.16b and 7.16c).

Figure 7.16 shows the pressure gradient ratio versus area ratio relationship of all asphalt specimens. It can clearly be seen from the Figure 7.17a that the pressure gradient ratio generally increases with increasing area ratio. Such a trend was expected since the area ratio increases when the gap between the average and the minimum pore cross sectional area increases. This large gap can cause large pressure differences, thus large local pressure gradients. Furthermore, a linear curve best fit to the observed data produced an R^2 of 0.68 (Figure 7.17b).

Figure 7.17 also shows that in most of the specimens, the pressure gradient ratio was between 1.2 and 5, indicating that the maximum pressure gradients in most of the specimens were 1.2 to 5 times higher than the average pressure gradient. However, pressure gradient ratios up to 15 are also visible where the maximum pressure gradient is more than one order of magnitude higher than the overall average pressure gradient.

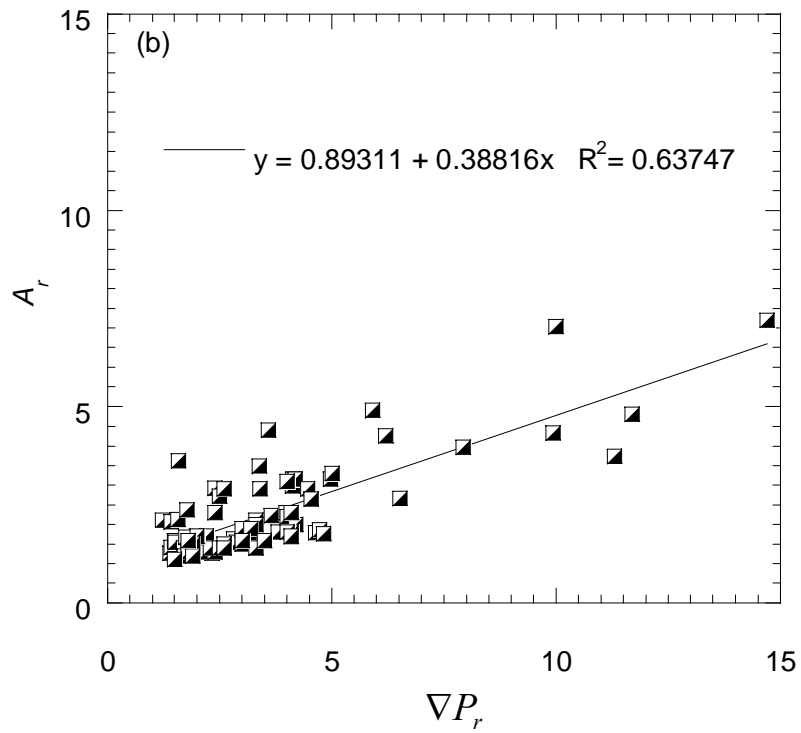
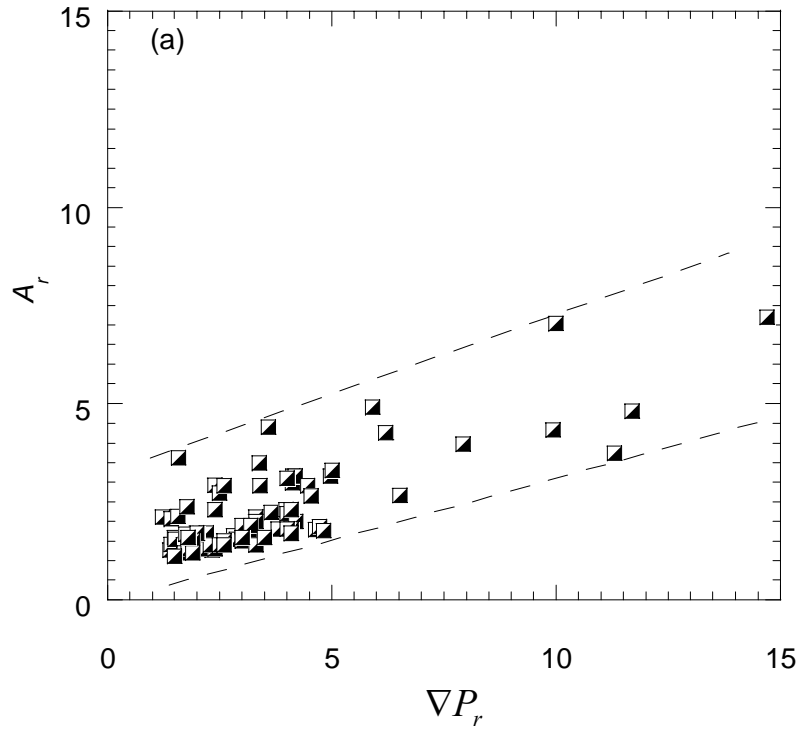


Figure 7.17 (a) Pressure gradient ratio versus area ratio relationship, and (b) best fit to the observed data.

7.4.2 Shear Stress Variation

Large local pressure gradients at the constriction zones can cause the fluid to move much faster. High velocities at these zones directly affect the magnitude of the force acting on the pore-solid interface, which is directly related to the magnitude of the velocity gradient. The following equation defines the fluid force acting on a surface (Panton, 1996):

$$R_i = \eta_i T_{ij} \quad (7.22)$$

where R_i is the surface force per unit area, η_i is the unit normal vector of the surface and T_{ij} is the stress tensor. The physical meaning of the stress tensor is that a component of the stress tensor T_{ij} is equal to the stress in direction j on a plane with a unit normal vector in direction i . Eq. 7.22 is given in index notation and a more explicit form can be rewritten as follows:

$$\begin{bmatrix} R_x \\ R_y \\ R_z \end{bmatrix} = \begin{bmatrix} \eta_x & \eta_y & \eta_z \end{bmatrix} \begin{bmatrix} T_{xx} & T_{xy} & T_{xz} \\ T_{yx} & T_{yy} & T_{yz} \\ T_{zx} & T_{zy} & T_{zz} \end{bmatrix} \quad (7.23)$$

Eq. 7.23 implies that the force acting on a surface can simply be calculated by multiplying the stress tensor with the unit normal vector of a surface. In the current study, the unit normal vectors of each voxel surface in 3D images of asphalt specimens were orthogonal to each other, which facilitated the computations. For example, for a given

plane with unit normal $\eta_i = [1, 0, 0]$ (Figure 7.18), the components of the surface force can be calculated as follows:

$$R_j = 1T_{xj} + 0T_{yj} + 0T_{zj}$$

then the surface force components become:

$$R_x = T_{xx} \quad R_y = T_{xy} \quad R_z = T_{xz} \quad (7.24)$$

Figure 7.18 also presents the surface force components acting on different faces of a cubical voxel. It can clearly be seen from the Figure 7.18 that surface force components acting in shear are actually the shear components of the stress tensor (i.e., T_{ij} with $i \neq j$), which indicates that these components can directly be used for computing shear stresses.

The stress tensor can be decomposed into two parts: pressure term and viscous term (Panton, 1996):

$$T_{ij} = -P\delta_{ij} + \tau_{ij} \quad (7.25)$$

where δ_{ij} is called Kronecker delta (i.e. $\delta_{ij}=1$ when $i=j$, $\delta_{ij}=0$ when $i \neq j$), P is the pore water pressure and τ_{ij} is the viscous stress tensor. The matrix form of Eq. 7.25 can be written as:

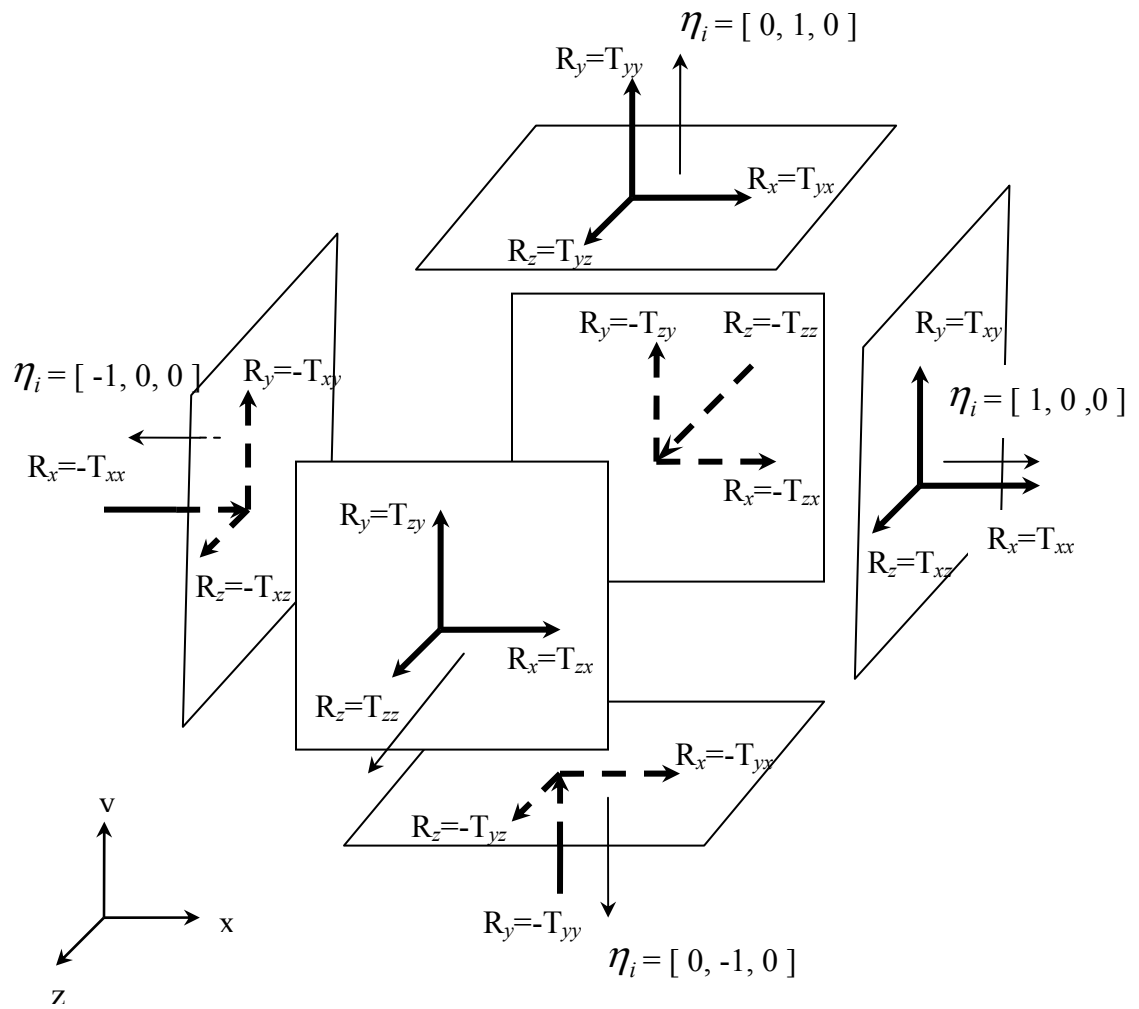


Figure 7.18 The components of a surface force acting on different faces of a cubical voxel

$$\begin{bmatrix} T_{xx} & T_{xy} & T_{xz} \\ T_{yx} & T_{yy} & T_{yz} \\ T_{zx} & T_{zy} & T_{zz} \end{bmatrix} = -P \begin{bmatrix} 1 & 0 & 0 \\ 0 & 1 & 0 \\ 0 & 0 & 1 \end{bmatrix} + \begin{bmatrix} \tau_{xx} & \tau_{xy} & \tau_{xz} \\ \tau_{yx} & \tau_{yy} & \tau_{yz} \\ \tau_{zx} & \tau_{zy} & \tau_{zz} \end{bmatrix} \quad (7.26)$$

The pressure term in Eq. 7.25 ($P\delta_{ij}$) is directly linked to the pore water pressure, whereas, the viscous term (τ_{ij}) is caused by the viscous fluid movement. The pressure term does not have a direct influence on the shear components of the stress tensor. Therefore:

$$T_{ij} = \tau_{ij} \quad \text{when } i \neq j \quad (7.27)$$

The viscous stress tensor components were computed using following formulas (Panton, 1996):

$$\tau_{xy} = \tau_{yx} = \mu \left(\frac{\partial u_x}{\partial y} + \frac{\partial u_y}{\partial x} \right) \quad (7.28)$$

$$\tau_{yz} = \tau_{zy} = \mu \left(\frac{\partial u_y}{\partial z} + \frac{\partial u_z}{\partial y} \right) \quad (7.29)$$

$$\tau_{zx} = \tau_{xz} = \mu \left(\frac{\partial u_z}{\partial x} + \frac{\partial u_x}{\partial z} \right) \quad (7.30)$$

where μ is the kinematic viscosity of the fluid. The partial differentiations in Eqs. 7.28-7.30 were computed numerically at the end of LB simulations. Figures 7.19 and 7.20 shows the shear stress components computed at the lattice nodes. The color code

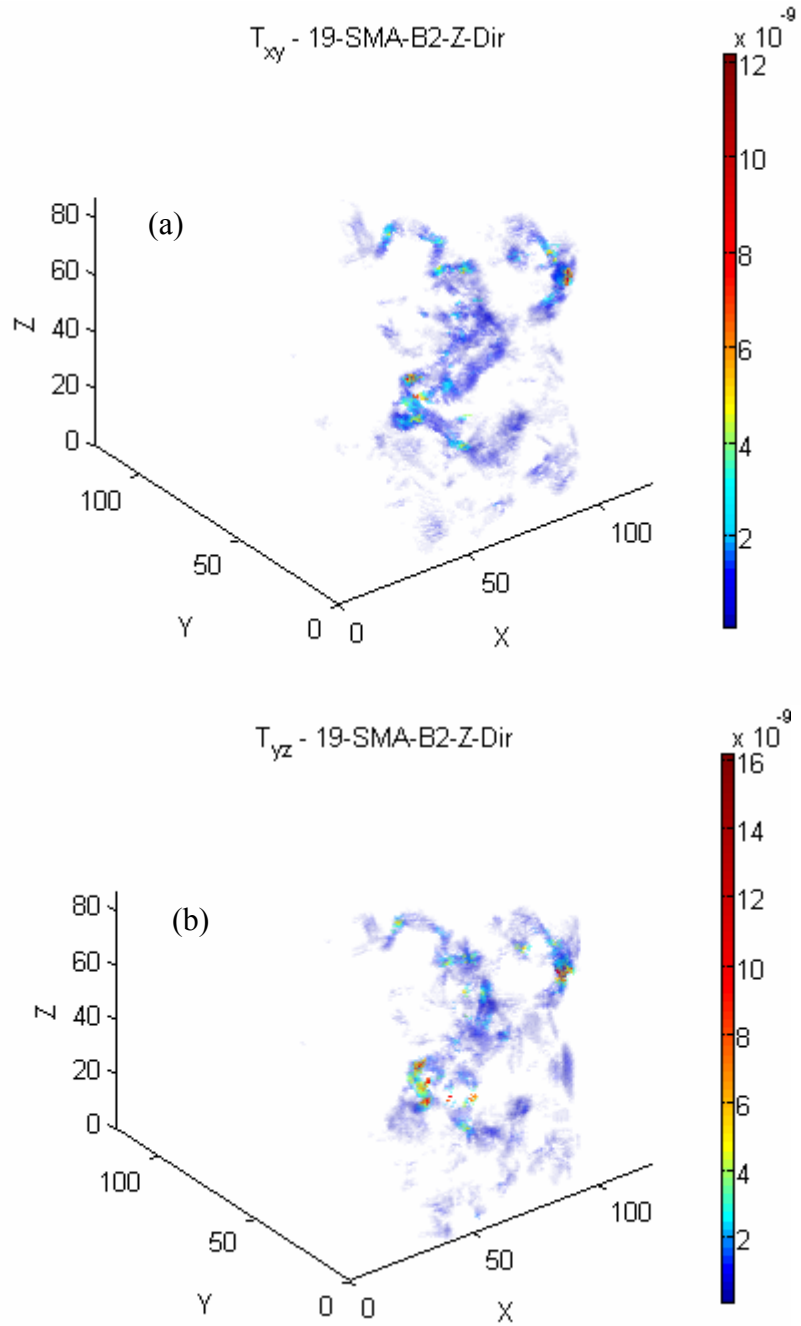


Figure 7.19 Viscous stress tensor components: (a) $\tau_{zx} = \tau_{xz}$, and (b) $\tau_{yz} = \tau_{zy}$. Dimensions on axes are in pixels and pixel resolution is 0.8 mm/pixel.

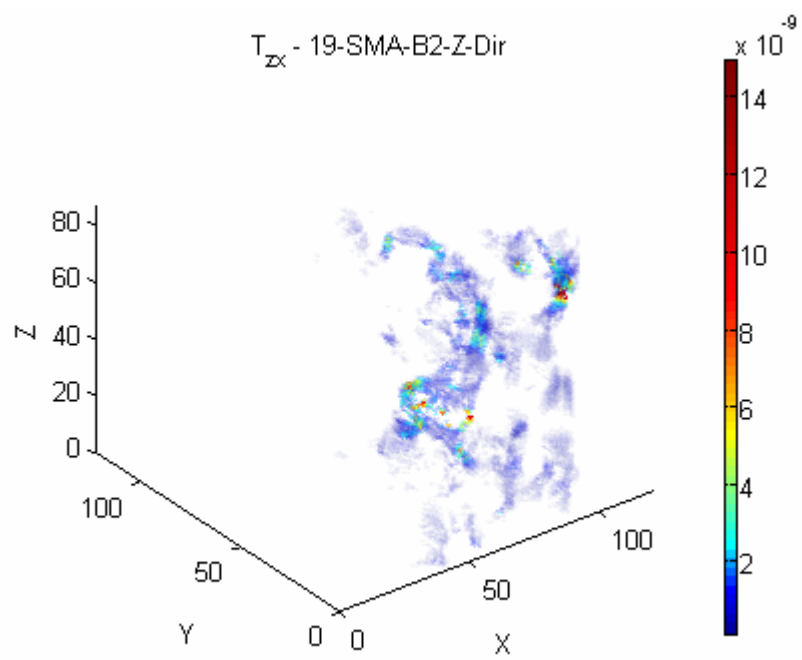


Figure 7.20 Viscous stress tensor components: $\tau_{xy} = \tau_{yx}$. Dimensions on axes are in pixels and pixel resolution is 0.8mm/pixel.

represents the magnitude, whereas, x , y and z axes indicates the spatial location of the pore. The zones of high shear stresses, thus the possible location of binder stripping, are clearly visible in the Figures 7.19 and 7.20 for specimen 19SMA-B2.

In order to study the variation of the shear stresses throughout the specimen, mean value of shear stress tensor components at each depth were computed and plotted versus the depth. An example plot for 9.5C50 is given in Figure 7.21. At a depth of about 60 mm, all three components of shear stress tensor exhibited a jump. It was evident from Figure 7.15c that the pore cross sectional area is lowest at this depth. This is meaningful since at this zone the pressure gradient is highest (Figure 7.15b) leading to high velocities, thus shear stresses. Similar observations were made in all asphalt specimens. The variation of shear stress tensor components with depth is provided for all specimens in Appendix G.

Similar to the ratio defined in previous section for the pressure gradient (i.e. ∇P_r), shear stress ratios were defined to investigate the effect of minimum pore area on shear stress components:

$$T_{xy}^r = \frac{T_{xy}^{\max}}{T_{xy}^{\text{ave}}} \quad (7.31)$$

$$T_{yz}^r = \frac{T_{yz}^{\max}}{T_{yz}^{\text{ave}}} \quad (7.32)$$

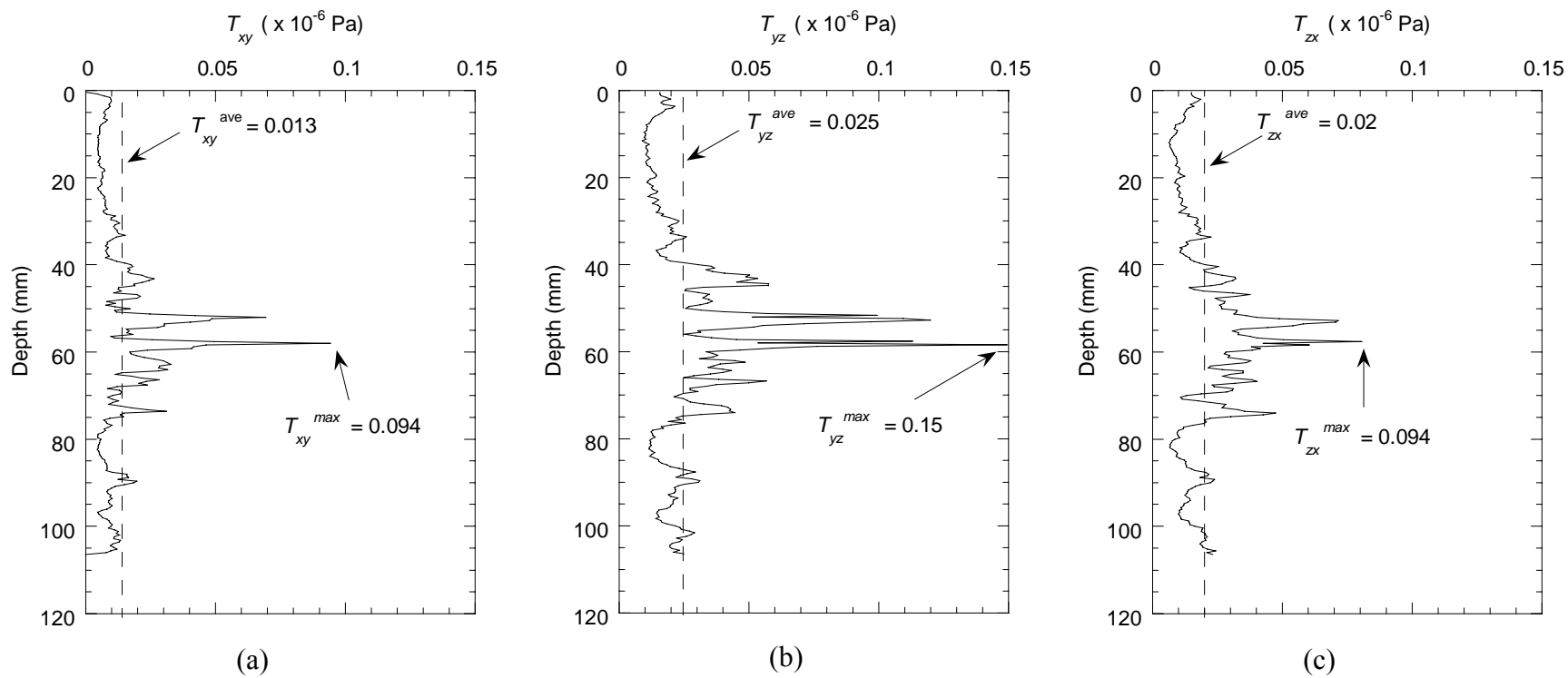


Figure 7.21 Shear stress tensor components: (a) T_{xy} , (b) T_{yz} , and (c) T_{zx}

$$T_{zx}^r = \frac{T_{zx}^{\max}}{T_{zx}^{\text{ave}}} \quad (7.33)$$

where T_{ij}^r is the shear stress ratio, T_{ij}^{\max} and T_{ij}^{ave} are the maximum and average values of shear stress components, respectively (see Figure 7.21). The shear stress ratios were plotted against the area ratio (A_r) in Figures 7.22 and 7.23. The figures suggest that a linear relationship exists between the shear stress ratios and the area ratio. The R^2 ranged from 0.70 to 0.87 for the best fit curves. It can also be seen from the figures that the stress ratios in the direction of applied pressure gradient (i.e. T_{yz}^r and T_{zx}^r) are better correlated with the area ratio.

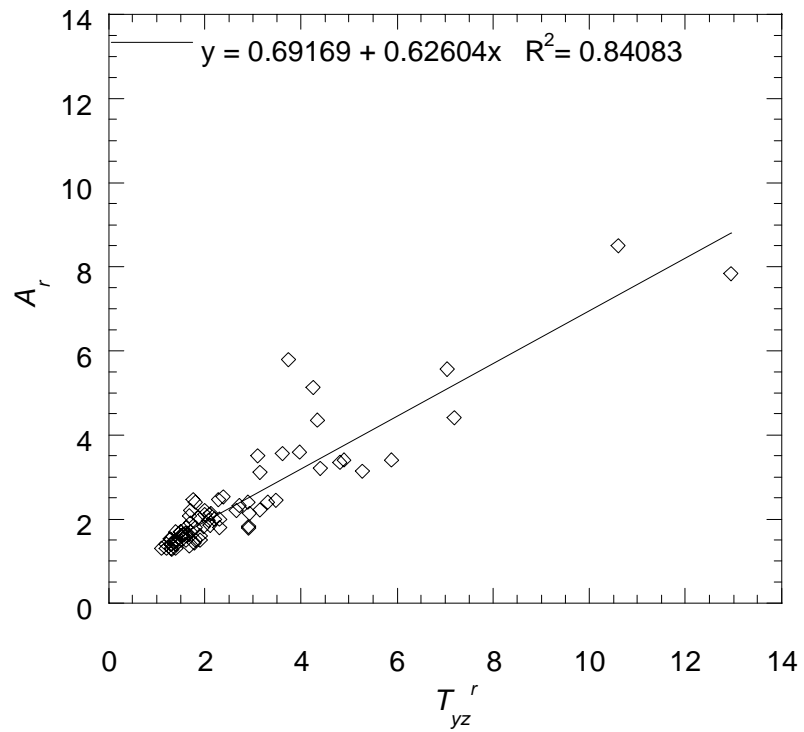
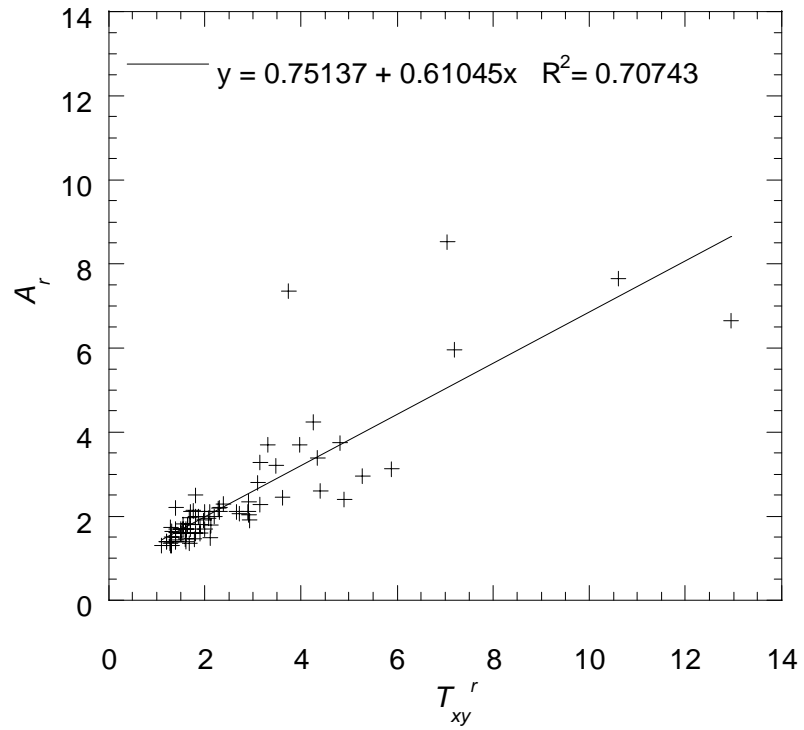


Figure 7.22 Shear stress ratios T_{xy}^r and T_{yz}^r versus area ratio relationship.

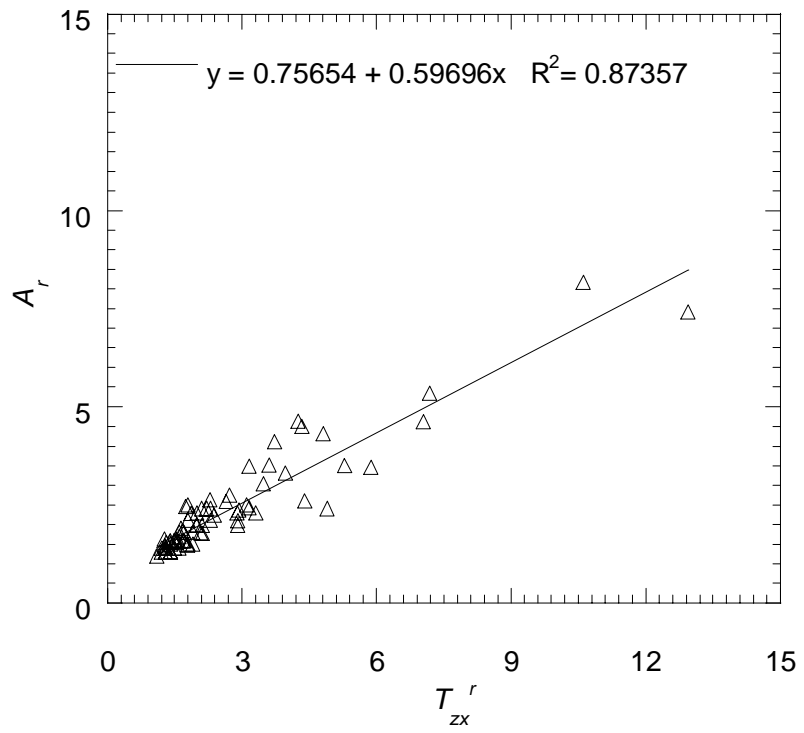


Figure 7.23 Shear stress ratio T_{zx}^r versus area ratio relationship.

CHAPTER 8 DYNAMIC FLOW SIMULATIONS IN ASPHALT PAVEMENTS

8.1 VALIDATION OF LB ALGORITHMS FOR DYNAMIC (UNSTEADY) FLOW

The validation of LB algorithms was performed in Chapter 4 for steady flows. In order to investigate the stability and accuracy of developed LB algorithms for unsteady flow conditions, pulsatile flow through a circular tube was simulated and compared with the analytical solution. The analytical solution of the velocity profile in a tube subject to an oscillating pressure gradient of $\nabla P_z = \nabla P_z^a e^{i\omega t}$ is given as (McDonald, 1974);

$$u_z = \frac{\nabla P_z^a R^2}{i \omega \alpha^2} \left[1 - \frac{J_0(\alpha y i^{3/2})}{J_0(\alpha i^{3/2})} \right] e^{i\omega t} \quad (8.34)$$

where u_z is the velocity in z -direction, ∇P_z^a is the amplitude of the oscillating pressure gradient, ω is the angular velocity ($\omega = 2\pi f$, where f = frequency), i is the complex number, R is the radius of the tube, J_0 is the Bessel function of the first kind of order zero, y is the normalized distance to the centerline ($y=r/R$, where r = distance to centerline), t is time and α is the dimensionless Womersley number. Womersley number is a non-dimensional parameter that characterizes the kinematic similarities in an oscillating fluid motion and given as (McDonald, 1974):

$$\alpha = R\sqrt{\omega/\nu} \quad (8.35)$$

where ν is the kinematic viscosity.

The simulations were carried out by applying an oscillating pressure gradient through use of a body force given in Eq. 3.6, and periodic boundary conditions were applied in the z -direction. The amplitude of the oscillating pressure gradient (∇P_z^a) was 10^{-8} g/mm²-s² and the frequency was $1/6$ s⁻¹. A dynamic viscosity of 0.001 g/mm-s was applied to simulate the flow of water. The corresponding Womersley number of the simulated pulsatile flow was 9.72. Twenty lattice nodes were used along the diameter which provided a lattice resolution of 1 mm/pixel.

Figure 8.1 shows the velocity profiles computed for a half cycle using analytical solution (straight lines) as well as the velocities computed after LB simulation (shown with a marker '+'). An excellent fit is clearly visible from Figure 8.1 indicating the validity of the LB method in simulating dynamic flow. It should be noted that a phase lag of 0.1 radians was observed between the applied pressure gradient and velocity.

8.2 DYNAMIC FLOW SIMULATIONS IN ASPHALT PAVEMENTS

8.2.1 Boundary Conditions

Dynamic flow simulations were performed using similar boundary conditions that were applied at steady flow simulations. The boundary conditions at the solid walls and the domain boundaries were identical, which were described in Section 3.3. However, a different approach was used to trigger the flow at the inlet nodes, where a variable momentum influx with a shape of a half-sinusoid was applied. Past research

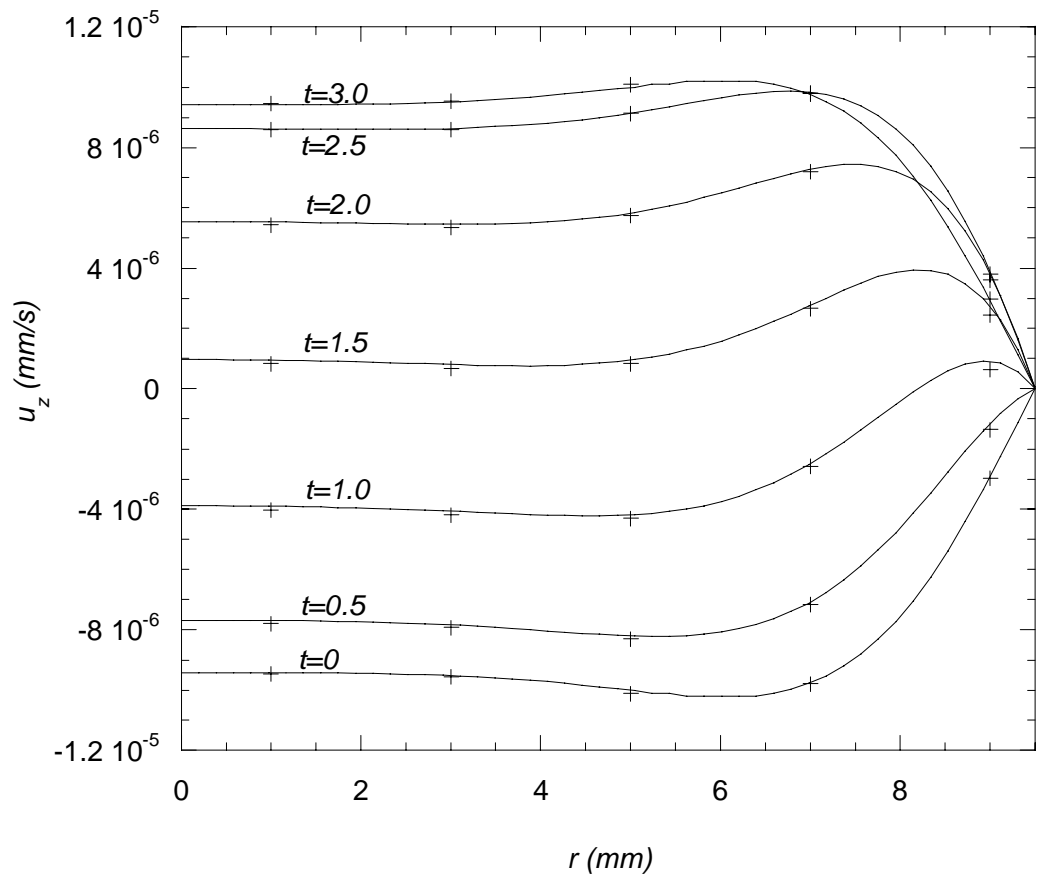


Figure 8.1 Oscillating flow through a circular tube; '+' is the LB simulation, and straight lines are the analytical solution.

(Papagiannakis et al., 1996) showed that the shape of the pressure on the pavement caused by the tire of a moving vehicle was a half-sinus of power six (Figure 8.2). Therefore, the following momentum influx was applied at the inlet:

$$U_{z-in} = U_0 f(t) \quad (8.36)$$

where U_{z-in} is the momentum influx at the inlet nodes, U_0 is the amplitude of the momentum influx and $f(t)$ is a function representing the shape of the pulse and given in Figure 8.2. Figure 8.2 illustrates two half-sinusoidal pulses with a wavelength λ and separated with a rest time of 2λ . The wavelength herein represents the time that tire has a contact with the pavement. In current simulations, the duration of tire contact (λ) was assumed to be 0.5 sec.

At inlet nodes, a momentum in z-direction was prescribed using Eq. 8.36 and the x- and y- direction momentum values were set to zero. Then, the density at the inlet nodes and the unknown components of the distribution function were computed using the relations given in Table 3.3. It should be recalled that these relations were derived based on the assumption that the bounce-back scheme is valid for the non-equilibrium part of the particle distribution function (Zou and He 1997). At outlet nodes, a constant pressure (i.e. density) was prescribed. Initially, velocities of all nodes were set to zero and densities were set to be same as the density prescribed at the outlet nodes. As the cycles of inlet momentum were applied, the density values at each node were computed and the resulting pressure values at each node were calculated using the equation of state (Eq. 3.21).

8.2.2 Calculation of Dynamic Hydraulic Conductivity

Frequency dependent permeability (i.e., $\mathbf{K}^d(\omega)$) of porous media has been studied by several researchers (Sheng and Zhou 1988, Zhou and Sheng 1989 and Duarte et. al. 1992). It was shown that for a given frequency of an oscillating pressure gradient, the permeability of a porous structure exhibits universal behavior and can be defined by the following equation (Sheng and Zhou 1988):

$$\mathbf{u}^d(\omega) = -\frac{1}{\mu} \mathbf{K}^d(\omega) \nabla \mathbf{P}^d(\omega) \quad (8.37)$$

where $\mathbf{u}^d(\omega)$ is the flow velocity averaged over a cycle, $\mathbf{K}^d(\omega)$ is the dynamic permeability, $\nabla \mathbf{P}^d(\omega)$ is the applied dynamic pressure gradient and μ is the dynamic viscosity. Another form of Eq. 8.4 can be written for the dynamic hydraulic conductivity as follows:

$$\mathbf{u}^d(\omega) = -\frac{1}{\gamma n_{eff}} \mathbf{k}^d(\omega) \nabla \mathbf{P}^d(\omega) \quad (8.38)$$

where $\mathbf{k}^d(\omega)$ is the dynamic hydraulic conductivity, γ is the unit weight of the fluid and n_{eff} is the effective porosity. Applying an oscillating pressure gradient in z -direction and keeping the pressure gradients in x - and y - directions equal to zero reveals the following equations for the shear and normal components of the dynamic hydraulic conductivity in z -direction:

$$k_{xz}^d = -\gamma n_{eff} (u_x^d / \nabla P_z^d) \quad (8.39)$$

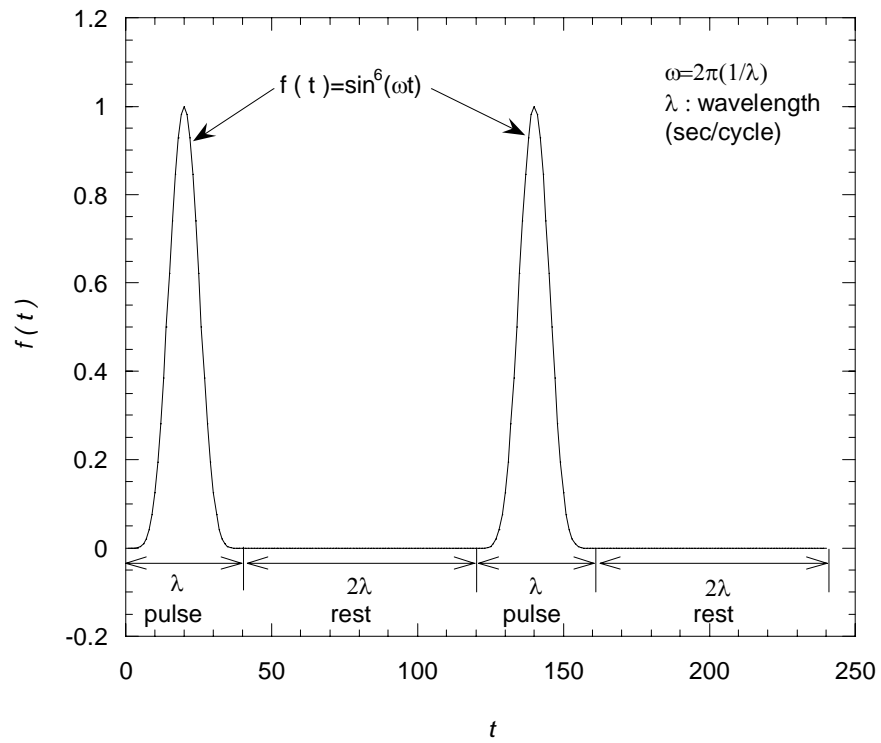


Figure 8.2 The function representing the shape of the momentum influx applied in dynamic LB simulations.

$$k_{yz}^d = -\gamma n_{eff} (u_y^d / \nabla P_z^d) \quad (8.40)$$

$$k_{zz}^d = -\gamma n_{eff} (u_z^d / \nabla P_z^d) \quad (8.41)$$

where ∇P_z^d is the mean pressure gradient and u_x^d , u_y^d , and u_z^d are the mean velocities in x -, y - and z -directions, respectively. The mean pressure gradient used in the dynamic hydraulic conductivity equations (∇P_z^d) was computed by subtracting outlet pressure at the outlet nodes (a pre-set boundary condition) from the inlet pressure observed at the peak of a cycle at the inlet nodes and dividing by the entire length of the specimen. Selection of an appropriate mean velocity was somewhat difficult because there was a phase lag between the applied pulse pressure and the resulting velocity. There were also phase lags (or delays) as the fluid travels through the deeper parts of the specimen, i.e., beginning and the end of cycles at different depths were not necessarily the same as the inlet nodes. Selection of one particular time instant and computing average velocities at each depth was not realistic because the peak average velocities at different depths occurred at different time instances. Therefore, a set of mean velocities occurred at the peak of cycles observed in different depths was computed, and then average of these mean velocities was used in the hydraulic conductivity equation.

8.2.3 Results of Simulations

8.2.3.1 Effect of Amplitude of Pressure Gradient

In order to investigate the universal behavior of dynamic hydraulic conductivity at a given wavelength (i.e., frequency), a set of simulations were performed by keeping the

wavelength constant and varying the amplitude of the pressure gradient. Figure 8.3 shows the change in velocity and dynamic hydraulic conductivity over time steps of the simulations. It is visible that the mean velocity increases sharply as the pressure gradient increased. However, the dynamic hydraulic conductivities collapse on a single curve independent of the applied pressure gradient, confirming its universal behavior. The universal behavior of the dynamic permeability of the porous media was also shown by Sheng and Zhou (1988).

8.2.3.2 *Effect of Wavelength of Pressure Gradient on the Dynamic Hydraulic Conductivity*

It was shown in previous section that the dynamic hydraulic conductivity exhibits universal behavior at a given wavelength independent of the magnitude of the applied pressure gradient. A set simulations was performed at different wavelengths to investigate the effect of wavelengths on the magnitude of the dynamic hydraulic conductivity. Three different asphalt specimens were analyzed at wavelengths ranging from 0.2 sec/cycle to 32 sec/cycle. Corresponding Womersley numbers ranged from 1.3 to 15.5. In order to calculate the Womersley number using Eq. 8.2, a characteristic radius (i.e., R) was needed. This radius was computed using the minimum pore cross sectional area (A_{\min}) as follows:

$$R = \sqrt{A_{\min} / \pi} \quad (8.42)$$

Figure 8.4a shows the variation of dynamic hydraulic conductivity at different wavelengths. It is visible from the figure that the dynamic hydraulic conductivity increases with increasing wavelength. The logarithmic best fit lines produced excellent

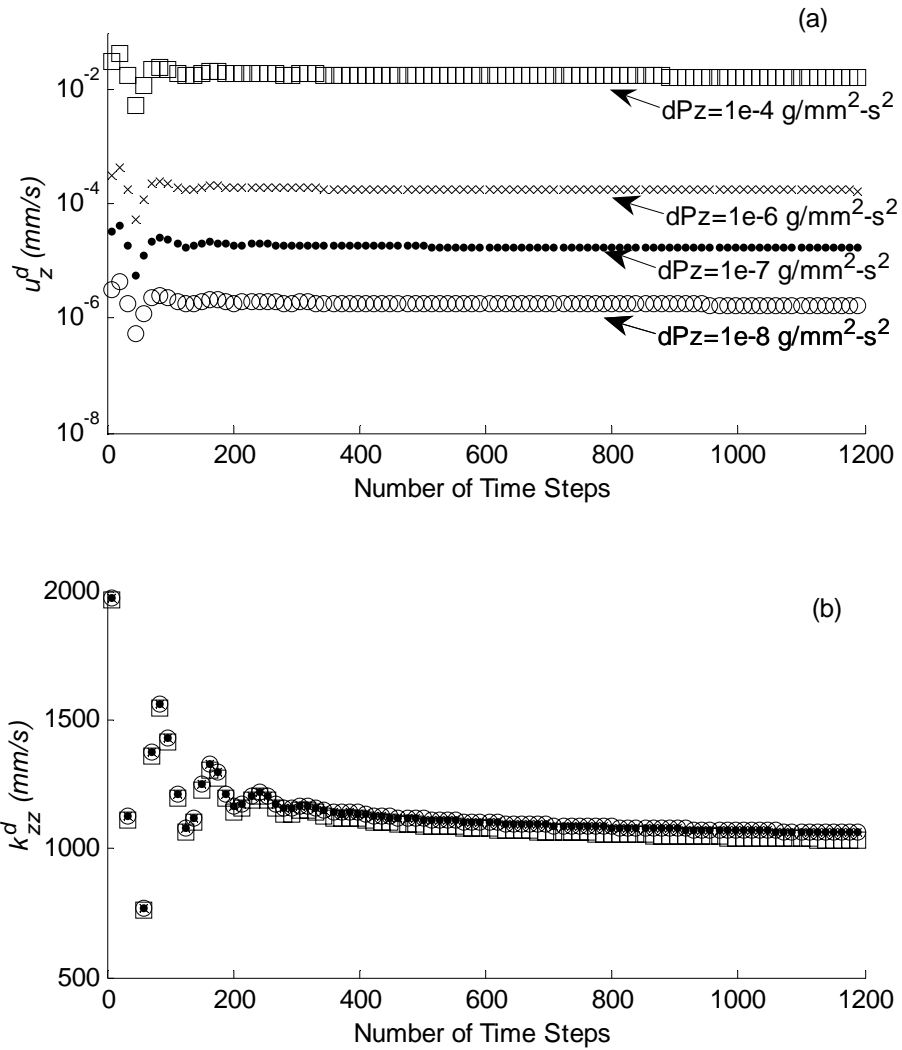


Figure 8.3 (a) Velocities and (b) dynamic hydraulic conductivities computed at different pressure gradient amplitudes.

fits with R^2 ranging from 0.981 to 0.999. Therefore, the hydraulic conductivity of a specimen at any desired wavelength can be computed by using these regression equations. Figure 8.4b shows the relation between the dynamic hydraulic conductivity and the Womersley number, where the hydraulic conductivity decreases with increasing Womersley number. It can be seen from the Eq. 8.2 that the Womersley number is directly related to the angular velocity (ω) which is inversely proportional to the wavelength. Therefore, the Figures 8.4a and 8.4b are identical; however, both of them were shown in here to present the range of wavelengths and Womersley numbers used. The numerical analysis of Sheng and Zhou (1988) on uniformly packed beads also showed a decrease in dynamic permeability with increasing angular velocity (i.e., increasing Womersley number); however, the rate of decrease in dynamic permeability in their analysis was larger than that observed in the current study. Relatively low rate of change of dynamic hydraulic conductivity in asphalt specimens was attributed to their pore structure variation where the porosity decreases with depth. Therefore, the impact of different frequencies of pressure at the inlet could have probably been dissipated at the surface, and relatively less dynamic effects were observed at greater depths within the specimens. As a result, the dynamic hydraulic conductivity of overall specimen was not significantly affected by the change in frequency.

8.2.3.3 Dynamic Hydraulic Conductivities versus (steady) Hydraulic Conductivity Relationship

Figure 8.5 shows the relationship between the dynamic hydraulic conductivities computed from dynamic flow simulations and hydraulic conductivities computed after a steady state flow. The observed trend is that the dynamic hydraulic conductivity increases

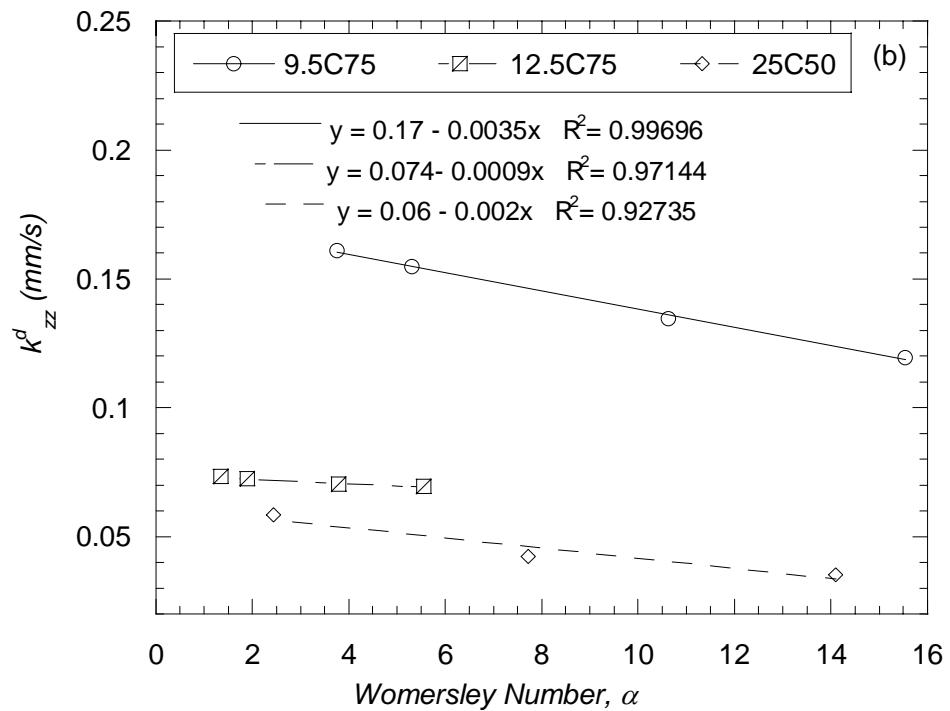
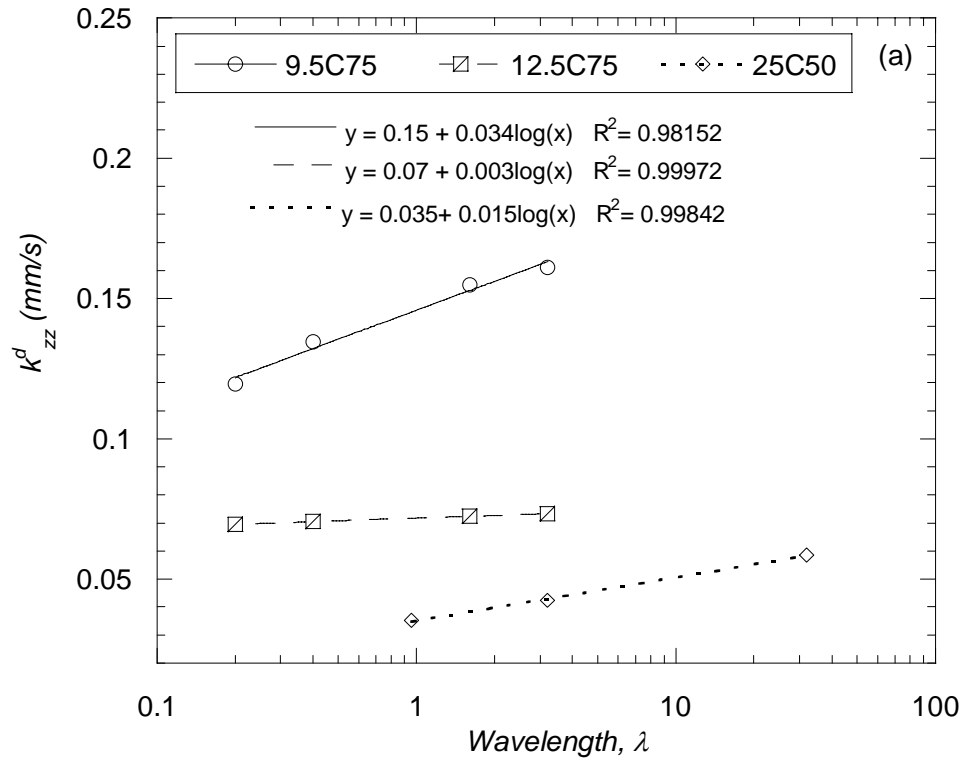


Figure 8.4 Change in dynamic hydraulic conductivity at different (a) wavelengths and (b) Womersley numbers.

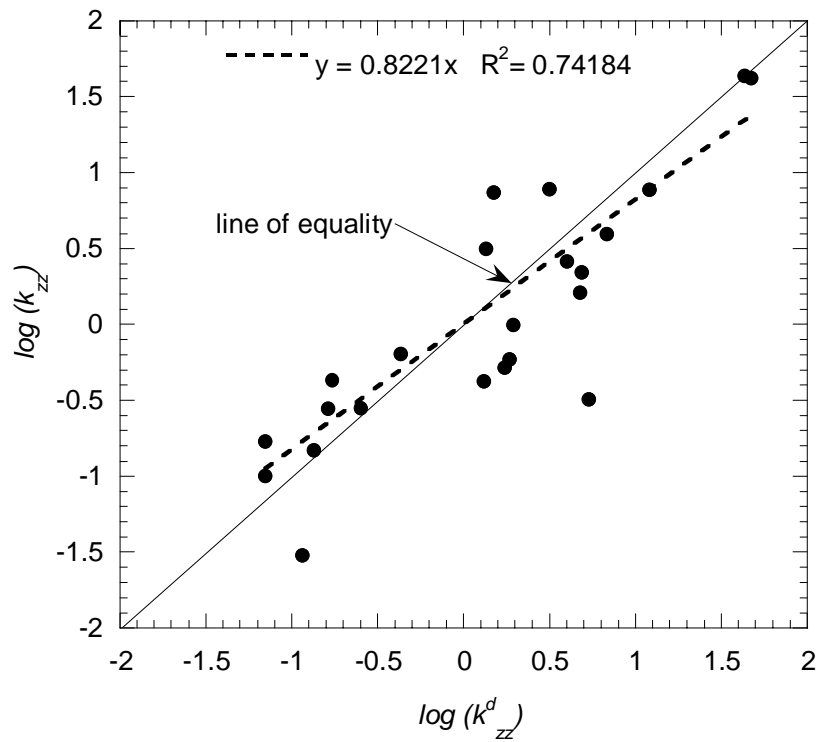
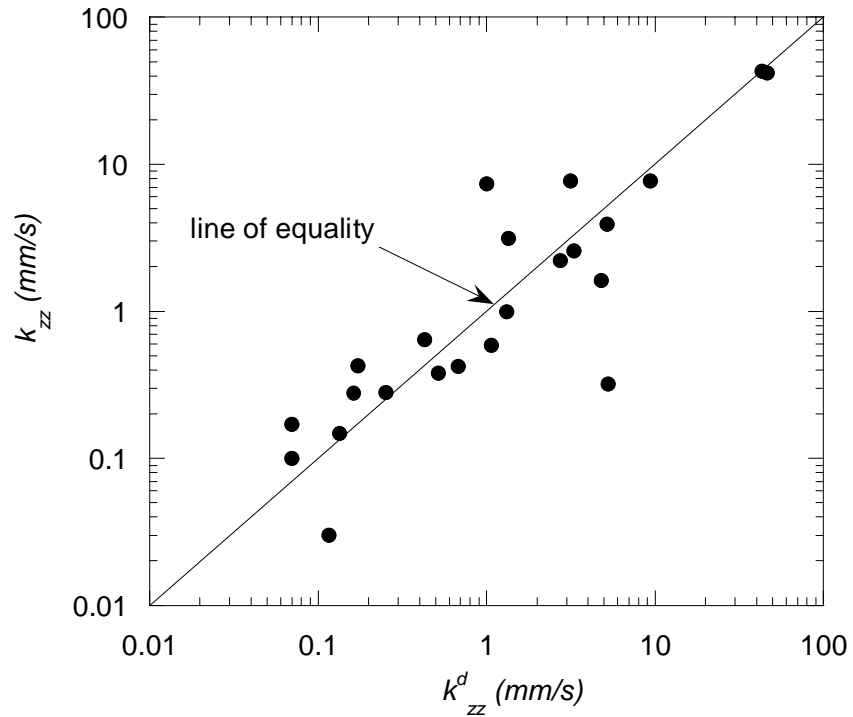


Figure 8.5 Dynamic hydraulic conductivity versus hydraulic conductivity relationship.

with increasing (steady) hydraulic conductivity. The points in the Figure 8.5 scatter around the line of equality indicating that the dynamic and steady hydraulic conductivities are relatively close. However, it may be difficult to quantitatively predict one from the other, as there is a wide variability in the data. Relatively less difference between the dynamic and steady hydraulic conductivities was expected due to the reasons described in the previous subsection, where the dynamic effects are usually confined to the surface of the pavements and less influence was observed on the overall hydraulic conductivity.

8.2.3.4 Comparison of Pressure Gradients in Steady and Dynamic Flow Conditions

In the previous chapter, it was shown that for a constant pressure difference between two ends of a specimen, which provides a steady-state flow, local pressure gradients at the constriction zones were much higher than the overall average pressure gradient. In order to investigate the change in the shape of the pressure gradient during an unsteady flow, the dynamic flow simulations were carried out so that the amplitude of the pressure at the inlet is the same as the inlet pressure applied during the steady flow simulations. The outlet pressures were also set to be equal for dynamic and steady flow cases. Figure 8.6a is given as an example to show the pressure gradient variation in z-direction at the peak of a cycle for specimen 9.5SMA-B2. Figure 8.6a also includes the pressure gradient variation during the steady-state flow in the same specimen. The pressure gradient versus depth relationship for the steady and dynamic flow cases are given in Appendix H for the rest of the specimens. Figure 8.6a indicates that, in general, the pressure gradient curves of dynamic and steady flow conditions are similar in shape. However, the pressure gradient observed in dynamic flow at the surface is higher than

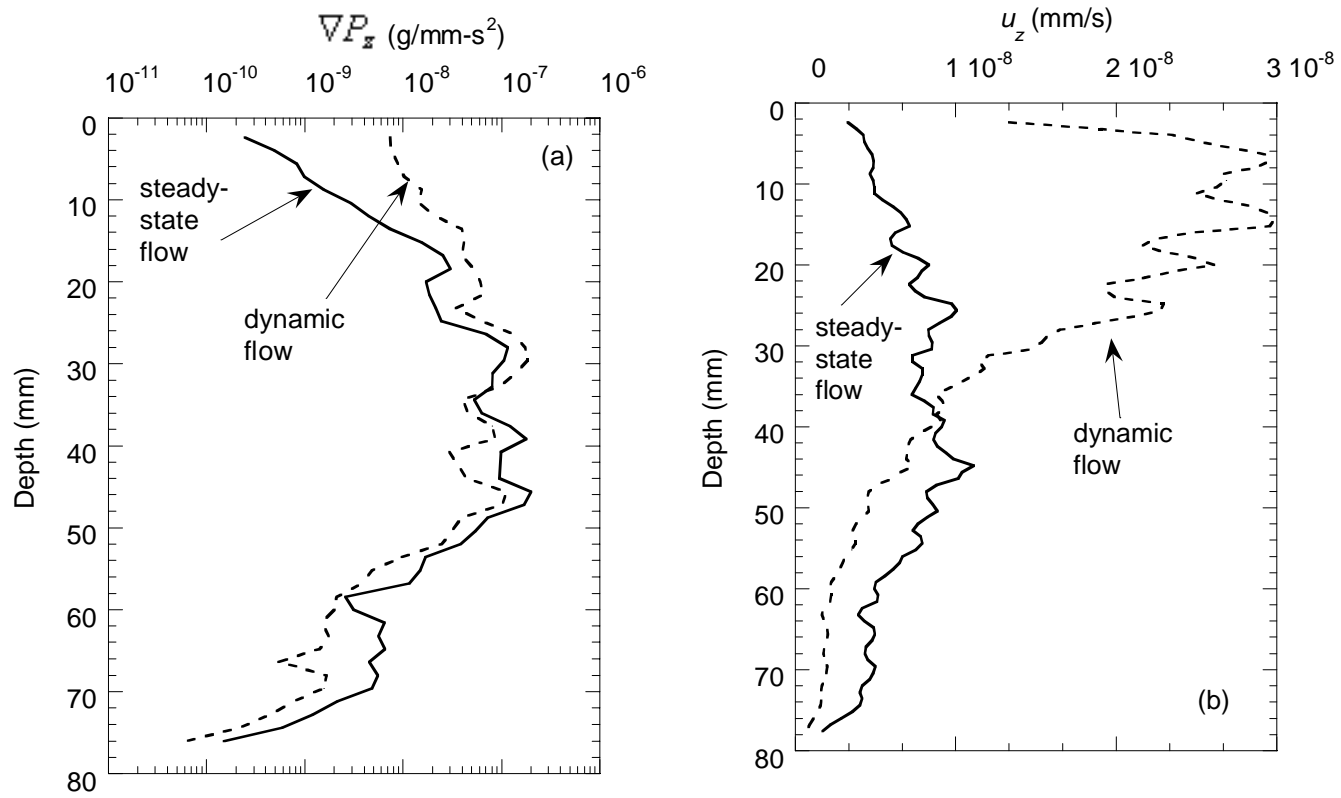


Figure 8.6 (a) Pressure gradient and (b) u_z versus depth relationships of specimen 9.5SMA-B2.

that of steady flow and the difference decreases with increasing depth. This phenomenon supports the argument explained in the previous subsections, where dynamic effects were limited to the surface of the pavements due to the decreasing porosity with depth and possible constrictions in the mid-zone. This can easily be visualized by an analogy with a funnel filled with glass beads, where the pore area decreases with depth. In this case a dynamic fluid pressure at the surface will be dissipated and become relatively steady as it travels towards the constriction of the funnel, limiting the dynamic effects only to the surface. Similar observations can be made on the pressure gradient versus depth plots of other asphalt specimens (Appendix H), where the dynamic conditions produce higher pressure gradients in the upper parts ranging from top 10 to top 40 mm in different specimens. The impact of higher pressure gradient at the upper parts in case of dynamic flow is clearly shown in Figure 8.6b, where dynamic velocity in z-direction is much higher at the upper parts. This can cause higher shear stresses near the surface which were discussed in the next section.

The difference in the pressure gradients at the surface for dynamic and steady flow cases can be seen for different specimens in Figure 8.7. The pressure gradient at the surface is one to three orders of magnitude higher for the dynamic flow than that for the steady flow.

8.2.3.5 Comparison of Shear Stresses in Steady and Dynamic Flow Conditions

The variation of mean shear stress components with depth is shown in Figure 8.8 for specimen 9.5SMA-B2 during both dynamic and steady flow. The curves for the rest of the specimens are available in Appendix I. Based on the indications of pressure gradient and velocity analyses in the previous section, high shear stresses were expected

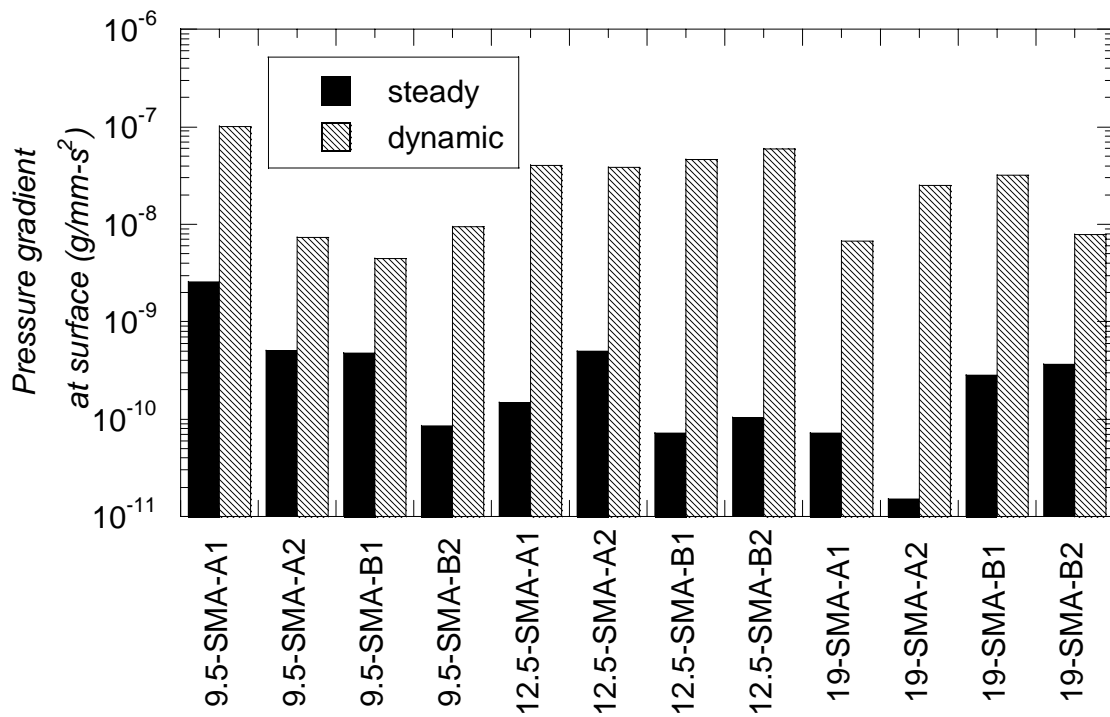


Figure 8.7 Comparison of pressure gradients at surface for steady and dynamic flow cases.

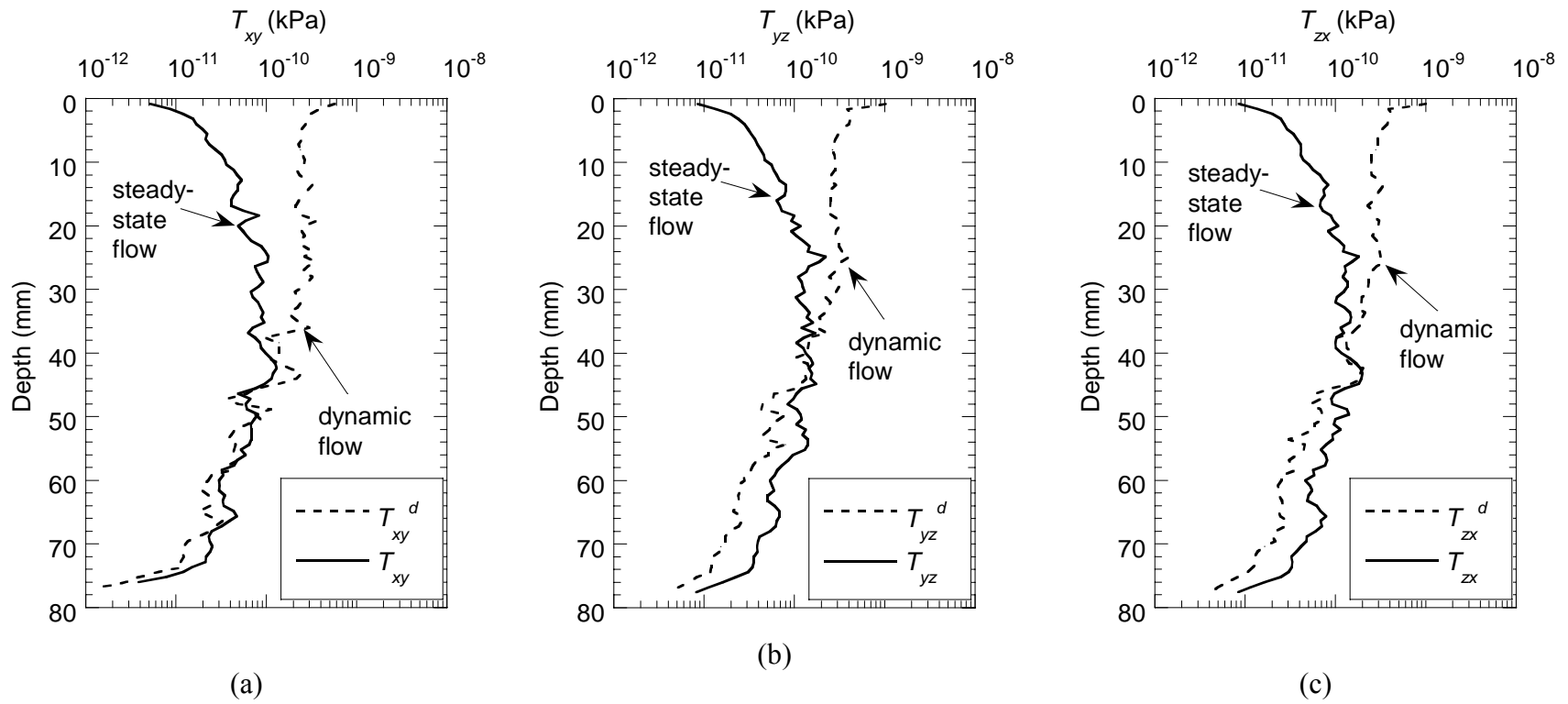


Figure 8.8 The comparison of shear stresses on the pore-solid interface of the internal pore structure of 9.5-SMA-B2 caused by the steady-state and dynamic flow conditions.

at the upper parts of the specimens during dynamic flow. Figure 8.8 clearly confirms these expectations where shear stresses observed at the surface of the specimen based on the dynamic flow simulations are much higher than the shear stresses during the steady flow. The difference is highest at the surface and decreases with depth, which also shows that the dynamic effects are limited to surface. Then, after approximately the same depth (approximately 40 mm) where the dynamic pressure gradient has fallen below steady pressure gradient (Figure 8.6a), the shear stresses under dynamic conditions fell below the shear stresses due to steady flow. Similar trend was observed in all of the specimens (Appendix I).

To investigate the range of differences in viscous shear stresses due to dynamic and steady flow conditions, the surface shear stresses of all specimens were plotted in Figures 8.9 and 8.10. The figures indicate that the dynamic shear stresses are one to two orders of magnitude higher than the steady shear stresses. The steady shear stresses at different specimens varies from 1.63×10^{-12} to 6.33×10^{-11} kPa in T_{xy} , 4.85×10^{-12} to 1.76×10^{-10} kPa in T_{yz} and from 4.77×10^{-12} to 1.82×10^{-10} kPa in T_{zx} , where the variation is greater than one order of magnitude. On the other hand, the variation in dynamic shear stresses is minimal, where dynamic shear stresses ranges from 3.15×10^{-10} to 7.10×10^{-10} kPa in T_{xy}^d , 3.50×10^{-10} to 6.66×10^{-10} kPa in T_{yz}^d and from 3.44×10^{-10} to 6.40×10^{-10} kPa in T_{zx}^d . This phenomenon can also be explained by the pore structure of the specimens where the porosities of the analyzed specimens at the surface were comparable. Since the dynamic effects were seen at the surface (as described in the previous subsections), the variation of surface shear stresses was minimal in different specimens due to similar pore structures at the surface.

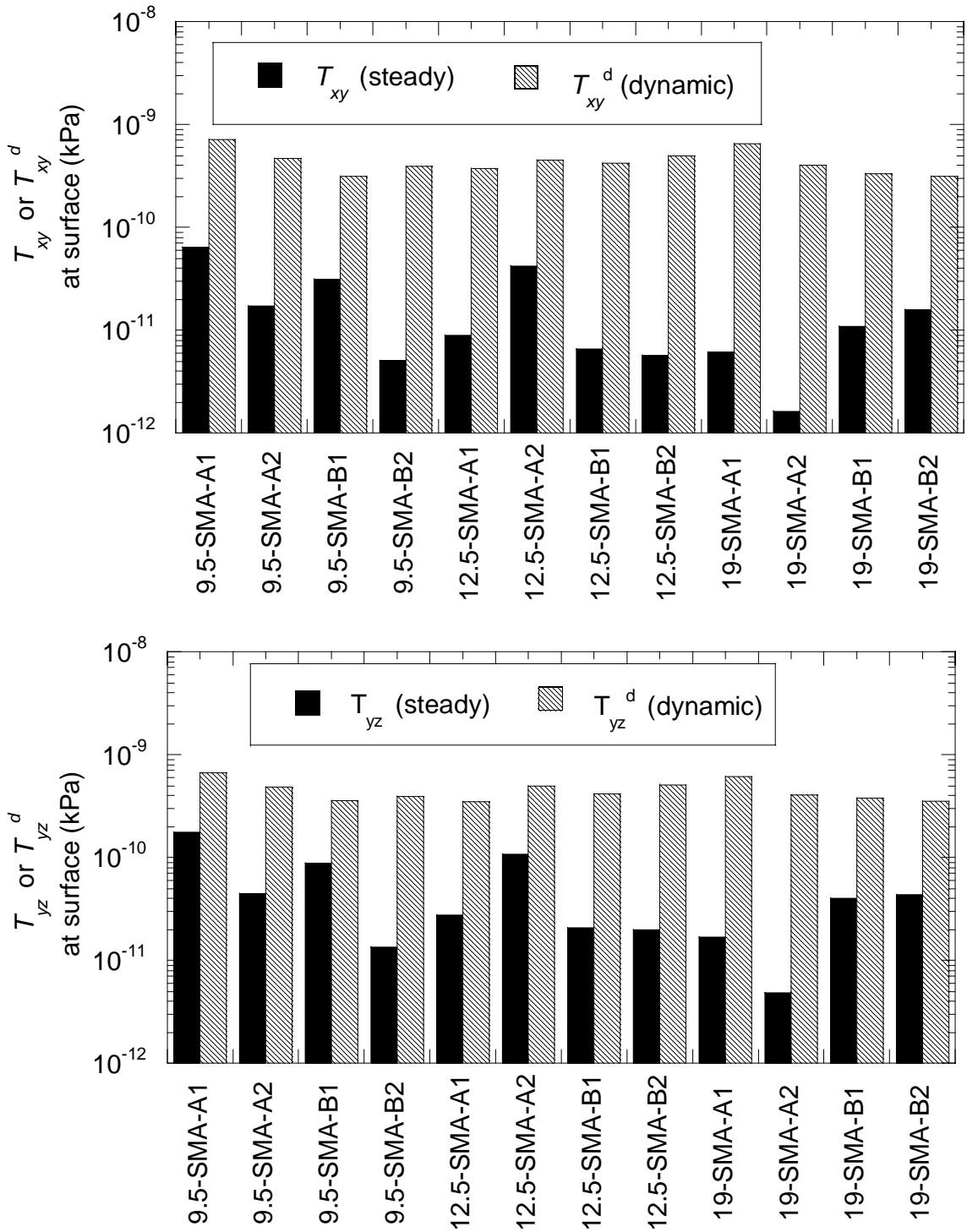


Figure 8.9 Comparison of shear stresses at the surface caused by the steady-state and dynamic flow conditions: (a) T_{xy} and (b) T_{yz}

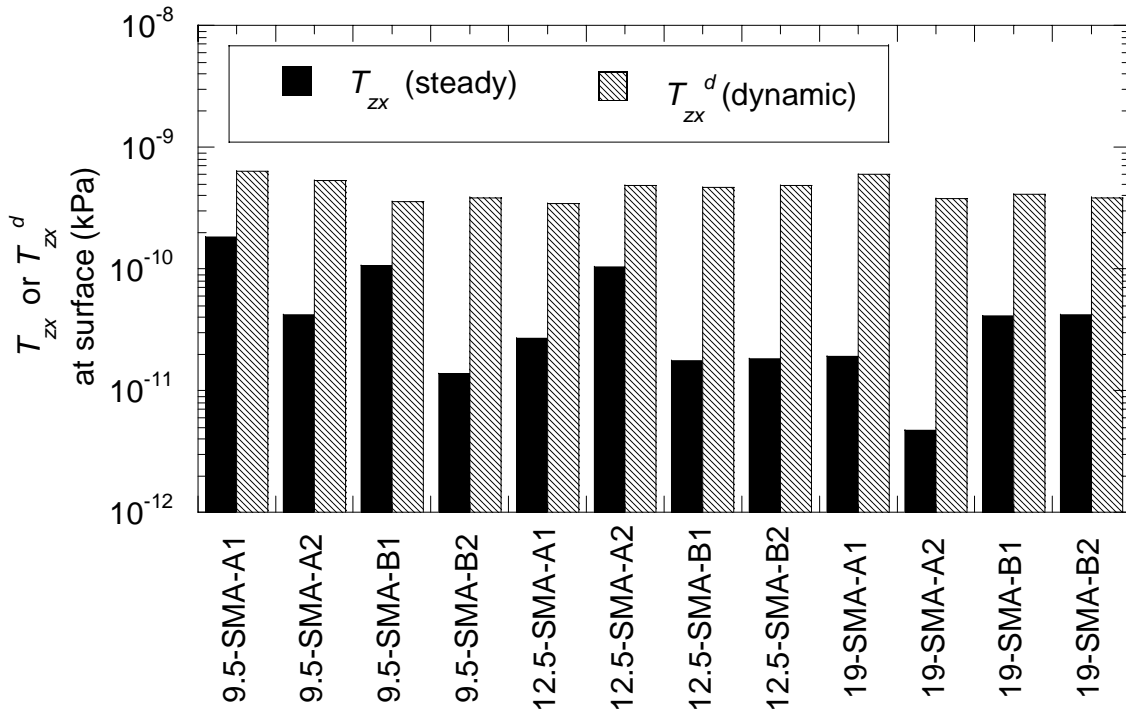


Figure 8.10 Comparison of shear stresses at the surface caused by the steady-state and dynamic flow conditions

CHAPTER 9 CONCLUSIONS AND RECOMMENDATIONS

9.1 SUMMARY AND CONCLUSIONS

Understanding fluid transport characteristics of asphalt pavements is critical in design life of these structures. The moisture penetrating into the pores of an asphalt pavement can quickly cause distresses such as frost cracks and pot holes due to the destruction of adhesive bond between the aggregates and the binders. Modeling fluid flow in these structures is challenging due to their complex pore structure. Simple analytical models were developed to estimate the hydraulic conductivity of these materials (Walsh and Brace 1984, Al-Omari et al. 2002). Derivations of these analytical models are usually based on the approximation of pore structure with simpler geometries, such as tubes and cones, and often the accuracy of these models is questionable. Additionally, most of these techniques do not consider pore channel shape and connectivity, which are critical in fluid flow modeling and the estimation of material hydraulic conductivity. Conversely, finite-difference and finite-element techniques can provide more accurate estimates of hydraulic conductivity; however, their implementation can be challenging, especially at the complex pore geometries such as asphalt pavements. There has been progress in the development of computational fluid dynamics methods based on cellular automata ideas to overcome these challenges. A relatively new method called the lattice Boltzmann (LB) has emerged as a versatile technique for the computational modeling of a wide variety of fluid flow problems. The technique is advantageous because of its ease in implementation of boundary conditions and the computational efficiency by allowing parallel computing.

Two different algorithms were developed for conducting the two- and three-dimensional fluid flow simulations through the pores of the asphalt pavements using the LB technique. The accuracy of these algorithms was verified with the well-known analytical and theoretical solutions of simple geometries such as flow through parallel plates, flow past a circular cylindrical caused by a moving plate (Wannier flow) and flow through a circular tube (Poiseuille flow). An excellent agreement was observed between these solutions and the LB simulations. Furthermore, it was shown that the LB methods implemented herein have second order accuracy, i.e., doubling the number of lattice sites decreases the error four times. The performance of the three-dimensional LB model was further evaluated through laboratory hydraulic conductivity tests conducted on compacted aggregates commonly used in civil engineering construction. X-ray Computed Tomography and mathematical morphology-based techniques were used to analyze the pore structure of the aggregates and these pore structures were input into the LB model. A very good agreement was observed between the model predictions and the laboratory data where the laboratory-based hydraulic conductivities were 1.4 to 1.9 times lower than those predicted by the lattice Boltzmann technique. This difference was attributed to the difficulties associated with the application of low hydraulic gradients to keep the flow in laminar range and head losses due to the relatively small fittings of the traditional laboratory hydraulic conductivity device.

The study of moisture transport in asphalt pavements included field cores and laboratory prepared specimens. Field cores were obtained from the current testing sections of the Accelerated Loading Facility (ALF) at the Turner-Fairbank Highway Research Center (TFHRC) of Federal Highway Administration (FHWA). The laboratory

specimens were fabricated to study a number of mixture variables that are likely to affect the pore structure. The selected variables included NMAS (Nominal Maximum Aggregate Size), compaction energy (number of gyrations in the gyratory compactor) and gradation shape. Three dimensional pore geometries of the asphalt specimens were obtained using X-ray Computed Tomography (CT) technique. X-ray CT is a nondestructive technique for visualizing features in the interior of opaque solid objects to obtain digital information on their 3-D geometry. The geometrical parameters of the specimens; i.e. porosity, pore connectivity, specific surface area and tortuosity were determined using different image analysis algorithms developed in Matlab. The relation of the pore structure and asphalt mix design parameters to the laboratory measured unidirectional hydraulic conductivity was investigated. A state-of-the-art flexible-wall permeameter, “Bubble Tube Constant Head Permeameter”, was utilized for measuring hydraulic conductivity of the asphalt specimens.

Laboratory based validation of the LB model on asphalt specimens was done through performing various LB fluid flow simulations on different specimens, by assigning appropriate boundary conditions to simulate the laboratory hydraulic conductivity test (i.e., membrane confinement and inlet and outlet pressure conditions). Three-dimensional interconnected pore structures of the asphalt specimens, acquired using X-ray CT technique and processed through the *PORECON* algorithm, were used as an input to the LB model. A highly good agreement was observed between the LB results and laboratory based hydraulic conductivity measurements.

All nine components of the hydraulic conductivity tensor for each specimen were computed after a separate set of simulations to study the directional hydraulic

conductivity of asphalt pavements. The magnitudes of the hydraulic conductivities in different directions were compared to study the isotropy of the asphalt specimens. Effect of pore constrictions on the hydraulic conductivities in different directions was analyzed. The shear stress and pore pressure distributions were computed for each direction and their relation to the constriction areas was investigated. Furthermore, the hydraulic conductivity variation at different depths of the asphalt pavements was studied.

To study the effects of dynamic vehicle loading on the flow of water in the pore structure of asphalt pavements, unsteady flow simulations were performed. Pulse-shaped inlet boundary conditions were assigned to simulate the dynamic tire loading on the asphalt pavements. Dynamic hydraulic conductivities were computed as a result of unsteady flow and compared to the steady hydraulic conductivities. Pore pressure and shear stress distribution due to dynamic flow was computed and compared to their corresponding values under steady conditions.

The following conclusions were reached as a result of the activities performed:

1. The analyses revealed that the pores are segregated at the top and bottom of the asphalt pavements, where much higher porosities were observed at these locations as compared to the porosities in the mid-depths. In specimens with coarse and fine graded aggregate gradation, the surface porosities were comparable; however, mid-depth porosities of the fine graded specimen were less than that of coarse graded specimens. The porosity variation with depth in field cores was similar to the trends observed in coarse graded specimens. The trends were similar for the SMA specimens; however, much higher porosities were observed in both mid-zone and at the top and bottom. On the other hand, porosity variation in radial direction was minimal in most

of the specimens, indicating less variability in lateral direction. Furthermore, lower porosities were observed in the specimens compacted at higher number of gyrations.

2. Comparison of the laboratory based hydraulic conductivities to the pore structure parameters (i.e., total porosity, effective porosity, normalized specific surface area and tortuosity) revealed that, even though the trends in general are meaningful and comparable with previous studies, clear cut relationships between the individual parameters and the hydraulic conductivity are not visible. A trend was not visible when the hydraulic conductivities were compared to the mixture parameters such as NMAS and compaction effort (number of gyrations). On the other hand, a relatively good relationship between the amount of fines in each mixture and the hydraulic conductivity was observed, in which the hydraulic conductivity decreased exponentially as the percentage of fines increased. The trend was especially visible in the specimens compacted at low gyration level. Therefore, the hydraulic conductivity of the asphalt pavements could significantly be decreased by introducing additional amounts of fine graded soil in the mixture.
3. Commonly used semi-analytical hydraulic conductivity equations for porous structures were evaluated by comparing their predictions to the laboratory based results for asphalt specimens. Results revealed that the estimations of analytical equations were relatively accurate at high hydraulic conductivities (i.e., $k_{zz} > 1$ mm/s), whereas, their estimations were up to two order of magnitude higher than those measured in the laboratory when low-hydraulic conductivity (i.e., $k_{zz} < 1$ mm/s) specimens are considered. Therefore, use of these equations is not recommended to estimate the hydraulic conductivity of dense graded asphalt specimens, which

typically have hydraulic conductivities less than 1 mm/s. However, Kozeny-Carman equation, which performed relatively well in predicting laboratory based hydraulic conductivities in highly porous SMA specimens, can be used for predicting hydraulic conductivities of porous asphalt pavements such as Open Graded Friction Course (OGFC).

4. The three-dimensional fluid flow simulations through asphalt specimens using LB technique revealed accurate estimations of hydraulic conductivity. Furthermore, the simulations were able to produce exact flow pathways as well as the pore pressure distributions, which could be used by the engineers designing structures with complex pore geometries. The presented models can also provide accurate values of velocities and shear stresses during fluid flow in the pore channels. It is believed that the techniques implemented herein can be useful in developing future micro- and nano-scale fluid flow models.
5. Analysis of hydraulic conductivity tensor of the asphalt pavements revealed that the horizontal hydraulic conductivities (i.e., k_{xx} and k_{yy}) were up to two orders of magnitude higher than the vertical hydraulic conductivity (i.e., k_{zz}). Whereas, the hydraulic conductivities in two horizontal directions (i.e., k_{xx} and k_{yy}) were comparable within a 50% confidence interval. It should be noted that this characteristic was observed in both laboratory compacted specimens and the field cores. These observations indicated that the asphalt pavements are isotropic comparing two horizontal directions (x - and y -directions) and anisotropic comparing horizontal and vertical directions. This property of asphalt specimens explains the differences encountered while comparing laboratory based and field measured hydraulic

conductivities of the asphalt pavements, where it is usually assumed that laboratory based unidirectional hydraulic conductivity is constant in all directions. However, higher hydraulic conductivities in the horizontal directions can quickly cause the water to flow in the horizontal direction during a field hydraulic conductivity test leading to false measurements. Unfortunately, current field hydraulic conductivity measurement methodologies do not account for this effect. Therefore, it is strongly recommended that a new field testing standard be developed.

6. The degree of relationship between the minimum porosity and hydraulic conductivity varied in different directions. Relatively good relationship was observed when the minimum porosity in z-direction (n_{\min}^z) was plotted against the hydraulic conductivity in the same direction. Therefore, n_{\min}^z could be used by the field engineers to predict the hydraulic conductivity in z- direction based on the regression lines produced in this study. Minimum porosity in z-direction can be approximated by cutting the specimens into layers and measuring the porosity in the mid-zones. On the other hand, the degrees of correlation between the horizontal hydraulic conductivities (i.e., k_{xx} and k_{yy}) and the minimum porosities in the two horizontal directions (i.e., n_{\min}^x and n_{\min}^y) were much lower. This phenomenon was attributed to the differences in the pore structure variation in different directions, where there is usually one zone where the PCSA is minimal in z-direction. The constriction controlling the hydraulic conductivity in that direction most likely located at this particular zone. However, in x- and y- directions, low PCSAs may be observed at different locations where different constrictions might be located. Therefore, it is difficult to relate the hydraulic conductivity in x- and y-directions to one single variable.

7. The analysis of hydraulic conductivity at different depths revealed a rapid decrease in the hydraulic conductivity as the analysis depth was increased. In most of the specimens, the decrease was one order of magnitude when the analysis depth was doubled. The specimens compacted at higher compaction effort (i.e. higher number of gyrations) generally exhibited a more rapid decrease in hydraulic conductivity than those prepared with lower compaction effort. It can be concluded that increasing the compaction effort in the field can significantly reduce the depth to which the water can penetrate, thus limit the possible moisture damage only to the surface of the pavement
8. It was observed during LB fluid flow simulations that the number of time steps required for a steady-state flow condition varies from 1000 to 150000 in different specimens. Generally, the specimens with less angular pore space reached to a steady state flow faster. The researchers using LB method can reduce their computation time by smoothing the surfaces of the solid boundaries within their domain.
9. LB simulations revealed that when a constant pressure difference was applied between the inlet and the outlet of the asphalt specimens, a linear decrease in pressure was not observed, therefore, the pressure gradient was not constant. The pressure gradient varied greatly in different specimens depending on the existence of a pore constriction. The local pressure gradients at constrictions were up to one order of magnitude higher than the average pressure gradient, which created very high velocities at these locations. Two ratios, i.e., pressure gradient ratio (∇P_r) and area ratio (A_r), were defined to investigate the degree of increase in pressure gradient in constriction zones and relate it to the minimum area observed at the constriction. It was observed that the pressure gradient ratio was between 1.2 and 5 in most of the

specimens, indicating that the maximum pressure gradients were 1.2 to 5 times higher than the average pressure gradient. However, pressure gradients ratios up to 15 were also observed where the maximum pressure gradient is more than one order of magnitude higher than the overall average pressure gradient.

10. LB simulations showed that maximum shear stresses caused by the viscous fluid movement occurred at the constrictions where the porosity is minimal. The ratios of the maximum shear stresses observed at the constrictions to the overall average shear stress ranged from 1 to 13, indicating the high vulnerability of these zones to moisture induced binder stripping.
11. Unsteady flow simulations revealed that the dynamic hydraulic conductivities of asphalt specimens were relatively close to the steady hydraulic conductivities. However, it may be difficult to quantitatively predict one from the other, as there is a wide variability in the data.
12. The pressure gradient variation with depth in dynamic and steady flow conditions are similar in general, except at the surface, where the pressure gradient observed in dynamic flow is higher than that of steady flow. The difference is highest at the surface and decreases with increasing depth.
13. The shear stresses observed at the surface of the specimen based on the dynamic flow simulations are much higher than the shear stresses during the steady flow under same pressure conditions, i.e., when pressure gradient amplitude in dynamic flow is the same as the average pressure gradient in steady flow. It was observed that the dynamic shear stresses at the surface are one to two orders of magnitude higher than

the steady shear stresses, indicating that moisture damage is more likely to occur in the upper zones of the pavements.

9.2 PRACTICAL IMPLICATIONS OF THE FINDINGS

The practical implications of the analyses conducted for characterization of moisture transport in asphalt pavements are summarized as follows:

1. Based on the pore structure analyses, it was shown that mid-depth porosity can be decreased by increasing compaction energy. As a result, field engineers will have better understanding of the effect of compaction on the pore structure. Depth versus hydraulic conductivity analysis also revealed that the depth of water penetration can be decreased by increasing compaction effort.
2. Hydraulic conductivity of asphalt pavements in z-direction have found to be significantly affected by the percent fines in the mixture. Therefore, it was concluded that the most effective way of reducing hydraulic conductivity would be adding more fines in the mixture.
3. A new hydraulic conductivity testing standard is necessary for accurate characterization of moisture transport, since the hydraulic conductivities in horizontal directions were found to be much higher than the vertical hydraulic conductivity. The field k_{xx} , k_{yy} and k_{zz} should be measured separately using specially designed field devices.
4. Empirical hydraulic conductivity equations (e.g., Kozeny-Carman) which are typically used for granular materials do not apply to asphalt pavements with hydraulic conductivities less than 1 mm/s. Because the constriction usually play a key role on the reduction of flow instead of the overall pore structure in those pavements.

Therefore, use of these analytical equations to estimate hydraulic conductivity is not recommended as most of the asphalt pavements include dense mix design. Alternatively, these equations can be used for highly porous pavements such as open graded friction course.

5. Developed LB model has shown to be able to produce pore pressures and shear stresses at the pore solid interfaces due to both steady state and dynamic flow cases. This model can be used by the researchers to estimate the critical values of pore pressures and shear stresses in certain asphalt types. These stresses can be utilized in the micro-level moisture damage modeling studies similar to those conducted by Kringos and Scarpas (2005).

9.3 RECOMMENDATIONS FOR FURTHER RESEARCH

The following research topics are recommended to succeed the activities of this study:

1. Even though this study included a wide variety of different asphalt pavement types with different mixture parameters such as aggregate gradation, NMAS and compaction level, the analyses can be extended to other asphalt pavement types with different mix designs (e.g., recycled asphalt pavement, open graded HMAs).
2. Different field cores with similar mixture parameters to the laboratory prepared specimens can be obtained to study the variability between the laboratory compacted mixtures and field cores. Directional hydraulic conductivity, pressure gradients and shear stresses can be compared for laboratory prepared and field compacted mixtures.
3. Field instrumentation could be made to study the dynamic flow caused by the tire loading. The tire loading can be applied by using a Miniature Mobile Load Simulator

(MMLS) for more controlled loading conditions. The instrumentation can include load cells and piezometer tubes placed at different depths to measure the water heads and pressures caused by the dynamic tire loading. Then dynamic LB simulations can be performed to simulate the exact boundary conditions in the MMLS and the results can be used for field validation of the numerical model.

4. Since the scope of dynamic flow modeling part of this study was to conduct preliminary analyses to investigate the differences between the dynamic and steady flow cases in asphalt pavements, current dynamic LB simulations were performed using relatively smaller pressures than those usually encountered during a car or truck loading. Using high pressure levels could cause turbulent flows of very high Reynolds numbers and the current LB model is under development to be suitable for solving turbulent and two phase flows (e.g., water and air). Therefore, turbulent flow within the pore structure due to large pressures as well as splash and spray above pavement shall be studied in the future.

5. Micro-scale pores of the asphalt pavements can be obtained by using X-ray Microtomography technique, which requires smaller specimens. LB fluid flow simulations can be performed in fine graded specimens to estimate the hydraulic conductivities. The measured micro-pores can also be used to calculate diffusion coefficient of the asphalt mastic or asphalt binder to study the micro-scale flow within the binder or mastic. This could aid in-depth understanding of moisture damage or binder stripping problem.

APPENDIX A CALCULATION OF UNKNOWN COMPONENTS OF THE DISTRIBUTION FUNCTION

The following relationships are given for density and momentum:

$$\rho = \sum_{i=1}^Q F_i \quad (A1)$$

$$\mathbf{U} = \rho \mathbf{v} = \sum_{i=1}^Q \mathbf{F}_i \mathbf{e}_i \quad (A2)$$

The momentum equation (A2) can also be written in the following form for the D2Q9 LB model (see Figure 6):

$$\rho v_x = F_1 + F_5 + F_8 - (F_3 + F_6 + F_7) \quad (A3)$$

$$\rho v_y = F_2 + F_5 + F_6 - (F_4 + F_7 + F_8) \quad (A4)$$

Inlet Nodes

Unknown components at the inlet nodes can be written in terms of known components as follows:

$$F_1 + F_5 + F_8 = \rho_{in} - (F_9 + F_2 + F_4 + F_3 + F_6 + F_7) \quad (A5)$$

Combining Equations A3 and A5 eliminates the unknown components and provides the following equations:

$$\boxed{v_{x(in)} = 1 - \frac{F_9 + F_2 + F_4 + 2(F_3 + F_6 + F_7)}{\rho_{in}}} \quad (A6a)$$

or

$$\rho_{in} = \frac{1}{1 - v_{x(in)}} [F_9 + F_2 + F_4 + 2(F_3 + F_6 + F_7)] \quad (A6b)$$

Given the velocity or density, the other can be calculated from Equation A6. The remaining unknown components of the distribution function can be found by assuming the bounce-back rule to be valid for non equilibrium part of the distribution function, i.e., $F_1 - F_1^{eq} = F_3 - F_3^{eq}$.

$$F_1^{eq} = \frac{1}{9}\rho \left[1 + 3v_x + \frac{9}{2}v_x^2 - \frac{3}{2}(v_x^2 + v_y^2) \right] \quad (A7)$$

$$F_3^{eq} = \frac{1}{9}\rho \left[1 - 3v_x + \frac{9}{2}v_x^2 - \frac{3}{2}(v_x^2 + v_y^2) \right] \quad (A8)$$

$$F_1^{eq} - F_3^{eq} = \frac{2}{3}\rho v_x \quad (A9)$$

Using the relationship $F_1 - F_1^{eq} = F_3 - F_3^{eq}$:

$$\boxed{F_1 = F_3 + \frac{2}{3}\rho v_x} \quad (A10)$$

Subtracting A4 from A3 gives:

$$\rho v_x - \rho v_y = F_1 - F_3 - (F_2 - F_4) - 2F_6 + 2F_8 \quad (A11)$$

Rearranging A11 and substituting in $F_1 - F_3 = (2/3)\rho v_x$ gives:

$$\boxed{F_8 = F_6 + \frac{1}{2}(F_2 - F_4) + \frac{1}{6}\rho v_x - \frac{1}{2}\rho v_y} \quad (A12)$$

Adding A4 to A3 gives:

$$\rho v_x + \rho v_y = -(F_1 - F_3) + (F_2 - F_4) - 2F_7 + 2F_5 \quad (A13)$$

Rearranging A13 and substituting in $F_1 - F_3 = (2/3)\rho v_x$ gives:

$$\boxed{F_5 = F_7 - \frac{1}{2}(F_2 - F_4) + \frac{1}{6}\rho v_x + \frac{1}{2}\rho v_y} \quad (A14)$$

Outlet Nodes

Similarly, density equation (A1) at outlet no reveals:

$$F_3 + F_6 + F_7 = \rho_{out} - (F_9 + F_2 + F_4 + F_1 + F_5 + F_8) \quad (A15)$$

Adding Equations A15 and A3 gives:

$$v_{x(out)} = -1 + \frac{F_9 + F_2 + F_4 + 2(F_3 + F_6 + F_7)}{\rho_{out}} \quad (A16a)$$

or

$$\rho_{out} = \frac{1}{1 + v_{x(out)}} [F_9 + F_2 + F_4 + 2(F_3 + F_6 + F_7)] \quad (A16b)$$

Rearranging equations A10, A12, and A14 gives the following relationships at outlet nodes:

$$F_3 = F_1 - \frac{2}{3} \rho v_x \quad (A17)$$

$$F_6 = F_8 - \frac{1}{2} (F_2 - F_4) - \frac{1}{6} \rho v_x + \frac{1}{2} \rho v_y \quad (A18)$$

$$F_7 = F_5 + \frac{1}{2} (F_2 - F_4) - \frac{1}{6} \rho v_x - \frac{1}{2} \rho v_y \quad (A19)$$

Bottom Nodes

Similarly, density equation (A1) at bottom nodes reveals:

$$F_2 + F_5 + F_6 = \rho_{bottom} - (F_9 + F_1 + F_3 + F_4 + F_7 + F_8) \quad (A20)$$

then from A20 and A4;

$$v_{y(bottom)} = 1 - \frac{F_9 + F_1 + F_3 + 2(F_4 + F_7 + F_8)}{\rho_{bottom}} \quad (A21a)$$

or

$$\boxed{\rho_{bottom} = \frac{1}{1 - v_{y(bottom)}} [F_9 + F_1 + F_3 + 2(F_4 + F_7 + F_8)]} \quad (A21b)$$

Similar to the calculation done at inlet nodes, equilibrium distribution functions are:

$$F_2^{eq} = \frac{1}{9} \rho \left[1 + 3v_y + \frac{9}{2} v_y^2 - \frac{3}{2} (v_x^2 + v_y^2) \right] \quad (A22)$$

$$F_4^{eq} = \frac{1}{9} \rho \left[1 - 3v_y + \frac{9}{2} v_y^2 - \frac{3}{2} (v_x^2 + v_y^2) \right] \quad (A23)$$

$$F_2^{eq} - F_4^{eq} = \frac{2}{3} \rho v_y \quad (A24)$$

then given that $F_2 - F_2^{eq} = F_4 - F_4^{eq}$:

$$\boxed{F_2 = F_4 + \frac{2}{3} \rho v_y} \quad (A25)$$

Now F6 and F5 need to be calculated. Subtracting A4 from A3 gives:

$$\rho v_x - \rho v_y = F_1 - F_3 - (F_2 - F_4) - 2F_6 + 2F_8 \quad (A26)$$

Rearranging A26 and plugging in $F_2 - F_4 = (2/3)\rho v_y$ gives:

$$\boxed{F_6 = F_8 + \frac{1}{2}(F_1 - F_3) + \frac{1}{6} \rho v_y - \frac{1}{2} \rho v_x} \quad (A27)$$

Adding A4 to A3 gives:

$$\rho v_x + \rho v_y = -(F_1 - F_3) + (F_2 - F_4) - 2F_7 + 2F_5 \quad (A28)$$

Rearranging A28 and plugging in $F_2 - F_4 = (2/3)\rho v_y$ gives;

$$\boxed{F_5 = F_7 - \frac{1}{2}(F_1 - F_3) + \frac{1}{6} \rho v_y + \frac{1}{2} \rho v_x} \quad (A29)$$

Top Nodes

Density equation (A1) at top nodes reveals:

$$F_4 + F_7 + F_8 = \rho_{top} - (F_9 + F_1 + F_3 + F_2 + F_6 + F_5) \quad (A30)$$

then adding Equations A30 and A4 gives:

$$v_{y(top)} = -1 + \frac{F_9 + F_1 + F_3 + 2(F_2 + F_6 + F_5)}{\rho_{top}} \quad (A31a)$$

or

$$\rho_{top} = \frac{1}{1 + v_{y(top)}} [F_9 + F_1 + F_3 + 2(F_2 + F_6 + F_5)] \quad (A31b)$$

Rearranging Equations A25, A27, and A29 gives the following relationships at top nodes:

$$F_4 = F_2 - \frac{2}{3} \rho v_y \quad (A32)$$

$$F_8 = F_6 - \frac{1}{2} (F_1 - F_3) - \frac{1}{6} \rho v_y + \frac{1}{2} \rho v_x \quad (A33)$$

$$F_7 = F_5 + \frac{1}{2} (F_1 - F_3) - \frac{1}{6} \rho v_y - \frac{1}{2} \rho v_x \quad (A34)$$


```

        'Total area of specimen (A) in (pixel^2) :'},...
        'Input for permeability calculation ...',1,...
        {num2str(dPz),'1','9.81','1',num2str(L)}}

dPz=str2num(result{1});
dz=str2num(result{2});
gamma=str2num(result{3});
visc_k_w=str2num(result{4});
L=str2num(result{5});

fid=fopen([FilePath '\Input-' filename '.txt'],'w');
fprintf(fid,'%50s \n', ['Simulation of Fluid Flow Using Lattice Boltzmann Equation']);
fprintf(fid,'%50s \n', ['Type:D2Q9 Lattice']);
fprintf(fid,'%50s \n', ['Program By: Muhammed Emin Kutay']);
fprintf(fid,'%50s \n', ['-----']);
fprintf(fid,'%35s %20s \n', 'Simulation Date: ', date);
fprintf(fid,'%35s %20s \n', 'Description: ', FilePath);
fprintf(fid,'%35s %20s \n', 'Image Name:', filename);
fprintf(fid,'%35s %20s \n', 'Image size in x direction :', num2str(SI));
fprintf(fid,'%35s %20s \n', 'Image size in y direction :', num2str(SJ));
fprintf(fid,'%35s %20s \n', 'Inlet Density : ', num2str(pin));
fprintf(fid,'%35s %20s \n', 'Outlet Density: ', num2str(pout));
fprintf(fid,'%35s %30s \n', 'Acceleration body force vector:',[[' num2str(F) ' ]]);
fprintf(fid,'%35s %20s \n', 'Termination time: ', num2str(tend));
fprintf(fid,'%35s %20s \n', 'Max tolerance for termination: ', num2str(TOL) );
fprintf(fid,'%35s %20s \n', 'TAO: ', num2str(TAO) );
fclose(fid);

tic
for i=1:8
    i
    Xp=[X(:,1)-e(i,1) X(:,2)-e(i,2)];

    [C, IA, IB]=intersect(X, Xp,'rows');

    [C, Io]=setdiff(Xp, X,'rows'); %in Xp but not in X

    fid=fopen([FilePath '\IA-' num2str(i) '.bin'],'wb');
    fwrite(fid, IA, 'double');
    fclose(fid);

    fid=fopen([FilePath '\IB-' num2str(i) '.bin'],'wb');
    fwrite(fid, IB, 'double');
    fclose(fid);

    fid=fopen([FilePath '\Io-' num2str(i) '.bin'],'wb');
    fwrite(fid, Io, 'double');
    fclose(fid);

    El_Time_Ind=toc
end
clear C IA IB Io

for i=1:8
    i
    fid=fopen([FilePath '\IA-' num2str(i) '.bin'],'r');
    IA(i).v=fread(fid, 'double');
    fclose(fid);

    fid=fopen([FilePath '\IB-' num2str(i) '.bin'],'r');
    IB(i).v=fread(fid, 'double');
    fclose(fid);

    fid=fopen([FilePath '\Io-' num2str(i) '.bin'],'r');
    Io(i).v=fread(fid, 'double');
    fclose(fid);

```

```

end
t=1;
p=pin-(pin-pout)/(SJ)*X(:,1)
% dPz=pin*F(3,1);
Lp=size(p,1)/SJ;
dPz=(1/3)*(pin-pout)/SJ;
Ones4l=ones(4,1);
Ones4sp=ones(4,size(p,1));
Ons3l=ones(3,1);
% % break
visc_k_l=(2*TAO-1)/6;
dt=dz^2*(visc_k_l)/(visc_k_w);
gamma=gamma*dz^2*dt^2;
while t < tend%-----

%*****Beginning of propogation *****

    if t==1
        Neq(:,1:4)=1/9*(p*ones(1,4));
        Neq(:,5:8)=1/36*(p*ones(1,4));
        Neq(:,9)=4/9*p;

        N=Neq;
%       U=Neq*zeros(9,2);
%       V(:,1)=U(:,1)./p;
%       V(:,2)=U(:,2)./p;
    end

    for a=1:8
%       BF=3*Wght(a)*p(IA(a).v)*(e(a,:)*F);
%       BF=3*Wght(a)*p(IA(a).v).*(e(a,:)*F-
V(IA(a).v,:)*F+3*(V(IA(a).v,:)*e(a,:)).*(e(a,:)*F));
        N(IB(a).v,a)=N(IA(a).v,a)-1/TAO*(N(IA(a).v,a)-Neq(IA(a).v,a))+
3*Wght(a)*p(IA(a).v)*(e(a,:)*F);%BF;

%       BF_w=3*Wght(Fa(a))*p(Io(a).v)*(e(Fa(a,:)*F);
%       BF_w=3*Wght(Fa(a))*p(Io(a).v).*(e(Fa(a,:)*F-
V(Io(a).v,:)*F+3*(V(Io(a).v,:)*e(Fa(a,:)).*(e(Fa(a,:)*F));
        N(Io(a).v,a)=N(Io(a).v,Fa(a))-1/TAO*(N(Io(a).v,Fa(a))-Neq(Io(a).v,Fa(a)))+
3*Wght(Fa(a))*p(Io(a).v)*(e(Fa(a,:)*F);%BF_w;

    end

    N(:,9)=N(:,9)-1/TAO*(N(:,9)-Neq(:,9));

    %Density
    p(:,1)=sum(N,2);

    %%Velocities
    U=(N*e);
    V(:,1)=U(:,1)./p;
    V(:,2)=U(:,2)./p;

    %Boundary conditions Zou and He (1997)
    p(Iin,1)=pin;
    p(Iout,1)=pout;

    %-----Calculate velocity at the inlet and the outlet nodes----
    V(Iin,2)=0;
    V(Iout,2)=0; %set uy=0
    %---For Inlet
    Ia1=[9,2,4]';
    Ia2=[3,6,7]';

    V(Iin,1)=1-(N(Iin,Ia1)*Ons3l+2*(N(Iin,Ia2)*Ons3l))/pin;
    %---For Outlet
    Ia2=[1,5,8]';
    V(Iout,1)=-1+(N(Iout,Ia1)*Ons3l+2*(N(Iout,Ia2)*Ons3l))/pout;
    %-----Calculate missing components of the distribution function

    N(Iin,1)= N(Iin,3)+(2/3)*pin*V(Iin,1);

```

```

N(Iin,5)= N(Iin,7)-(1/2)*(N(Iin,2)- N(Iin,4))+(1/6)*pin*V(Iin,1);
N(Iin,8)= N(Iin,6)+(1/2)*(N(Iin,2)- N(Iin,4))+(1/6)*pin*V(Iin,1);

N(Iout,3)= N(Iout,1)-(2/3)*pout*V(Iout,1);
N(Iout,7)= N(Iout,5)+(1/2)*(N(Iout,2)- N(Iout,4))-(1/6)*pout*V(Iout,1);
N(Iout,6)= N(Iout,8)-(1/2)*(N(Iout,2)- N(Iout,4))-(1/6)*pout*V(Iout,1);

%Calculate new Neq
Neq=Neq';
U(:,1)=V(:,1).*p;
U(:,2)=V(:,2).*p;

Neq(1:4,:) =1/9*((Ones41*p')+3*e(1:4,:)*U'+9/2*(e(1:4,:)*U').^2-
3/2*(Ones41*sum(U.*U,2)'));
Neq(5:8,:)=1/36*((Ones41*p')+3*e(5:8,:)*U'+9/2*(e(5:8,:)*U').^2-
3/2*(Ones41*sum(U.*U,2)'));
Neq(9,:) =4/9*(p'-3/2*sum(U.*U,2)');

Neq(1:4,:) =1/9*(Ones4sp+3*e(1:4,:)*V'+9/2*(e(1:4,:)*V').^2-
3/2*(Ones41*sum(V.*V,2)'));
Neq(5:8,:)=1/36*(Ones4sp+3*e(5:8,:)*V'+9/2*(e(5:8,:)*V').^2-
3/2*(Ones41*sum(V.*V,2)'));
Neq(9,:) =4/9*(1-3/2*sum(V.*V,2)');

Neq=Neq.*(ones(9,1)*p');
%
% %%Neq fom Munk
% Neq(1:4,:) =1/9*((Ones41*p')+3*e(1:4,:)*U');
% Neq(5:8,:)=1/36*((Ones41*p')+3*e(5:8,:)*U');
% Neq(9,:) =4/9*p';

Neq=Neq';

pause (0.0001)
t=t+1;

%-----END OF MAIN CALCULATIONS-----
----
\

%-----Plot graphs-----
if t/50==round(t/50)
    disp(['t= ' num2str(t) ' , el_time per step= ' num2str(toc) ' sec'])
    tic
% V2=U/mean(p);
Kint2=mean(U(:,1))/(6*dPz);
k2=(1/visc_k_1)*(9.81e3)*(dt)*Kint2*(Lp/L);
% permeability from flowrate
Utot=norm(mean(U));
Q=Utot/mean(p)*Lp;
k3=Q/L*gamma/dPz *(dz/dt);

fid=fopen([FilePath '\Vav.txt'],'a');
fprintf(fid,'%6.0f %12.3e %12.3e \n',[t, mean(U/mean(p))]);
fclose(fid);

fid=fopen([FilePath '\k.txt'],'a');
fprintf(fid,'%6.0f %12.6e %12.6e %12.6e\n',[t k2 k3 Kint2]);
fclose(fid);

figure(1)
% subplot(2,1,1), plot(t,mean(U(:,1))/mean(p)),'.'), hold on,title('Vx (pixel/time)')
subplot(2,1,1),plot(t,k2,'r+',t,k3,'kx'), hold on, title('k (mm/s)'),
legend('k2=6*(9.81e3)*(dt)*Kint2*(Lp/L)', 'k3=Q/L*gamma/dPz*(dz/dt)')
subplot(2,1,2), plot(t,Kint2,'r. '), hold on,title('K (pixel^2)')
end

```

```

    if round(t/50)==t/50
    %         save([FilePath '\data'])
    %         for j=1:size(X,1)
    %             P(X(j,2),X(j,1))=p(j);
    %             Vy(X(j,2),X(j,1))=V(j,2);
    %             Vx(X(j,2),X(j,1))=V(j,1);
    %         end
    %         close (figure(2))
    %         figure(2), subplot(2,1,1),contourf(P,20),title(['P, time= '
num2str(t)]), axis ij
    %         saveas(gcf,[FilePath 'P-' numtostr(t) '.bmp'],'bmp')
    %
    %         figure(2)
    %         visc_d_l=mean(p)*visc_k_l;
    %         W=size(Iin,1);
    %         z=[0.5:W-.5]';
    %         Vanal=dPz/(2*visc_d_l)*z.*(W-z);
    %         Vlb=U(Iin,1)/mean(p);
    %         Perc_Err=mean(abs(Vlb-Vanal)./Vanal*100);
    %         C_err=[C_err; [t,Perc_Err]]
    %         subplot(2,1,1),plot(t,Perc_Err,'g. '),title('Average Percent Error'), hold on
    %         subplot(2,1,2),plot(Vanal,'b-'),hold on,
    %         subplot(2,1,2),plot(Vlb,'b.:'),
    %         legend('Analytical', 'Lattice Boltzmann'), hold on

    %         fid=fopen([FilePath '\TAO-' numtostr(TAO) '.txt'],'a');
    %         fprintf(fid,'%6.0f %12.6e \n',[t Perc_Err]);
    %         fclose(fid);

    end
end

function nega=Fa(a)
switch a
case 1
    nega=3;
case 2
    nega=4;
case 3
    nega=1;
case 4
    nega=2;
case 5
    nega=7;
case 6
    nega=8;
case 7
    nega=5;
case 8
    nega=6;
case 9
    nega=9;
end

function j=NumToStr(n)

if n<10, j=['00' num2str(n)]; end
if n>=10, j=['0' num2str(n)]; end
if n>=100, j=num2str(n); end

```

***LB-D3Q19* ALGORITHM**

```

clear all
pwd=pwd;

```

```

% cd('G:')

% % directional velocity vectors
e(1,:)=[ 1 0 0];
e(2,:)=[-1 0 0];
e(3,:)=[ 0 1 0];
e(4,:)=[ 0 -1 0];
e(5,:)=[ 0 0 1];
e(6,:)=[ 0 0 -1];
e(7,:)=[ 1 1 0];
e(8,:)=[-1 1 0];
e(9,:)=[-1 -1 0];
e(10,:)=[1 -1 0];
e(11,:)=[ 1 0 1];
e(12,:)=[ 1 0 -1];
e(13,:)=[-1 0 -1];
e(14,:)=[-1 0 1];
e(15,:)=[ 0 1 1];
e(16,:)=[ 0 1 -1];
e(17,:)=[ 0 -1 -1];
e(18,:)=[ 0 -1 1];
e(19,:)=[ 0 0 0];

% % weight factors for each direction
Wght(1:6)=1/18;
Wght(7:18)=1/36;
Wght(19) =1/3;

%-----load image data
[filename, FilePath] = uigetfile('*..*', 'Select First Image to open ...');
im=imread([FilePath,filename]);
cd(cwd);
ImgBaseName=filename(1:size(filename,2)-7);
Ext=filename(size(filename,2)-3:size(filename,2));
tifs=dir([FilePath '*' Ext]);
result=inputdlg({'Image Base Name: ', ...
                'Extension', ...
                'First image number to start: ',...
                ['Number of Files (Total ' num2str(size(tifs,1)) ' files)'],...
                'Output folder: ',...
                'Input Image Information ',1,...
                {ImgBaseName,Ext,'1',num2str(size(tifs,1)), FilePath,})
ImgBaseName=result{1};
Ext=result{2};
StartImage=str2num(result{3});
NumFiles=str2num(result{4});
fldout=result{5};
clear tifs

% % R=5;%mm
res=inputdlg({'Enter the resolution, dz (mm/pixel)', 'Pressure Gradient, dPz
(g/(mm2s2))', 'Tao'},...
            'Resolution',1,{'0.4', '1e-6', '1'});

dz=str2num(res{1});%mm/pixel
dPz_w=str2num(res{2});%g/(mm2s2)
tao=str2num(res{3});

clear p N Neq V U
EndImage=NumFiles+StartImage-1;
cancelButton=0;
h = waitbar(0, ' ', ...
            'Position',[ 243 343 270 93],...
            'Name','Finding Indices...',...
            'CreateCancelBtn','cancelButton = 1;closereq;' );
for k=StartImage:EndImage
Z=k-(StartImage)+1;
waitbar((Z)/NumFiles,h,['Reading Images, image ' num2str(Z) ' of ' num2str(NumFiles)];if
cancelButton==1, break, end
im(:,:,Z)=imread([FilePath ImgBaseName NumToStr(k) Ext]);

```

```

pause (0.0001)
end
close(h)
X=findn(im);
SI=size(im,1);SJ=size(im,2);
% Ai=squeeze(sum(sum(double(im)/max(max(max(double(im))))));
disp('Will Start in 2 sec')
pause(2)
tic
[IA, IB, Io]=find_ind_n3(X,e,FilePath,SI,SJ,NumFiles);
% [IA, IB, Io]=find_ind_n3_periodic(X,e,FilePath,SI,SJ,NumFiles);%may take longer time to
run
toc
save([FilePath '\LBdata-DensityGrad'])

%
Iin=find(X(:,3)==1);
Iout=find(X(:,3)==NumFiles);

SK=NumFiles;
% % I1=find(X(find(X(:,3)==1),2)==SJ/2);
% % I10=intersect(find(X(:,3)==.1*SK),find(X(:,2)==round(SJ/2)));
% % I20=intersect(find(X(:,3)==.2*SK),find(X(:,2)==SJ/2));
% % I30=intersect(find(X(:,3)==.4*SK),find(X(:,2)==SJ/2));
% % I40=intersect(find(X(:,3)==.7*SK),find(X(:,2)==SJ/2));
% % I50=intersect(find(X(:,3)==.9*SK),find(X(:,2)==SJ/2));
t=1;
Ones61=ones(6,1);
Ones121=ones(12,1);

p_w=0.001;%g/mm3
v_w=1;%mm2/s
mu_w=0.001;%g/mm-s
grav_accel=9.81e3;%mm/s2

% % D_w=2*R;
% % D_l=D_w/dz;
p_l=p_w*dz^3;
v_l=(2*tao-1)/6;
mu_l=v_l*p_l;
dt=v_l*dz^2/v_w;
dPz_l=dPz_w*dz^2*dt^2;
gamma_w=p_w*grav_accel;

pin=1.5*NumFiles*dPz_l+p_l
pout=p_l-1.5*NumFiles*dPz_l

F(3,1)=0;%dPz_l/p_l;

% % f_w=1;%1/sec
% % f_l=f_w*dt;%1/time

% p(Iout,1)=p_l;

p=pin-(pin-pout)/(NumFiles-1)*(X(:,3)-1);
Neq(:,1:19)=p*ones(1,19);
clear X im

tend=1e6;
writetodisk%-----
tic
c1=1/4;
c2=1/6;

Porosity=size(p,1)*dz^3/(pi*150^2/4*(SK*dz))

% % % Amp=0.22988;
% try
% % % alfa=R/dz*sqrt(2*pi*f_l/v_l);

```

```

% % % aviobj = avifile([FilePath '-Re-' num2str(Re) '-alfa-' num2str(alfa) ,'-A-'
num2str(Amp) '.avi'])
% % % aviobj.Quality=100; aviobj.Compression='Cinepak'
while t<tend

% F(3,1)=Fmean*(1+Amp*cos(2*pi*f_1*(t-1)));

%-----BEGINNING OF MAIN CALCULATIONS-----
-----
    if t==1
        V(Iin,1:2)=0;
        V(Iin,3)=0;%*(1+Amp*sin(2*pi*f_1*(t-1)));
        V(Iout,1:2)=0;
        V(:,3)=0;%mean(Vpos_1);%Vin_1_av;

        Neq=Neq';
        U(:,1)=V(:,1).*p;
        U(:,2)=V(:,2).*p;
        U(:,3)=V(:,3).*p;

        Neq(1:6,:) =1/18*((Ones61*p')+3*ndmtimes(e(1:6,:), U')+...
        9/2*ndmtimes(e(1:6,:), U').^2-...
        3/2*(Ones61*sum(U.*U,2)'));

        Neq(7:18,:) =1/36*((Ones121*p')+3*ndmtimes(e(7:18,:), U')+...
        9/2*ndmtimes(e(7:18,:), U').^2-...
        3/2*(Ones121*sum(U.*U,2)'));

        Neq(19,:) =1/3*(p'-3/2*sum(U.*U,2)');
        Neq=Neq';
        N=Neq;

    end

    for a=1:18
%       N(IB(a).v,a)=Neq(IA(a).v,a) ;
        N(IB(a).v,a)=N(IA(a).v,a)-1/tao*(N(IA(a).v,a)-Neq(IA(a).v,a))...
        +3*Wght(a)*p(IA(a).v)*(e(a,:)*F);

%       N(Io(a).v,a)=Neq(Io(a).v,Fa3D(a));
        N(Io(a).v,a)=N(Io(a).v,Fa3D(a))-1/tao*(N(Io(a).v,Fa3D(a))-Neq(Io(a).v,Fa3D(a))...
        +3*Wght(Fa3D(a))*p(Io(a).v)*(e(a,:)*F);

    end
    N(:,19)=Neq(:,19);

%Density
p(:,1)=sum(N,2);

%%Velocities
U=(N*e);
V(:,1)=U(:,1)./p;
V(:,2)=U(:,2)./p;
V(:,3)=U(:,3)./p;

%       Inlet Nodes
p(Iin,1)=pin;%*(1+Amp*cos(2*pi*f_1*(t-1)));
V(Iin,1:2)=0;
V(Iin,3)=1-(sum(N(Iin,1:4),2)+sum(N(Iin,7:10),2)+N(Iin,19)+...
        2*(N(Iin,6)+sum(N(Iin,12:13),2)+sum(N(Iin,16:17),2)))./p(Iin,1);

%       N(Iin,5)= N(Iin,6)+1/3*p(Iin,1).*V(Iin,3);
%       N(Iin,15)= N(Iin,17)-c1*(N(Iin,3)-N(Iin,4))+c2*p(Iin,1).*V(Iin,3);
%       N(Iin,18)= N(Iin,16)+c1*(N(Iin,3)-N(Iin,4))+c2*p(Iin,1).*V(Iin,3);
%       N(Iin,11)= N(Iin,13)-c1*(N(Iin,1)-N(Iin,2))+c2*p(Iin,1).*V(Iin,3);
%       N(Iin,14)= N(Iin,12)+c1*(N(Iin,1)-N(Iin,2))+c2*p(Iin,1).*V(Iin,3);
%       Uin=(N(Iin,:)*e);
%       dU=(p(Iin,1).*V(Iin,3)./Uin(:,3))

```

```

% Outlet Nodes
p(Iout,1)=pout;%%*(1-Amp*sin(2*pi*f_l*(t-1)));
V(Iout,1:2)=0;

V(Iout,3)=-1+(sum(N(Iout,1:4),2)+sum(N(Iout,7:10),2)+N(Iout,19)+...

2*(N(Iout,5)+sum(N(Iout,14:15),2)+N(Iout,11)+N(Iout,18)))./p(Iout,1);
% N(Iout,6)= N(Iout,5)-1/3*p(Iout,1).*V(Iout,3);
% N(Iout,17)= N(Iout,15)+c1*(N(Iout,3)-N(Iout,4))-c2*p(Iout,1).*V(Iout,3);
% N(Iout,18)= N(Iout,18)-c1*(N(Iout,3)-N(Iout,4))-c2*p(Iout,1).*V(Iout,3);
% N(Iout,13)= N(Iout,11)+c1*(N(Iout,1)-N(Iout,2))-c2*p(Iout,1).*V(Iout,3);
% N(Iout,12)= N(Iout,14)-c1*(N(Iout,1)-N(Iout,2))-c2*p(Iout,1).*V(Iout,3);
%
% % Vdiff=Vin_l_av*(1+Amp*sin(2*pi*f_l*(t-1)))-mean(V(:,3));

% % Inlet Nodes
% V(Iin,1:2)=0;
% V(Iin,3)= Vin(Iin,1);%mean(V(Iin,3))*(1+Amp*cos(2*pi*f_l*(t-1)));
% % % V(Iin,3)=Vin_l_av*(1+Amp*sin(2*pi*f_l*(t-1)));
% p(Iin,1)=1./(1-V(Iin,3)).*(sum(N(Iin,1:4),2)+sum(N(Iin,7:10),2)+N(Iin,19)+...
% 2*(N(Iin,6)+sum(N(Iin,12:13),2)+sum(N(Iin,16:17),2)));
%
% % Outlet Nodes
% V(Iout,1:2)=0; %%%fix velocity in x and y directions to zero
% V(Iout,3)=Vin(Iin,1);%V(Iout,3)+Vdiff;
%
% p(Iout,1)=1./(1+V(Iout,3)).*(sum(N(Iout,1:4),2)+sum(N(Iout,7:10),2)+N(Iout,19)+...
% 2*(N(Iout,5)+sum(N(Iout,14:15),2)+N(Iout,11)+N(Iout,18)));

%---Calculate new Neq
Neq=Neq';
U(:,1)=V(:,1).*p;
U(:,2)=V(:,2).*p;
U(:,3)=V(:,3).*p;
Neq(1:6,:) =1/18*((Ones61*p')+3*ndmtimes(e(1:6,:), U')+...
9/2*ndmtimes(e(1:6,:), U').^2-...
3/2*(Ones61*sum(U.*U,2)'));
Neq(7:18,:) =1/36*((Ones121*p')+3*ndmtimes(e(7:18,:), U')+...
9/2*ndmtimes(e(7:18,:), U').^2-...
3/2*(Ones121*sum(U.*U,2)'));
Neq(19,:) =1/3*(p'-3/2*sum(U.*U,2)');
Neq=Neq';

% pause (0.0001)
t=t+1;
disp(['t= ' num2str(t) ' , el_time per step= ' num2str(toc) ' sec'])
tic

%-----END OF MAIN CALCULATIONS-----
----
if round(t/l)==t/l
Re=mean(U(:,3))/mean(p)*(SI)/v_l;
Vmean_l=mean(U(:,3))/mean(p);
Vmean_w=Vmean_l*dz/dt;
Vdarcy_w=Vmean_w*Porosity;
k_w=Vdarcy_w/(dPz_w/gamma_w);

%
% MFR_l=U(:,3).*Ai(X(:,3))
figure(1)
subplot(3,1,1),plot(t,k_w,'. '),hold on,ylabel('k (mm/s)')
title(['t= ' num2str(t-1) ' , k= ' num2str(k_w) ' mm/s, Re= ' num2str(Re)]);% ' ,
alfa= ' num2str(alfa)]
% subplot(3,1,2),hold on

subplot(3,1,3),newplot,plot(p,'r-'),title(['mean density= ', num2str(mean(p))])
pause (0.0001)

% frame = getframe(gcf);
% aviobj = addframe(aviobj,frame);
end

```

```

    if round(t/10)==t/10
        fid=fopen([FilePath '\k.txt'],'a');
        fprintf(fid,'%6.0f %12.6e %12.6e \n',[t k_w Vmean_w]);
        fclose(fid);
    end
    if round(t/1000)==t/1000
        close
    end

    if round(t/300)==t/300
        save([FilePath '\LBdata-5-DensityGrad'])
    end
% break
end
% aviobj = close(aviobj);
% catch
% save(['c:\temp\LBdata-5-DensityGrad'])
%
% % %    close all
% % %    aviobj = close(aviobj);
%     errordlg(lasterr,'Error')
% end
%
function nega=Fa3D(a)
switch a

case 1
    nega=2;
case 2
    nega=1;
case 3
    nega=4;
case 4
    nega=3;
case 5
    nega=6;
case 6
    nega=5;
case 7
    nega=9;
case 8
    nega=10;
case 9
    nega=7;
case 10
    nega=8;
case 11
    nega=13;
case 12
    nega=14;
case 13
    nega=11;
case 14
    nega=12;
case 15
    nega=17;
case 16
    nega=18;
case 17
    nega=15;
case 18
    nega=16;
case 19
    nega=19;

end

function [IAt2, IBt2, Iot2]=find_ind_n3(X,e,FilePath,SI,SJ,NumFiles)

```

```

ZI=[0];
for i=1:NumFiles
    I=find(X(:,3)==i);
    ZI=[ZI;max(I)];
end

ZI
% periodic BC does not work in this algorithm 11/29/04 ( at least hard to implement)
for i=1:18
    i, tic
    switch i
    case {1,2,3,4,7,8,9,10}
        IAF=[];
        IBf=[];
        Iof=[];
        for z=2:NumFiles+1

            Xp=[X(:,1)-e(i,1) X(:,2)-e(i,2) X(:,3)-e(i,3)];

            [C, IA, IB]=intersect(X(ZI(z-1)+1:ZI(z),:), Xp(ZI(z-1)+1:ZI(z),:),'rows');

            [C, Io]=setdiff(Xp(ZI(z-1)+1:ZI(z),:), X(ZI(z-1)+1:ZI(z),:),'rows'); %in Xp but
not in X

            IAF=[IAf;ZI(z-1)+IA];
            IBf=[IBf;ZI(z-1)+IB];
            Iof=[Iof;ZI(z-1)+Io];
            end
            fid=fopen([FilePath '\IA-' num2str(i) '.bin'],'wb');
            fwrite(fid, IAF, 'double');
            fclose(fid);

            fid=fopen([FilePath '\IB-' num2str(i) '.bin'],'wb');
            fwrite(fid, IBf, 'double');
            fclose(fid);

            fid=fopen([FilePath '\Io-' num2str(i) '.bin'],'wb');
            fwrite(fid, Iof, 'double');
            fclose(fid);

        case {6,12,13,16,17}
            IAF=[];
            IBf=[];
            Iof=[];
            for z=2:NumFiles
                Xp=[X(:,1)-e(i,1) X(:,2)-e(i,2) X(:,3)-e(i,3)];

                [C, IA, IB]=intersect(X(ZI(z)+1:ZI(z+1),:), Xp(ZI(z-1)+1:ZI(z),:),'rows');

                [C, Io]=setdiff(Xp(ZI(z-1)+1:ZI(z),:), X(ZI(z)+1:ZI(z+1),:),'rows'); %in Xp but
not in X

                IAF=[IAf;ZI(z)+IA];
                IBf=[IBf;ZI(z-1)+IB];
                Iof=[Iof;ZI(z-1)+Io];
            end
            Iof=[Iof;[ZI(NumFiles)+1:ZI(NumFiles+1)]];
            fid=fopen([FilePath '\IA-' num2str(i) '.bin'],'wb');
            fwrite(fid, IAF, 'double');
            fclose(fid);

            fid=fopen([FilePath '\IB-' num2str(i) '.bin'],'wb');
            fwrite(fid, IBf, 'double');
            fclose(fid);

            fid=fopen([FilePath '\Io-' num2str(i) '.bin'],'wb');
            fwrite(fid, Iof, 'double');
            fclose(fid);

        case {5,11,14,15,18}

```

```

    Iaf=[];
    IBf=[];
    Iof=[];
    for z=3:NumFiles+1
        Xp=[X(:,1)-e(i,1) X(:,2)-e(i,2) X(:,3)-e(i,3)];

        [C, IA, IB]=intersect(X(ZI(z-2)+1:ZI(z-1),:), Xp(ZI(z-1)+1:ZI(z),:),'rows');

        [C, Io]=setdiff(Xp(ZI(z-1)+1:ZI(z),:), X(ZI(z-2)+1:ZI(z-1),:),'rows'); %in Xp but
not in X

        IAf=[IAf;ZI(z-2)+IA];
        IBf=[IBf;ZI(z-1)+IB];
        Iof=[Iof;ZI(z-1)+Io];
    end
    Iof=[[ZI(1)+1:ZI(2)'];Iof];

    fid=fopen([FilePath '\IA-' num2str(i) '.bin'],'wb');
    fwrite(fid, IAf, 'double');
    fclose(fid);

    fid=fopen([FilePath '\IB-' num2str(i) '.bin'],'wb');
    fwrite(fid, IBf, 'double');
    fclose(fid);

    fid=fopen([FilePath '\Io-' num2str(i) '.bin'],'wb');
    fwrite(fid, Iof, 'double');
    fclose(fid);

end
toc
end

for i=1:18
disp('Reading ...')
    fid=fopen([FilePath '\IA-' num2str(i) '.bin'],'r');
    IA2(i).v=fread(fid, 'double');
    fclose(fid);

    fid=fopen([FilePath '\IB-' num2str(i) '.bin'],'r');
    IB2(i).v=fread(fid, 'double');
    fclose(fid);

    fid=fopen([FilePath '\Io-' num2str(i) '.bin'],'r');
    Iot2(i).v=fread(fid, 'double');
    fclose(fid);

end

function ind=findn(arr);

%FINDN Find indices of nonzero elements.
% I = FINDN(X) returns the indices of the vector X that are
% non-zero. For example, I = FINDN(A>100), returns the indices
% of A where A is greater than 100. See RELOP.
%
% This is the same as find but works for N-D matrices using
% ind2sub function
%
% It does not return the vectors as the third output argument
% as in FIND
%
% The returned I has the indices (in actual dimensions)
%
% x(:, :, 1)          x(:, :, 2)          x(:, :, 3)
%   = [ 1 2 3          =[11 12 13          =[21 22 23
%       4 5 6          14 15 16          24 25 26
%       7 8 9]         17 18 19]         27 28 29]

```

```

%
% I=find(x==25) will return 23
% but findn(x==25) will return 2,2,3
%
% Also see find, ind2sub

% Loren Shure, Mathworks Inc. improved speed on previous version of findn
% by Suresh Joel Mar 3, 2003

in=find(arr);
sz=size(arr);
if isempty(in), ind=[]; return; end;
[out{1:ndims(arr)}] = ind2sub(sz,in);
% ind = cell2mat(out);
ind(:,1)=out{: ,1};
ind(:,2)=out{: ,2};
ind(:,3)=out{: ,3};
function z = ndmtimes(x, y)
%NDMTIMES N-dimensional matrix multiply.
%
% NDMTIMES(X, Y) is equivalent to X*Y except that the former is vectorized
% along higher dimensions (dimensions three and above).
%
% NDMTIMES(X) is equivalent to NDMTIMES(X, X).
%
% Examples
% -----
% In this example we want to multiply a matrix X with every page (2-D slice)
% of a 3-D array Y.
%
%     X = randn(4, 3);
%     Y = randn(3, 5, 7);
%
%     % the way to do it with a loop
%     Z1 = zeros(4, 5, 7);
%     for i = 1:7
%         Z1(:, :, i) = X(:, :) * Y(:, :, i);
%     end
%
%     % this does it without a loop
%     Z2 = ndmtimes(X, Y);
%
% In the following example X is a 4-D array and Y is a 5-D array. Every page
% in X is multiplied with the corresponding page in Y. Scalar expansion is
% done along singleton dimensions (dimension 5 in X and dimension 4 in Y).
%
%     X = randn(4, 3, 6, 7, 1);
%     Y = randn(3, 5, 6, 1, 5);
%
%     % the way to do it with a loop
%     Z1 = zeros(4, 5, 6, 7, 5);
%     for k = 1:5
%         for j = 1:7
%             for i = 1:6
%                 Z1(:, :, i, j, k) = X(:, :, i, j, 1) * Y(:, :, i, 1, k);
%             end
%         end
%     end
%
%     % this does it without a loop
%     Z2 = ndmtimes(X, Y); % Z2 will be identical to Z1.
%
% Notes
% -----
% When X and Y are complex, the result might deviate a little from what a
% loop would give. The reason for this is that each element is computed by
% scalar multiplication and addition rather than vector multiplication. The
% effect can be seen in the example
%
%     N = 5;
%     X = complex(randn(1, N), randn(1, N));

```

```

%     Y = complex(randn(N, 1), randn(N, 1));
%     Z1 = sum(X(:) .* Y(:));
%     Z2 = X * Y;
%
%     The larger N is, the more frequently Z1 and Z2 will be different.
%
%     See also MTIMES.

%     Author:      Peter J. Acklam
%     Time-stamp:  2003-11-20 16:04:54 +0100
%     E-mail:      pjacklam@online.no
%     URL:         http://home.online.no/~pjacklam

nargsin = nargin;
error(nargchk(1, 2, nargsin));

if (nargsin == 1) | isequal(x, y)

    %
    % We're computing the square of X, i.e., X * X.
    %

    % Get size of input arguments.
    sx = size(x);
    dx = ndims(x);

    i = 1:sx(1); i = i(ones(1,sx(2)),:).';
    j = 1:sx(2); j = j(ones(1,sx(1)),:);

    y = permute(x, [2, 1, 3:dx]);
    z = reshape(sum(x(i,:,:) .* y(j,:,:), 2), sx);

else

    % Get size of input arguments.
    sx = size(x);
    sy = size(y);
    dx = ndims(x);
    dy = ndims(y);

    if dx == 2

        %
        % X is a 2D matrix.
        %

        if dy == 2

            %
            % X and Y are 2D matrices.
            %

            z = x * y;

        else

            %
            % X is a 2D matrix and Y is a 3+D array.
            %

            ny = numel(y);
            ytmp = reshape(y, [sy(1), ny/sy(1)]);
            z = reshape(x*ytmp, [sx(1), sy(2:dy)]);

        end

    else

        %
        % X is a 3+D array.
        %

```

```

if dy == 2

    %
    % X is a 3+D array and Y is a 2D matrix.
    %
    nx = numel(x);
    xtmp = permute(x, [1 3:dx 2]);
    xtmp = reshape(xtmp, [nx/sx(2), sx(2)]);
    z = xtmp*y;
    z = reshape(z, [sx([1 3:dx]) sy(2)]);
    z = permute(z, [1 dx 2:dx-1]);

else

    %
    % X is a 3+D array and Y is a 3+D array.
    %
    % See if inner matrix dimensions agree.
    if sx(2) ~= sy(1)
        error('Inner matrix dimensions must agree.');
```

end

```

    % Pad the size vectors with trailing singleton dimensions (if
    % necessary) so the vectors get the same length.
    sx = [sx, ones(1, dy-dx)];
    sy = [sy, ones(1, dx-dy)];

    % See if higher dimensions are compatible, remembering that we
    % allow expansion of singleton dimensions.
    if any( (sx(3:end) ~= sy(3:end)) ...
           & (sx(3:end) ~= 1) ...
           & (sy(3:end) ~= 1) )
        error('Incompatible higher dimensions.');
```

end

```

    %
    % Now expand any singleton dimensions in either argument to
    % match the size of the other argument.
    %

    % Compute the size of "z" and the number of dimensions.
    sz = [sx(1), sy(2), max(sx(3:end), sy(3:end))];
    dz = length(sz);

    % Replicate "x" along scalar dimensions.
    xrep = sz(3:end);
    xrep(sx(3:end) == sz(3:end)) = 1;
    x = repmat(x, [1, 1, xrep]);

    % Replicate "y" along scalar dimensions.
    yrep = sz(3:end);
    yrep(sy(3:end) == sz(3:end)) = 1;
    y = repmat(y, [1, 1, yrep]);

    %
    % Now compute the product of "x" and "y".
    %

    % for speed (doesn't save much though) inline
    %
    [j, i] = meshgrid(1:sz(2), 1:sz(1));
    %
    i = 1:sz(1); i = i(ones(1, sz(2)),:).';
    j = 1:sz(2); j = j(ones(1, sz(1)),:);

    y = permute(y, [2, 1, 3:dz]);
    z = reshape(sum(x(i,:,:).* y(j,:,:), 2), sz);

```

```

end

end

end

function writetodisk

fid=fopen([FilePath '\Input-' filename '.txt'],'w');
fprintf(fid,'%50s \n', ['Simulation of Fluid Flow Using Lattice Boltzmann Equation']);
fprintf(fid,'%50s \n', ['Type: D3Q19 Lattice']);
fprintf(fid,'%50s \n', ['Program By: Muhammed Emin Kutay']);
fprintf(fid,'%50s \n', ['-----']);
fprintf(fid,'%35s %20s \n', 'Simulation Date: ', date);
fprintf(fid,'%35s %20s \n', 'Description: ', fldout);
fprintf(fid,'%35s %20s \n', 'Image Base Name:', ImgBaseName);
fprintf(fid,'%35s %20s \n', 'First image number to start: ', num2str(StartImage));
fprintf(fid,'%35s %20s \n', 'Number of Images :', num2str(NumFiles));
fprintf(fid,'%35s %20s \n', 'Image size in x direction :', num2str(SI));
fprintf(fid,'%35s %20s \n', 'Image size in y direction :', num2str(SJ));
fprintf(fid,'%35s %20s \n', 'Density at Inlet: ', num2str(pin));
fprintf(fid,'%35s %20s \n', 'Density at Outlet: ', num2str(pout));
fprintf(fid,'%35s %40s \n', 'Acceleration body force vector:', [' ' num2str(F) ' ' ]
]);
% fprintf(fid,'%35s %20s \n', 'Termination time: ', num2str(tend));
% fprintf(fid,'%35s %20s \n', 'Max tolerance for termination: ', num2str(TOL) );
fprintf(fid,'%35s %20s \n', 'tao: ', num2str(tao) );
fclose(fid);

```

IMAGETHRESHOLD ALGORITHM

```

%           THIS PROGRAM CONVERTS GRAYSCALE IMAGES TO BINARY
%           (BLACK AND WHITE) IMAGES.
%           PROGRAM LETS YOU SELECT A CIRCULAR REGION OF INTEREST
%           OUTPUT BW IMAGES WILL BE CREATED IN FOLDER "C:\TEMP\output folder\"
%           *****MUHAMMED EMIN KUTAY*****

clear all,
close all
[filename, DirName] = uigetfile('*..*', 'Select First Image to open ...');
im=imread([DirName,filename]);

ImgBaseName=filename(1:size(filename,2)-7);
Ext=filename(size(filename,2)-3:size(filename,2));
tifs=dir([DirName '*' Ext]);
result=inputdlg({'Image Base Name: ', ...
'Extension', ...
'First image number to start: ',...
['Number of Files (Total ' num2str(size(tifs,1)) ' files)'],...
'Enter output folder (enter an existing folder): ',...
'Enter output filename: ',...
'Frame Rate: ',...
'Image Numbering Style (0 for image012, 1 for image12',...
'Gray Threshold Value (0-255):'},...
'Input Image Information ',1,...
{ImgBaseName,Ext,'1',num2str(size(tifs,1)),DirName, 'bw','1','0','255'})

FileName=result{1};
Ext=result{2};
StartImage=str2num(result{3});
NumFiles=str2num(result{4});
fldout=result{5};
fileout=result{6};
f=str2num(result{7});
NumbStyle=str2num(result{8});
Thresh=str2num(result{9});

```

```

clear tifs

ButtonName=questdlg('Import region of interest data ? ', ...
                    'ROI', ...
                    'Yes','No','No');

switch ButtonName,
case 'Yes',
    Qcontcir='Yes';
    [filenameT, pathnameT] = uigetfile('*.txt', 'Select XY data file...');
    data=load([pathnameT, filenameT]);
    D=load([pathnameT, 'D.txt']);
    X=data(:,1); Y=data(:,2)+2;
case 'No',
    Qcontcir='No ';
end % switch

cancelButton=0;
h = waitbar(0,'Please Wait', ...
            'Position',[ 243  343  270  93],...
            'Name','Please Wait',...
            'CreateCancelBtn','cancelButton = 1;closereg;','visible','off' );

for k = 1:NumFiles

    s1=f*k+StartImage-1;
    if NumbStyle==0
        j0=NumToStr(s1);
    else
        j0=num2str(s1);
    end

    if (Ext=='.ppm') | (Ext=='.pgm') |(Ext=='.pbm')
        im = pnmread([DirName FileName j0 Ext]);
    else
        im = imread([DirName FileName j0 Ext]);
    end

    %for uint16 images-----
    if max(max(im))>255
        disp('This image is a 16 bit image and will be converted to 8 bit
image')
        maxval=double(max(max(im)));
        im=uint8(255*double(im)/maxval);
    end

    %
    im(:,:,2:3)=[];

    %-----Apply a median filter (3x3)
    %
    im=medfilt2(im);
    %-----

    if Qcontcir=='No '
        [im, D, X, Y] = CirRegOI(im); % select circular region of interest
        Qcontcir=questdlg('Apply this region to all images ? (y/n) :', ...
                            'Apply All', ...
                            'Yes','No ','Yes');
    else
        im2=roipoly(im,X,Y);
        Qlogical=islogical(im2);

    %
        if Qlogical==0
            im2=immultiply(imcomplement(im2),255);
            im=imadd(im,im2);
        %
        else
            im2=imcomplement(im2)*255;
        %
    end
end

```

```

%             im=imadd(im,uint8(im2));
%             end

                end

im=imcomplement(im); %pores will be white in color, and rest will be black
bw1=im2bw(im,Thresh/255);
imwrite(bw1,[fldout fileout numtostr(k) '.tif'],'tif','compression','none')

TotPoreArea2(k)=bwarea(bw1);
TotPoreArea3(k)=sum(sum(bw1));

set(h,'visible','on')
waitbar(k/NumFiles, h,'Please wait while thresholding images...')
if cancelButton==1, break, end
end

close(h)

fid=fopen([fldout '\XY.txt'],'w')
fprintf(fid,'%6.1f %12.1f \n',[X,Y]);
fclose(fid);

fid=fopen([fldout '\D.txt'],'w')
fprintf(fid,'%6.0f \n', D);
fclose(fid);

%-----Calculate Porosity-----
SurfArea=pi*D^2/4;
Porosity2=TotPoreArea2/SurfArea*100;
Porosity3=TotPoreArea3/SurfArea*100;
avgpor2=mean(Porosity2);avgpor3=mean(Porosity3);
y=[[1:size(Porosity2,2)];TotPoreArea2;Porosity2;TotPoreArea3;Porosity3];
fid = fopen([fldout '\ ' FileName '_Porosity.txt'],'w');
fprintf(fid,'%5s\t %9s\t %9s\t %9s\t %9s
\n','Image','PoreArea','Porosity','PoreArea','Porosity' );
fprintf(fid,'%5s\t %9s\t %9s\t %13s\t %5s \n','
','(bwarea)','(%)','(sum(sum(im))','(%)');
fprintf(fid,'%5.0f %15.0f %7.1f %15.0f %7.1f \n',y);
fprintf(fid,'Average Porosity = %5.3f %% \t \t \t %5.3f %%\n',avgpor2,avgpor3);
fclose(fid);

        break
load handel; y=y(2500:5000);%to play music after threshold is done
sound(y,Fs)%to play music after threshold is done

```

POROSITYFIND ALGORITHM

```

% -----load image data
clear all
% tic
% while toc<36000
cwd=pwd;
% cd(['G:\0X-ray CT raw Images\'])
[filename, FilePath] = uigetfile('*..*', 'Select First Image to open ...');
im=imread([FilePath,filename]);
cd(cwd)
ImgBaseName=filename(1:size(filename,2)-7);
Ext=filename(size(filename,2)-3:size(filename,2));
tifs=dir([FilePath '*' Ext]);

```

```

k=0;
for i=1:size(tifs,1),
    SImg=size(ImgBaseName,2);
    if size(tifs(i).name,2)>=SImg
        if tifs(i).name(1:SImg)==ImgBaseName,
            k=k+1;
        end
    end
end
end
Ext=filename(size(filename,2)-3:size(filename,2))
def = {ImgBaseName,Ext,'1',num2str(k),FilePath,'pi/4*490^2'};
result=inputdlg({'Image Base Name: ', 'Extension', 'First image number to start: ',...
    ['Number of Files (Total ' num2str(k) ' files)'],...
    'Output Folder:','Cross sectional area'},...
    'Input Image Information ',1,def)
ImgBaseName=result{1}
Ext=result{2}
StartImage=str2num(result{3})
NumFiles=str2num(result{4})
fldout=result{5}
Acs=str2num(result{6})
clear tifs

EndImage=NumFiles+StartImage-1;
cancelButton=0;
h = waitbar(0,'Loading Images', ...
    'Position',[ 243 343 270 93],...
    'Name','Please wait ...',...
    'CreateCancelBtn','cancelButton = 1;closereq;' );

for k=StartImage:EndImage

    waitbar((k-StartImage+1)/NumFiles,h,['Reading Images, Current Image= ' num2str(k)])
    if cancelButton==1, break, end
    im=imread([FilePath ImgBaseName NumToStr(k) Ext]);
    if max(max(im))>1, im=im2bw(im,.00001);end
    TotPoreArea2(k-StartImage+1)=bwarea(im);
    TotPoreArea3(k-StartImage+1)=sum(sum(im));
    end
close(h)

%-----Calculate Porosity-----
Porosity2=TotPoreArea2/Acs*100;
Porosity3=TotPoreArea3/Acs*100;
avgpor2=mean(Porosity2);avgpor3=mean(Porosity3);
y=[[1:size(Porosity2,2)];TotPoreArea2;Porosity2;TotPoreArea3;Porosity3];
fid = fopen([fldout ImgBaseName '_Porosity.txt'],'a');
fprintf(fid,'%5s\t %9s\t %9s\t %9s\t %9s\t %9s\n',
    'Image','PoreArea','Porosity','PoreArea','Porosity' );
fprintf(fid,'%5s\t %9s\t %9s\t %13s\t %5s\n',
    '(bwarea)', '(%)', '(sum(sum(im))', '(%)');
fprintf(fid,'%5.0f %15.0f %7.1f %15.0f %7.1f\n',y);
fprintf(fid,'Average Porosity = %5.3f %% \t \t \t %5.3f
%%\n',avgpor2,avgpor3);
fclose(fid);

err_draw_l(Porosity2')
xlabel('Depth'),ylabel('Porosity (%)'),title(fldout)
saveas(gcf,[fldout '\Porosity.emf'],'emf')

```

PORECON ALGORITHM

```

% %          PROGRAM FINDS CONNECTED PORES AND ELIMINATES THE REST
% %          OUTPUT BW IMAGES WILL CONSIST OF ONLY CONNECTED PORES
% %          *****MUHAMMED EMIN KUTAY*****

```

```

%
clear all,
close all
[filename, FilePath] = uigetfile('*.tiff', 'Select First Image to open ...');
im=imread([FilePath,filename]);

ImgBaseName=filename(1:size(filename,2)-7);
Ext=filename(size(filename,2)-3:size(filename,2));
tifs=dir([FilePath '*.tiff']);
k=0;
for i=1:size(tifs,1),
    SImg=size(ImgBaseName,2);
    if size(tifs(i).name,2)>=SImg
        if tifs(i).name(1:SImg)==ImgBaseName,
            k=k+1;
        end
    end
end
end

result=inputdlg({'Image Base Name: ', ...
                'Extension', ...
                'First image number to start: ',...
                ['Number of Files (Total ' num2str(k) ' files)'],...
                'Diameter (for porosity calculation)',...
                'Input Image Information ',1,...
                {ImgBaseName,Ext,'1',num2str(k),'100'}})
ImgBaseName=result{1};
Ext=result{2};
StartImage=str2num(result{3});
NumFiles=str2num(result{4});
D=str2num(result{5});
% cd(cwd)
clear tifs

for k=StartImage:StartImage+NumFiles-1
    im=imread([FilePath ImgBaseName numtostr(k) Ext]);
    if max(max(im))>1, im=im2bw(im,.00001);end
    bw(:,:,k-StartImage+1)=im;
    k
end %k

tic;
disp('Labeling connected pores ...')
[L,Num] = bwlabeln(bw,18);
disp([' Labeling Complete in ' num2str(toc) ' seconds'])
L=uint32(L);

I=regionprops(double(L),'BoundingBox');
for j=1:Num, ch(j,:)=I(j).BoundingBox; end
hist(ch(:,6),NumFiles), ylabel('Number of occurrences of each depth');
xlabel('Depth (x0.8mm)');
title([ImgBaseName]); fig1=gcf;
% fid = fopen(['c:\temp\porosities\' ImgBaseName '-Connectivity.txt'],'a');
% fprintf(fid,'%10.2f %10.2f %10.2f %10.2f %10.2f %10.2f\n',ch');
% fclose(fid);

% break

disp (' Started seperating pores ...')

askeddepth=input('Enter channel depth : ');

ind=find(ch(:,6)>=askeddepth);

disp('Indices of the channels are:')
disp([ind])

% ind=0
% askedChannel=0

```

```

% askeddepth=96

askedChannel=input('Channel to generate image (press ''0'' to for all channels found):
');
if askedChannel ==0
    n=1, NumChannels=size(ind,1);
else
    n=find(askedChannel);, NumChannels=n;
end
tic;
% c=0;

while n <= NumChannels
    depth=0;
    disp(['Searching for channel ' num2str(ind(n))]% ' of ' num2str(NumChannels)])

        I=findn(L==ind(n));
    if isempty(I)==0
        stDepth=min(I(:,3));
        enDepth=max(I(:,3));
        depth=enDepth-stDepth+1;
        if depth>=askeddepth
            %
                c=c+1;
            %
                ChIndex(:,c)=I;
                disp(['Channel ' num2str(ind(n)) ' that has a depth of ' num2str(depth) ' is
being added to image matrix'])
                for i=1:size(I,1)
                    E(I(i,1), I(i,2), I(i,3))=uint8(255);
                end
                disp('Done ...')
                clear I
            end
        end
        n=n+1;

        if toc>100, break, end
end %while
E(size(E,1)+1, :, :)=0;
E(:, size(E,2)+1, :)=0;

[filename, pathname] = uiputfile('*..*', ['Pick a folder to write images for depth '
num2str(depth)] );
for k=1:size(L,3)
    bw1=im2bw(E(:, :, k), 0.0000000001);
    TotPoreArea2(k)=bwarea(bw1);
    TotPoreArea3(k)=sum(sum(bw1));
    imwrite(bw1,[pathname filename numtostr(k) '.tif'],'tif','compression','none')
end

%-----Calculate Porosity-----
SurfArea=pi*D^2/4;
Porosity2=TotPoreArea2/SurfArea*100;
Porosity3=TotPoreArea3/SurfArea*100;
avgpor2=mean(Porosity2);avgpor3=mean(Porosity3);
y=[1:size(Porosity2,2)];TotPoreArea2;Porosity2;TotPoreArea3;Porosity3];
fid = fopen([pathname filename '_Porosity.txt'],'w');
fprintf(fid,'%5s\t %9s\t %9s\t %9s\t %9s
\n','Image','PoreArea','Porosity','PoreArea','Porosity' );
fprintf(fid,'%5s\t %9s\t %9s\t %13s\t %5s \n','
','(bwarea)','(%)','(sum(sum(im))','(%)');
fprintf(fid,'%5.0f %15.0f %7.1f %15.0f %7.1f \n',y);
fprintf(fid,'Average Porosity = %5.3f %% \t \t \t %5.3f %%\n',avgpor2,avgpor3);
fclose(fid);

```

SSA ALGORITHM

```

clear all,cd('f:\0X-ray CT raw Images')
[filename, FilePath] = uigetfile('*..*', 'Select First Image to open ...');
ImgBaseName=filename(1:size(filename,2)-7)
Ext=filename(size(filename,2)-3:size(filename,2))
tifs=dir([FilePath '*.tif']);
k=0;
for i=1:size(tifs,1),
    SImg=size(ImgBaseName,2);
    if size(tifs(i).name,2)>=SImg
        if tifs(i).name(1:SImg)==ImgBaseName,
            k=k+1;
        end
    end
end
end
StartImage=1,%input('First image number to start ? : ');

NumFiles=k,%input('Number of Files :');
dz=0.8,%input('Enter Vertical Resolution: ');
PixRes=150/478,%input('Enter Horizontal Pixel Resolution (in mm/pixel) or press enter to
determine: ');
if isempty(PixRes)==1
    [filename2, FilePath2] = uigetfile('*..*', 'Select an Image ...');
    imshow(imread([FilePath2 filename2]))
    [X, Y]=getline(gcf);
    dist=round(sqrt((X(2)-X(1))^2+ (Y(2)-Y(1))^2));
    disp(['Distance = ' num2str(dist) ' pixels'])
    Distmm=input('Enter distance in mm : ');
    PixRes=Distmm/dist;
    disp(['Pixel Resolution is ' num2str(PixRes) ' mm/pixels'])
else
    Distmm=150,%input('Enter diameter of sample in mm : ');
end

i=1;Perimeter=[];
while i~=-NumFiles+StartImage

    if i<10, j=['00' num2str(i)];, end
    if i>=10, j=['0' num2str(i)];, end
    if i>=100, j=num2str(i);, end
    im=imread([FilePath ImgBaseName j Ext]);
    area(i,1)=bwarea(im);
        Pim=bwperim(im);Perimeter(i,1)=bwarea(Pim);
    i=i+1
end %while
Perimeter(:,2)= Perimeter(:,1) * PixRes;
Perimeter(:,3)= Perimeter(:,2) * dz;
area(:,2)=area(:,1) * (PixRes)^2;
Si=sum(Perimeter(:,3))
V=(pi*Distmm^2/4) * NumFiles * dz

S=Si/V

% break

[area Perimeter]
y=[1:size(area,1)];area'; Perimeter'];

[filename, pathname] = uiputfile('*..*', 'Select data location to save ...');

fid = fopen([pathname filename], 'w');
    fprintf(fid, '%10s\t %10s\t %15s\t %14s\t %14s %14s
\n', 'Slice', 'Area', 'Area', 'Perimeter', 'Perimeter', 'SurfArea' );
    fprintf(fid, '%10s\t %12s\t %13s\t %14s\t %14s %14s \n', '
', '(pixels)', '(mm^2)', '(pixels)', '(mm)', '(mm^2)');
%
    fprintf(fid, '%5.0f %7.1f %7.1f %9.1f %9.1f %9.1f \n', y);

```

```

        fprintf(fid,'%10.0f %15.2f %15.2f %15.2f %15.2f %15.2f \n',y);

        fprintf(fid,'%20s \t\t %5.1f \n', 'Total Surface Area of Pores (mm^2)    : ', Si);
        fprintf(fid,'%20s \t\t %5.1f \n', 'Total Volume of Specimen (mm^3)      : ', V);
        fprintf(fid,'%20s \t\t %5.6f \n', 'Specific Surface Area (1/mm)        : ', S);
fclose(fid);
disp(' All Done ...')

open([pathname filename])

```

TORT3D ALGORITHM

```

clear all,
% cd('g:\X-ray CT raw Images')
[filename, FilePath] = uigetfile('*..*', 'Select First Image to open ...');
ImgBaseName=filename(1:size(filename,2)-7)
Ext=filename(size(filename,2)-3:size(filename,2))
tifs=dir([FilePath '*.tif']);
k=0;
for i=1:size(tifs,1),
    SImg=size(ImgBaseName,2);
    if size(tifs(i).name,2)>=SImg
        if tifs(i).name(1:SImg)==ImgBaseName,
            k=k+1;
        end
    end
end
end
StartImage=1('First image number to start ? : ');
NumFiles=k,('Number of Files : ');
imdx=150/478,('Enter Horizontal Pixel Resolution (in mm/pixel) or press enter to
determine: ');
imdy=150/478
imdz=0.8,('Enter Vertical Resolution: ');
SK=NumFiles;
for i=1:SK-1
    z=i+StartImage-1

    im1=imread([FilePath ImgBaseName NumToStr(z) Ext]);
    im2=imread([FilePath ImgBaseName NumToStr(z+1) Ext]);
    if max(max(im1))>1, im1=im2bw(im1,.5);im2=im2bw(im2,.5);end
    L=bwlabeln(im1,8);
    Rpr=regionprops(L,'Centroid');
    for j=1:size(Rpr,1), ctr1(j,:)=Rpr(j).Centroid;end
    L=bwlabeln(im2,8);
    Rpr=regionprops(L,'Centroid');
    for j=1:size(Rpr,1), ctr2(j,:)=Rpr(j).Centroid;end

    ct{i}=ctr1;
    ct{i+1}=ctr2;
    Ind=[];
    for j=1:size(ctr1,1)
        dx=imdx*(ctr1(j,1)-ctr2(:,1));
        dy=imdy*(ctr1(j,2)-ctr2(:,2));
        dz=imdz*(1+0*ctr1(j,1));
        [D(j) I]=min(sqrt(dx.^2+dy.^2+dz.^2));
        Ind=[Ind;I];
    end

    mn_T(i)=mean(D)/(1*imdz); % mean tortuosity in each slice, D=distance
    cind{i}=Ind;

end

for z=1:SK-1
    ctr1=ct{z};

```

```

ctr2=ct{z+1};
Ind=cind{z};
plot3(ctr1(:,1),ctr1(:,2),ctr1(:,1)*0+z,'r. '),hold on
    for j=1:size(Ind,1),
        plot3([ctr1(j,1);ctr2(Ind(j),1)], [ctr1(j,2);ctr2(Ind(j),2)], [z;z+1]),
            end
end
TORT=mean(mn_T)
TORT_s=sum(mn_T)
FilePath
cd(FilePath)
save TortuosityData ct cind mn_T TORT TORT_s

```

RADIALPORE ALGORITHM

```

% -----load image data
clear all, close all
cd('f:\0X-ray CT raw Images')
[filename, FilePath] = uigetfile('*. *', 'Select Grayscale Image ...');
im=imread([FilePath,filename]);
%-----
st='No ';
while st~='Yes'
    imshow(im);hold on; pixval on, axis on
    [xi,yi]=getline(gcf);
    D=norm([xi(2)-xi(1) yi(2)-yi(1)]);
    jo=(xi(2)+xi(1))/2; io=(yi(2)+yi(1))/2; plot(jo,io,'+')
    xs=jo-D/2; xe=jo+D/2; ys=io-D/2; ye=io+D/2
    X=(0:D)'; Y=D/2-D/2*sin(acos((D/2-X)/(D/2))); %create a half circle
    X=[X;max(X)-X]; Y=[Y;D-Y];
    X=X+xs; Y=Y+ys;
    line(X,Y)
    im2=roipoly(im,X,Y);
    title(['D=' num2str(D)])
    st=questdlg('OK?', 'Circle ok?', 'Yes', 'No ', 'Yes');
end
cd(FilePath)
[filename, FilePath] = uigetfile('*. *', 'Select Corresponding Binary Image...');
im=imread([FilePath,filename]);
ImgBaseName=filename(1:size(filename,2)-7)
tifs=dir([FilePath '*.tif']);k=0;for i=1:size(tifs,1),if
tifs(i).name(1:size(ImgBaseName,2))==ImgBaseName, k=k+1; end ,end
disp(['Number of tif files : ' num2str(size(tifs,1))])
Ext=filename(size(filename,2)-3:size(filename,2))
lines= 1;
def = {ImgBaseName,Ext,'1',num2str(k),FilePath};
result=inputdlg({'Image Base Name: ', 'Extension', 'First image number to start: ',...
    ['Number of Files (Total ' num2str(size(tifs,1)) ' files)'], 'Output
Folder:'},...
    'Input Image Information ',lines,def)
ImgBaseName=result{1}
Ext=result{2}
StartImage=str2num(result{3})
NumFiles=str2num(result{4})
fldout=result{5}
clear tifs im2
%
%
N=10;
D=[N:-1:1]*D/N;%mm
V=pi/4*D.^2*NumFiles;%mm3

for i=1:N
xs=jo-D(i)/2; xe=jo+D(i)/2; ys=io-D(i)/2; ye=io+D(i)/2;
X=(0:D(i))'; Y=D(i)/2-D(i)/2*sin(acos((D(i)/2-X)/(D(i)/2))); %create a half circle

```

```

X=[X;max(X)-X]; Y=[Y;D(i)-Y];
X=X+xs; Y=Y+ys;
xc{i}=X;
yc{i}=Y;
im2(:,:,i)=roipoly(im,X,Y);
line(X,Y)
end
% break

%-----
EndImage=NumFiles+StartImage-1;
cancelButton=0;
h = waitbar(0,'Loading Images', ...
    'Position',[ 243 343 270 93],...
    'Name','Please wait ...',...
    'CreateCancelBtn','cancelButton = 1;closereq;');

for k=StartImage:EndImage
    waitbar((k-StartImage+1)/NumFiles,h,['Current Image= ' num2str(k)])
    if cancelButton==1, break, end
    Z=k-(StartImage)+1;
    im(:,:,Z)=im2bw(imread([FilePath ImgBaseName NumToStr(k) Ext]),.5);
end
close(h)

% break

if max(max(max(im)))~=1, errordlg('Image Must Be Binary'), break, end
pause(0.01)
tic
for j=1:N
    for k=1:NumFiles
        im(:,:,k)=double(im(:,:,k)).*double(im2(:,:,j));
        % Pdum(k)=bwarea(double(im(:,:,k))/255);
        end
    % Por(j)=sum(Pdum);
    Por(j)=sum(sum(sum(im)));
    disp(['Diameter=' num2str(D(j)), ', time= ' num2str(toc)])
end

dx=150/D(1);
dz=0.8;
% close,
figure(2)
set(figure(2),'position',[155 112 672 560])
V_w=V*dx^2*dz;
D_w=D*dx;
Por_w=Por*dx^2*dz;
% subplot(2,2,1),plot(V_w,Por_w,'.-'),xlabel('Vol(mm^3)','fontweight','bold'),
ylabel('Pore area (mm^3)','fontweight','bold')
% subplot(2,2,2),plot(D_w,Por_w,'.-'),xlabel('Diameter(mm)','fontweight','bold'),
ylabel('Pore area (mm^3)','fontweight','bold')
% subplot(2,2,3),plot(V_w,Por_w./V_w*100,'.-'),xlabel('Volume
(mm^3)','fontweight','bold'), ylabel('Porosity(%)','fontweight','bold')
% subplot(2,2,4),plot(D_w,Por_w./V_w*100,'.-
'),xlabel('Diameter(mm)','fontweight','bold'), ylabel('Porosity(%)','fontweight','bold')
% gtext(fldout,'fontweight','bold')
NameFile=input(' Enter the output file name...: ','s')

plot(D_w,Por_w./V_w*100,'.-'), xlabel('Diameter(mm)','fontweight','bold'),
ylabel('Porosity(%)','fontweight','bold')
title(fldout,'fontweight','bold')
saveas(gcf,[fldout NameFile '.emf'],'emf')

fid = fopen([fldout NameFile '.txt'],'w');
fprintf(fid,'%6f %6f \n', [D_w',Por_w'./V_w'*100]);
fclose(fid);

% open([fldout NameFile '.txt'])

```

APPENDIX C WANNIER'S ANALYTICAL SOLUTION OF STOKES FLOW AROUND A CIRCULAR CYLINDER IN THE VICINITY OF A MOVING PLATE

Analytical solution of the stream function ψ is given as:

$$\psi(x, y) = A \frac{\log(x^2 + (s+y)^2)}{x^2 + (s-y)^2} + B \frac{y(s+y)}{x^2 + (s+y)^2} + C \frac{y(s-y)}{x^2 + (s-y)^2} + D y + E(x^2 + y^2 + s^2) + F \frac{y \log(x^2 + (s+y)^2)}{x^2 + (s-y)^2}$$

where:

$$A = -d \frac{V}{\log\left(\frac{d+s}{d-s}\right)} - \frac{1}{2} d a \frac{v}{s}$$

$$B = 2(d+s) \frac{V}{\log\left(\frac{d+s}{d-s}\right)} + (d+s) a \frac{v}{s}$$

$$C = 2(d-s) \frac{V}{\log\left(\frac{d+s}{d-s}\right)} + (d-s) a \frac{v}{s}$$

$$D = -V$$

$$E = 0$$

$$F = \frac{V}{\log\left(\frac{d+s}{d-s}\right)}$$

$$s = \sqrt{d^2 - a^2}$$

Inputs; d , a , v and V are shown in Figure C-1

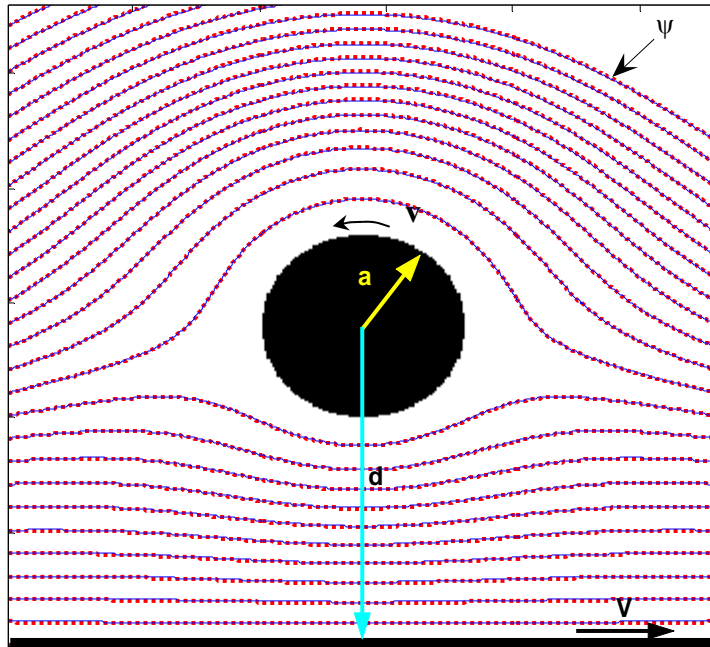


Figure C-1

APPENDIX D PROCEDURES TO CONDUCT HYDRAULIC CONDUCTIVITY TESTS USING THE BUBBLE TUBE CONSTANT HEAD PERMEAMETER

1. Place specimen on base. (see comments below concerning trapping air beneath the specimen)



2. Place membrane.



3. Place o-rings on membrane. The lower one to seal the membrane against the base tube, the upper one placed temporarily near the specimen top. Roll the membrane down over the top o-ring to expose the specimen top.



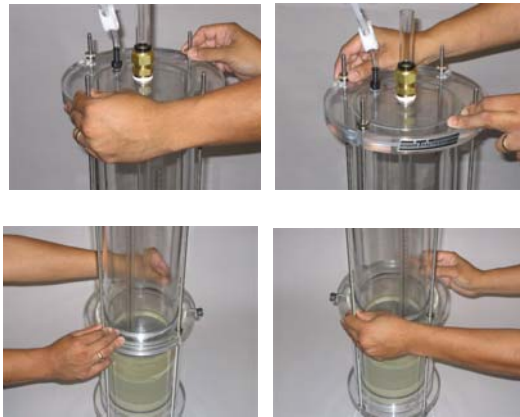
4. Place reservoir and confining tube on specimen. Be sure to align the slots in the reservoir top plate with those in the base. These slots need to be aligned before the membrane is placed on the reservoir tube otherwise, the membrane will twist when trying to align the slots.



5. Roll membrane and o-ring up on the reservoir tube. Roll membrane top down over top o-ring so that it does not obstruct viewing the bubble tube bottom.



6. Slide confining chamber down and install clamping rods. Tighten the top nuts first, (alternate tightening opposite pairs, keeping the rods pressed into their slots), then the nuts on the confining chamber.



<p>7. Attach pressure hose and apply 5 to 10 psi pressure to the confining chamber and check for leaks. Do not use pressure greater than 10 psi.</p>	
<p>8. Place assembly in tub. Place a water tube into the bubble tube and fill the reservoir. A vacuum source can be connected the top vent tube during filling to help de-air the filling water or to prevent it from flowing through the specimen to quickly. Seal the area between the filling tube and bubble tube to make the vacuum effective.</p>	
<p>9. Check Bubble tube slip fitting. The assembly consists of (from bottom up) (2) o-rings; a top ferrule turned upside down, a Swagelok nut, and (2) spare o-rings. The tube should be lubricated with vacuum grease. Push the nut, ferrule and o-rings down onto the fitting, then hand tighten the nut so that the o-rings are squeezed to form a seal around the tube. Loosen the nut slightly to slide the tube up or down to position it.</p>	

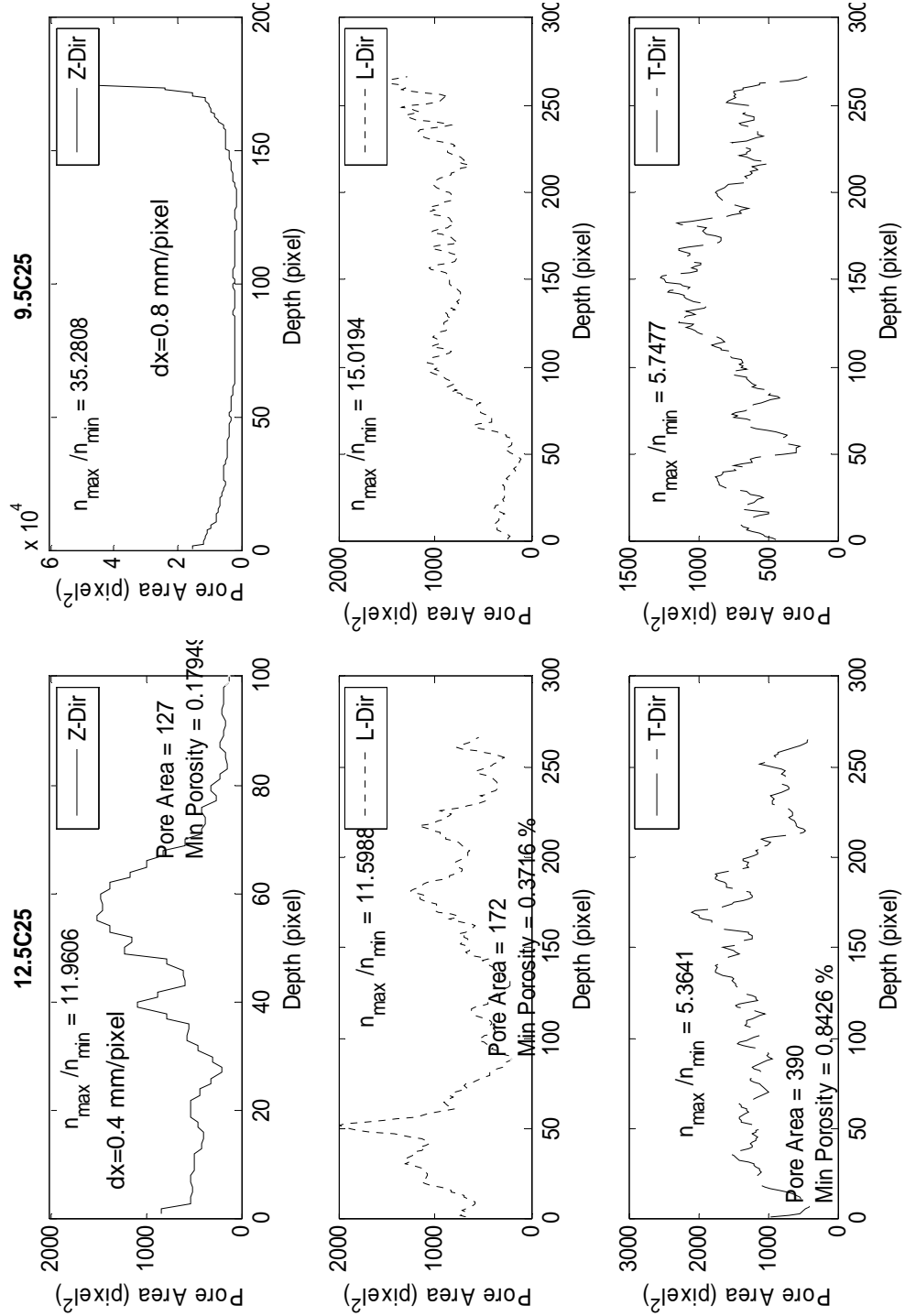
A few comments concerning the test are given below:

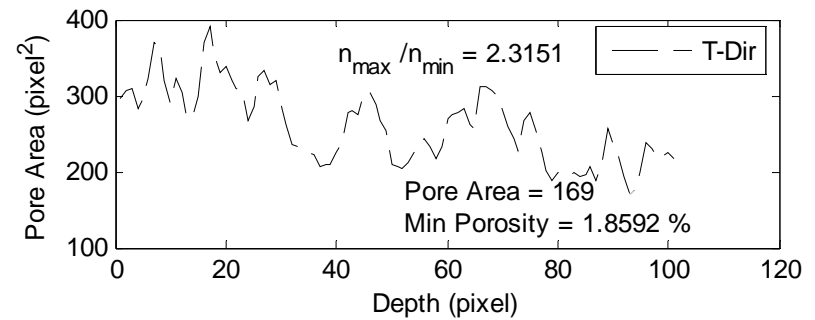
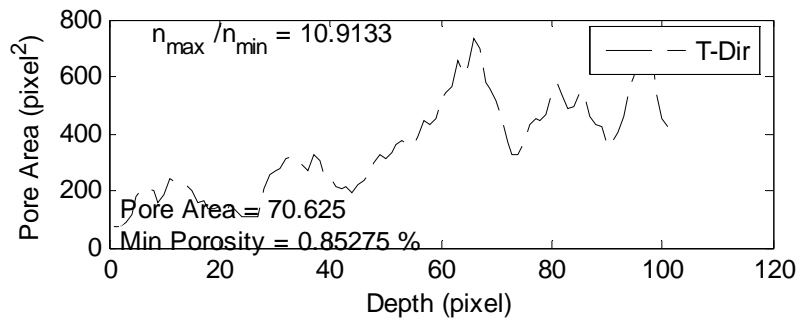
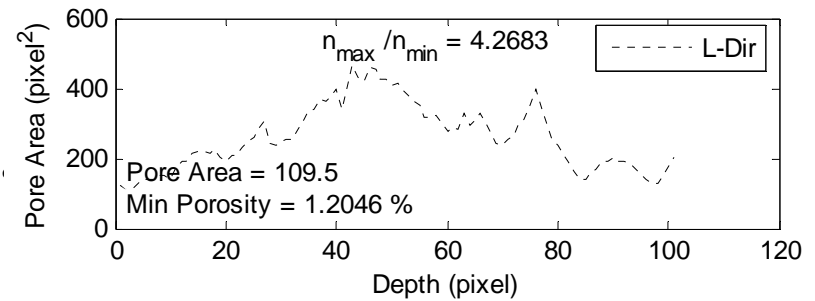
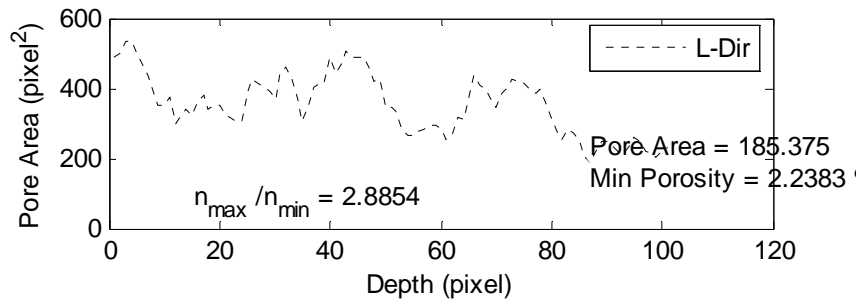
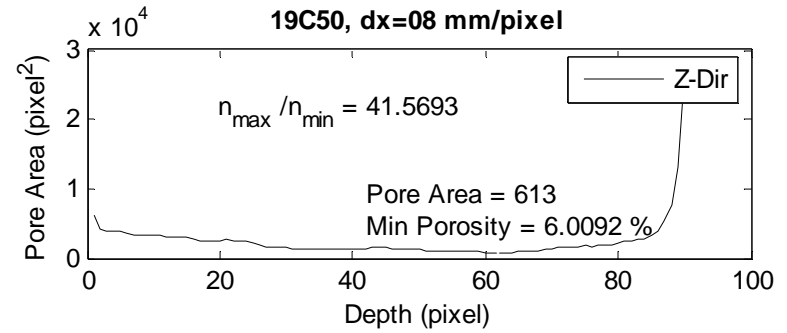
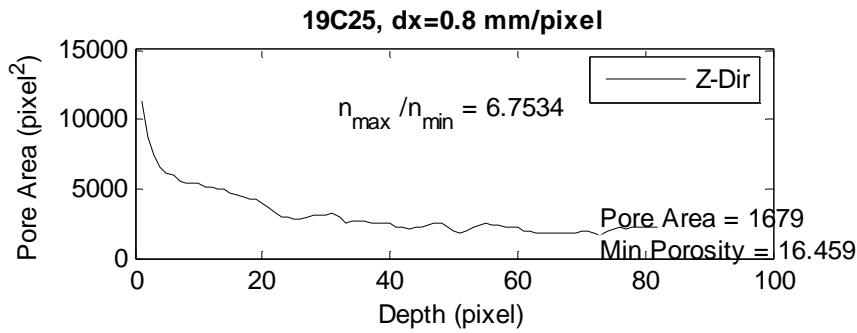
1. Push the bubble tube until it rests on the specimen top. Place tape or mark on the tube where it exits the top fitting. This serves as a convenient reference. The distance between the mark and the fitting top is the distance between the bubble tube bottom and the specimen top. The same can be accomplished by noting the distance between the top of the bubble tube and the reservoir top plate when the bubble tube rests on the specimen top.
2. Air can be trapped beneath the specimen during setup and needs to be removed before testing. This air can block or restrict flow if not removed. Placing the base in the tub of water with the water level above the specimen bottom before placing the specimen and membrane will eliminate trapping air. Otherwise, attach a vacuum source to bent tube placed through a base side port (long enough to reach the specimen bottom) and suck the air out.

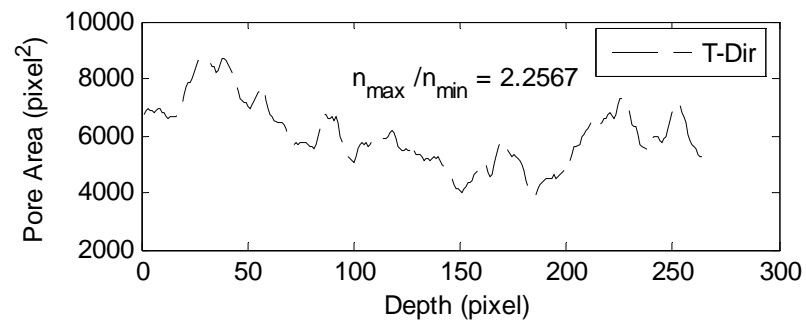
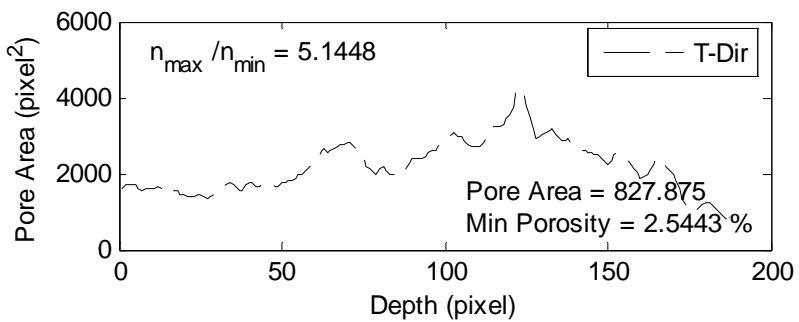
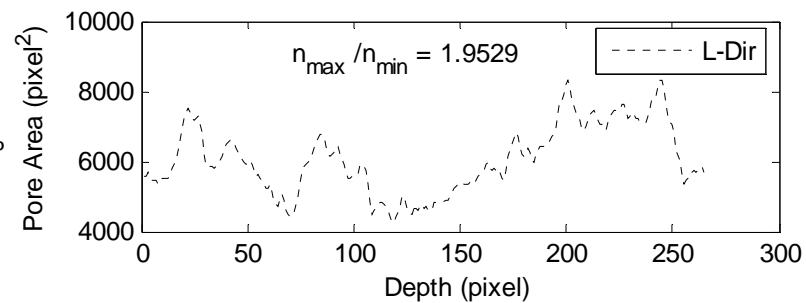
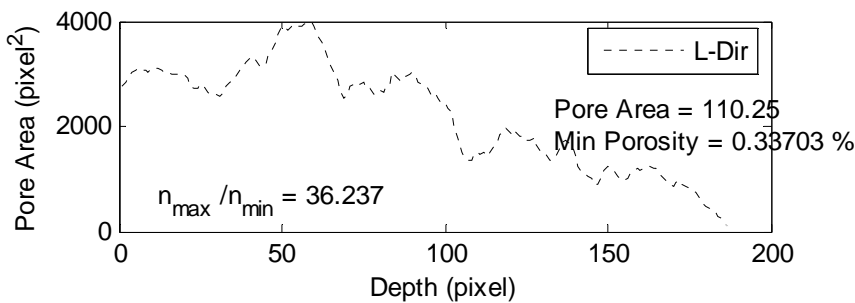
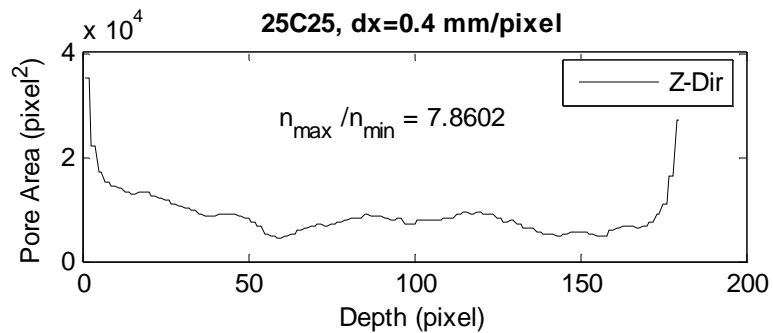
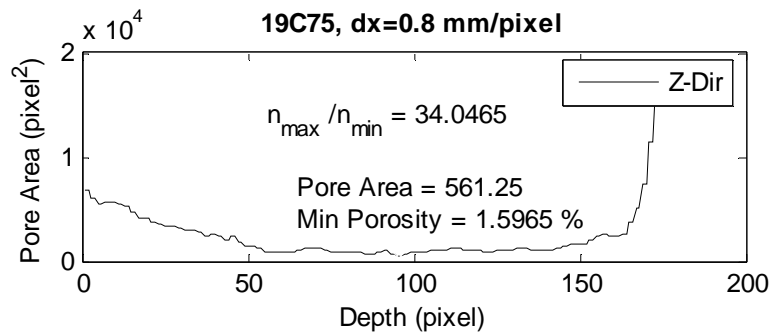
It is important that there are no air leaks into the space above the water in the reservoir tube. Leaks can occur because of a faulty seal around the bubble tube or through the fitting for the vacuum hose. To check for leaks, fill the reservoir with water, lower the bubble tube such that the bottom end is lower than the water in the tub, note the water level height in the reservoir, monitor it with time. It should not drop. Tighten the fittings or clamp valve if it does. Note that small leaks can be tolerated if the leak rate is 5 to 10 times less than the flow rate during testing.

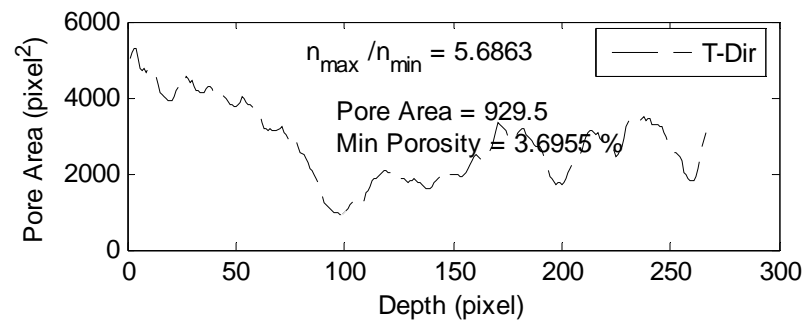
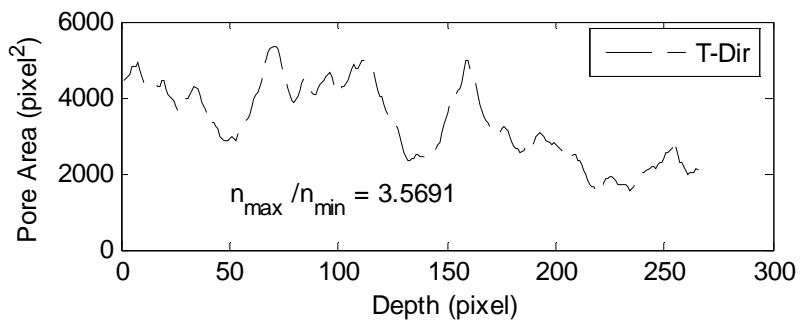
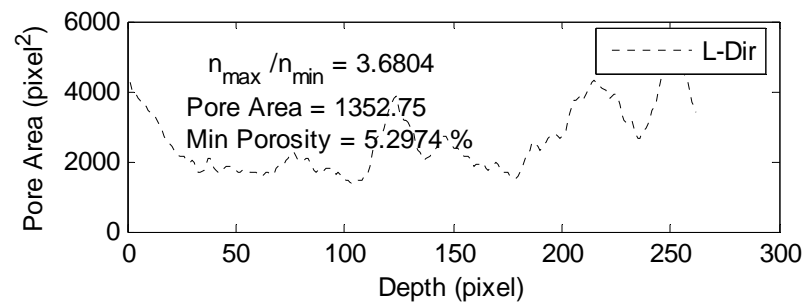
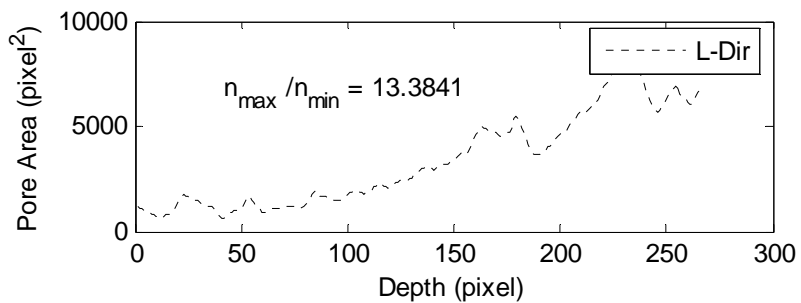
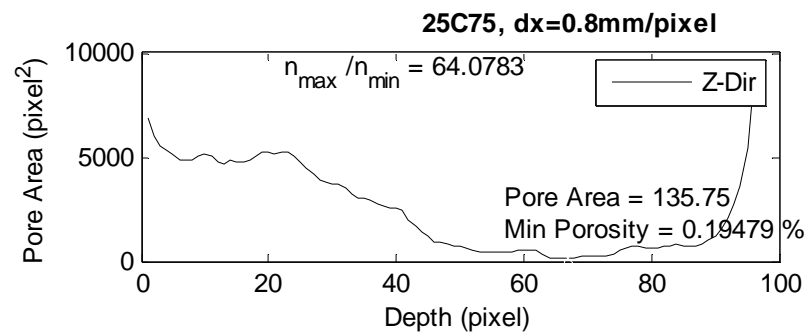
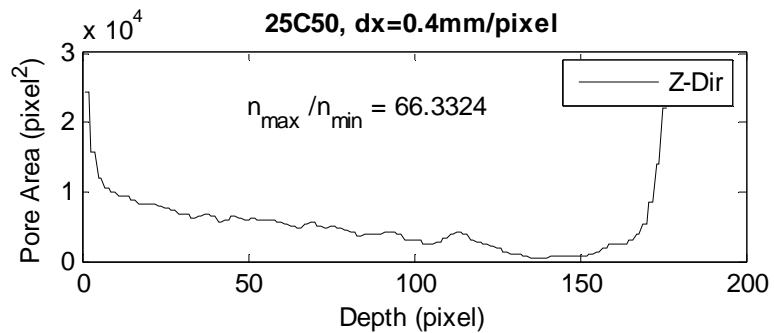
- a. Loosen the lower hose clamp on the top coupling and remove the reservoir tube.
 - b. Place test sample in the mold, level with a straight edge, place in the bucket
 - c. Measure the diameter of both the reservoir tube and bubble tube, length of mold,
- L.
- d. Measure the distance between the top of the mold and top of bucket, H1
 - e. Take the mold out of the bucket, place the reservoir tube back on the mold and tighten the clamps
 - f. Measure the distance from the bottom of the bubble tube to the top of the mold, H2; the water head difference will be H2-H1
 - g. Place permeameters in the bucket and fill slowly allowing water to saturate the sample from the bottom up
 - h. When water overflows, open the upper and lower ports to allow water in the reservoir tube, keep the water overflowing the bucket
 - i. Seal the top of the bubble tube, use vacuum, draw the water into the bubble tube so that the water level is between 20 and 25cm high as marked on the reservoir tube. Close the ports with clamps. Note the mark at which it starts
 - j. Open the bubble tube and start the timer, end test when the water level drops to the bottom of the bubble tube, or stop after between 15 and 30 minutes.

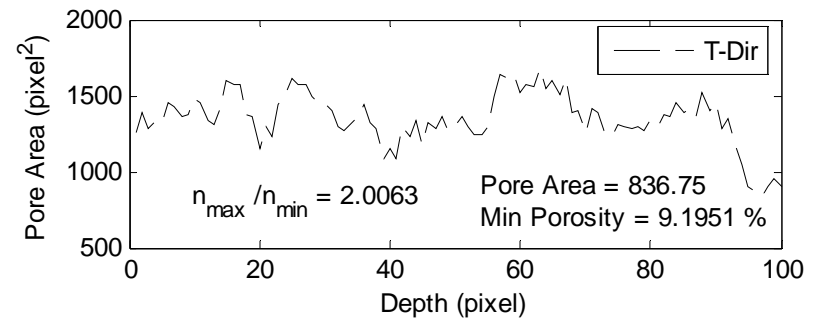
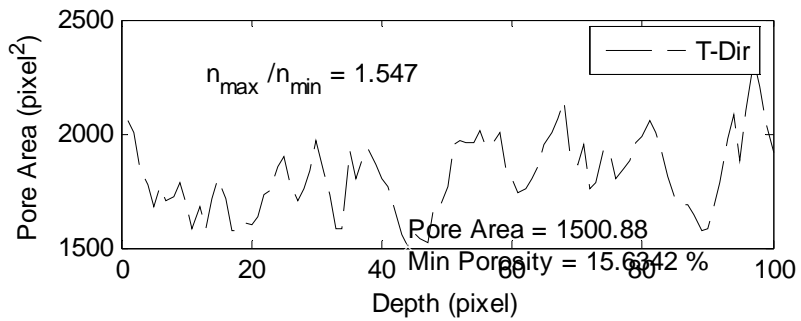
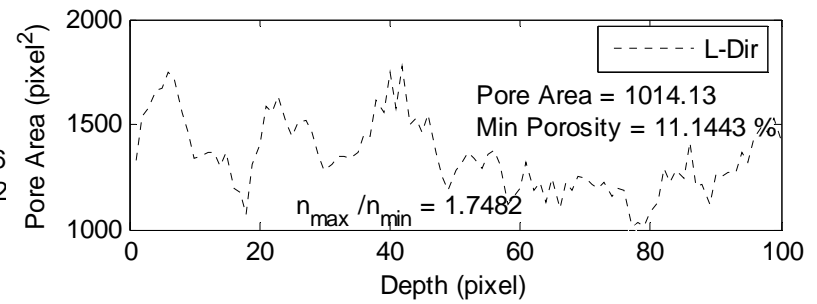
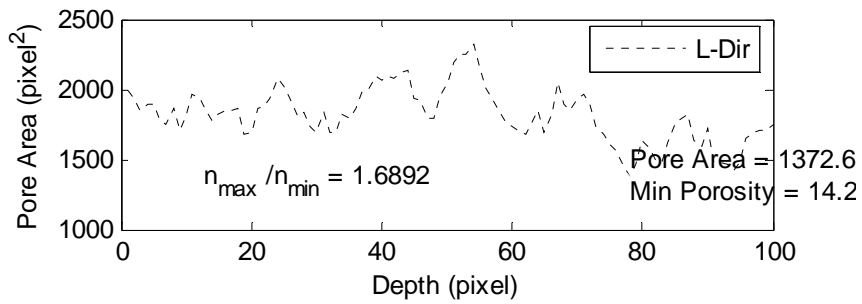
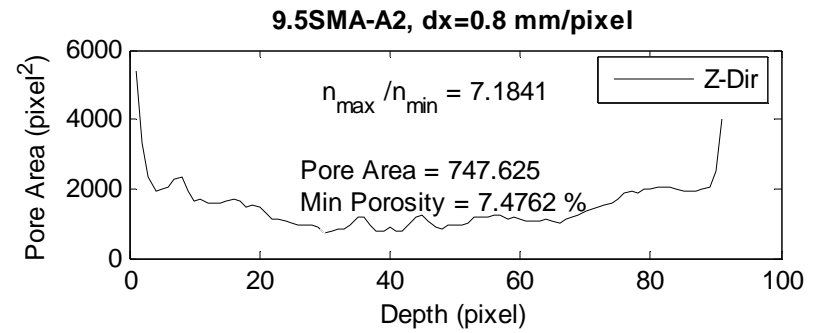
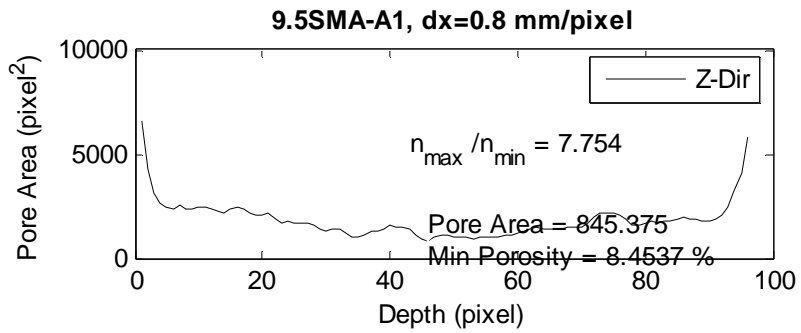
APPENDIX E THE VARIATION IN PORE CROSS-SECTIONAL AREA IN THREE DIFFERENT DIRECTIONS FOR ALL SPECIMENS

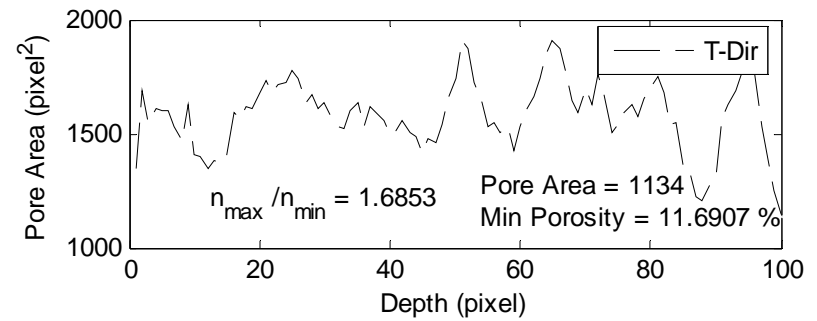
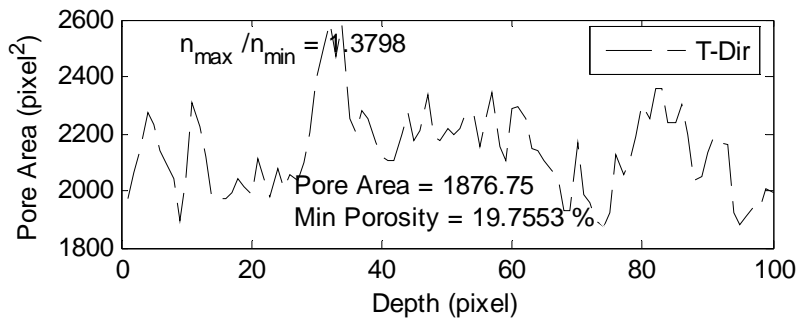
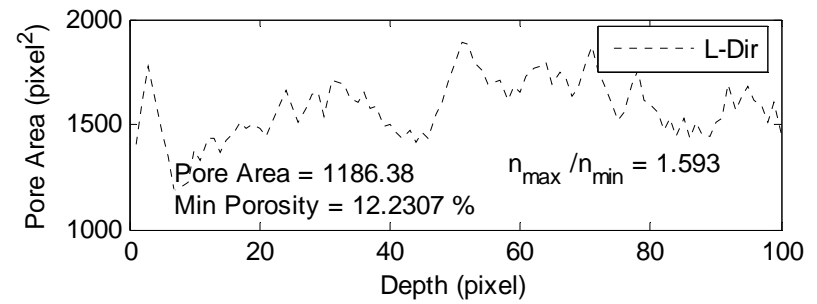
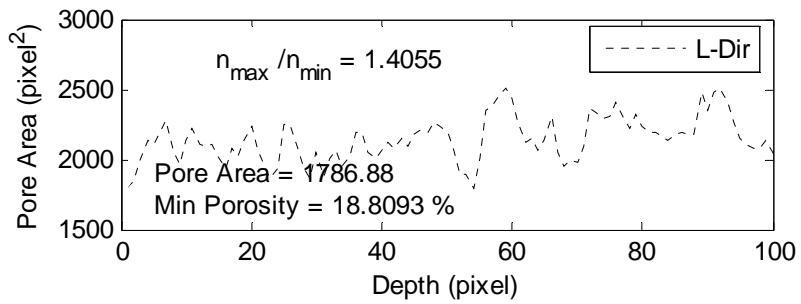
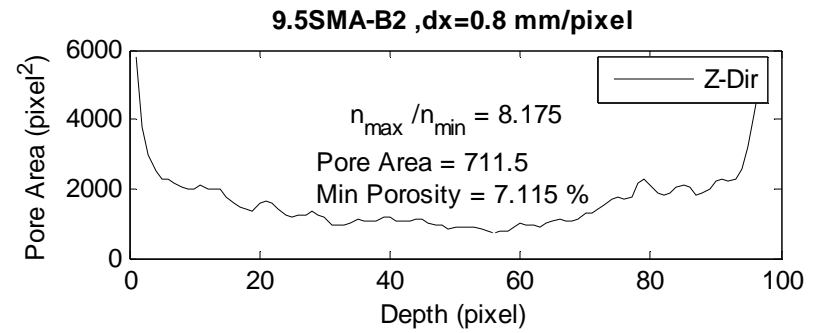
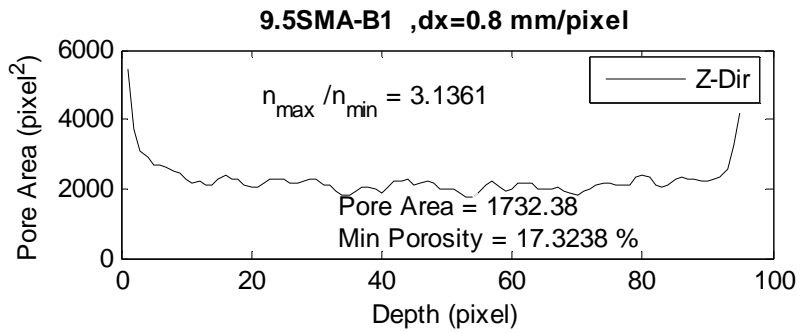


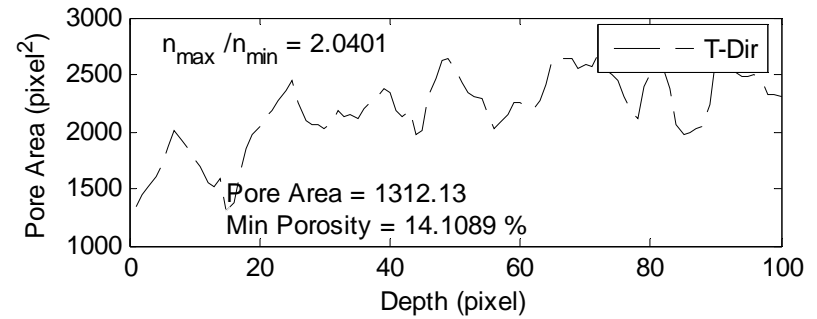
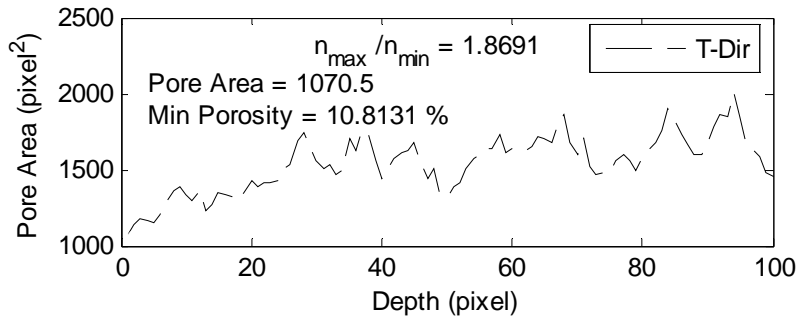
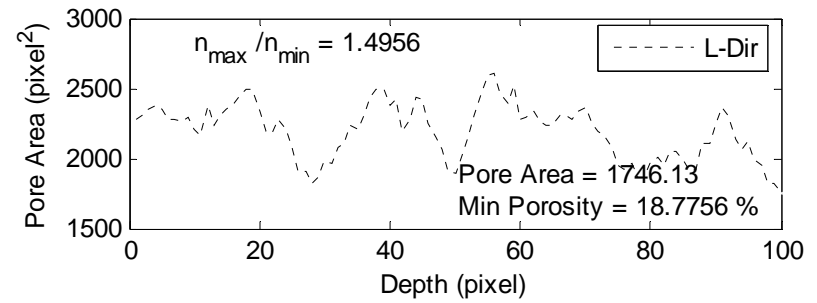
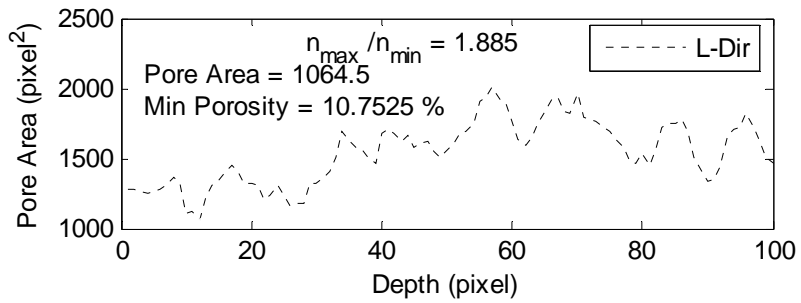
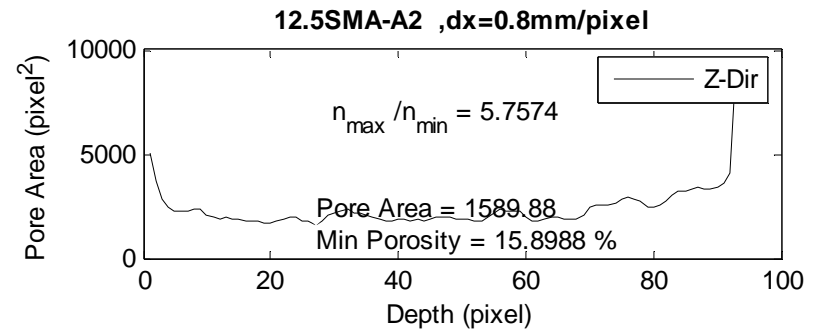
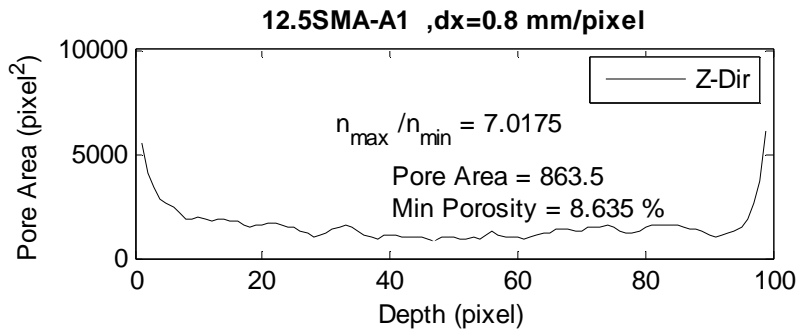


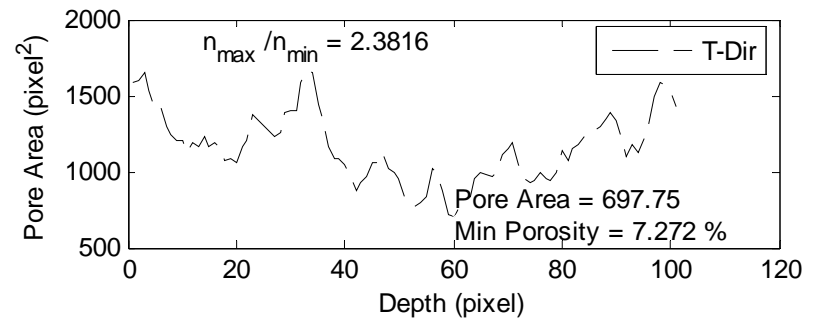
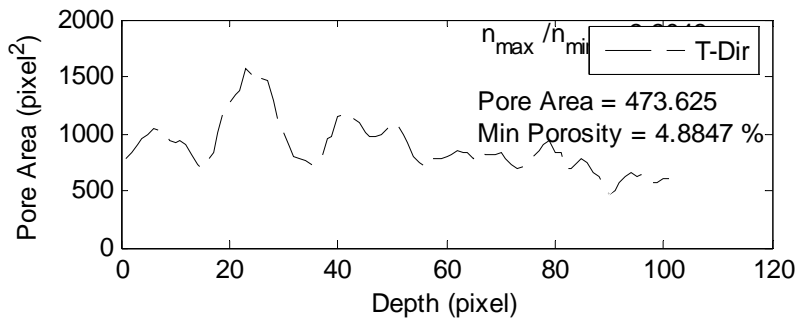
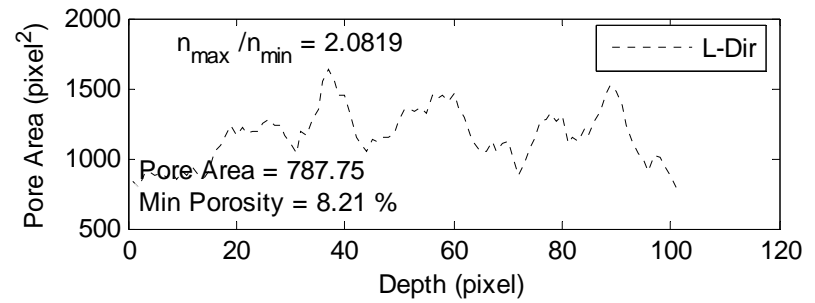
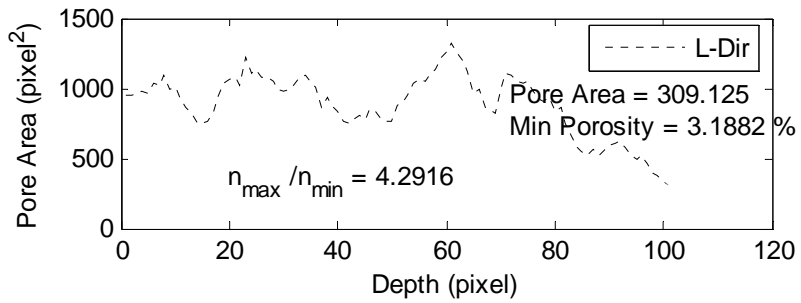
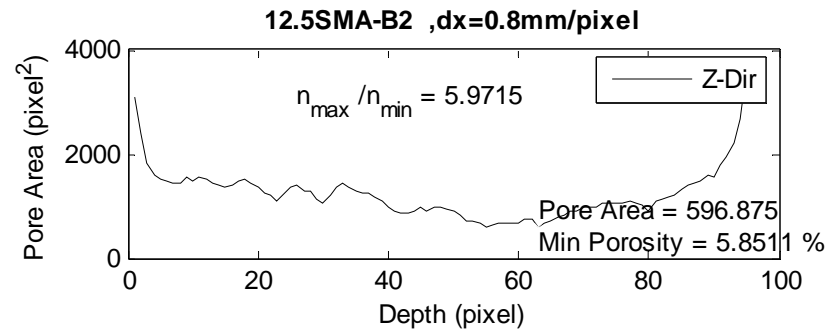
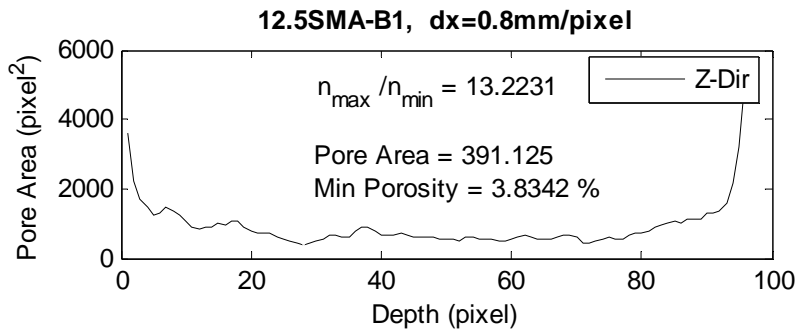


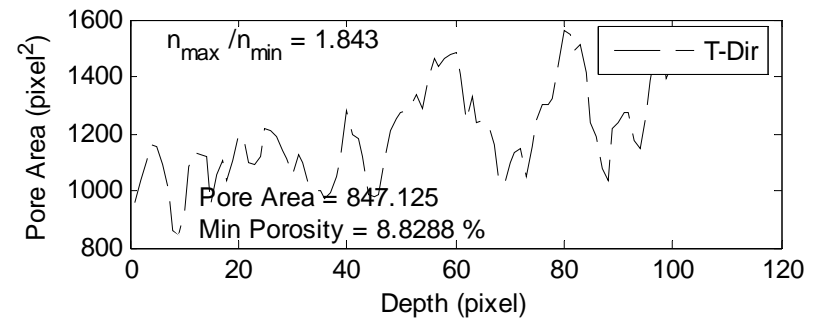
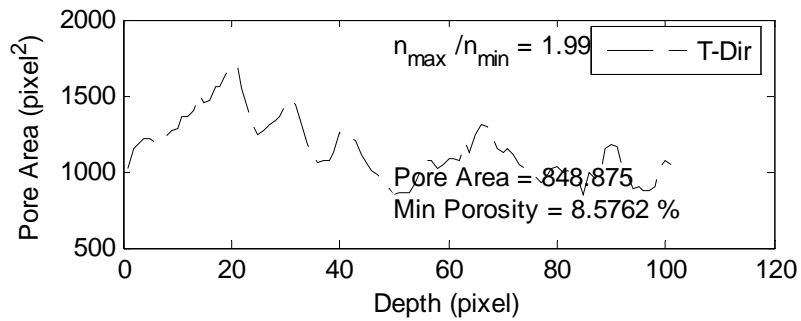
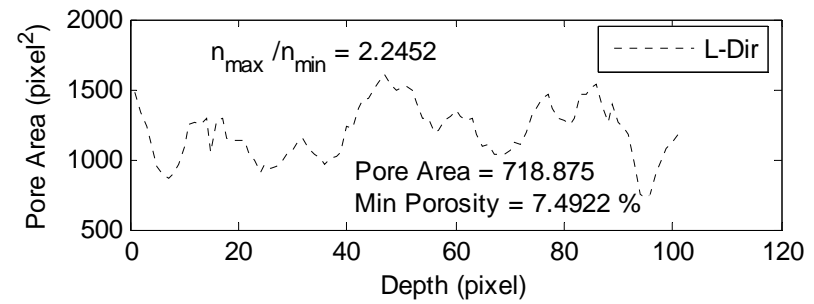
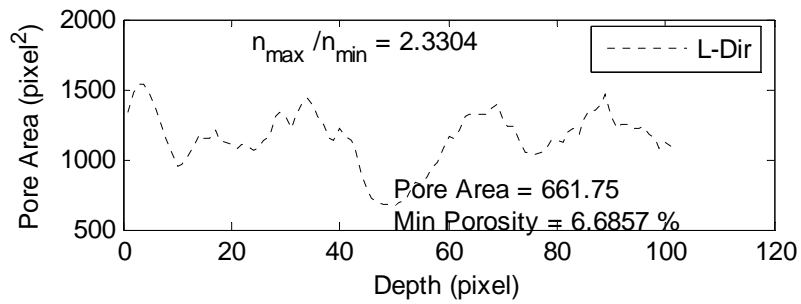
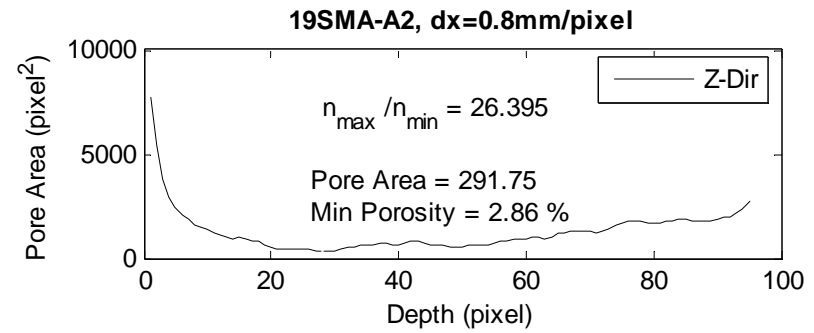
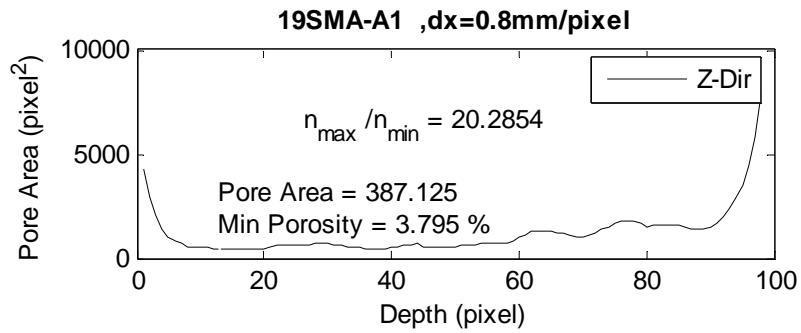


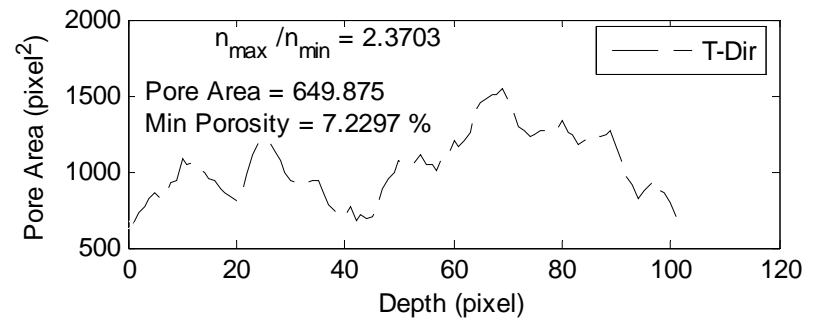
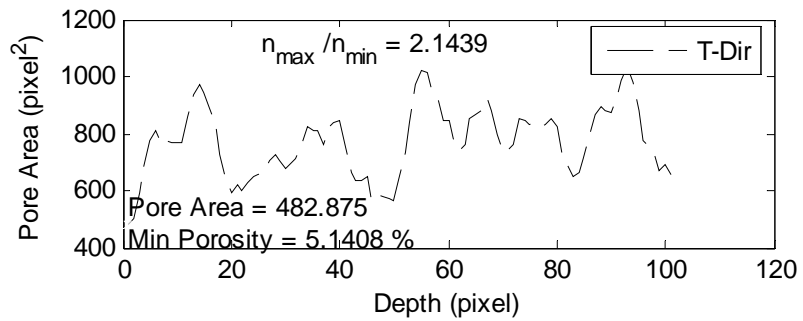
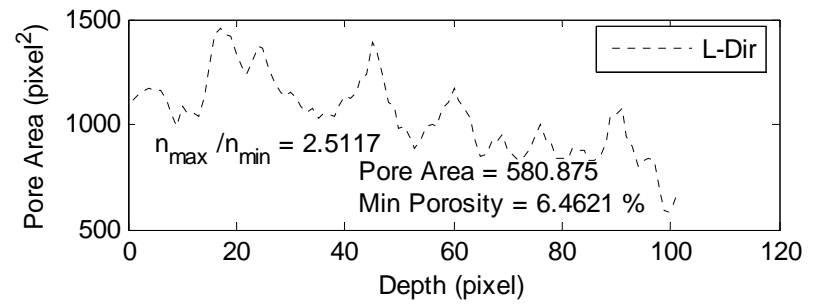
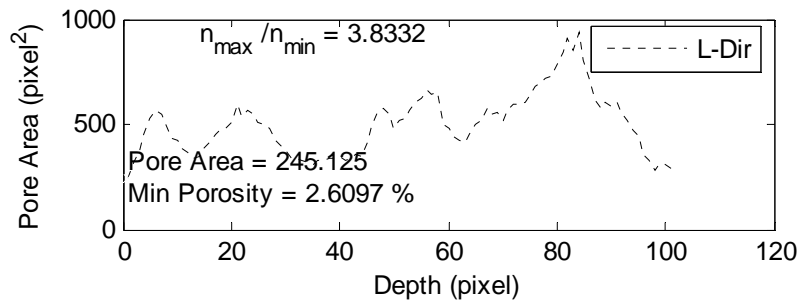
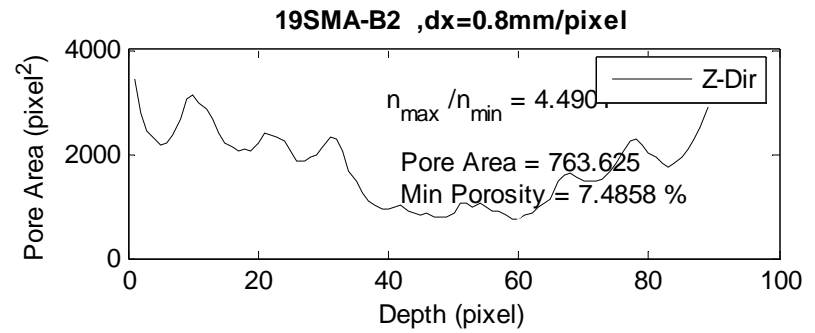
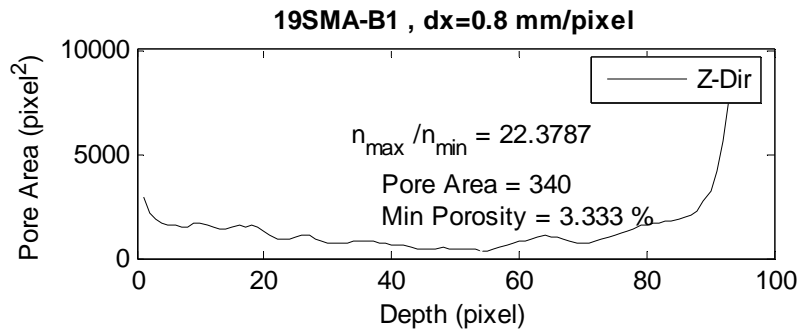




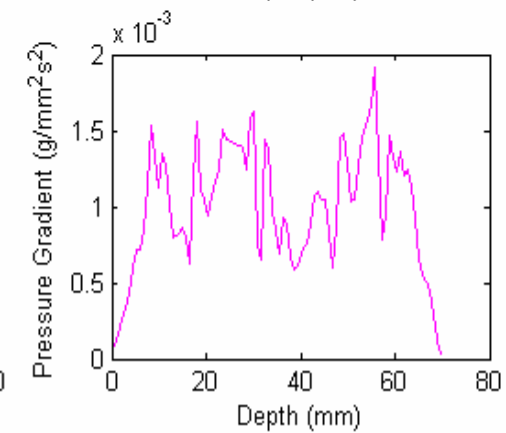
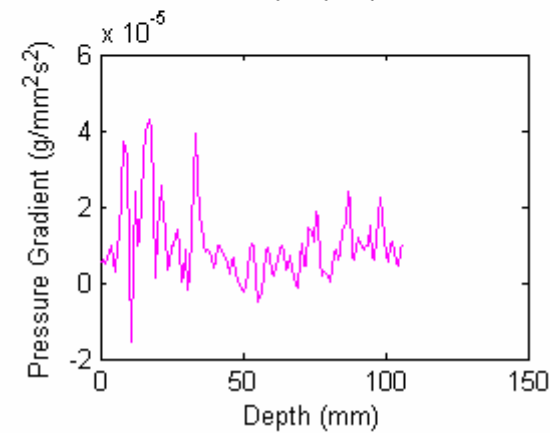
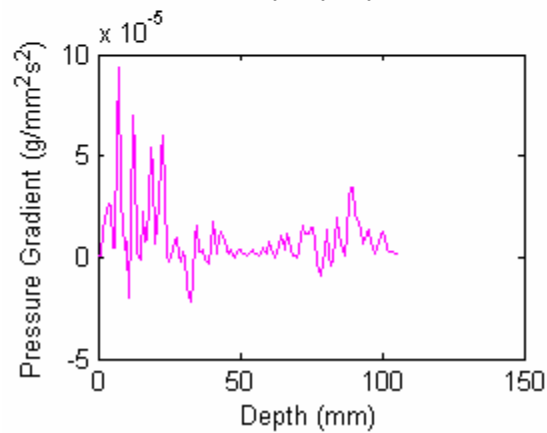
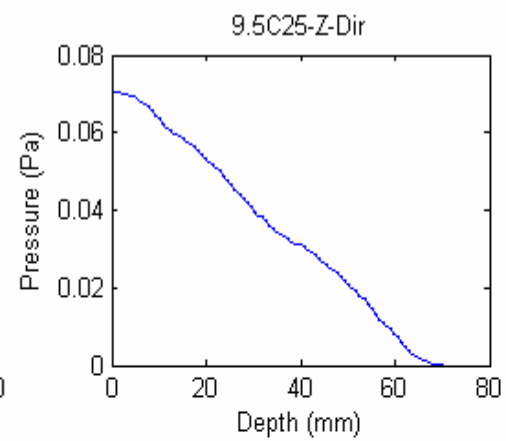
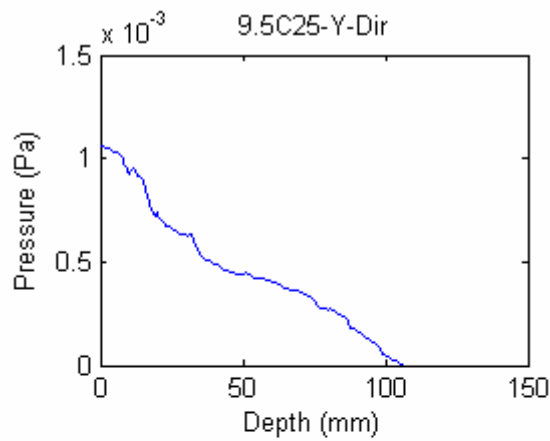
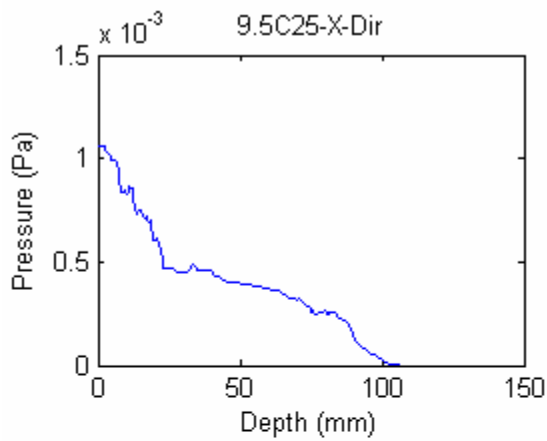


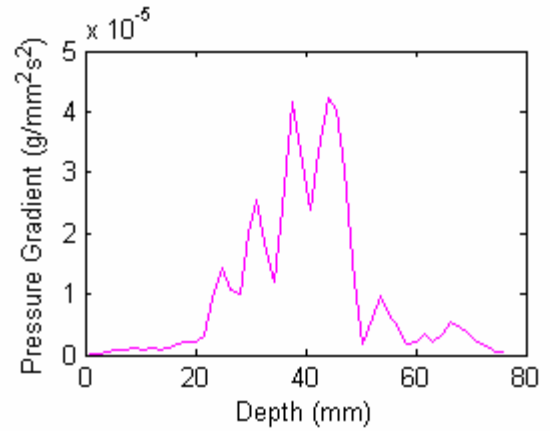
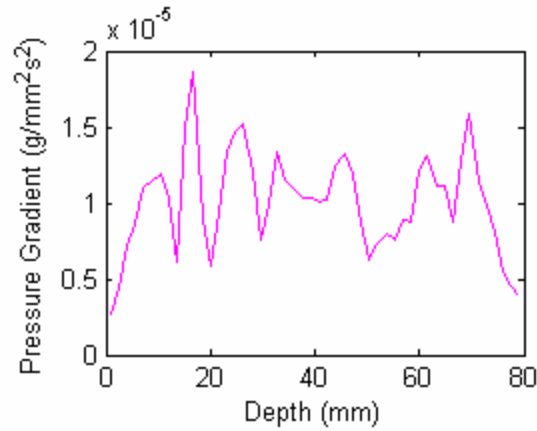
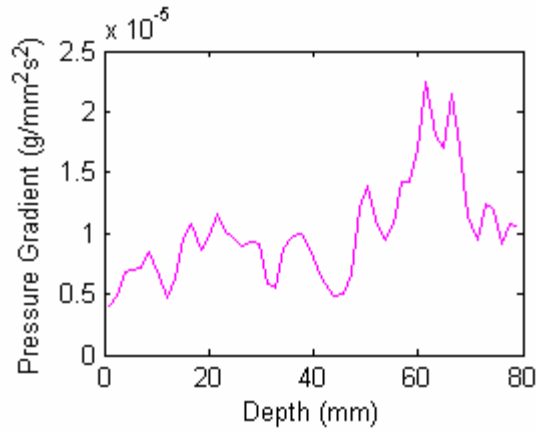
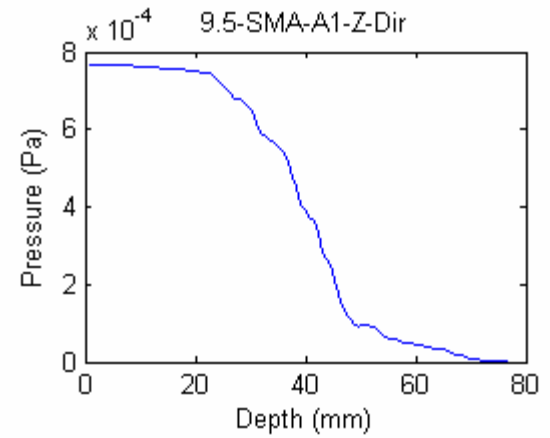
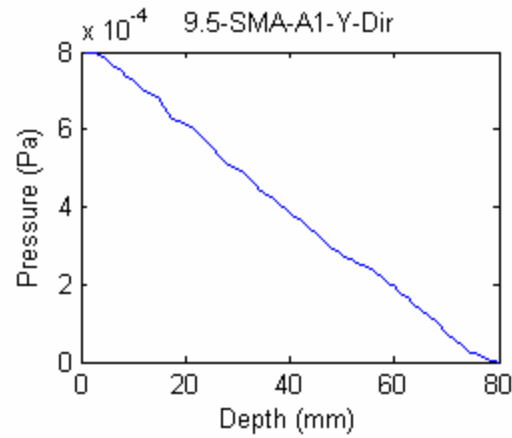
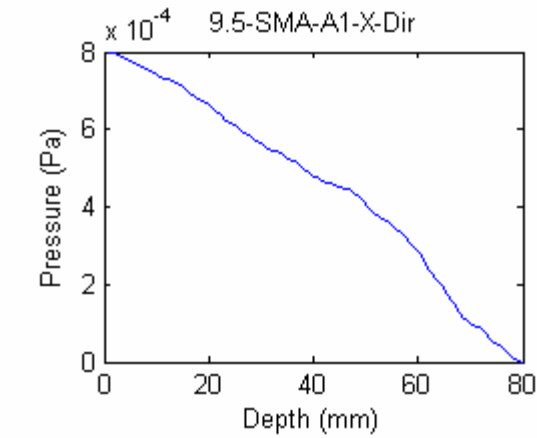


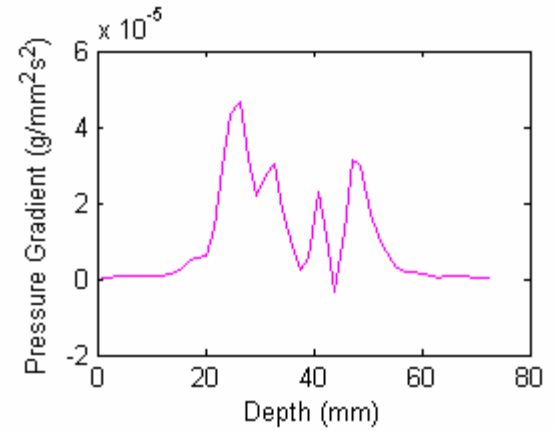
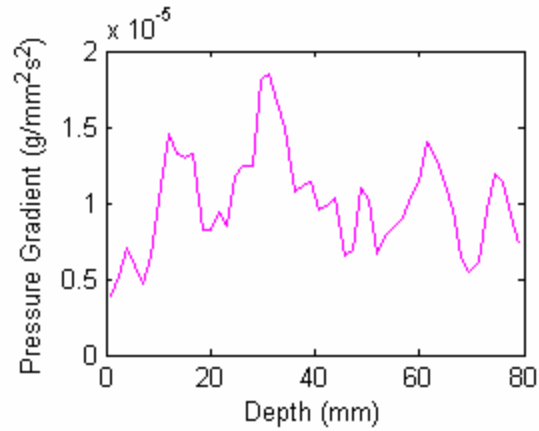
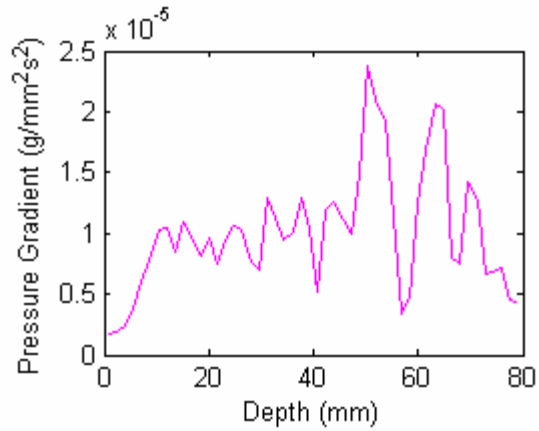
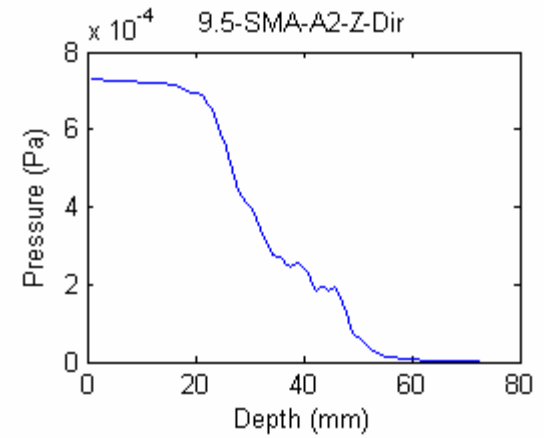
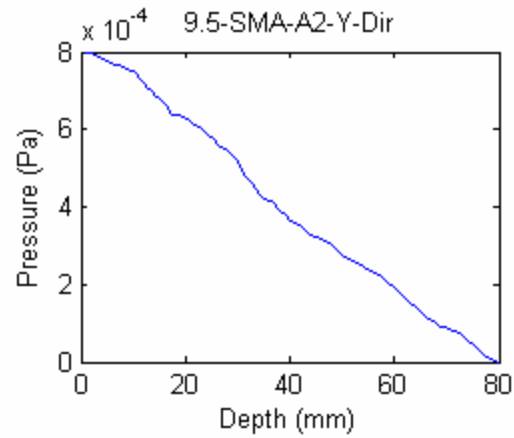
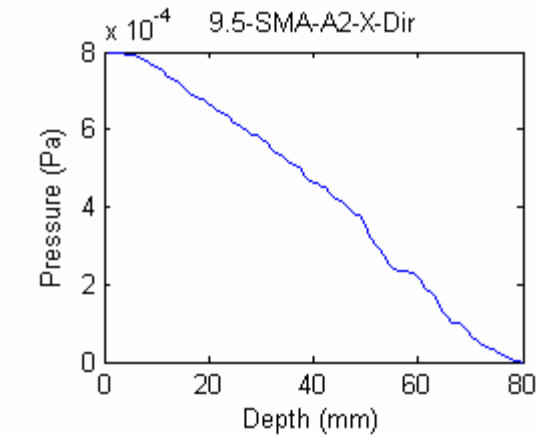


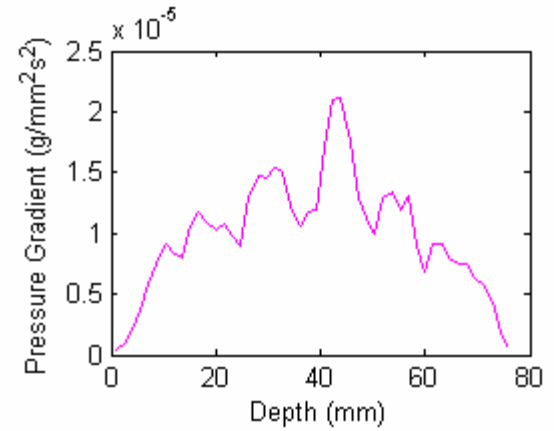
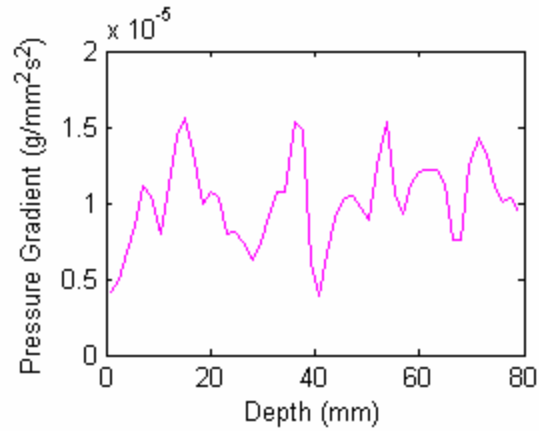
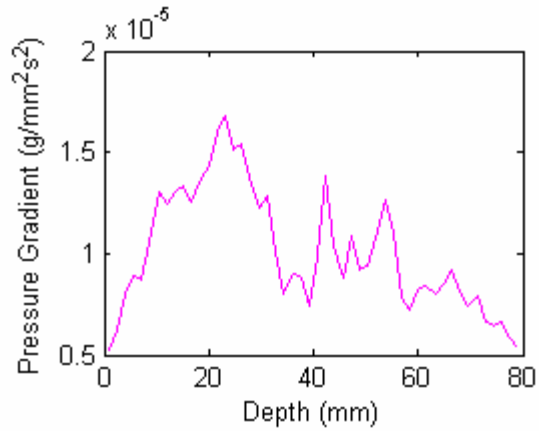
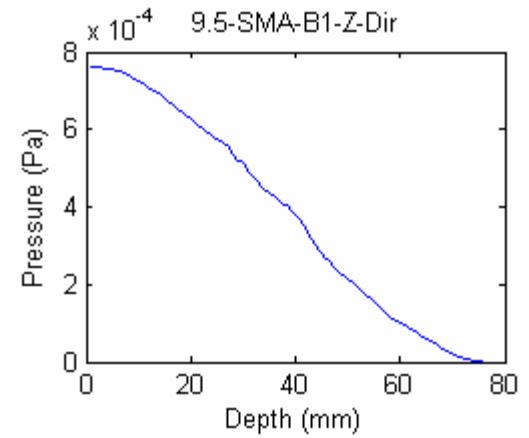
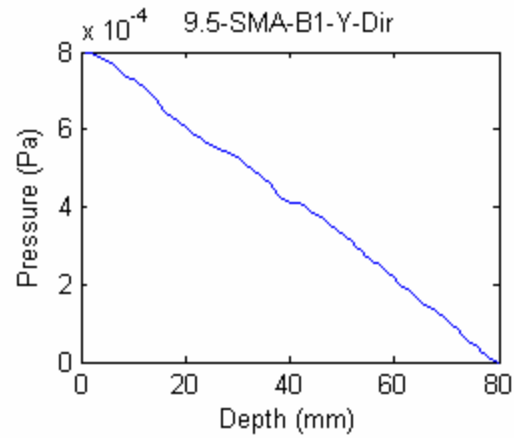
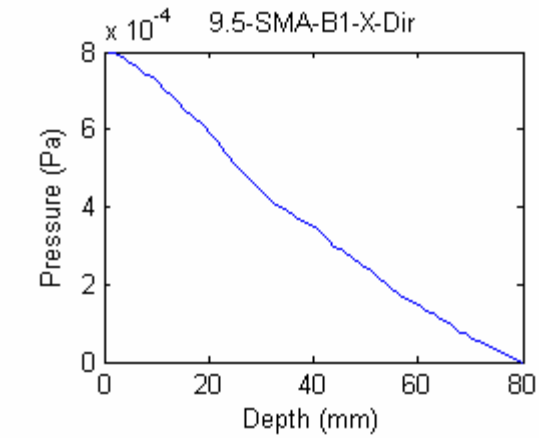


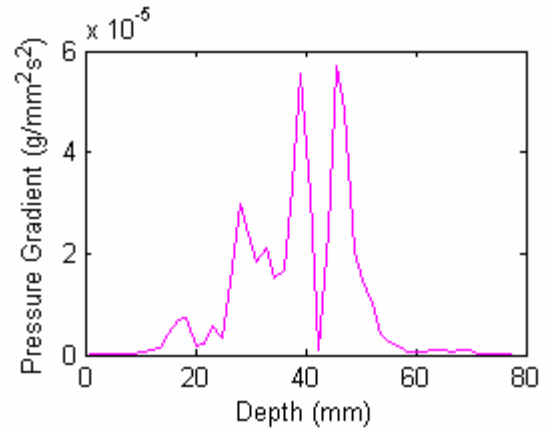
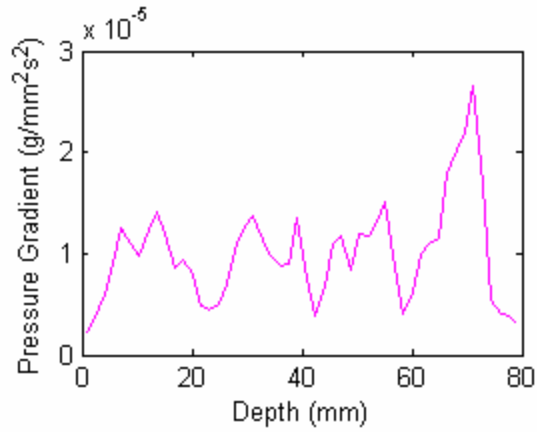
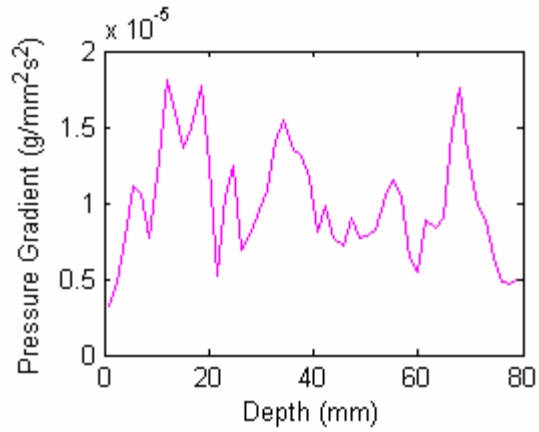
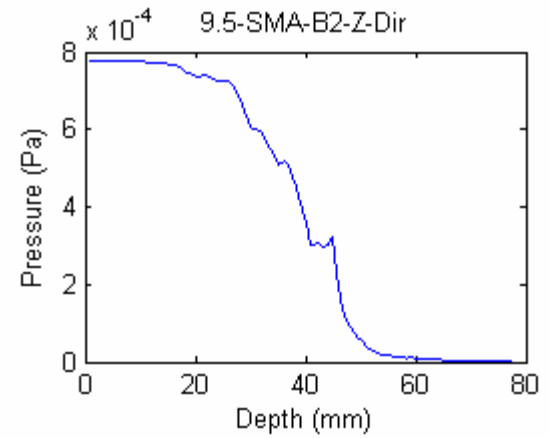
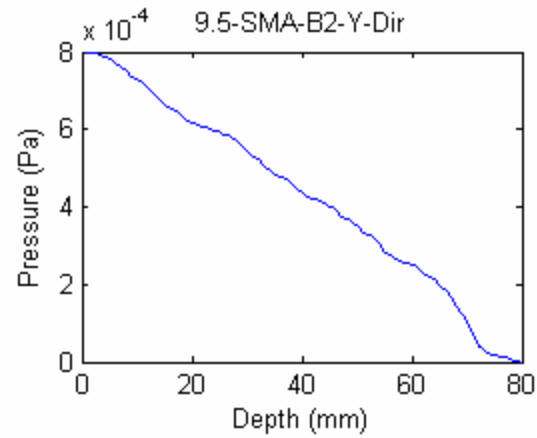
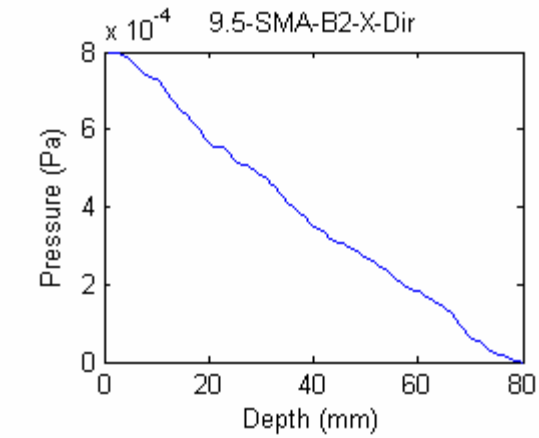
APPENDIX F PORE PRESSURE AND PRESSURE GRADIENT VARIATION IN DIFFERENT DIRECTIONS OF THE SPECIMENS

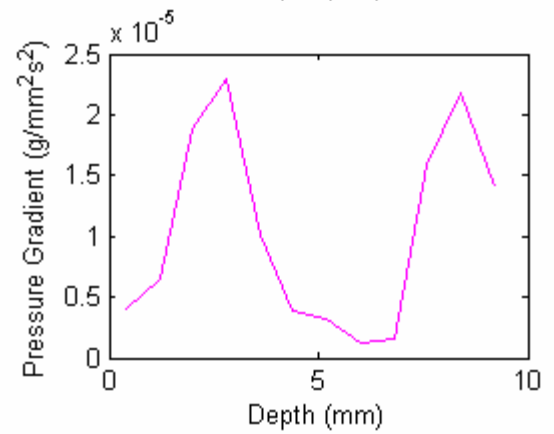
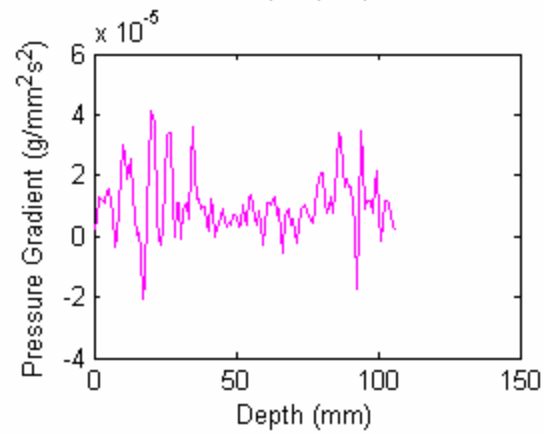
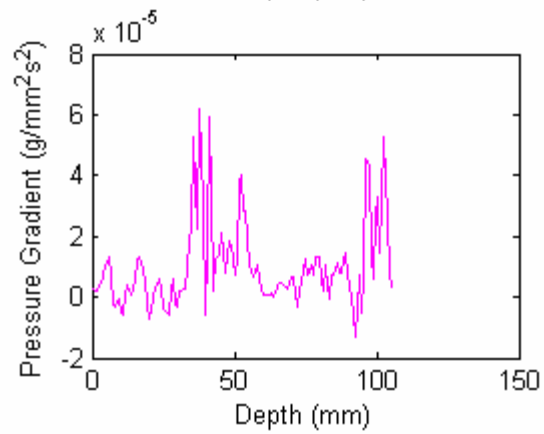
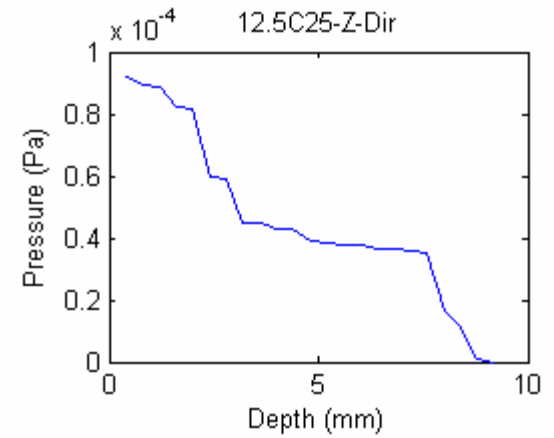
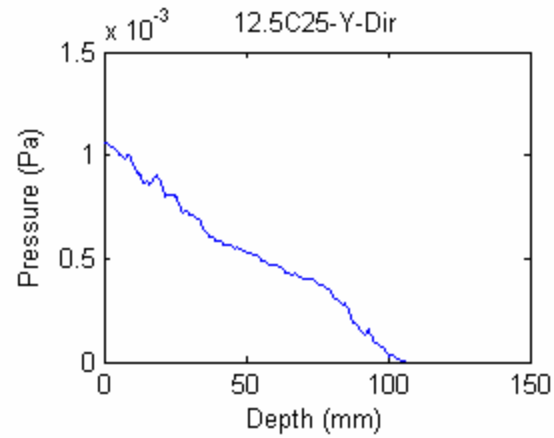
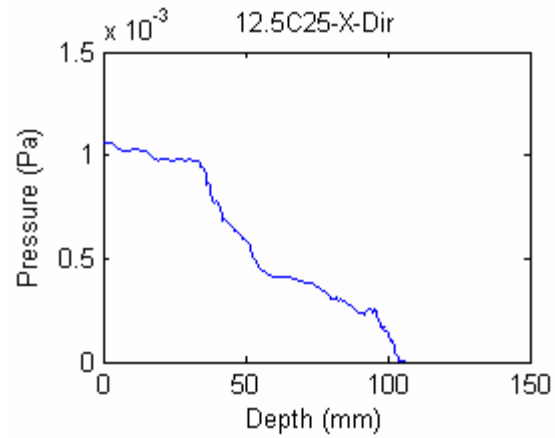


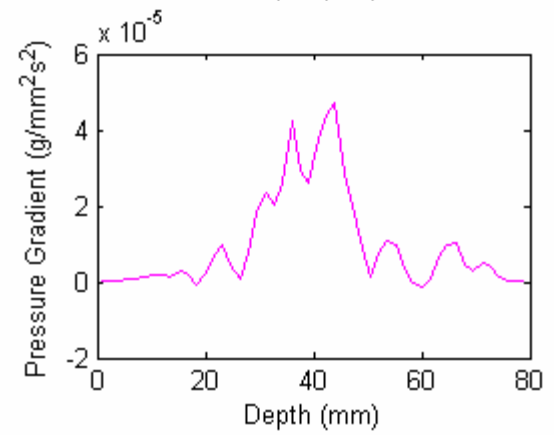
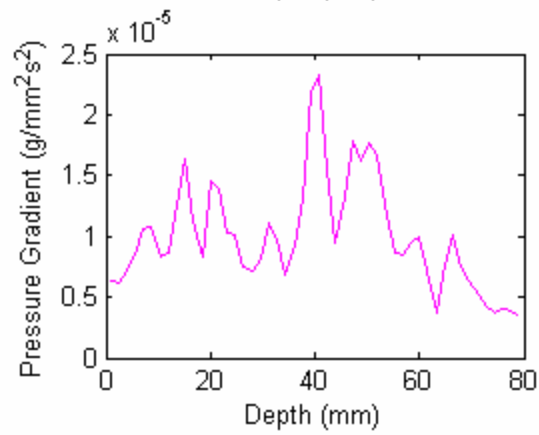
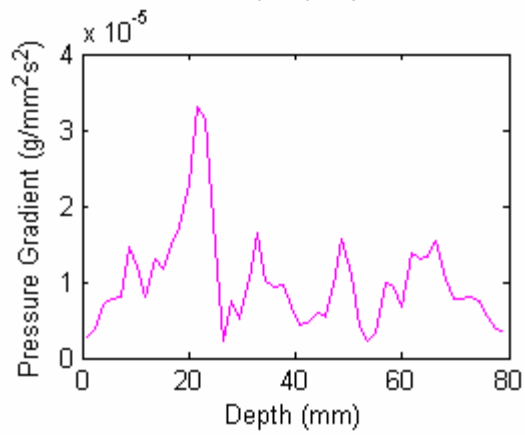
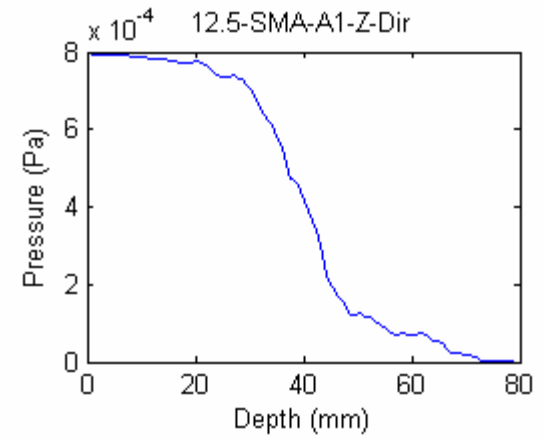
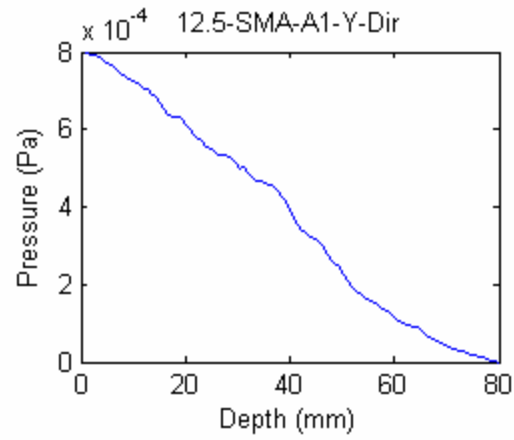
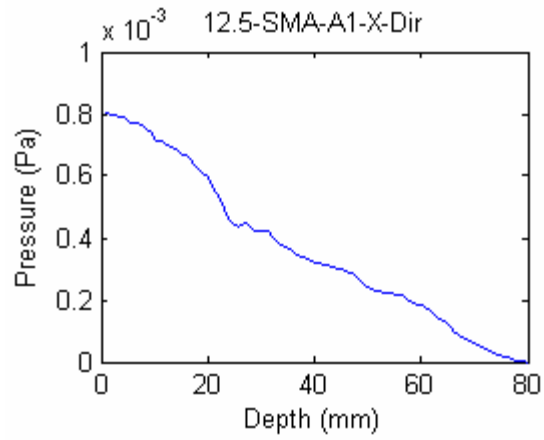


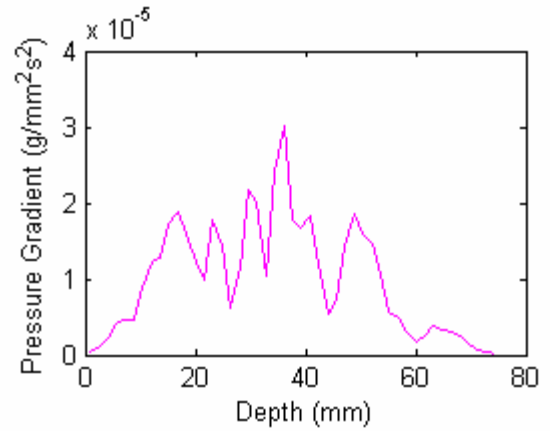
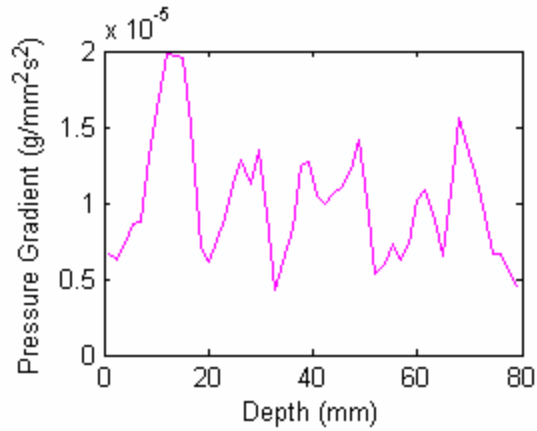
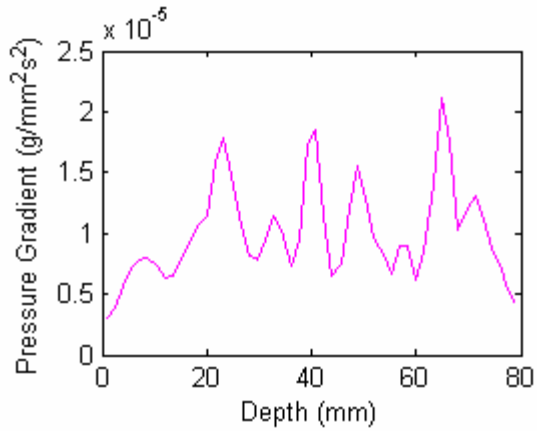
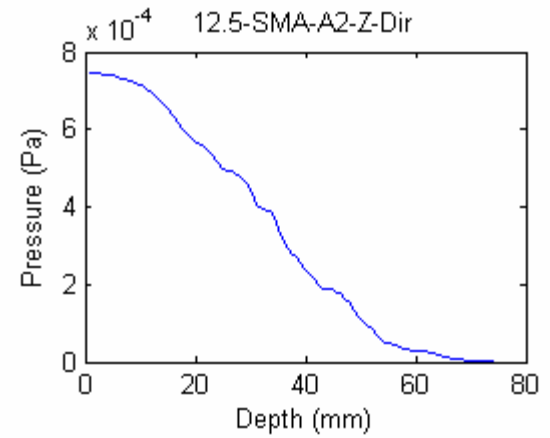
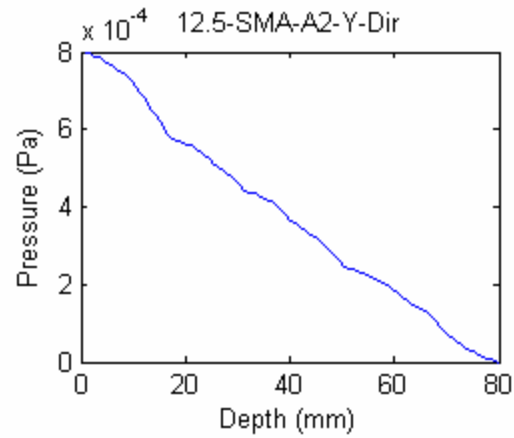
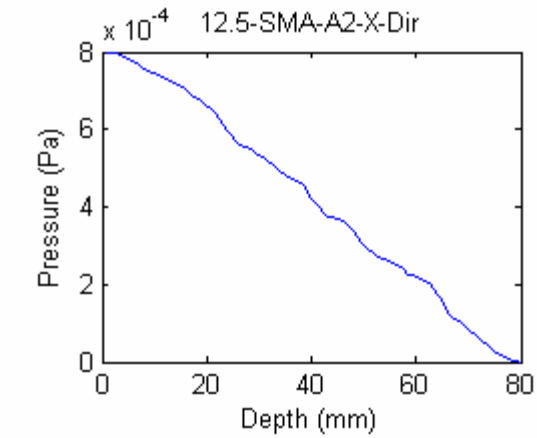


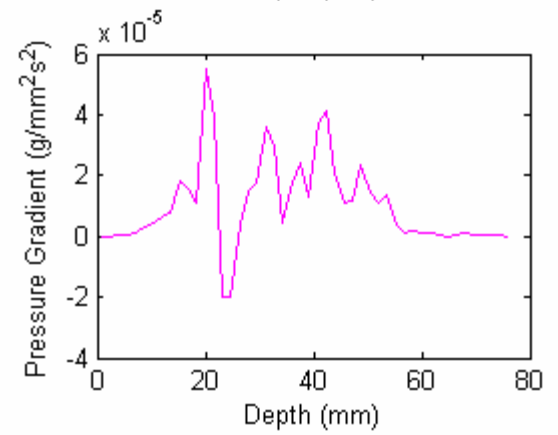
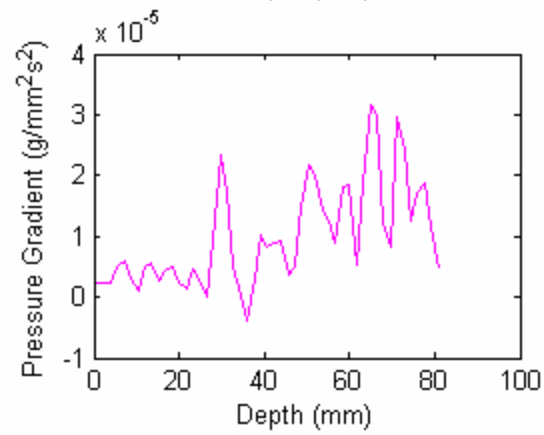
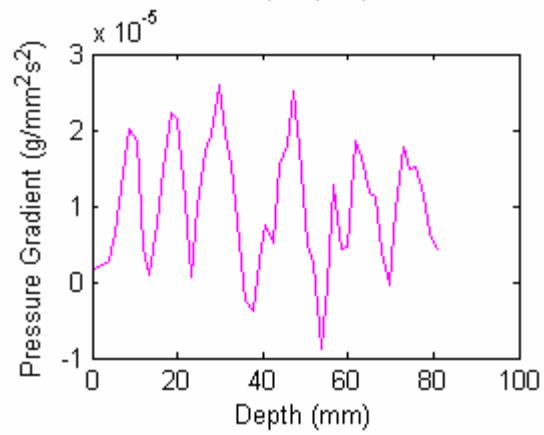
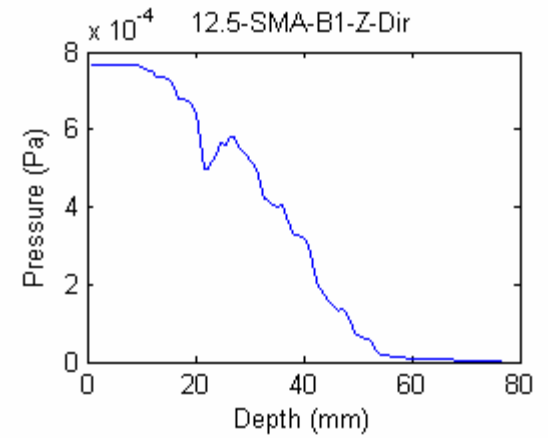
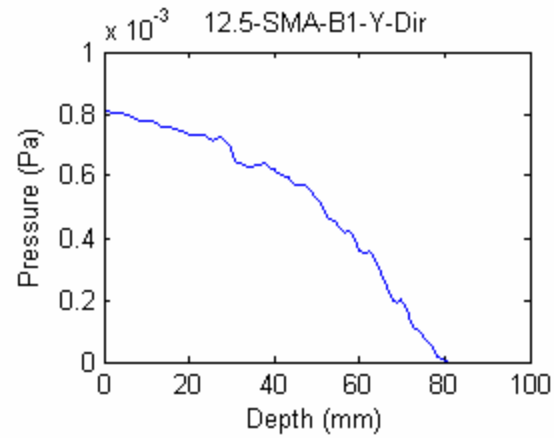
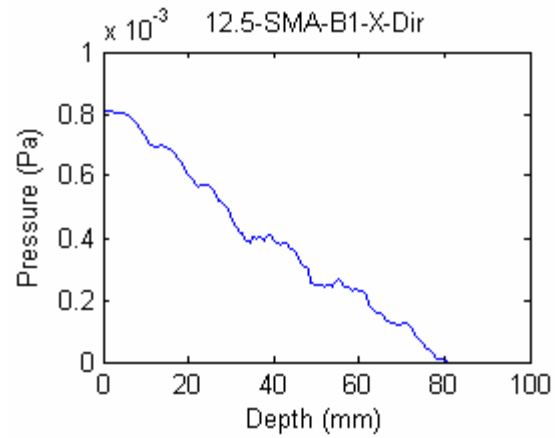


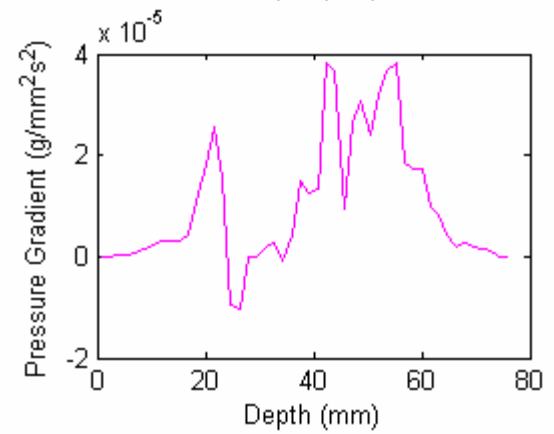
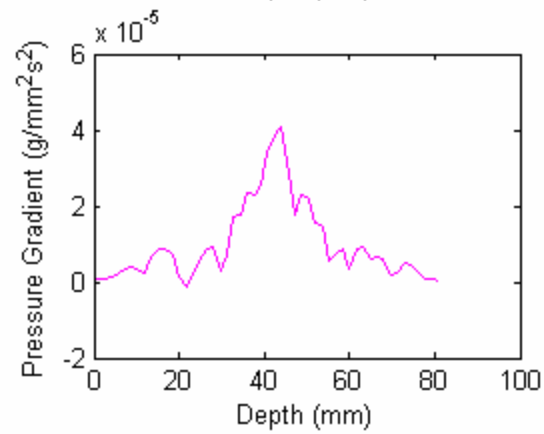
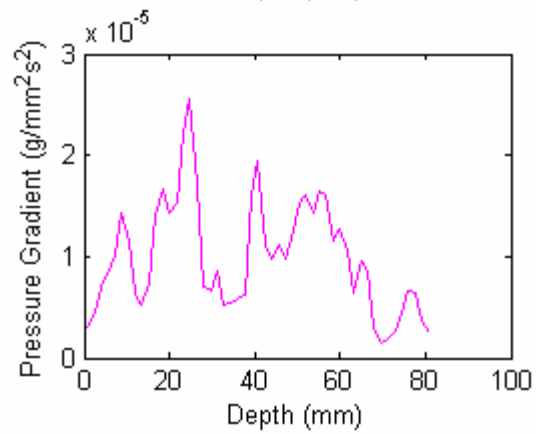
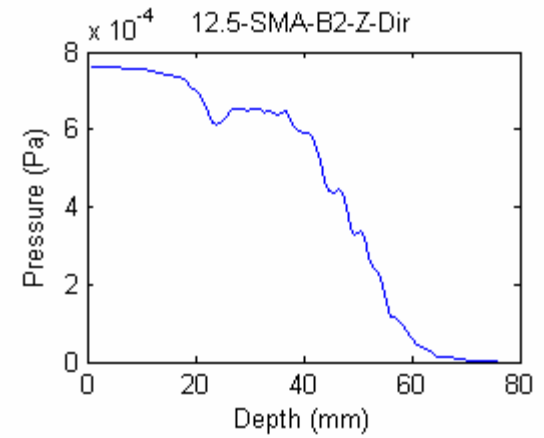
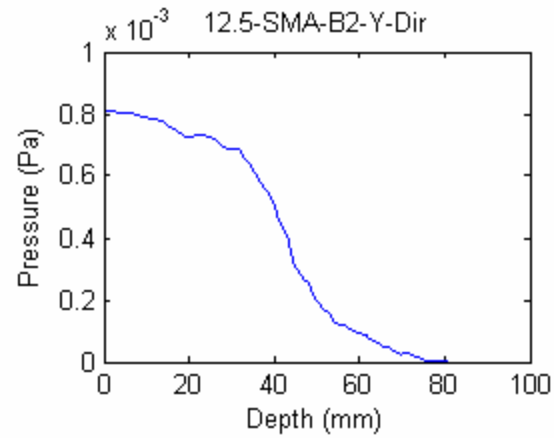
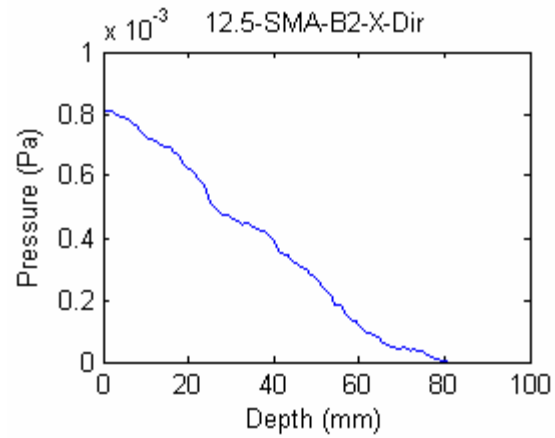


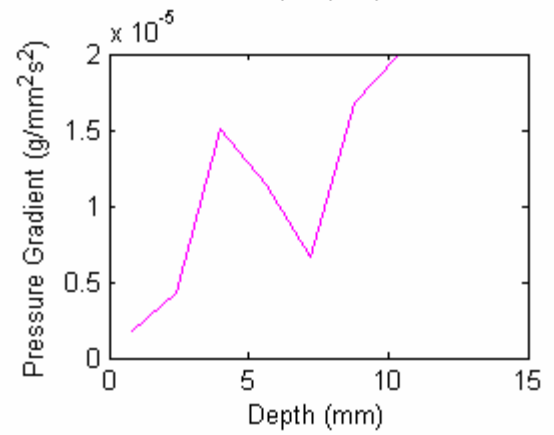
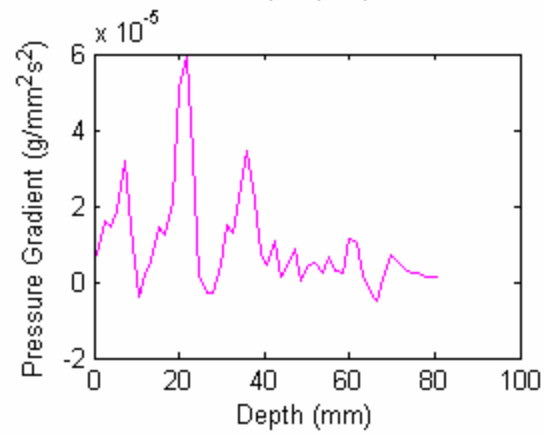
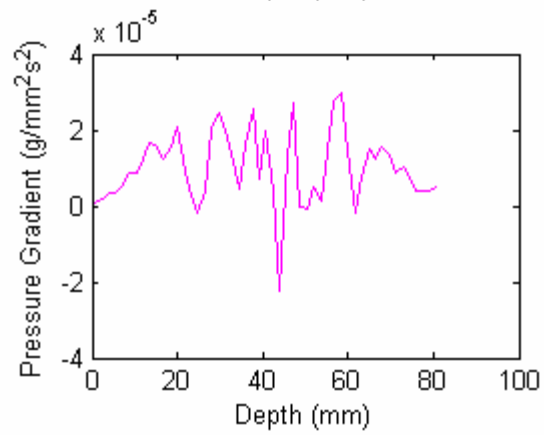
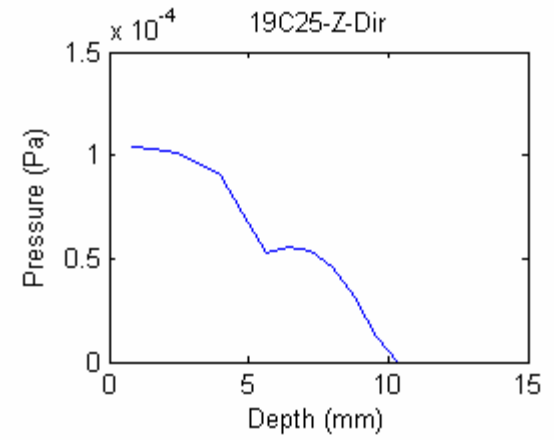
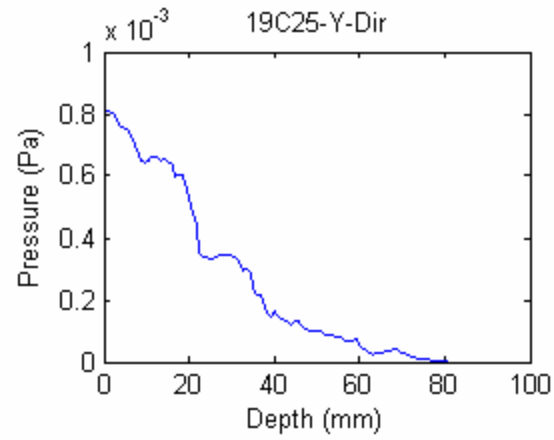
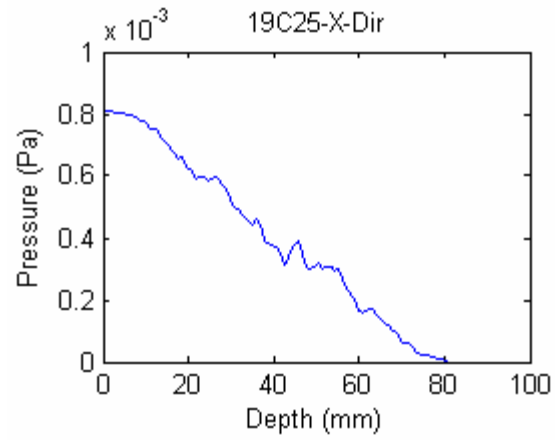


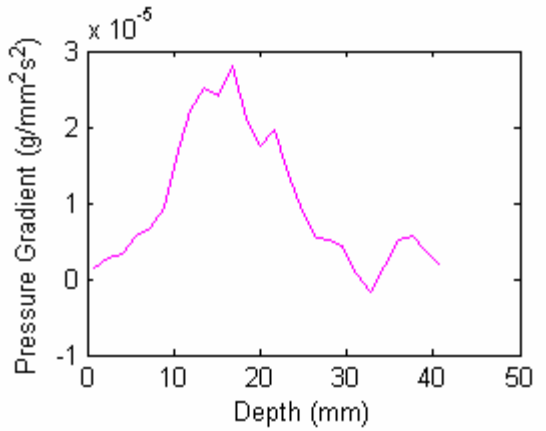
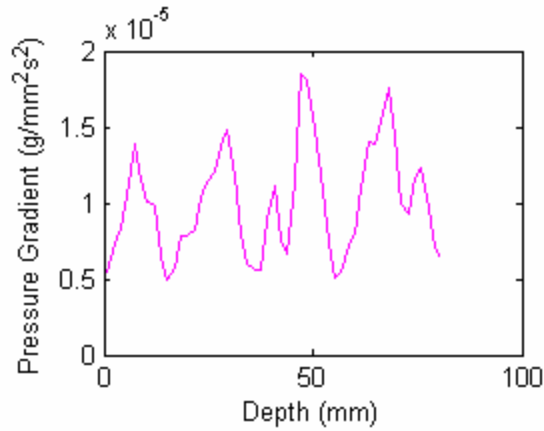
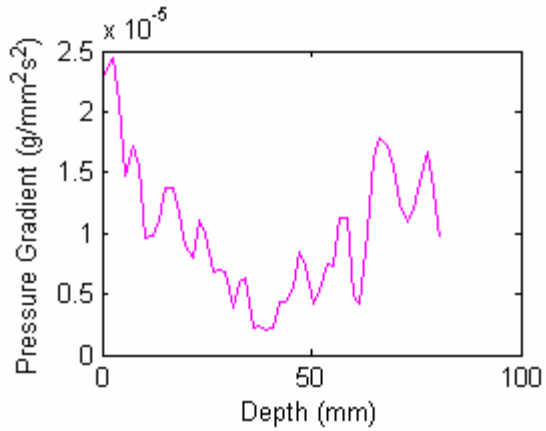
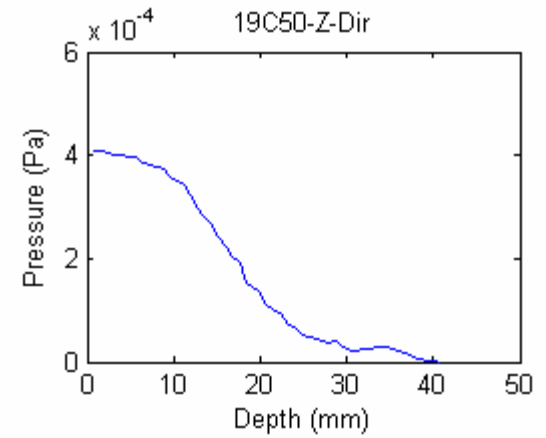
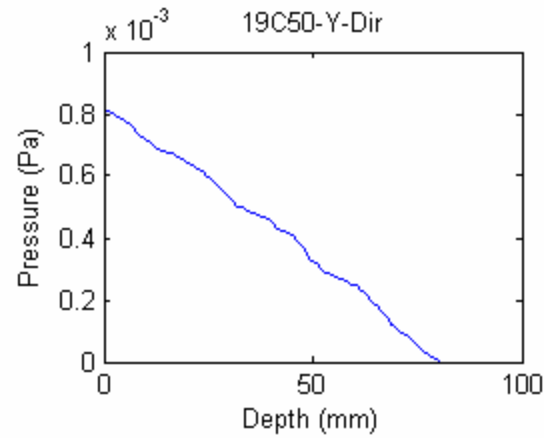
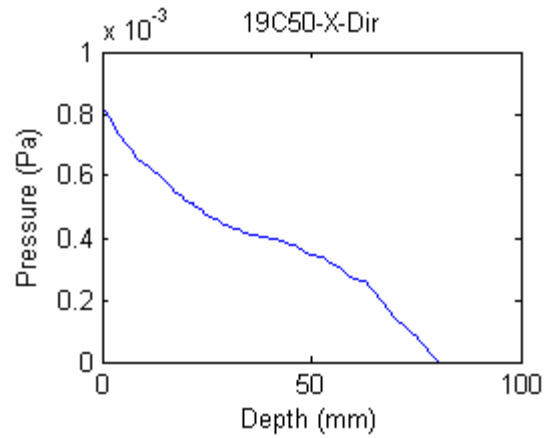


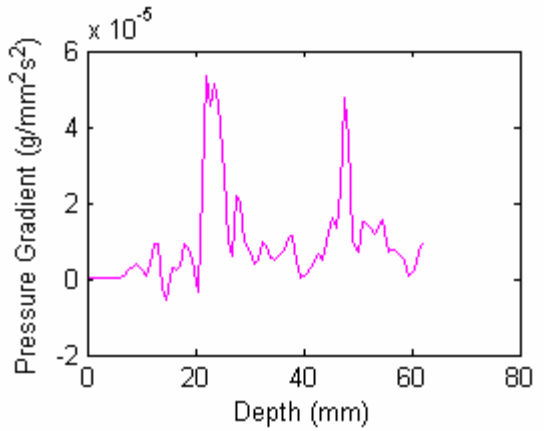
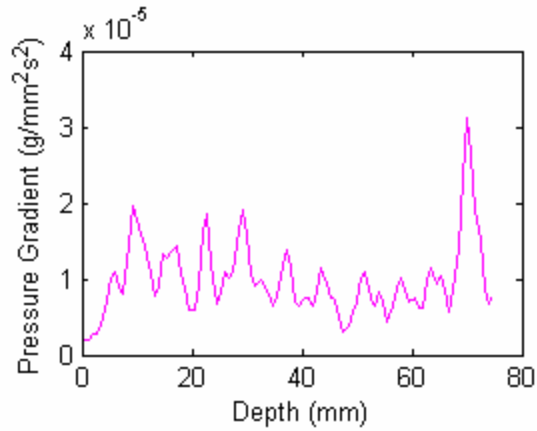
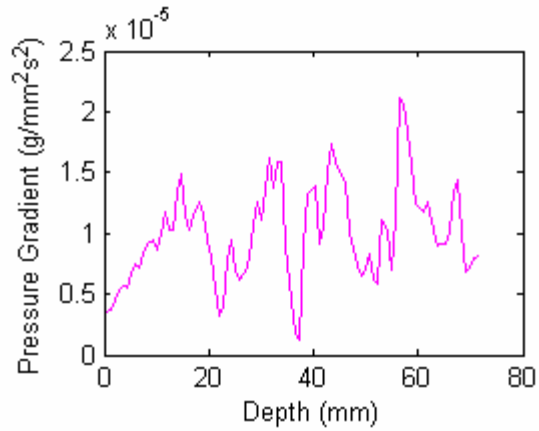
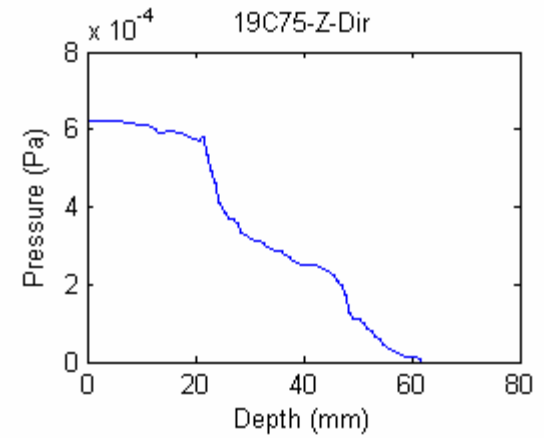
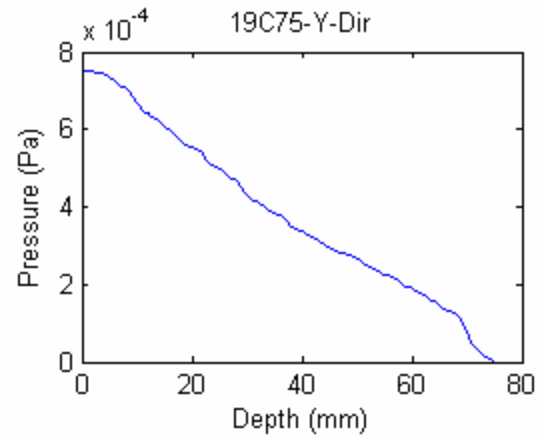
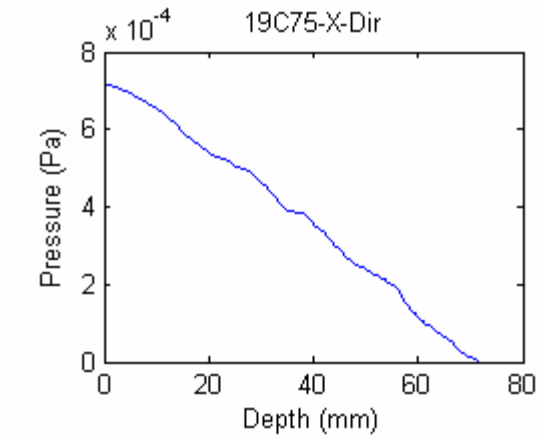


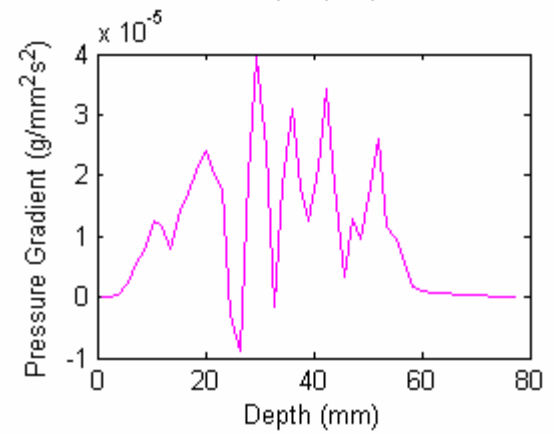
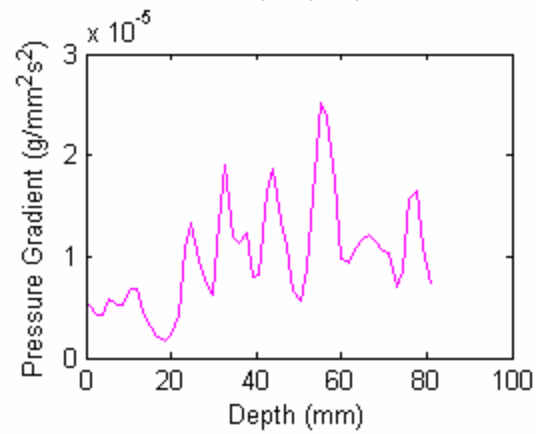
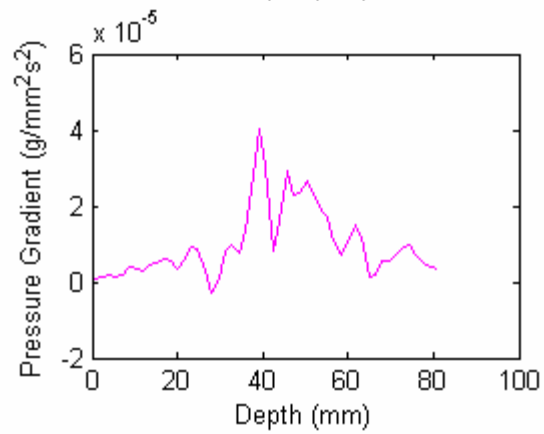
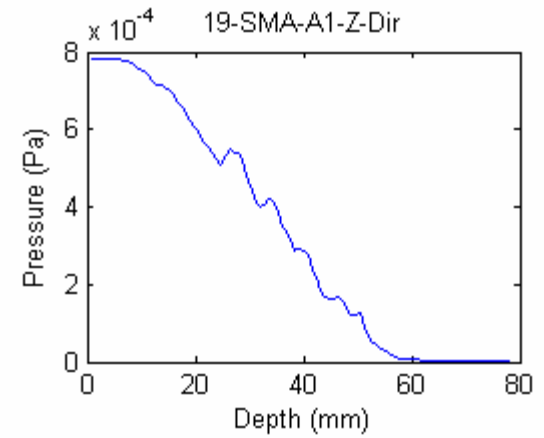
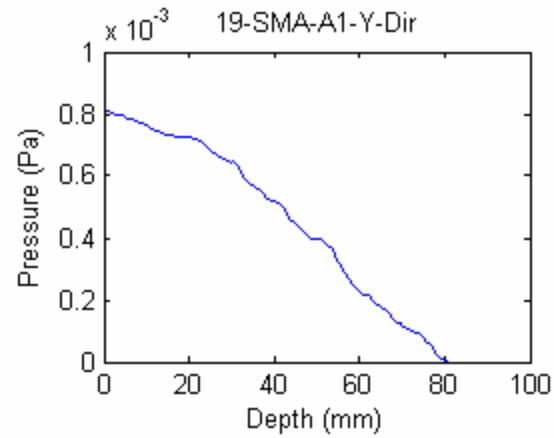
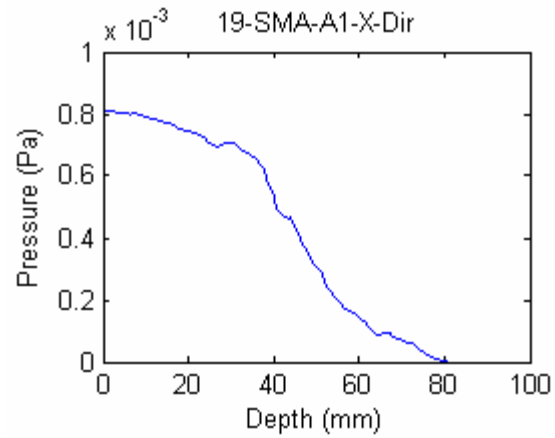


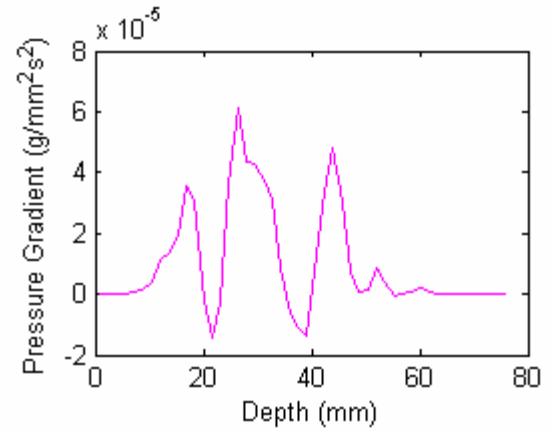
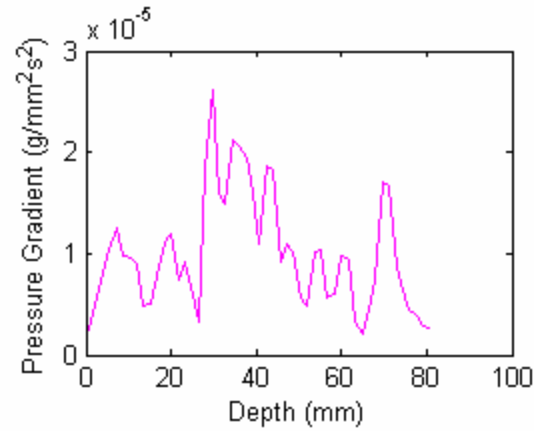
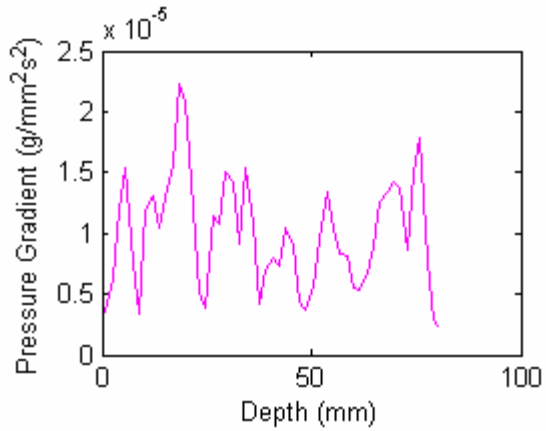
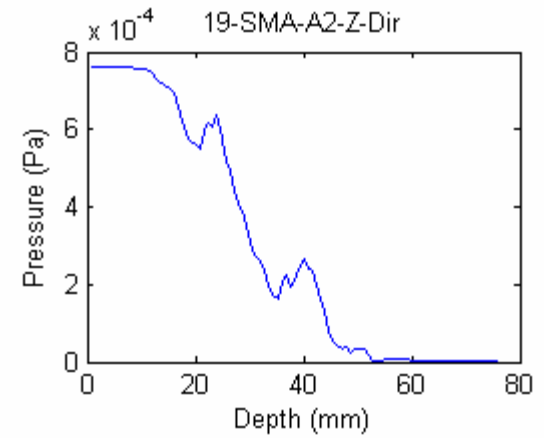
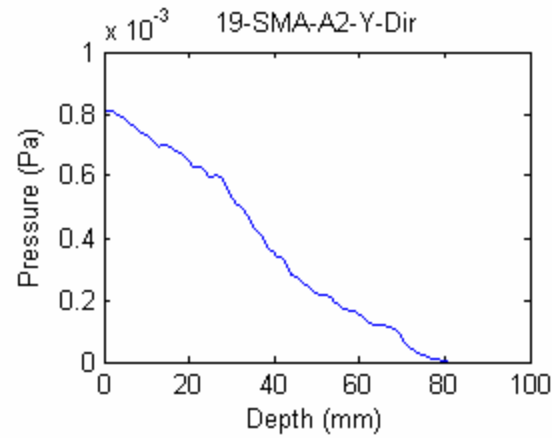
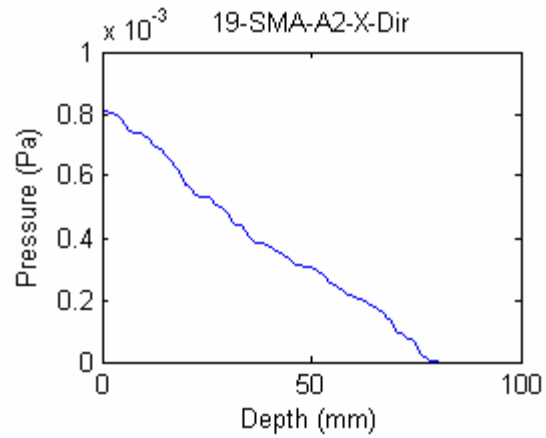


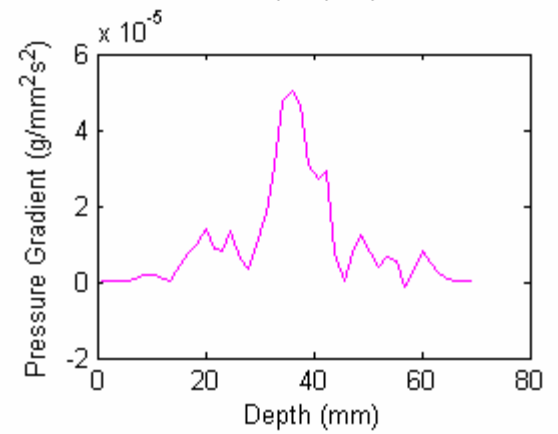
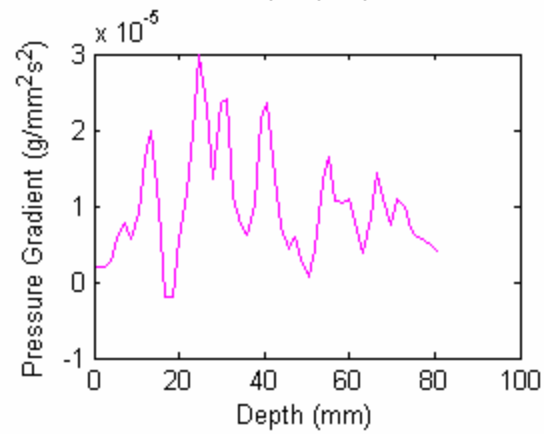
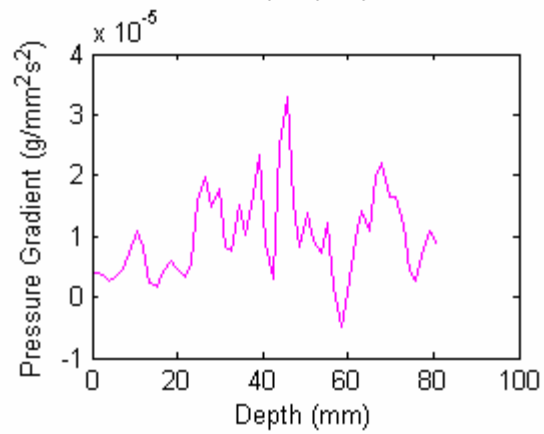
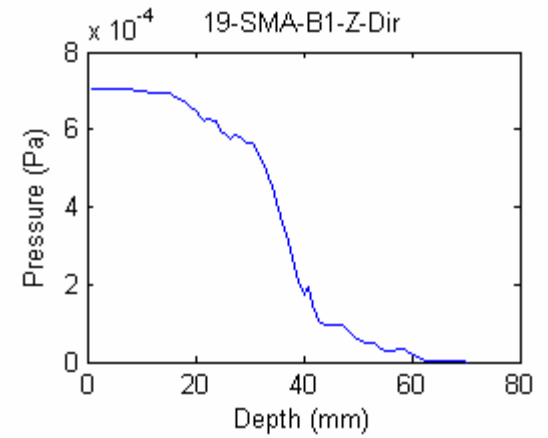
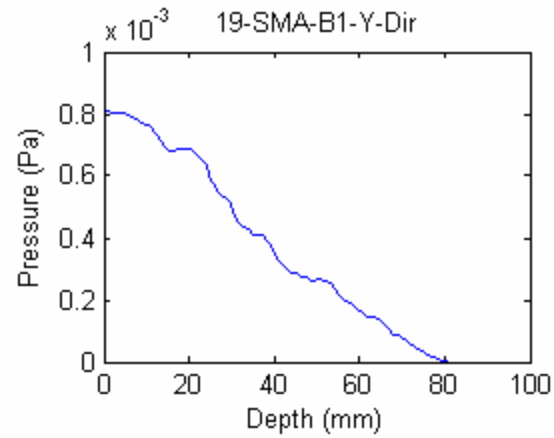
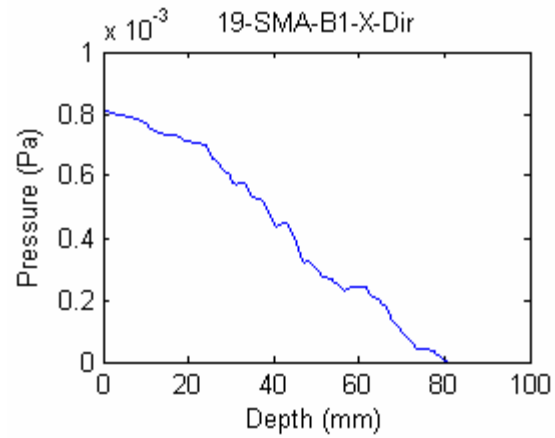


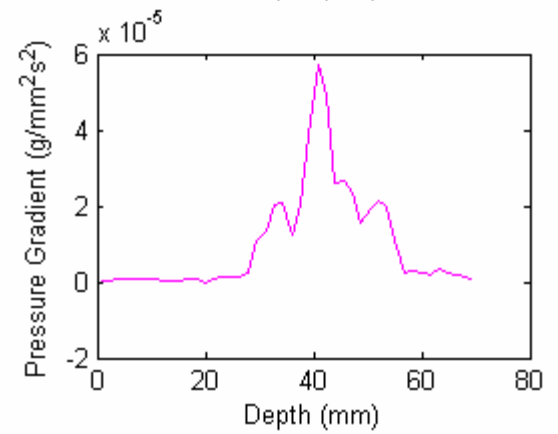
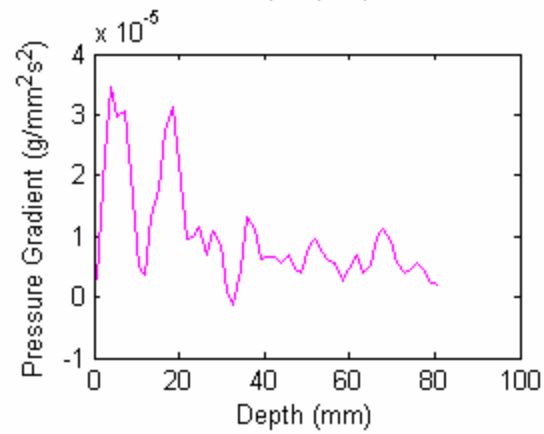
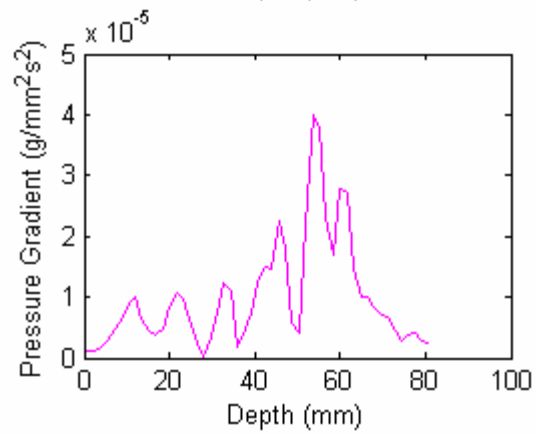
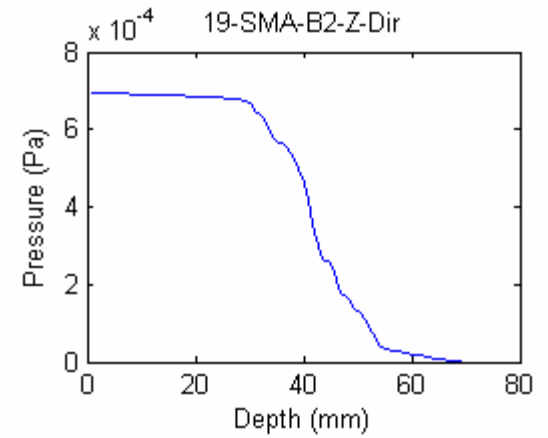
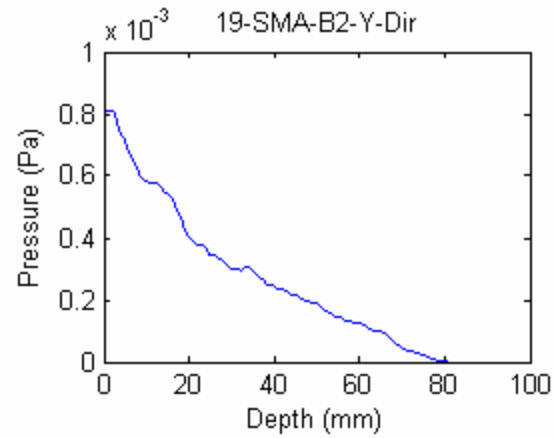
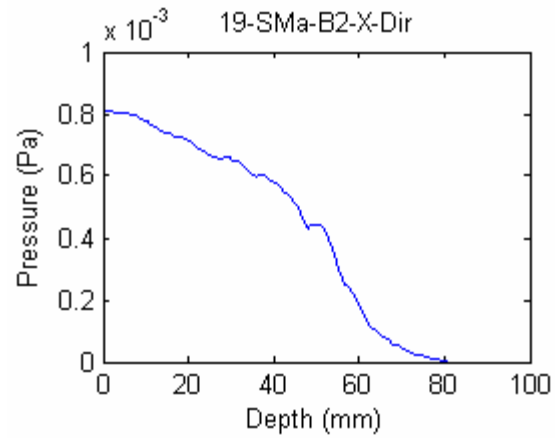


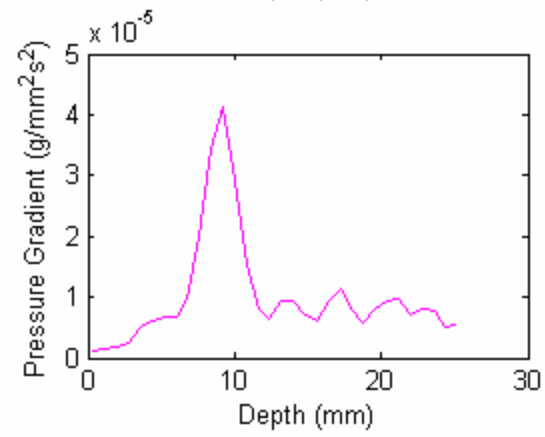
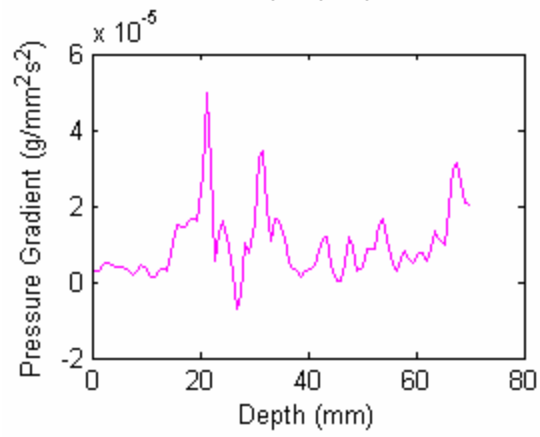
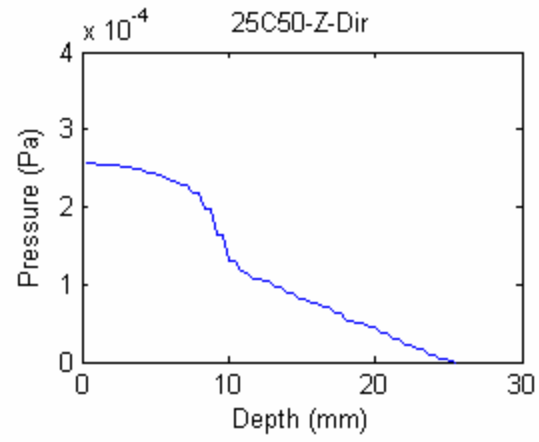
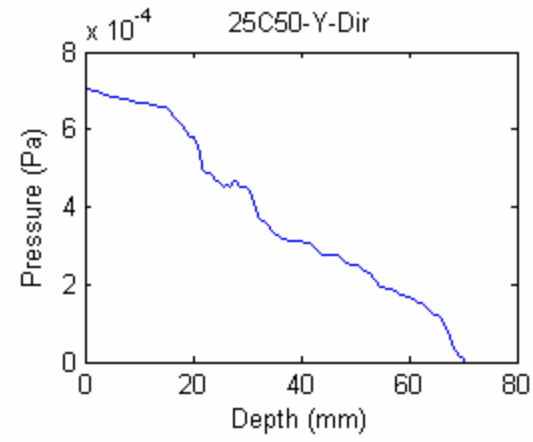


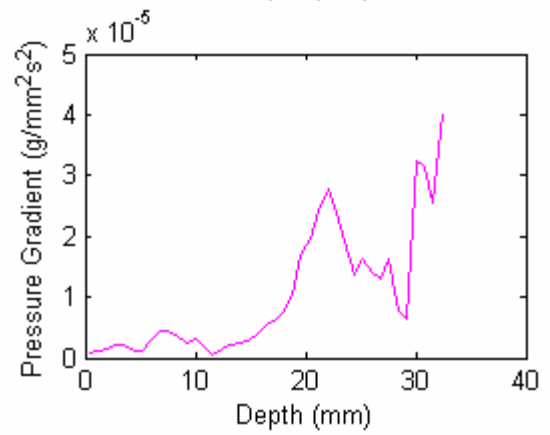
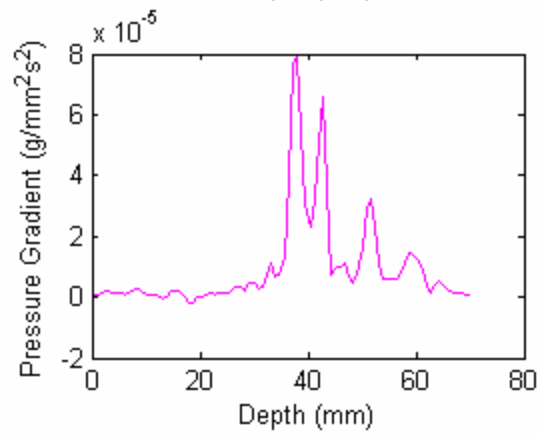
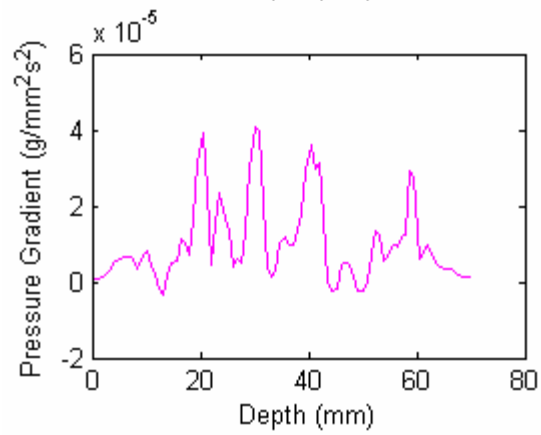
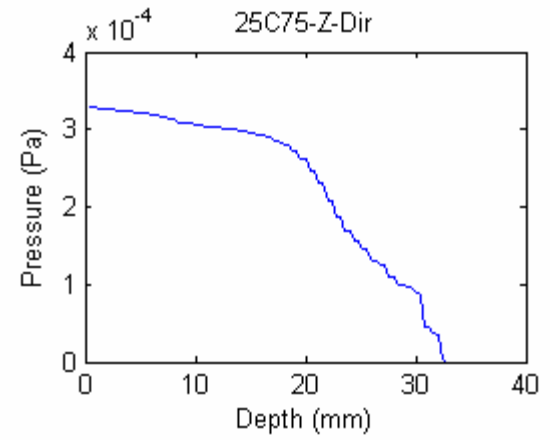
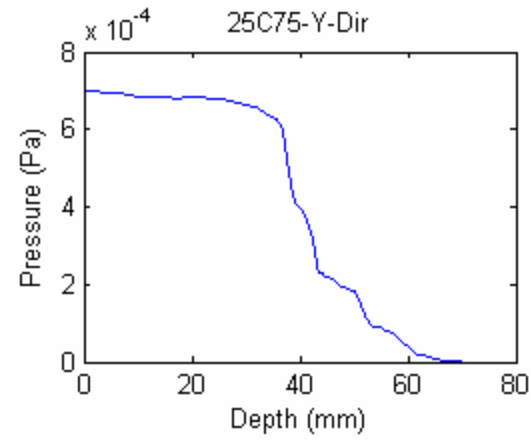
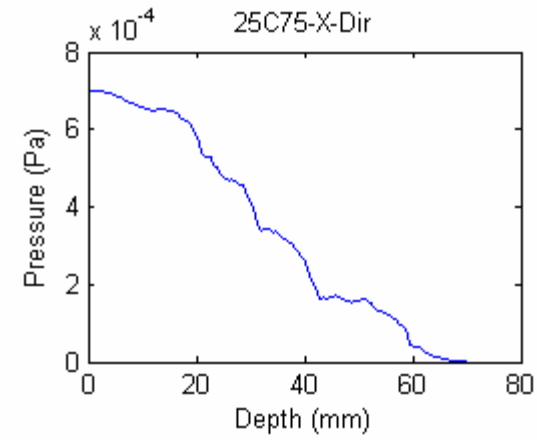




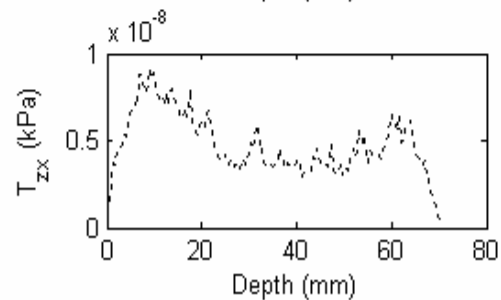
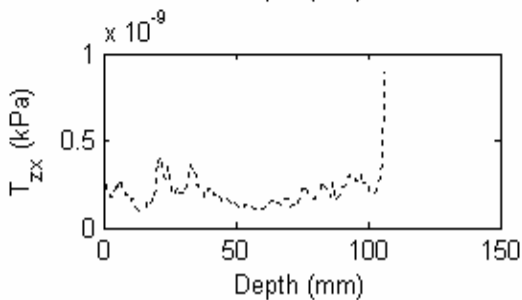
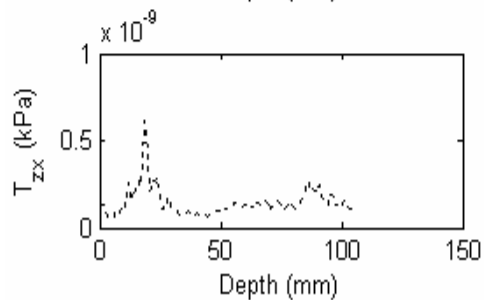
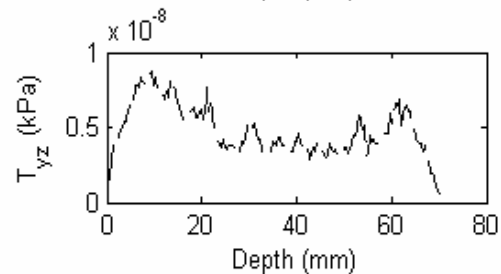
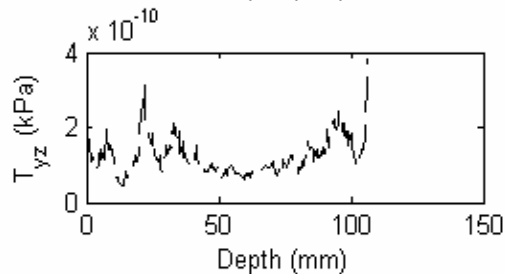
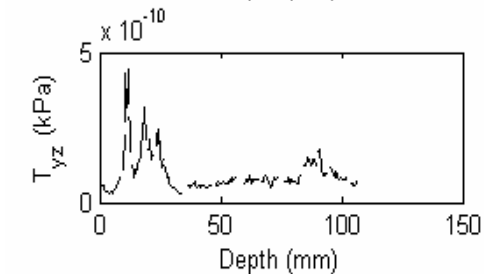
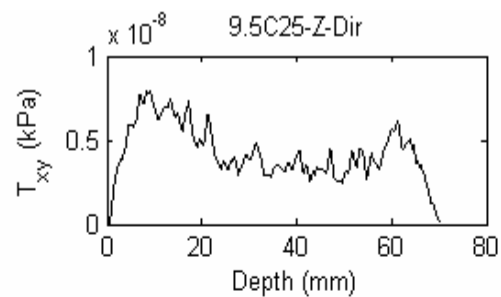
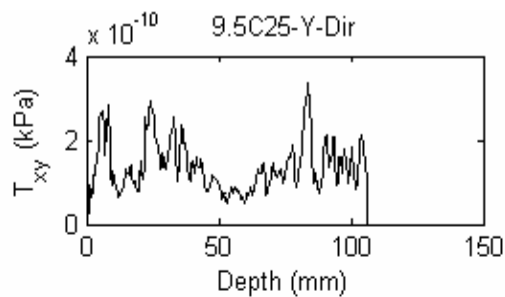
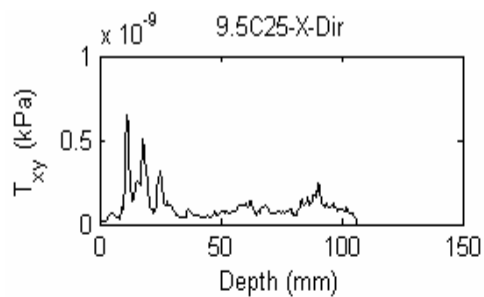


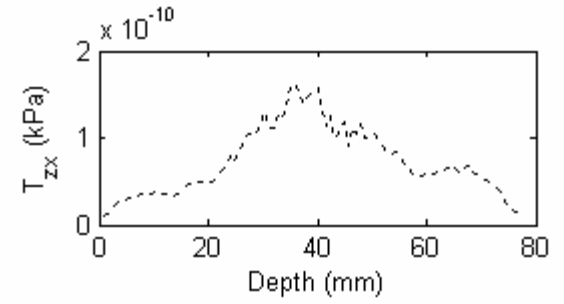
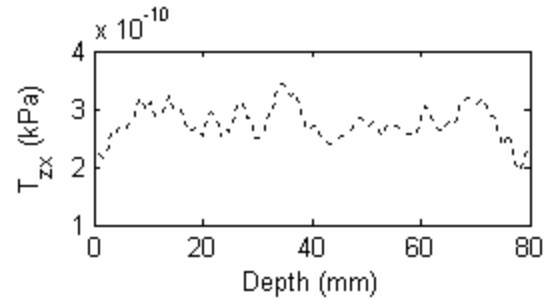
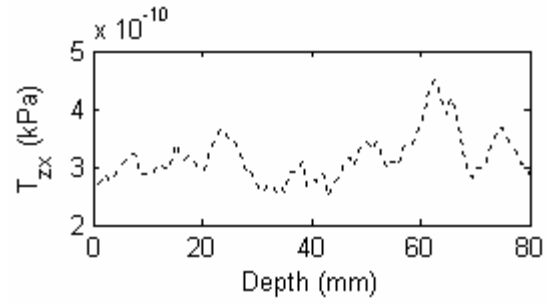
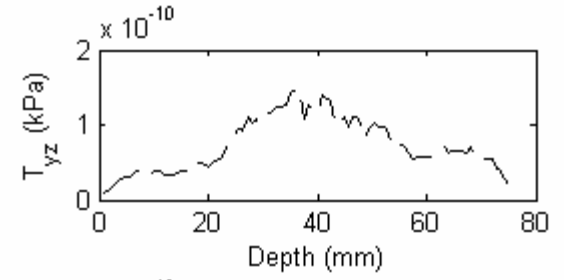
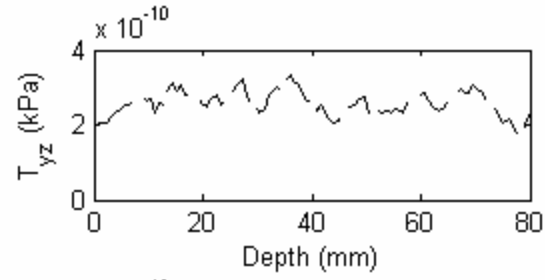
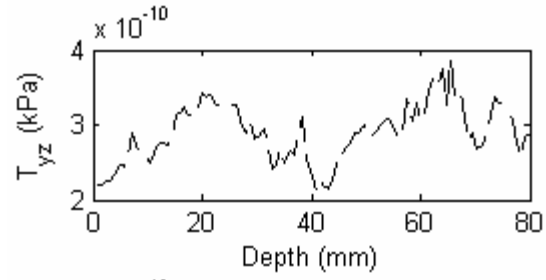
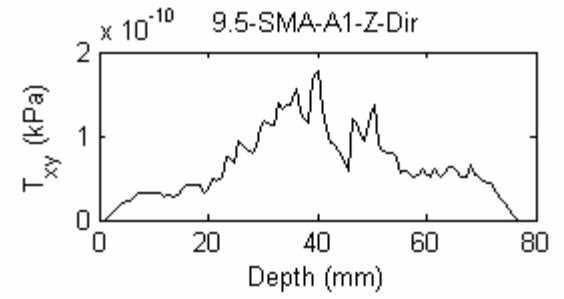
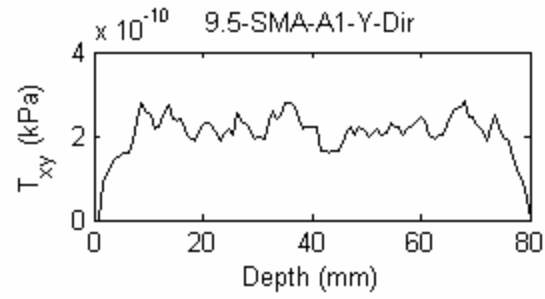
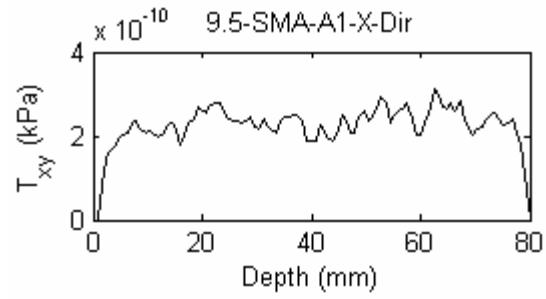


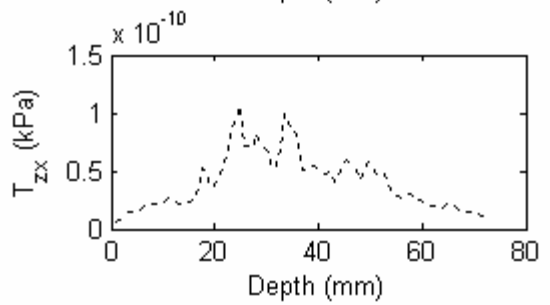
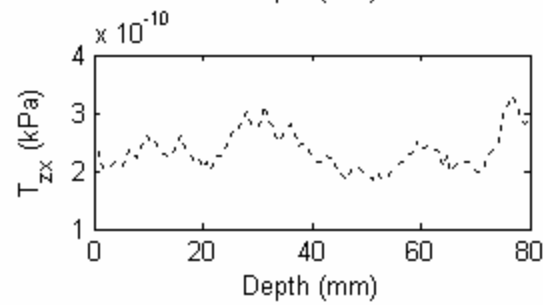
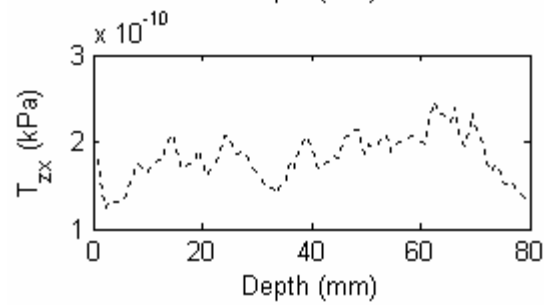
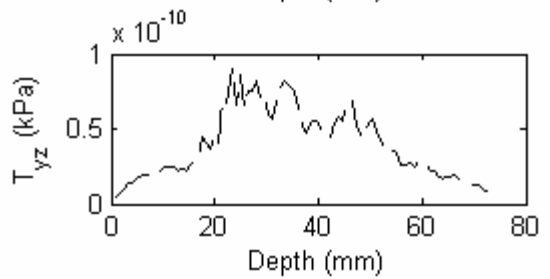
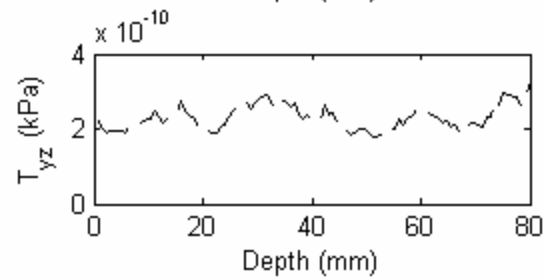
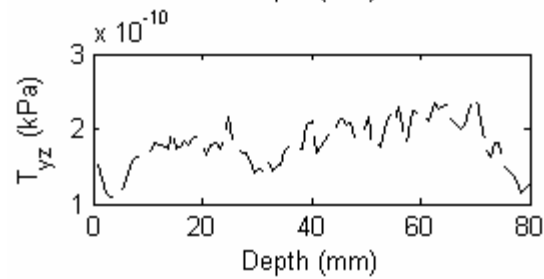
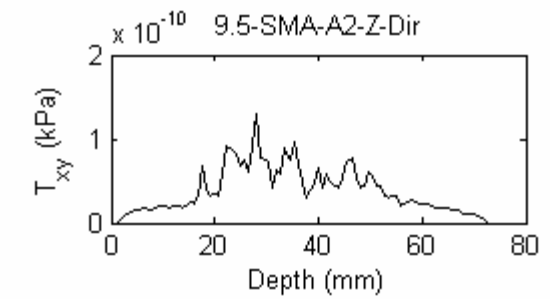
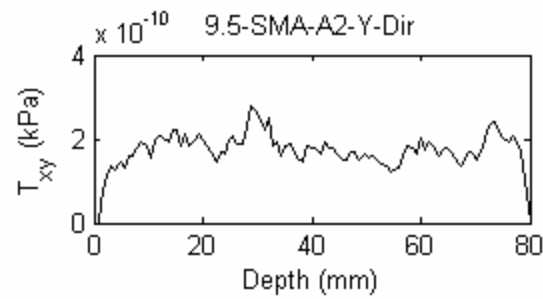
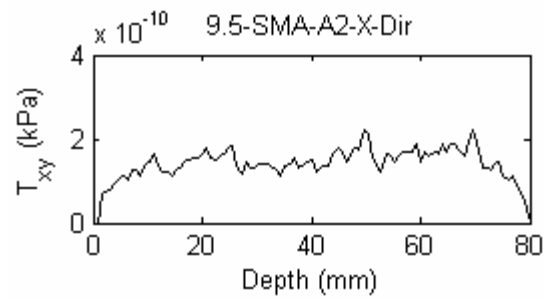


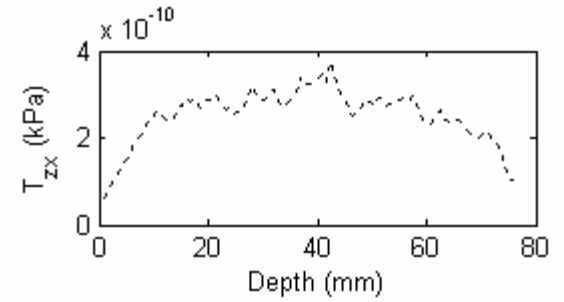
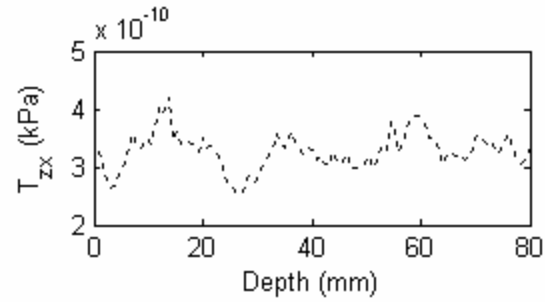
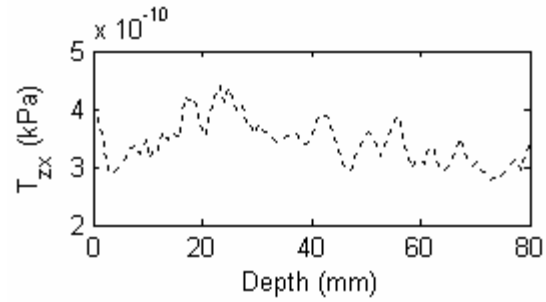
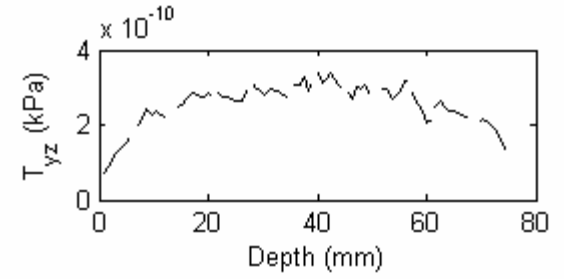
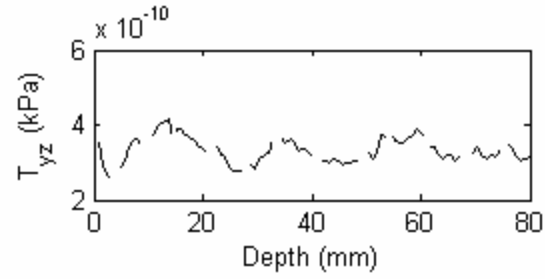
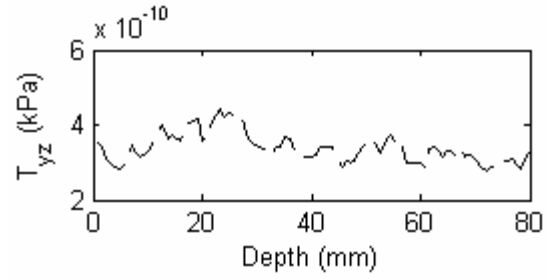
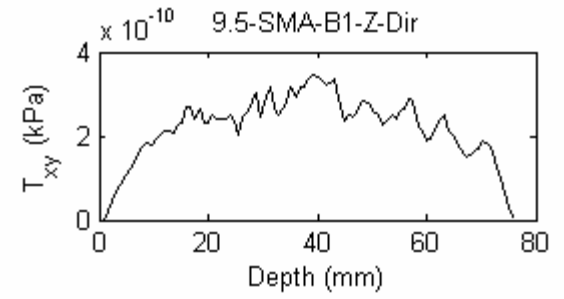
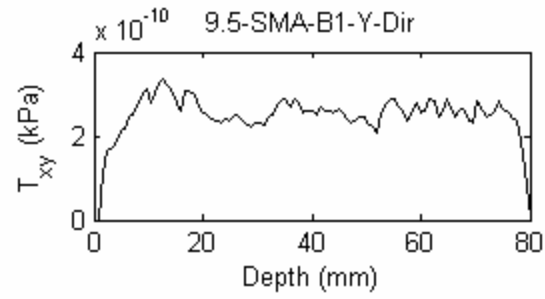
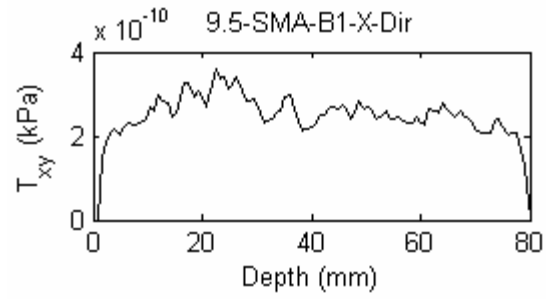


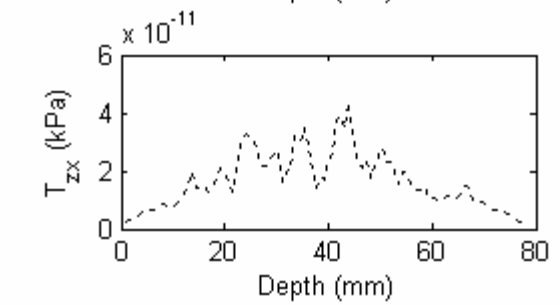
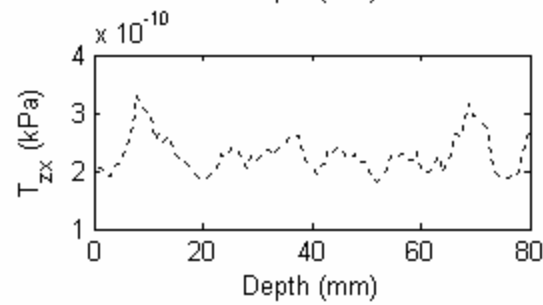
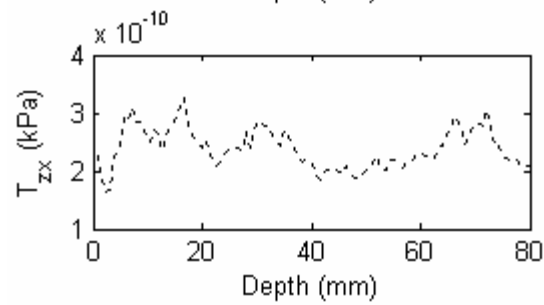
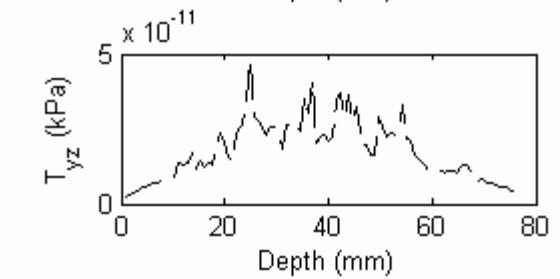
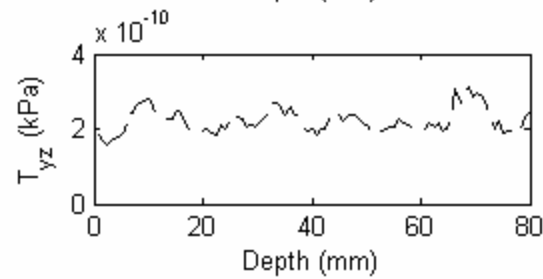
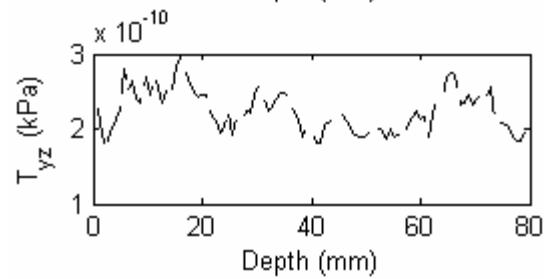
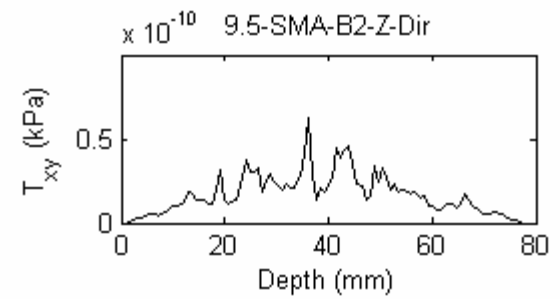
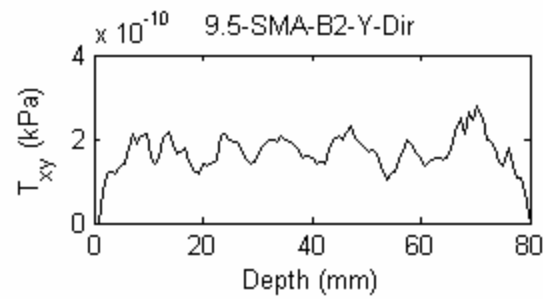
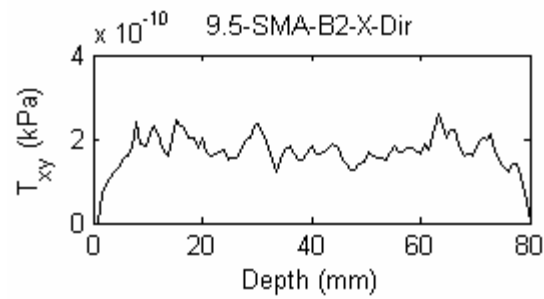
APPENDIX G VARIATION OF SHEAR STRESS TENSOR COMPONENTS OF ALL SPECIMENS

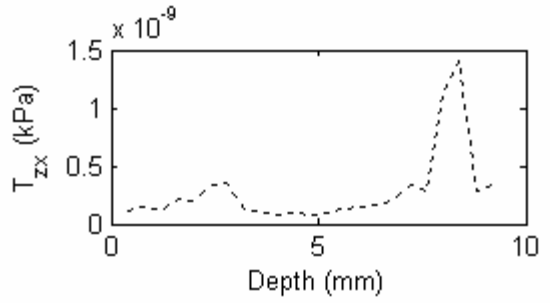
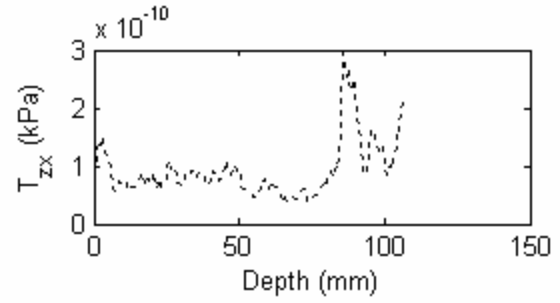
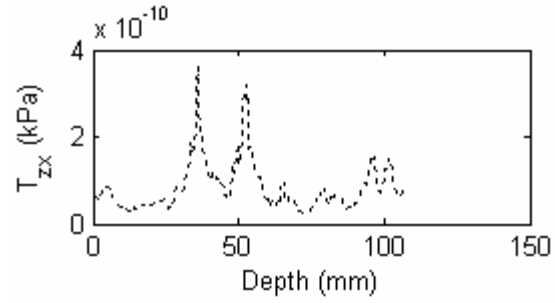
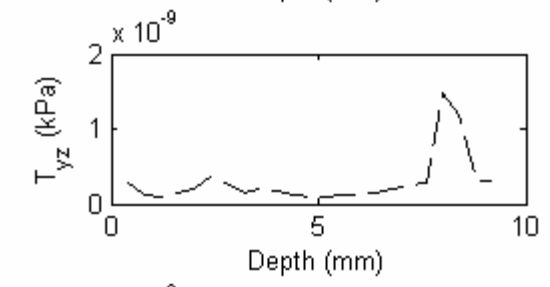
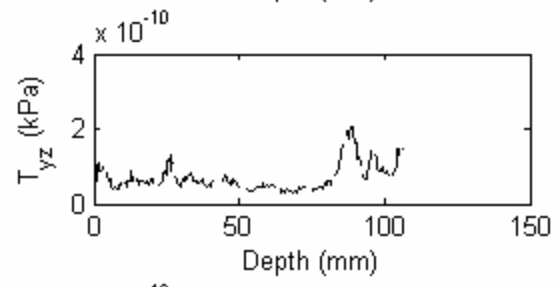
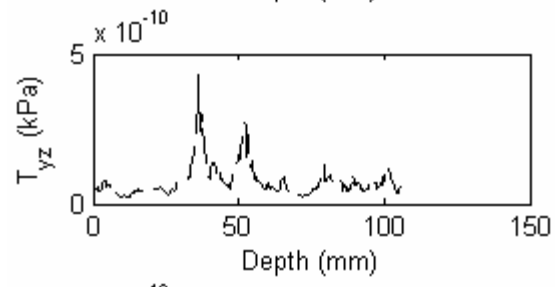
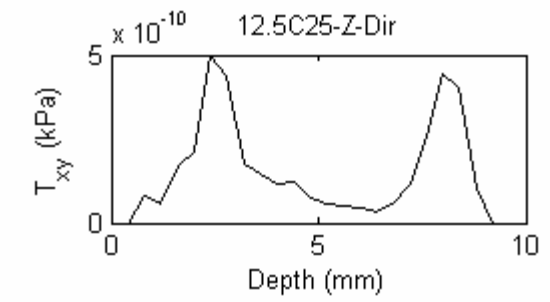
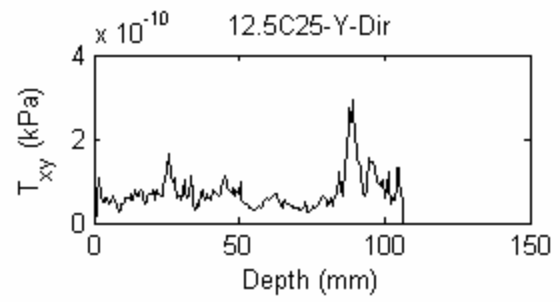
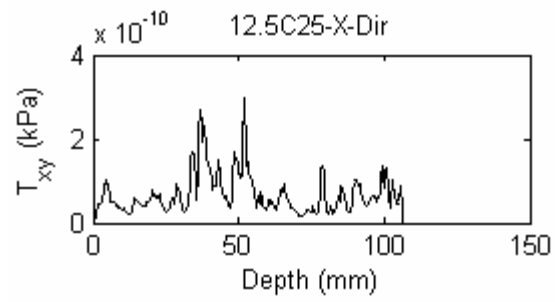


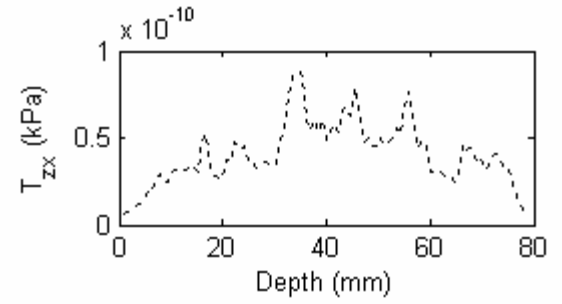
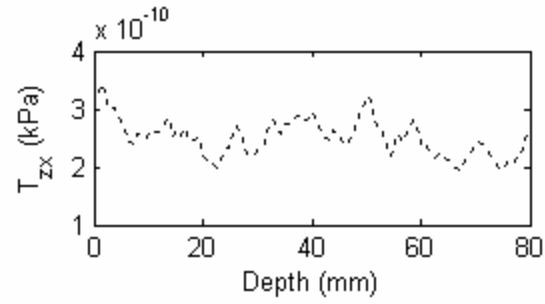
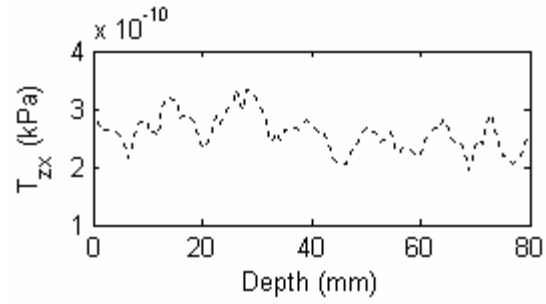
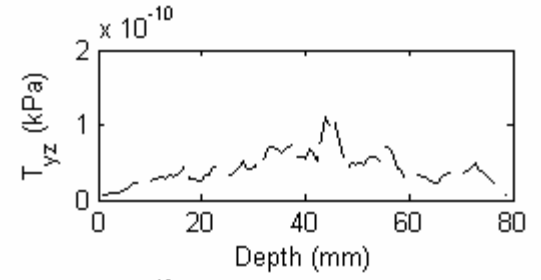
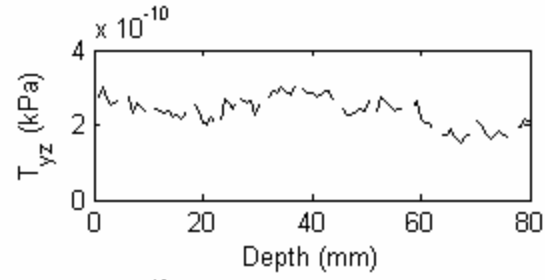
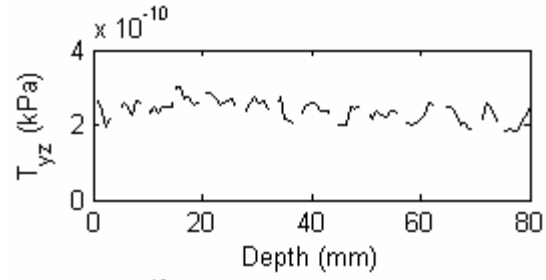
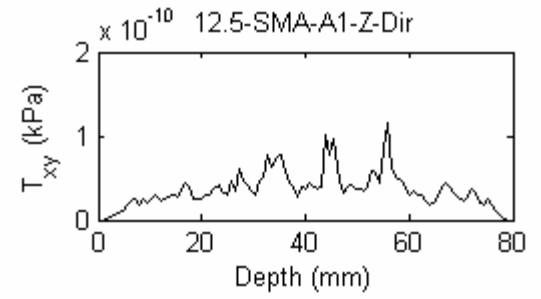
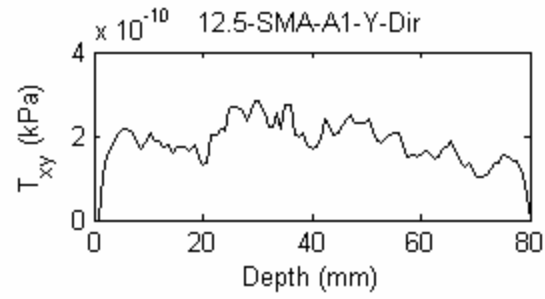
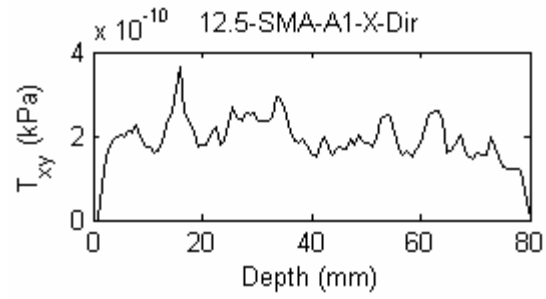


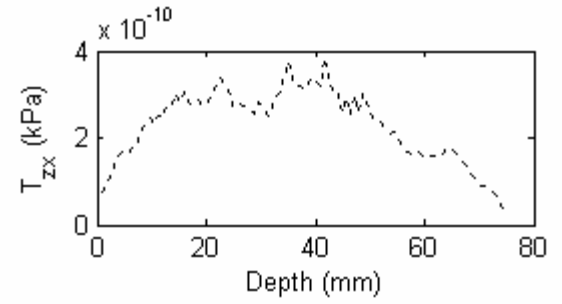
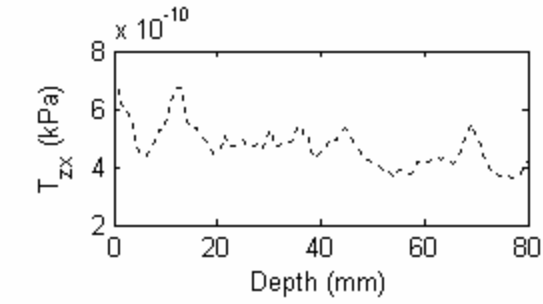
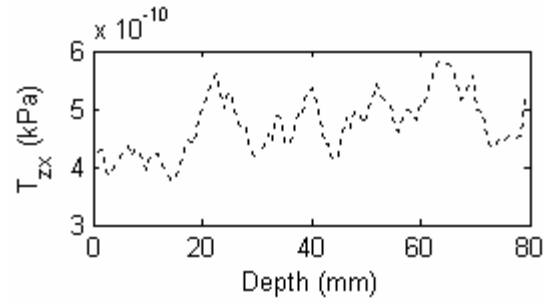
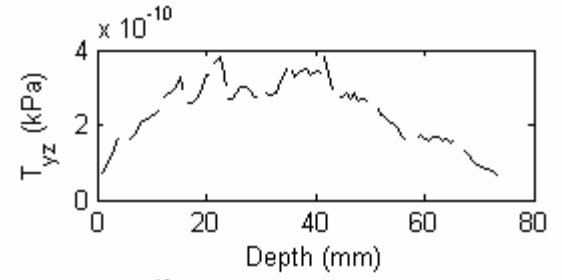
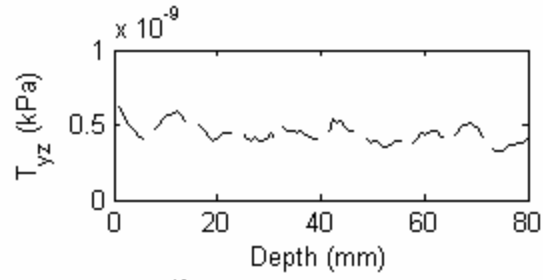
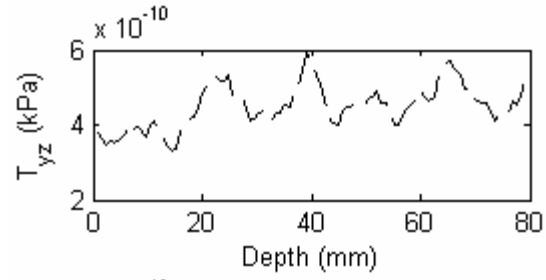
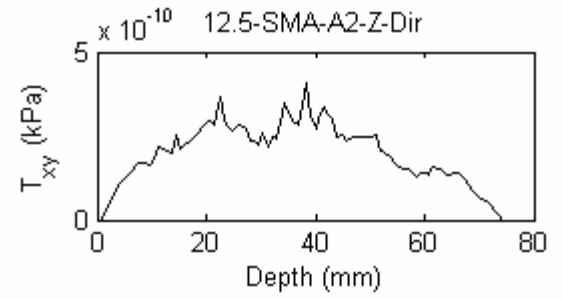
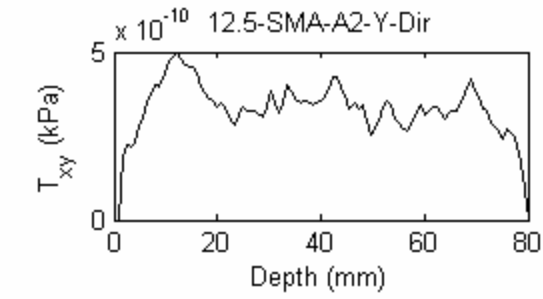
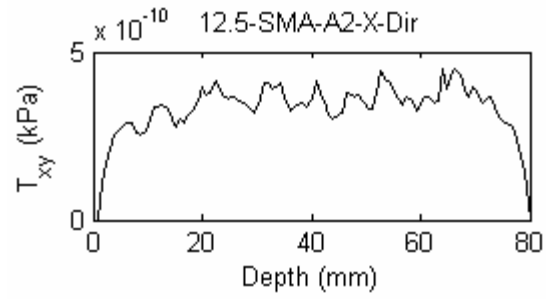


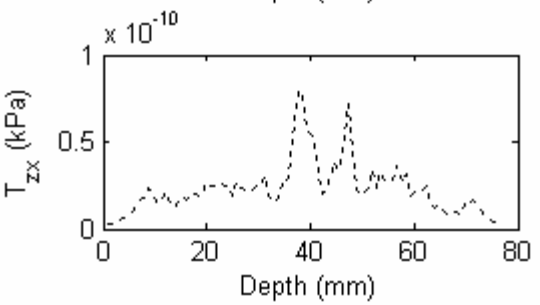
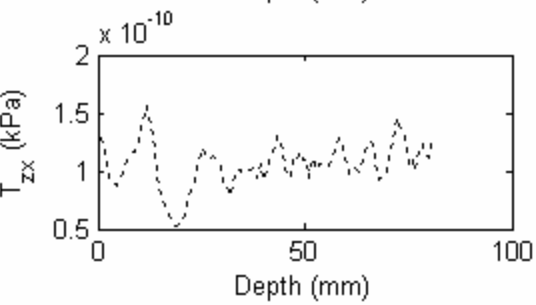
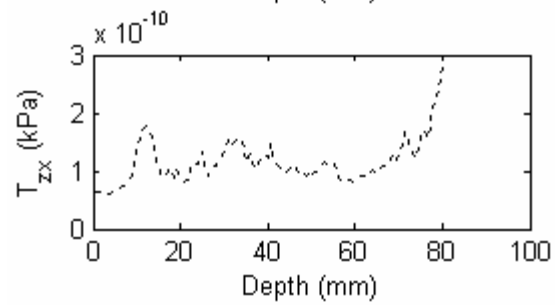
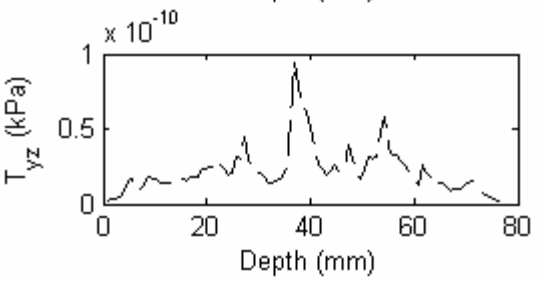
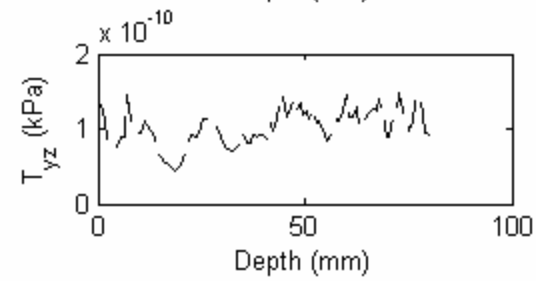
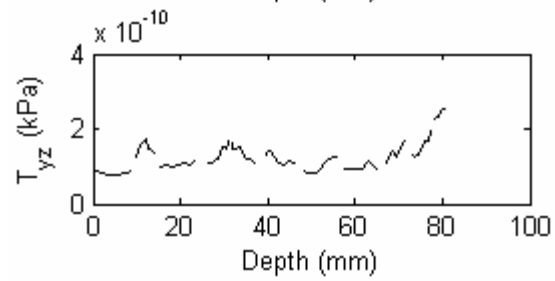
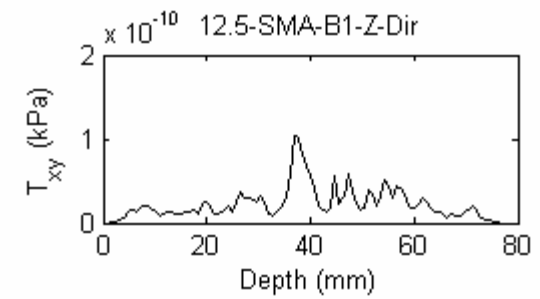
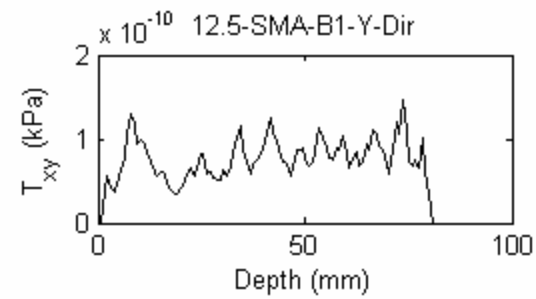
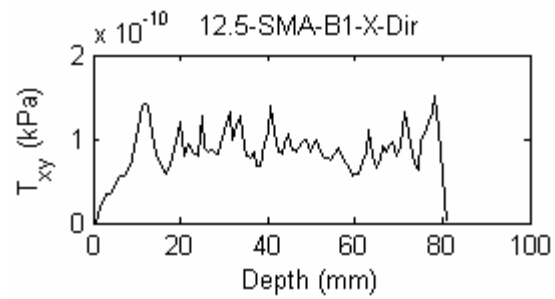


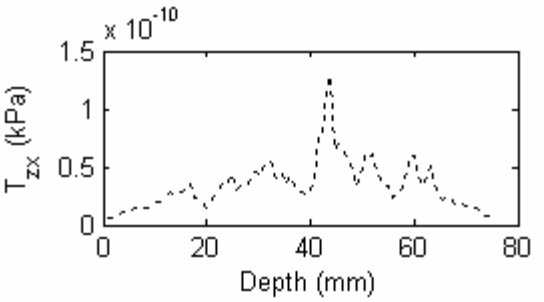
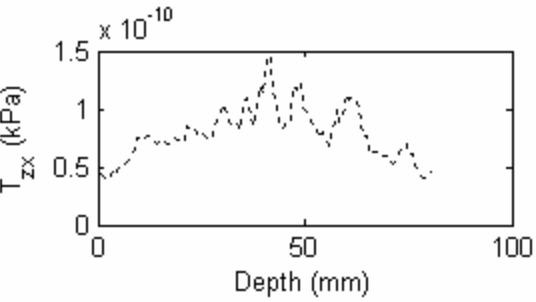
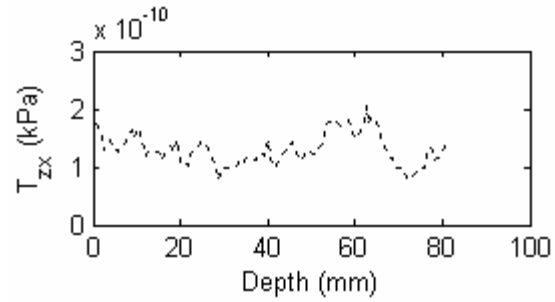
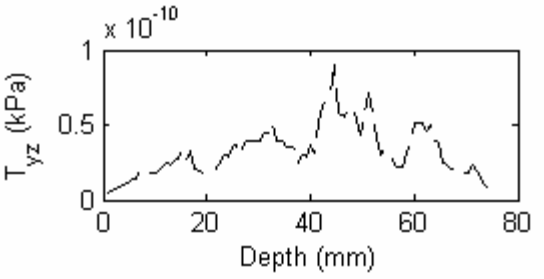
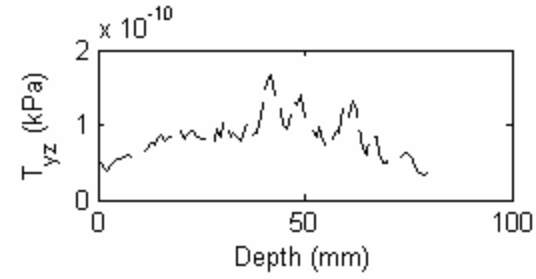
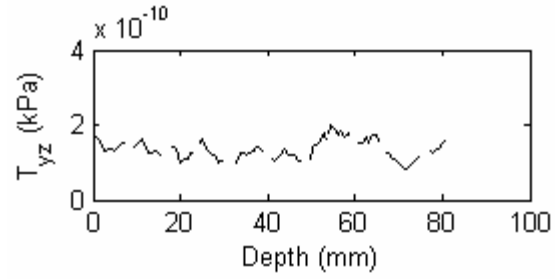
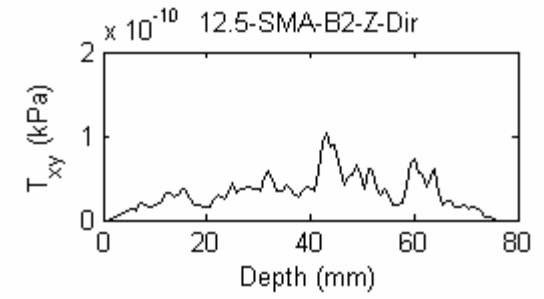
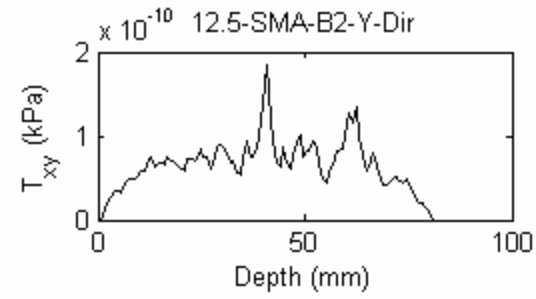
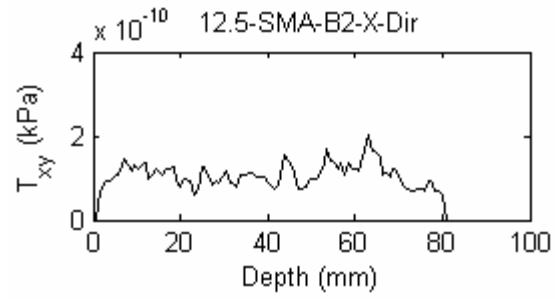


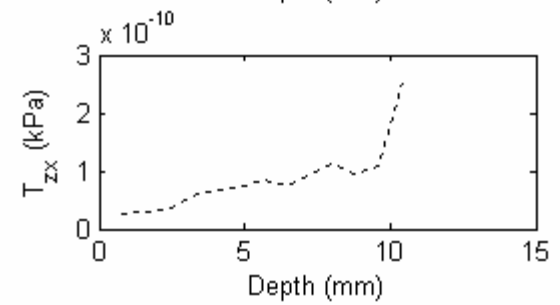
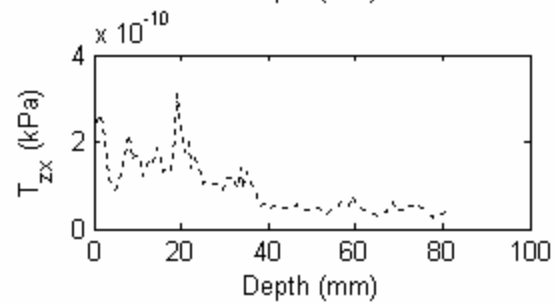
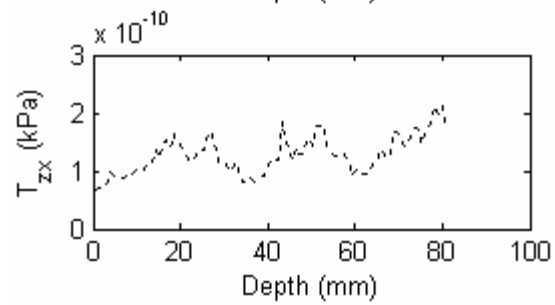
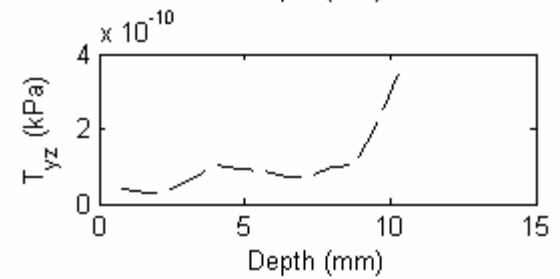
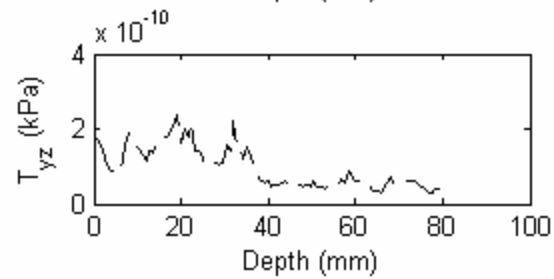
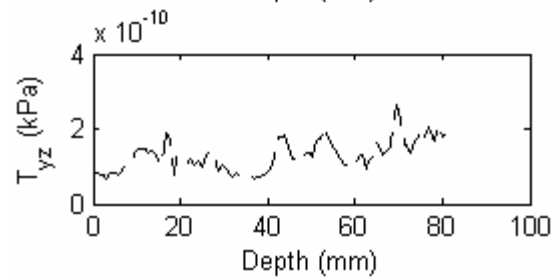
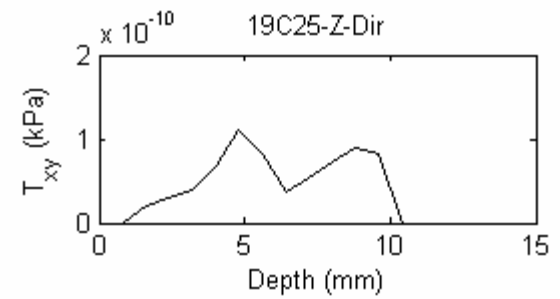
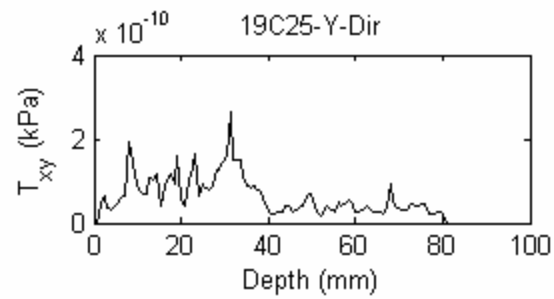
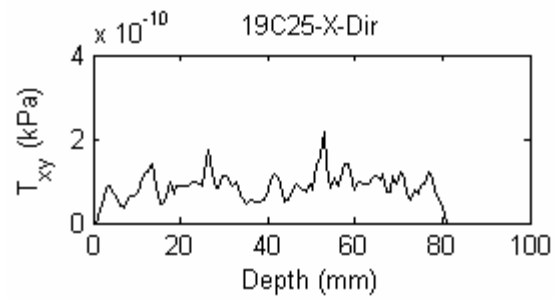


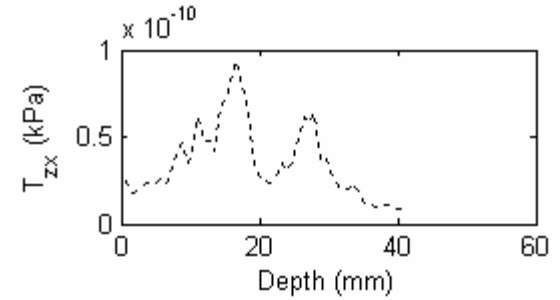
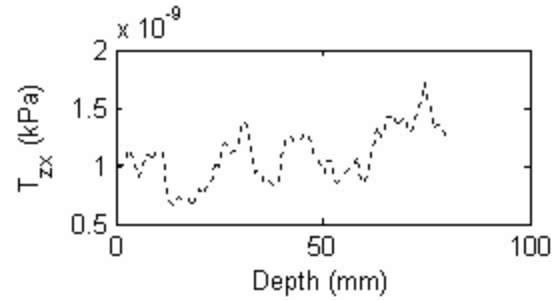
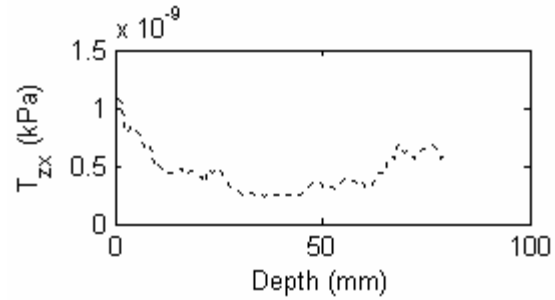
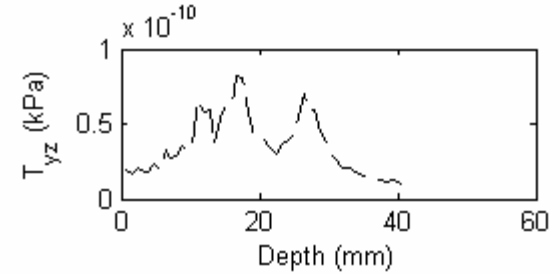
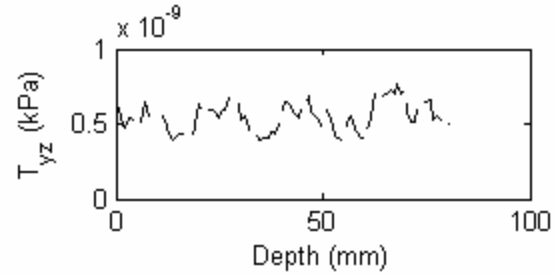
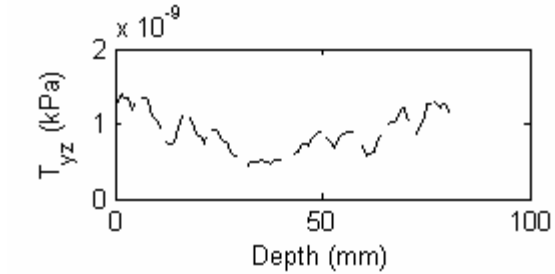
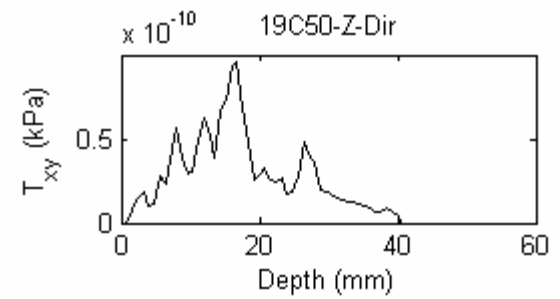
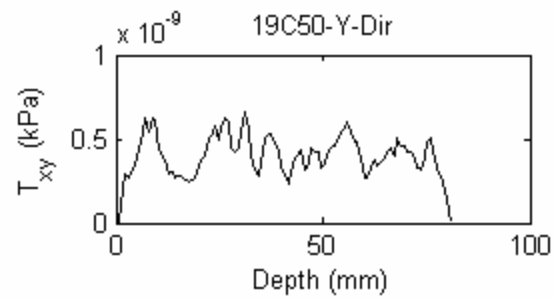
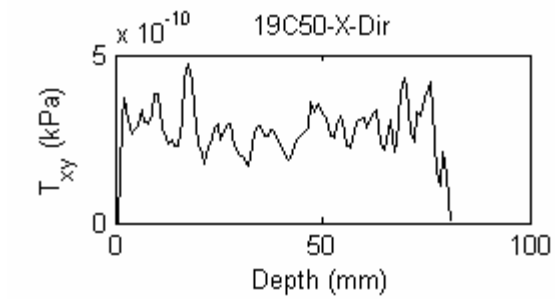


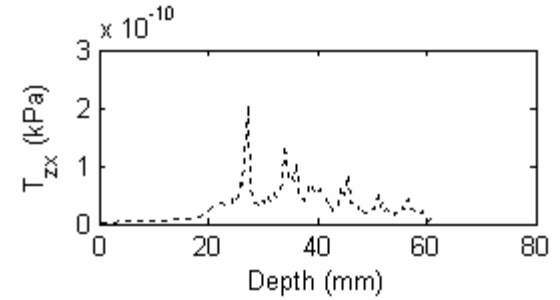
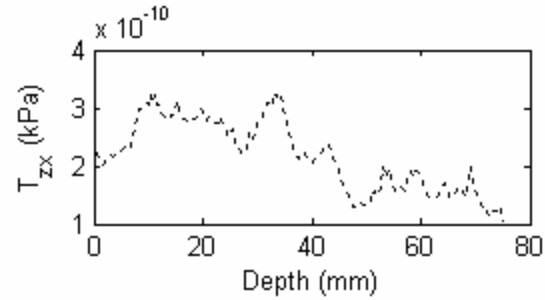
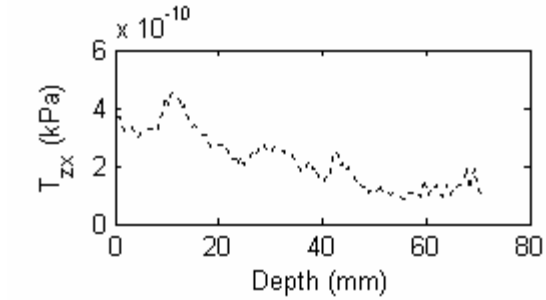
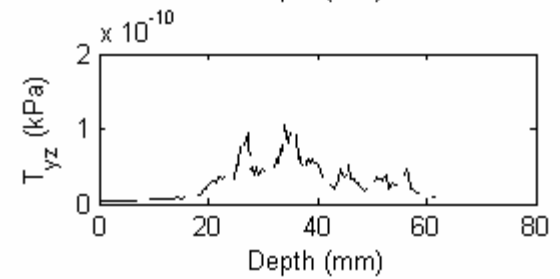
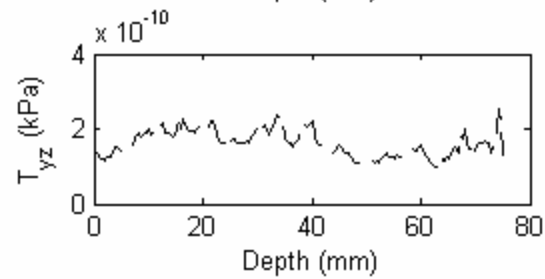
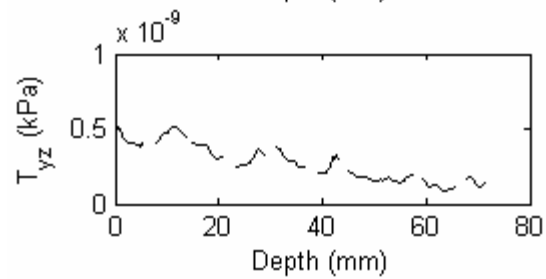
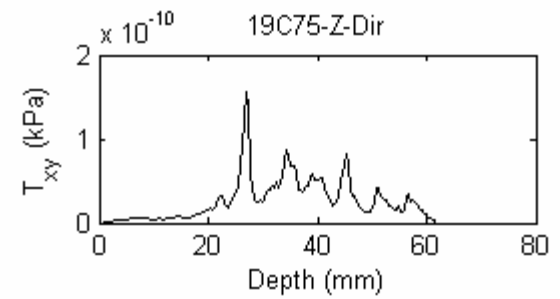
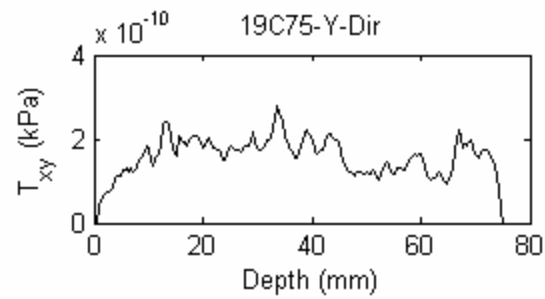
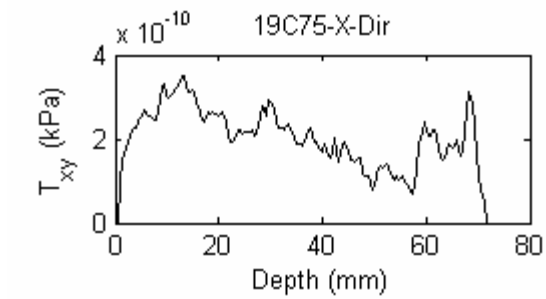


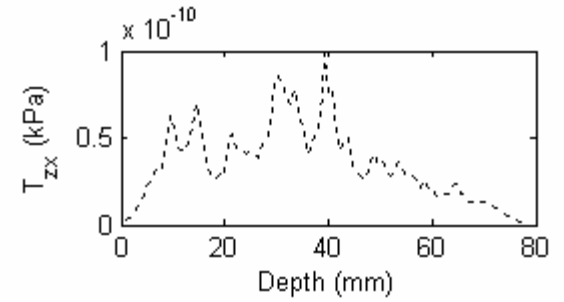
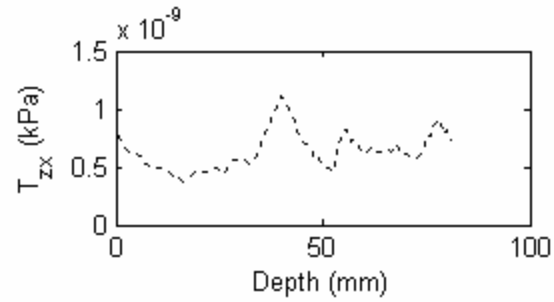
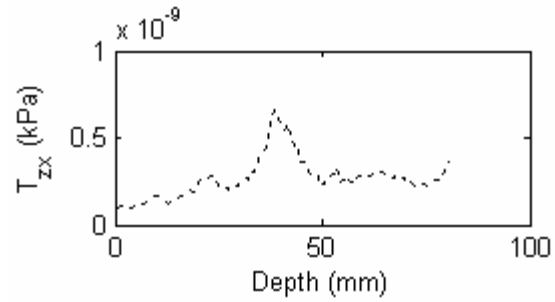
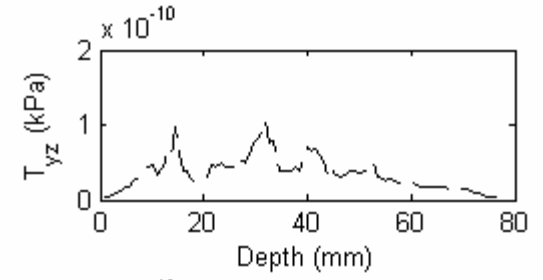
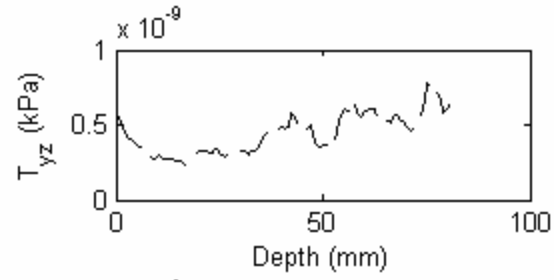
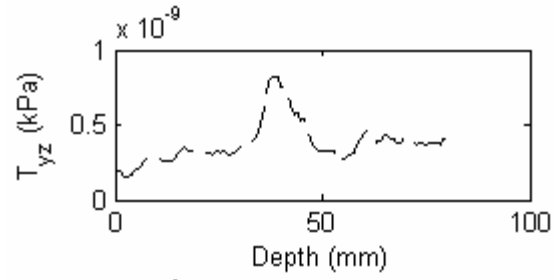
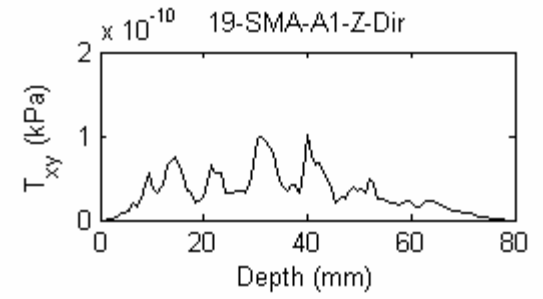
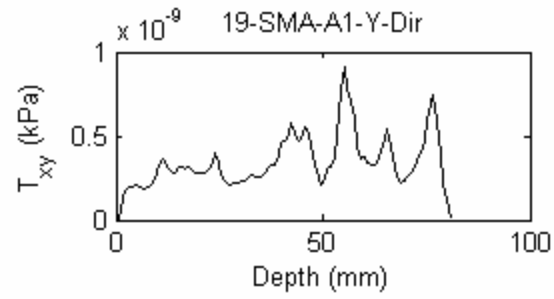
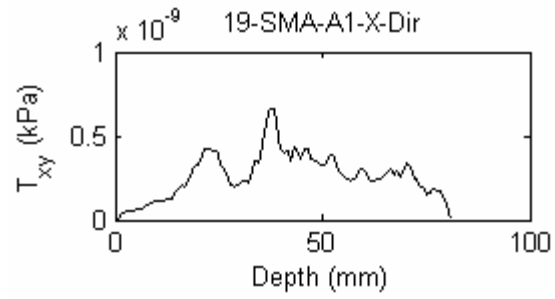


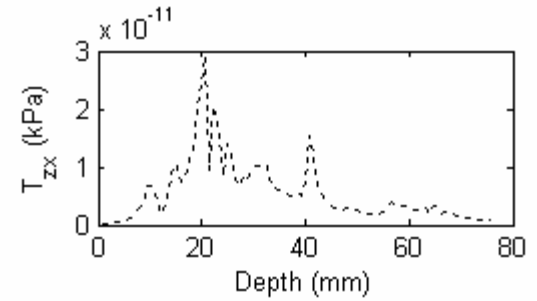
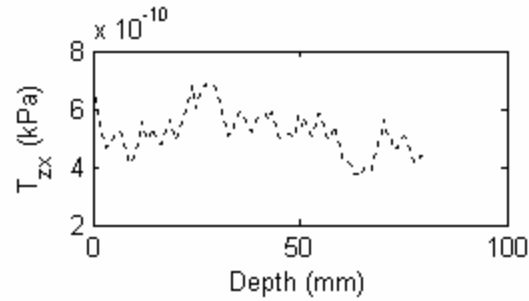
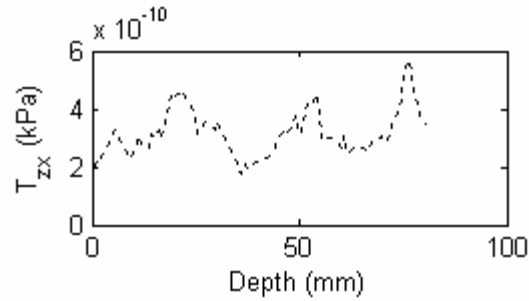
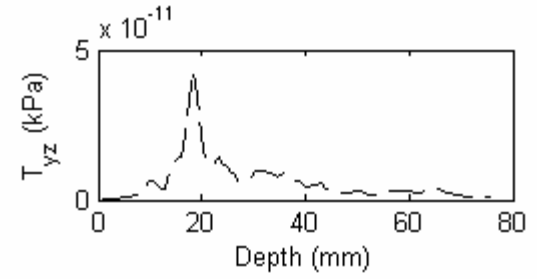
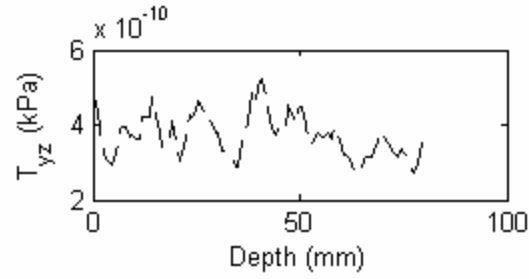
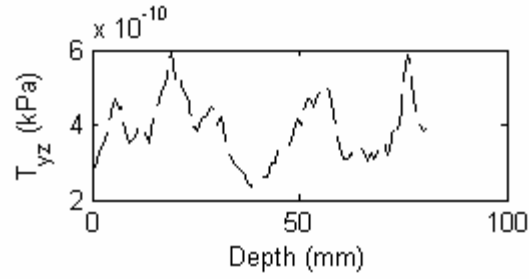
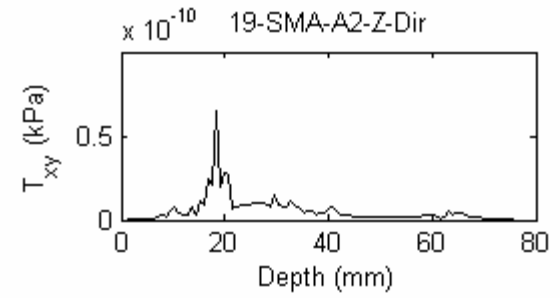
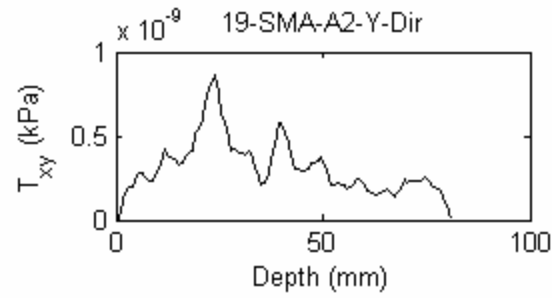
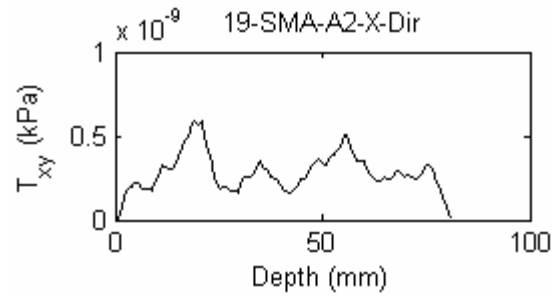


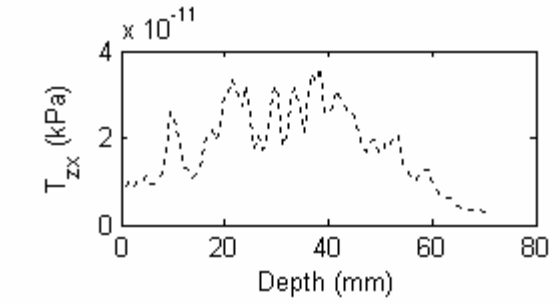
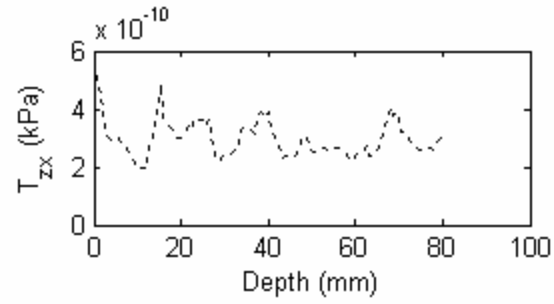
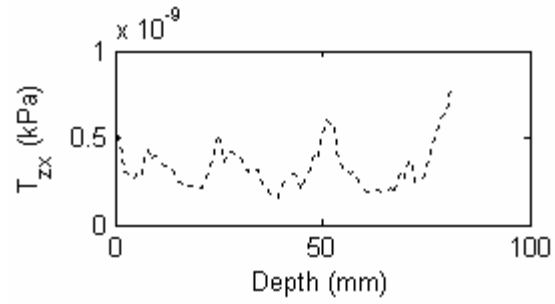
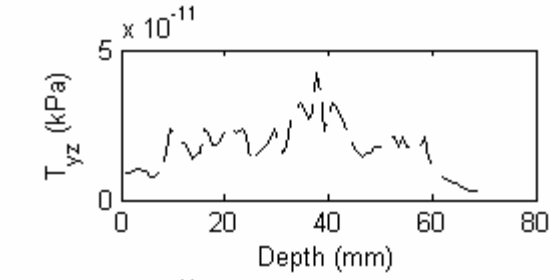
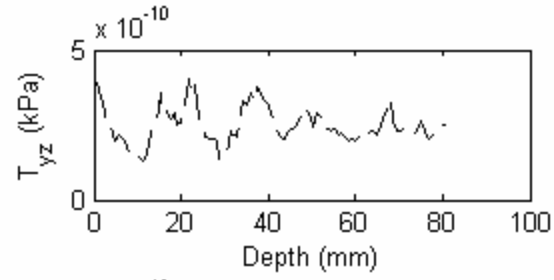
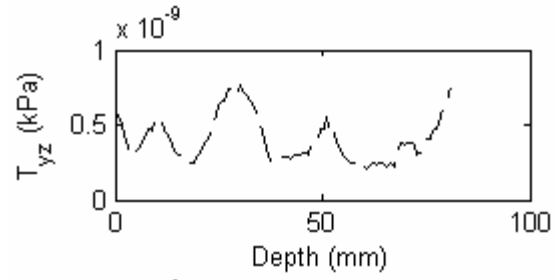
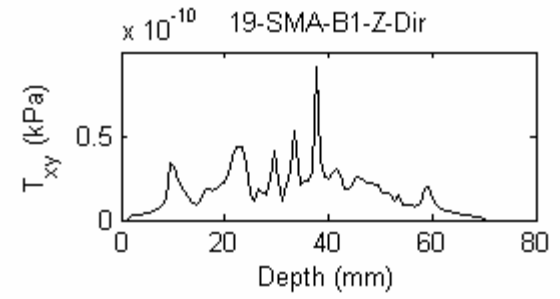
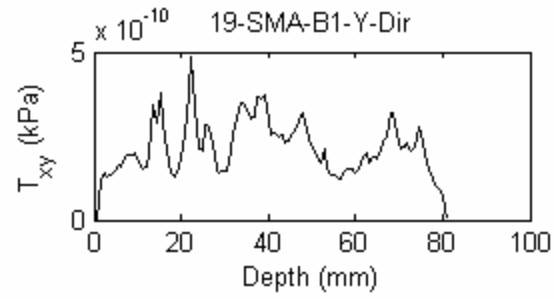
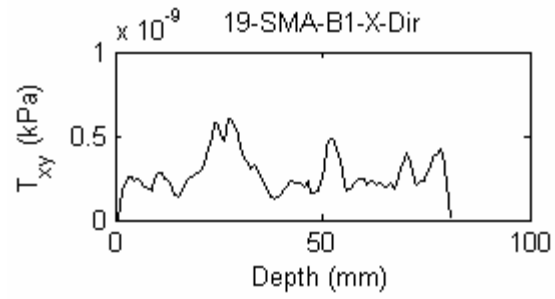


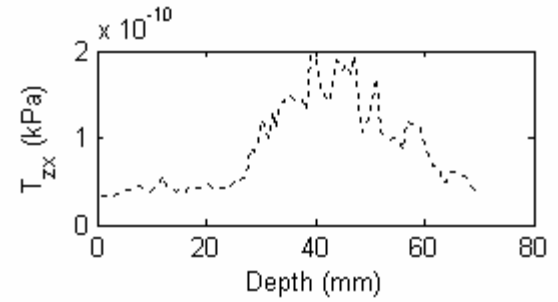
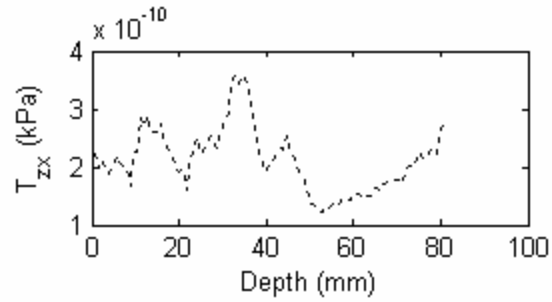
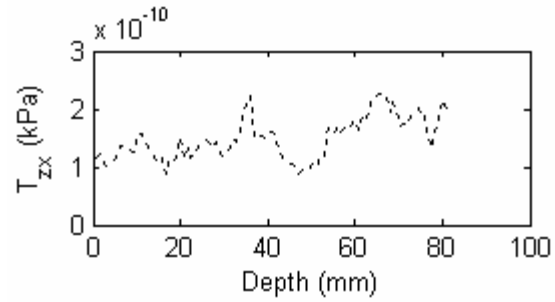
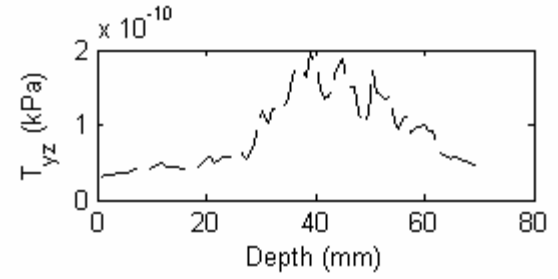
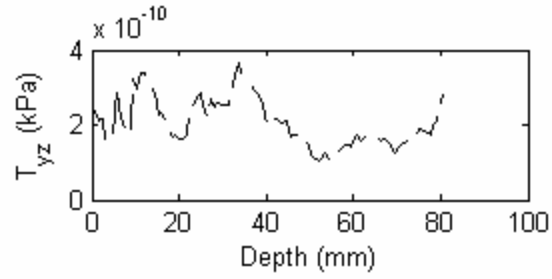
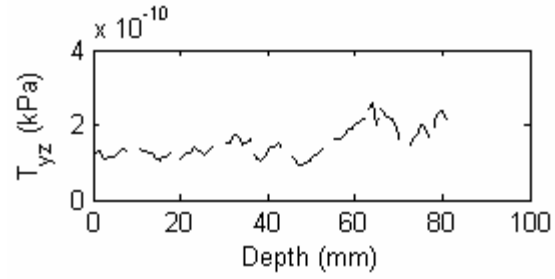
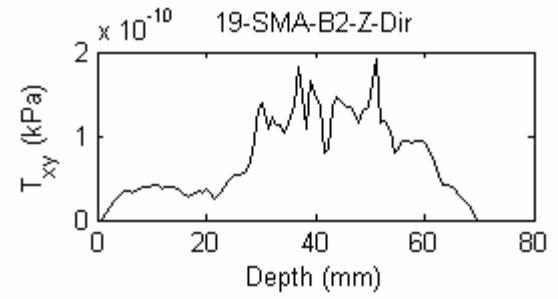
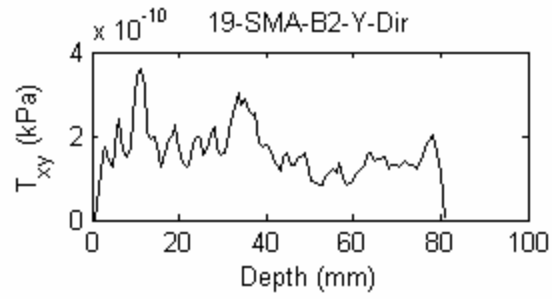
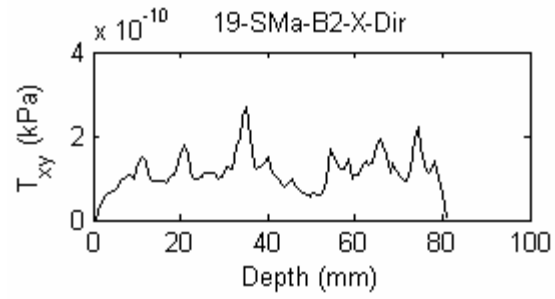


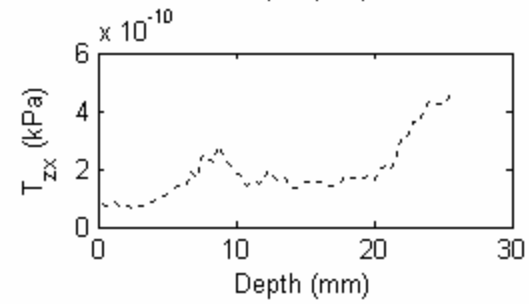
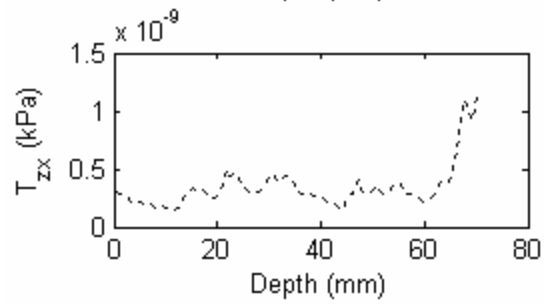
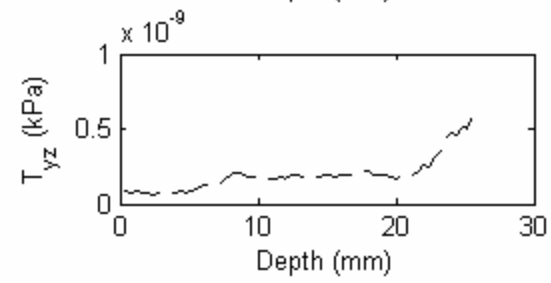
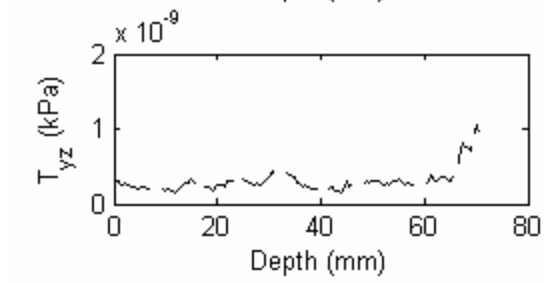
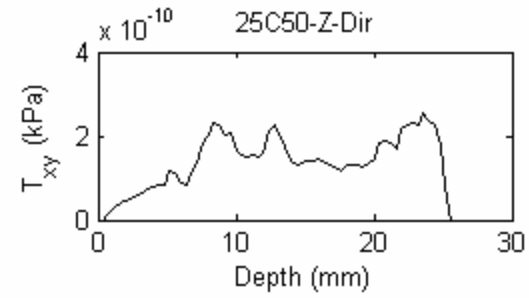
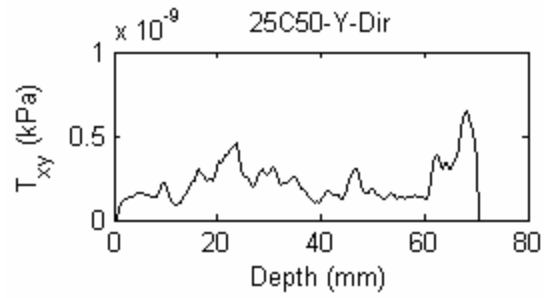


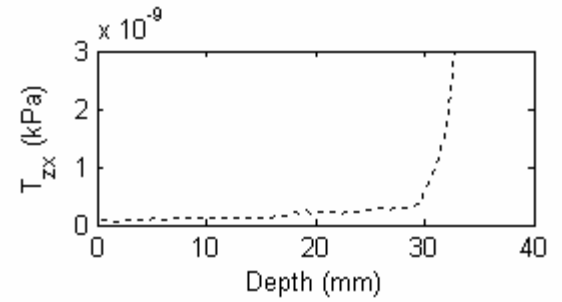
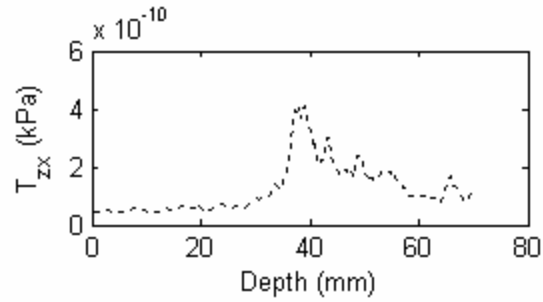
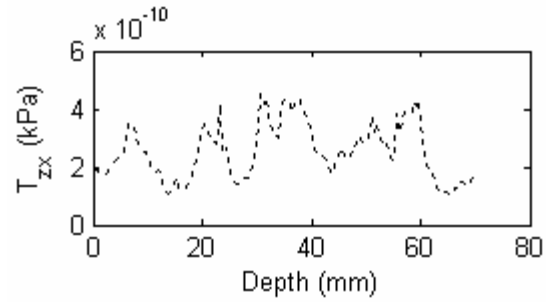
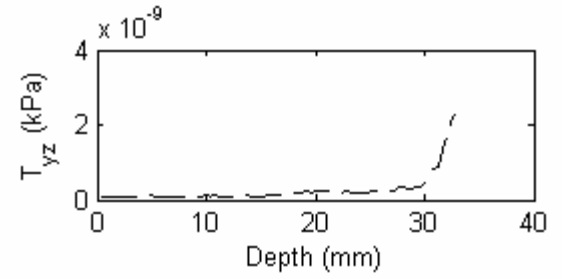
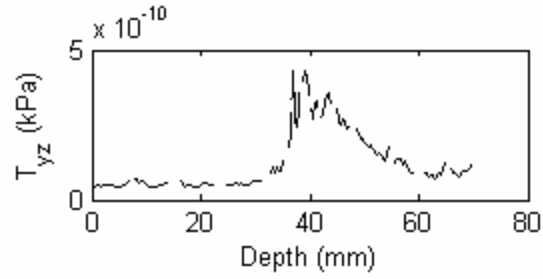
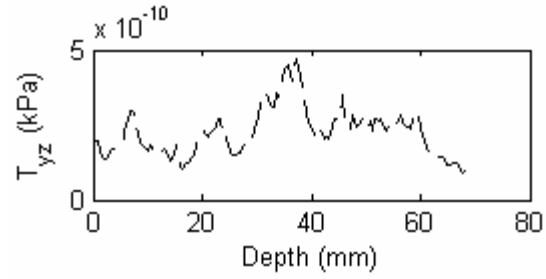
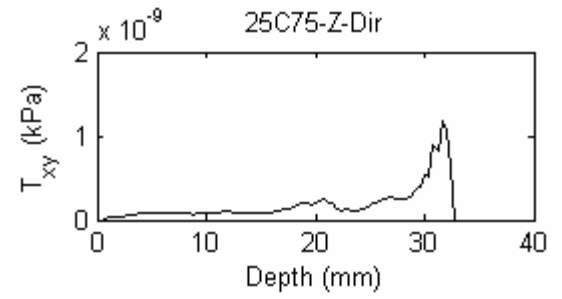
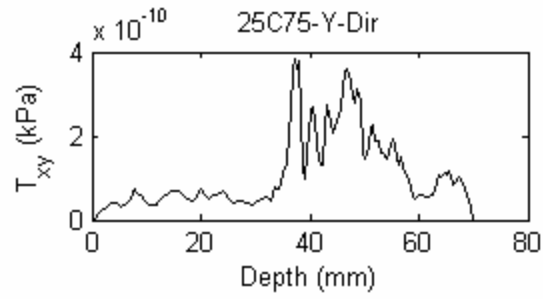
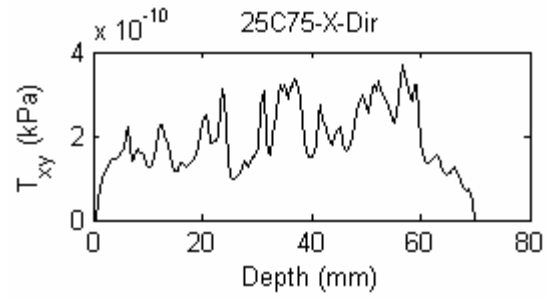




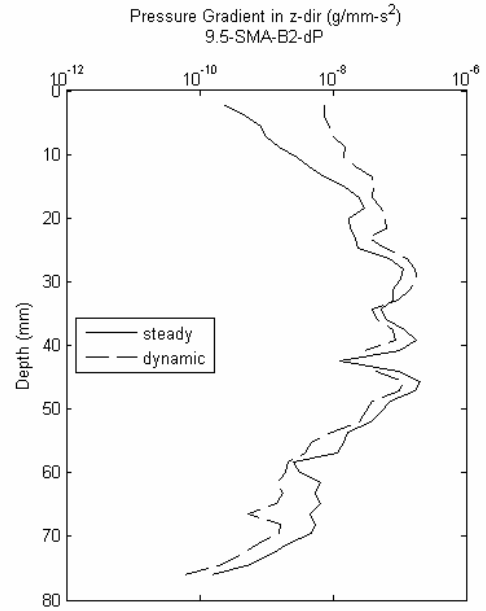
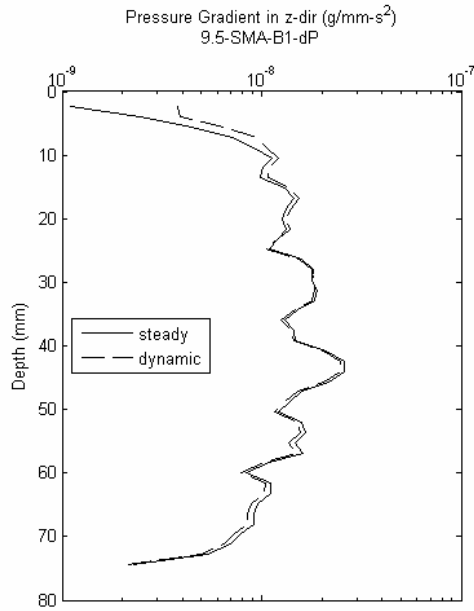
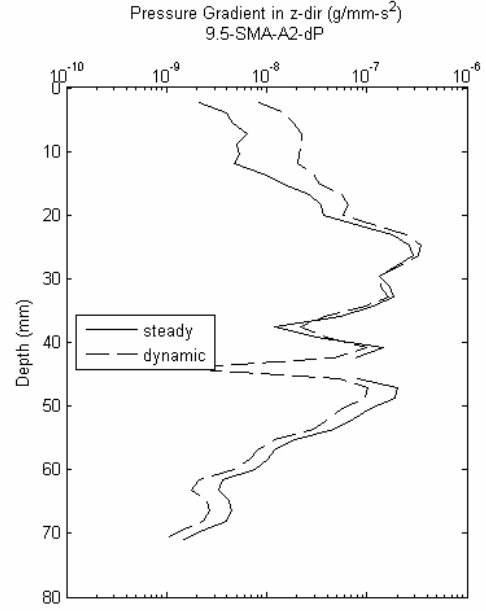
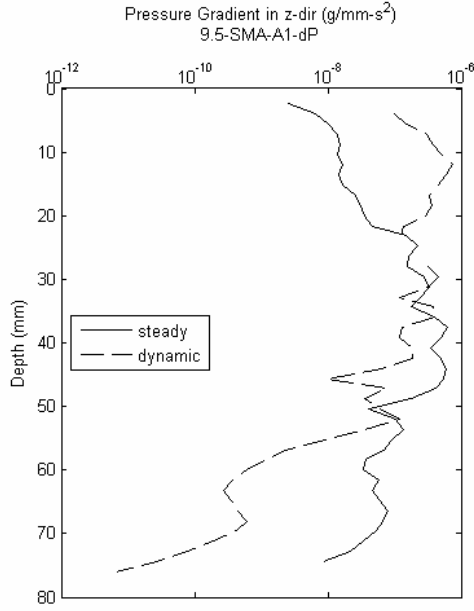


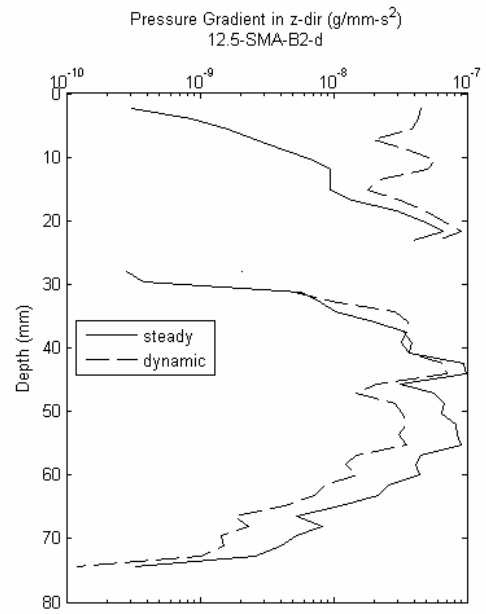
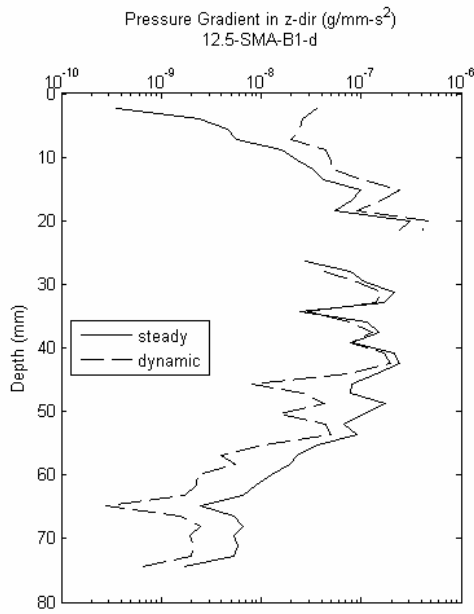
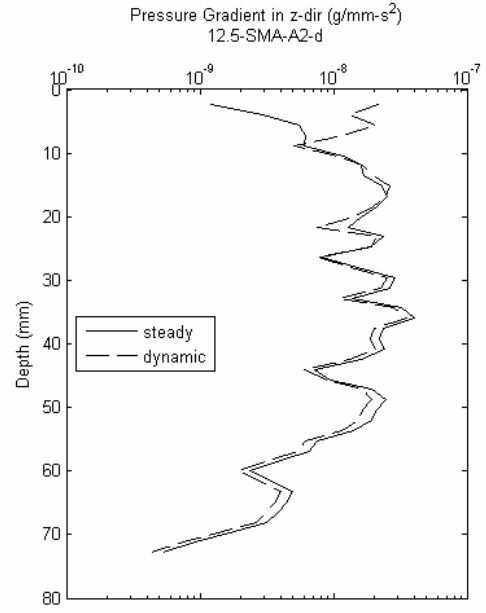
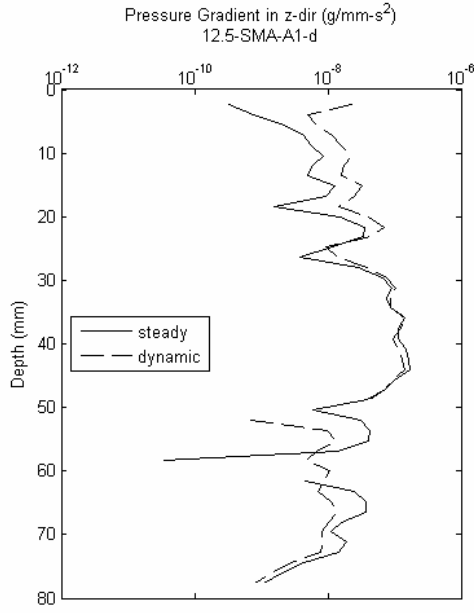


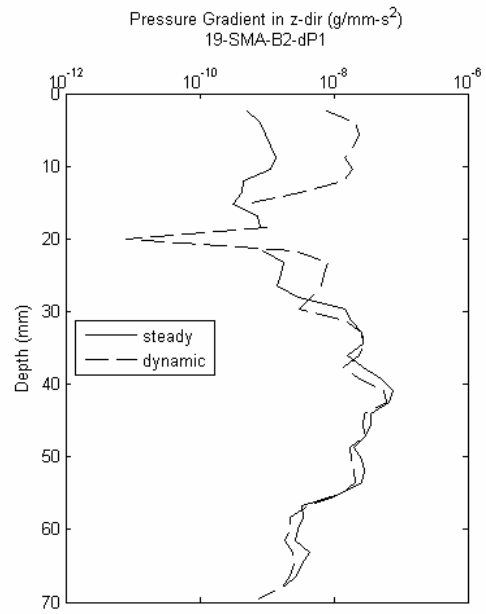
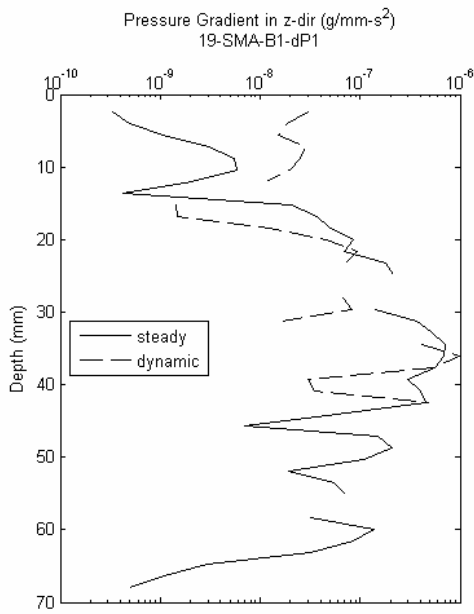
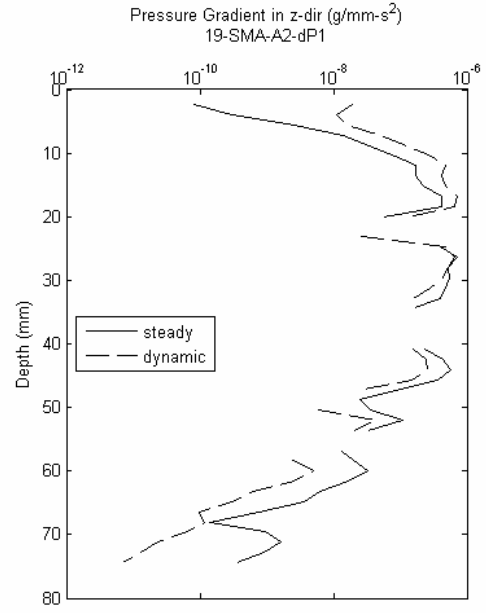
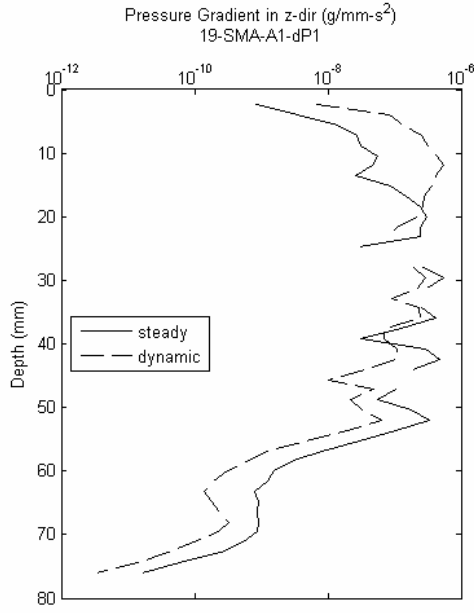




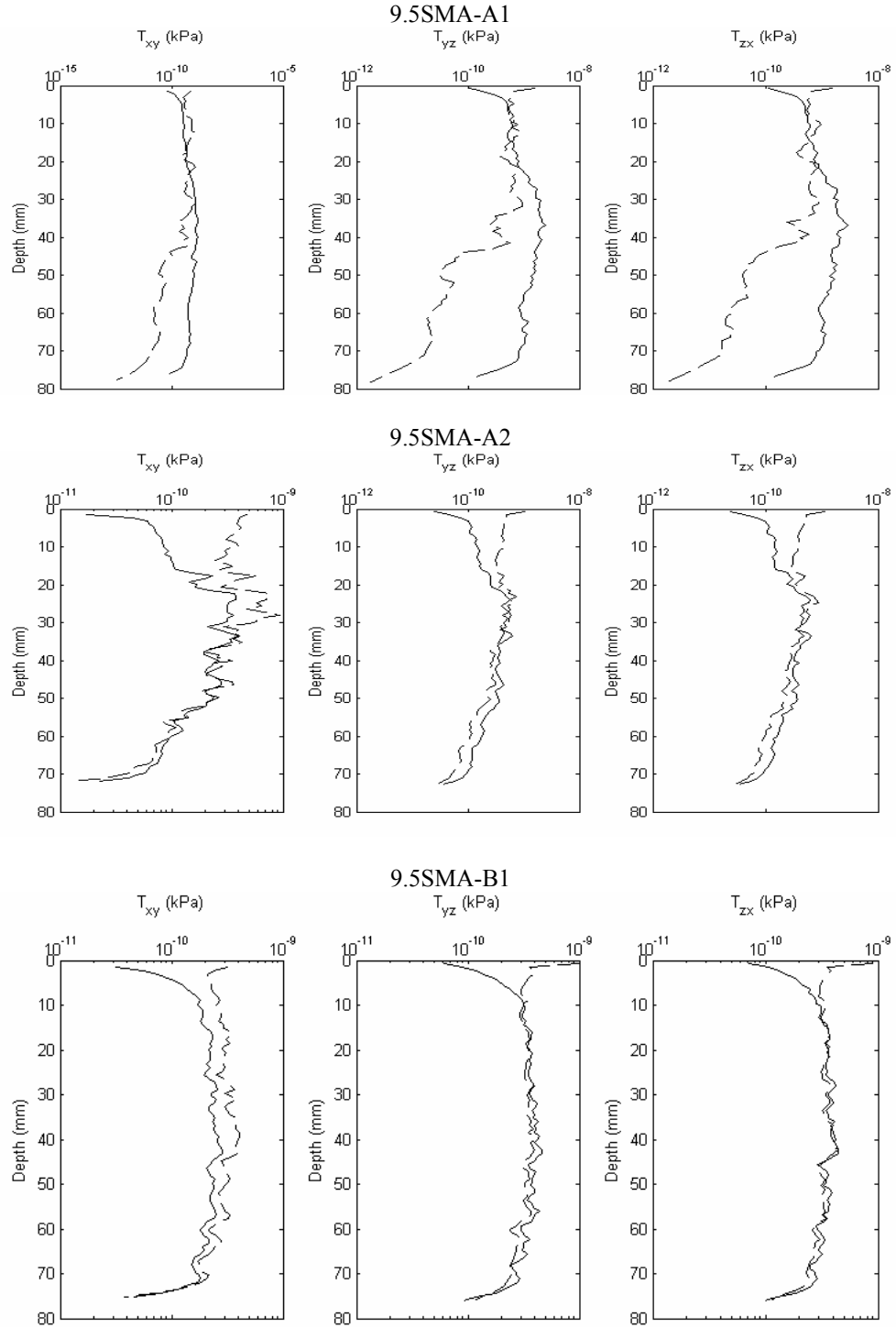
APPENDIX H PRESSURE GRADIENT VARIATION IN Z-DIRECTION FOR STEADY AND DYNAMIC FLOW CONDITIONS



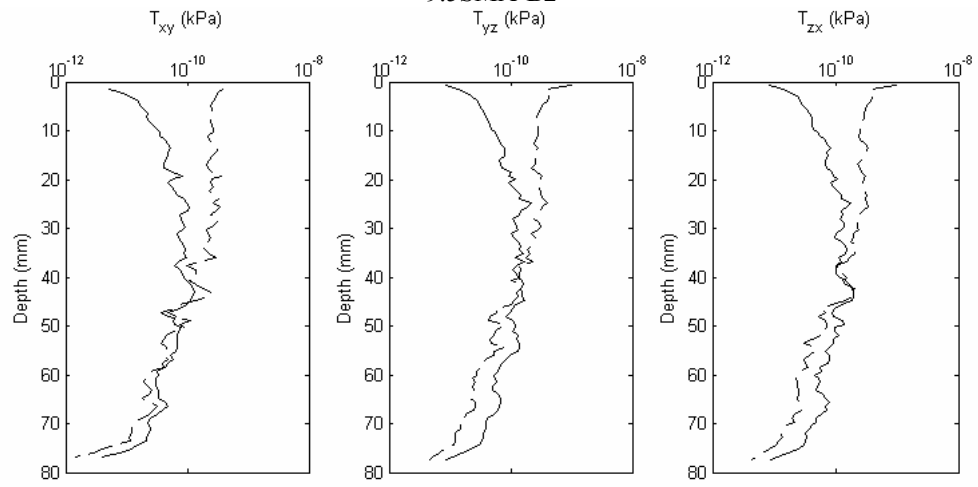




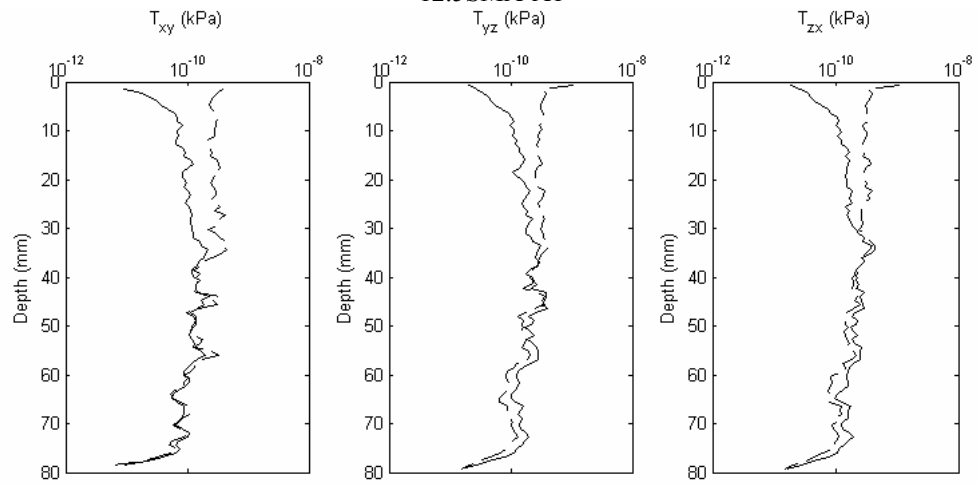
APPENDIX I THE VARIATION OF SHEAR STRESS COMPONENTS IN Z-DIRECTION FOR STEADY (STRAIGHT LINES) AND DYNAMIC (DASHED LINES) FLOW CASES



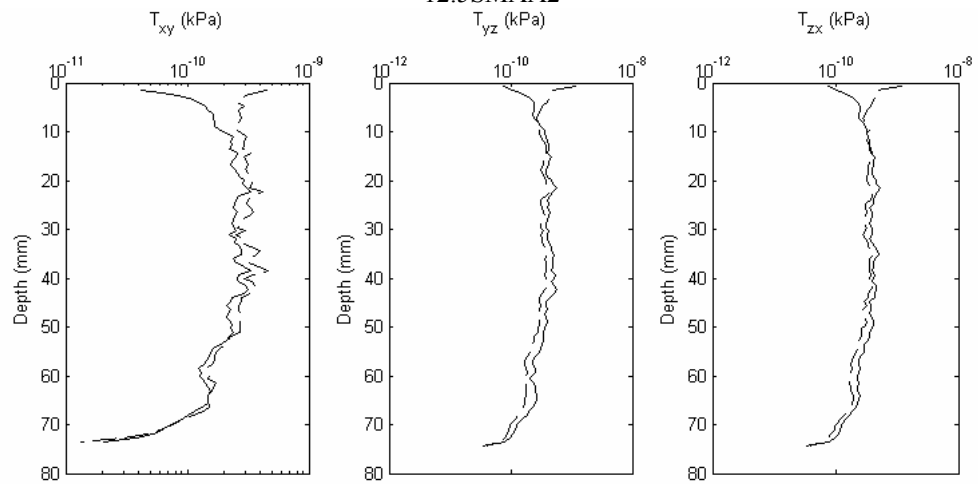
9.5SMA-B2



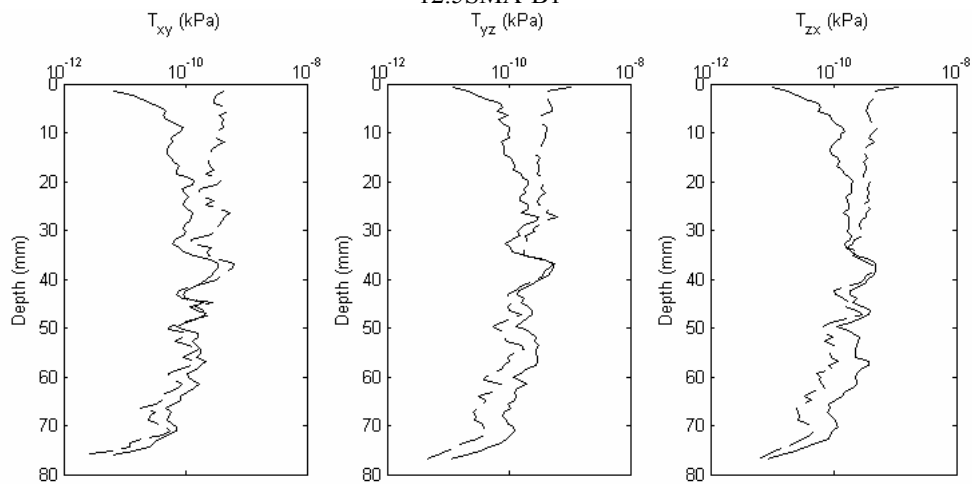
12.5SMA-A1



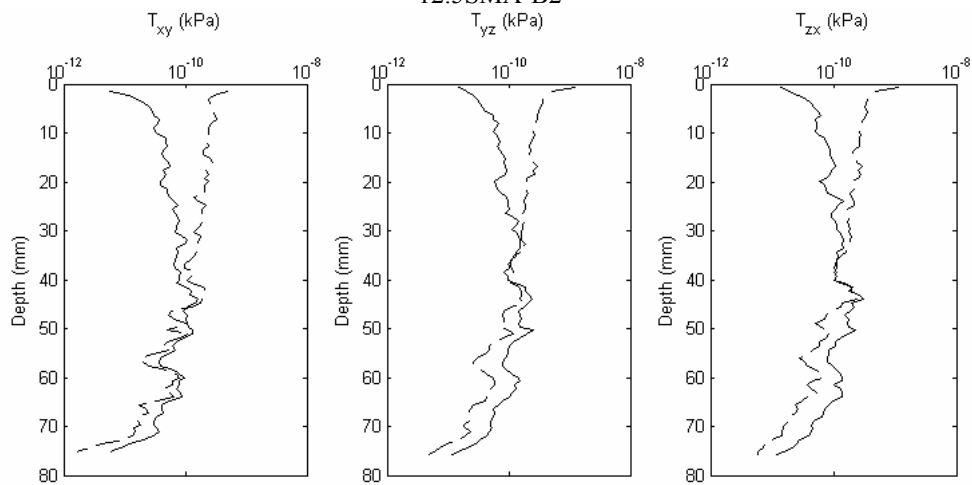
12.5SMAA2



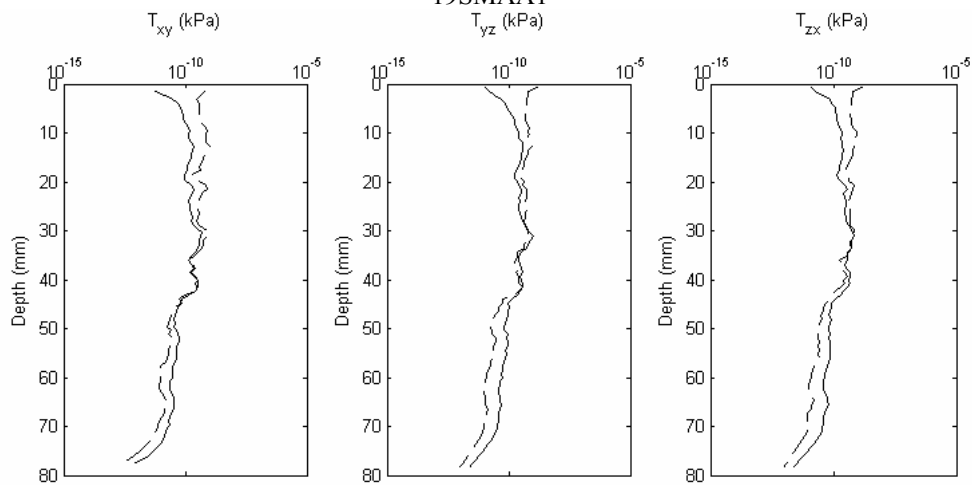
12.5SMA-B1



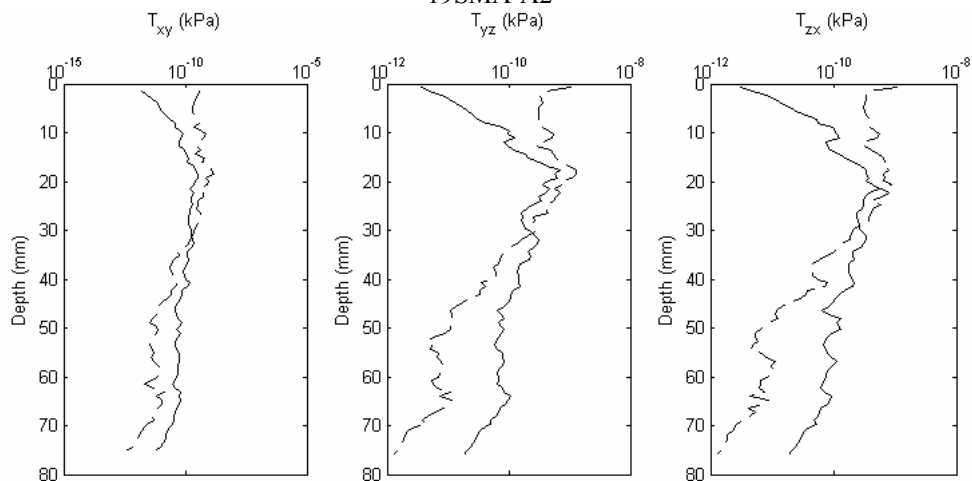
12.5SMA-B2



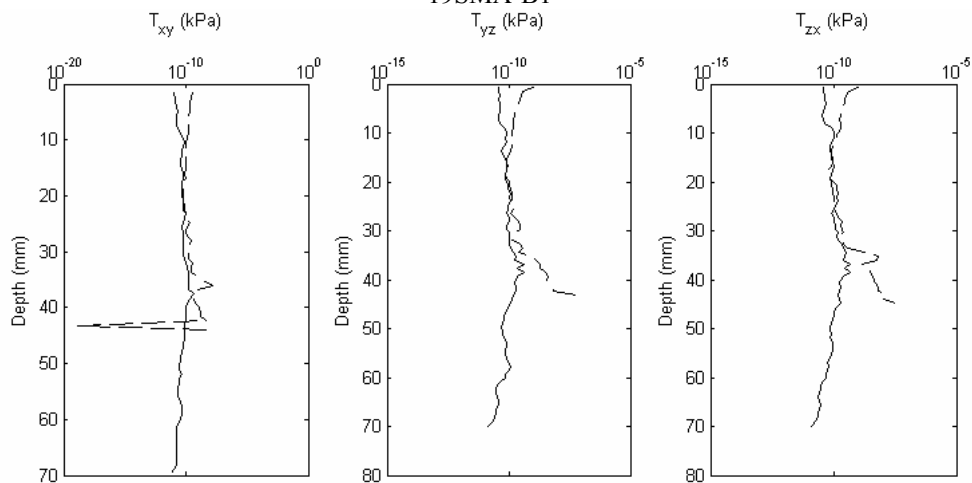
19SMAA1



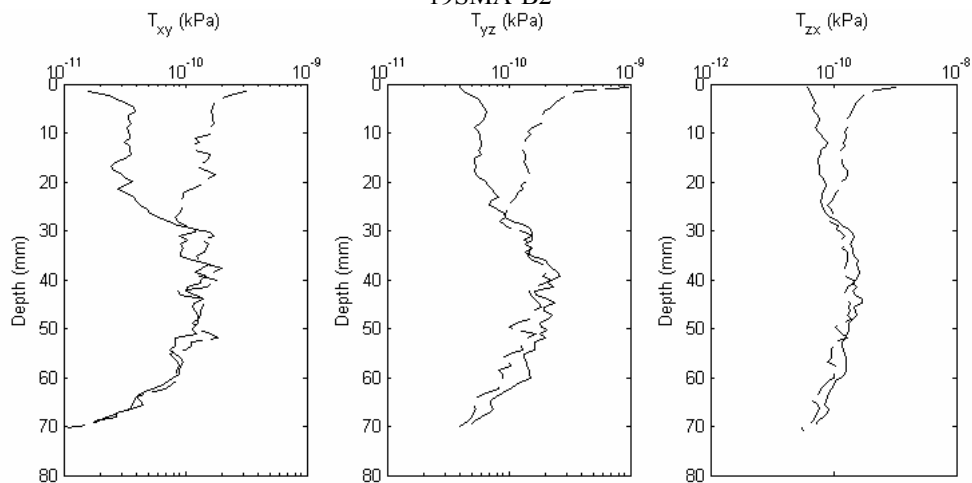
19SMA-A2



19SMA-B1



19SMA-B2



NOMENCLATURE

A	:specimen cross sectional area perpendicular to the direction of pressure gradient
c_s	:lattice speed of sound
D	:diameter of the tube
\mathbf{e}_i	:microscopic velocity vector (e.g. $\mathbf{e}_1=[1, 0]$ for D2Q9 model).
$F_i(\mathbf{x}, t)$:non-equilibrium particle velocity distribution function at node \mathbf{x} at time t
$F_i^{eq}(\mathbf{x}, t)$:equilibrium particle velocity distribution function at node \mathbf{x} at time t
i_h	:hydraulic gradient ($i_h = \nabla P / \gamma$)
i	:complex number
k	:hydraulic conductivity (for isotropic pore structure, i.e. $k=k_{zz}=k_{xx}=k_{yy}$)
N_x	:number of lattice sites in x-direction
N_y	:number of lattice sites in y-direction
N_D	:number of lattice sites along the diameter of a tube
P	:pressure
r	:distance from the centerline of the tube in radial direction
RMS	:root mean square error
q	:average flow rate
Q	:number of microscopic velocity vectors
u_x	:velocity in the x- direction
u_y	:velocity in the y- direction
u_z	:velocity in the z- direction
$u_{z(in)}$:velocity in z-direction at the inlet nodes
$u_{z(out)}$:velocity in z-direction at the outlet nodes

$\mathbf{U}(\mathbf{x}, t)$:momentum of particles at node \mathbf{x} , at time t
$\mathbf{u}(\mathbf{x}, t)$:macroscopic velocity at node \mathbf{x} , at time t
$\varepsilon_{\%}$:percent error
∇P_z	:pressure gradient
μ	:dynamic viscosity
ν	:kinematic viscosity
$\rho(\mathbf{x}, t)$:density at node \mathbf{x} , at time t
τ	:relaxation time
T	:tortuosity
V_p	:pore volume (in mm^3)
\hat{V}_p	:pore volume in lattice units (in pixel^3)
$\Delta x, \Delta y, \text{ and } \Delta z$: image (or lattice) resolution in x, y and z directions, respectively.
V	:total volume of specimen
S_a	:specific surface area
A_s	:surface area of pores (mm^2)
\hat{P}_i	:perimeter of the pores in each slice in pixels
A_i	:surface area of pores in each slice in mm^2
L_e	:longest path traveled by the fluid (for tortuosity calculation)
L	: shortest path between two ends of a specimen
SMA	:stone matrix asphalt
NMAS	:nominal maximum aggregate size
HMA	:hot mix asphalt
ALF	:accelerated loading facility
FHWA	:Federal Highway Administration

TFHRC	:Turner-Fairbank Highway research Center
CT	:computed tomography
PG	:binder performance grade
MDL	:maximum density line
n	:total porosity of a specimen
n_e	:effective porosity of a specimen
t_d	: thickness of the X-ray CT detector aperture

REFERENCES

- Al-Omari, A., Tashman, L., Masad, E., Cooley, A., and Harman, T., (2002) "Proposed Methodology for Predicting HMA Permeability", *Journal of Association of Asphalt Paving Tech.*, V. 71, pp. 30-57.
- Buick, J. M. (1997) "Lattice Boltzmann Methods in Interfacial Wave Modeling", PhD Thesis, University of Edinburgh
- Carman, P., C. (1956) "Flow of Gases through Porous Media", Academic Press, NY
- Castelblanco, A., Masad, E., Birgisson, B., (2005) "HMA Moisture Damage as a Function of Air Void Size Distribution, Pore Pressure and Bond Energy", 82nd Transportation Research Board Annual Meeting, CD-ROM.
- Cercignani C., *Theory and Application of the Boltzmann Equation*, Scottish Academic Press, 1975
- Chapman S. and Cowling T. G., *The Mathematical Theory of Non-Uniform Gases*, Cambridge University Press, 1970.
- Chen, S. and Doolen, G. D. (2001). "Lattice Boltzmann Method for Fluid Flows", *Annual Rev. Fluid Mech.* Vol. 30, pp. 329-364
- Chin, J., Boek, E.,S., and Covaney, P.,V., (2002) "Lattice Boltzmann Simulation of the Flow of Binary Immiscible Fluids with Different Viscosities Using the Shan-Chen Microscopic Interaction Model", *Phil. Trans. R. Soc. Lond.*, pp. 547-558.
- Chopard, B. and Droz, M. (1998). "*Cellular Automata Modeling of Physical Systems*", Ed. Claude Godrèche, Collection Aléa-Saclay: Monographs and Texts in Statistical Physics, Cambridge University Press, Cambridge, U.K.
- Clague, D. S., Kandhai, B. D., Zhang, R., Slood, P. M. A., (2000) "Hydraulic Permeability of (un) Bounded Fibrous Media Using the Lattice Boltzmann Method", *Phys. Rev. E* V 61, No 1, pp. 616-625.
- Duarte, J. A. M. S., Shaimi, M., Carvalho, J. M. (1992) "Dynamic Permeability of Porous Media by Cellular Automata", *J. Phys. II France*, Vol. 1, No 5.
- Dullien, F. (1992) *Porous Media - Fluid Transport and Pore Structure*. San Diego: Academic Press.
- Filippova, O. and Hanel, D. (1997) "Lattice Boltzmann Simulation of Gas-Particle Flow in Filters" *Computers and Fluids*, Vol. 26, No.7, pp. 697-712.
- Fischer, G. R., Holtz, R.,D., and Christopher, B.,R. (1996) "Evaluating Geotextile Flow Reduction Potential Using Pore Size Distribution", *Geofilters 96*, pp. 247-256

Fuente, L., Ingram, D., Mingham, C., Causon, D., (2003) "Enhancing Stability of Lattice Boltzmann Simulations via New Boundary Conditions", *Int. J. of Modern Phys. C*, V 14, No 1, pp. 29-40.

Giroud, J. P. (1996) "Granular Filters and Geotextile Filters", *Geofilters* 96, pp. 565

Gogula, A., Hossain, M., Romanoschi, S., and Fager, G. (2003) "Correlation Between the Laboratory and Field Permeability Values for the Superpave Pavements", *Proceedings of the 2003 Mid-Continent Transportation Research Symposium*, Ames, Iowa.

Guo, Z., Zheng, C., and Shi, B. (2002). "An Extrapolation Method for Boundary Conditions in Lattice Boltzmann Method", *Physics of Fluids*, Vol. 14, No. 6, pp. 2007-2010

Hazi, G. (2003). "Accuracy of Lattice Boltzmann Based on Analytical Solutions", *Physical Review E*, Vol. 67, pp. 056705-1 to 5.

He, X., Luo, L. (1997) "Theory of Lattice Boltzmann Method: From the Boltzmann equation to the Lattice Boltzmann", *Phys. Rev. E*, Vol. 56, pp. 6811-6817.

Hornero, F. J., Giraldez, J.V., and Laguna, A. (2004) "Estimation of the Role of Obstacles in the Downslope Soil Flow with a Simple Erosion Model: the Analytical Solution and its approximation with the Lattice Boltzmann Model", *Catena*, 57, pp.261-275.

Kandhai, D., Vidal, D. J. E., Hoekstra, A. G., Hoefsloot, H., Iedema, P., and Sloot, P. M. A. (1999). "Lattice Boltzmann and Finite Element Simulations of Fluid Flow in a SMRX Static Mixer Reactor". *International Journal of Numerical Methods in Fluids*, Vol. 31, No. 6, pp. 1019.

Kim, I., (2002) "Fluid Flow in a Rock Fracture using Finite Difference Lattice Boltzmann Method", PhD Thesis, State Univ. of New York.

Koponen, A., Kandhai, D., Hellen, E., Alava, M., Hoekstra, A., Kataja, M., Niskanen, K., Sloot, P. and Timonen, J. (1998) "Permeability of Three Dimensional Random Fiber Webs", *Phys. Rev. Lett.* Vol. 80, No 4, pp. 716-719.

Kozeny, J. (1927) "Ueber Kapillare Leitung des Wassers im Boden", *Wien, Akad. Wiss.*, 136 (2A), 271.

La Fuente, L., Ingrams, D., Mingham, C and Causon, D (2003) "Enhancing Stability of Lattice Boltzmann Method Via New Boundary Conditions", *Int. J. Of. Mod. Phys.* Vol.14, No 1, pp 29-40.

Latini, R.G. (1967). *Measurement of Directional Permeabilities*. M.S. Thesis, Department of Chemical Engineering and Metallurgy, Syracuse University, Syracuse NY, 1967.

- Maier, R. S., Bernard, R. S., Grunau, D. W., (1996) "Boundary Conditions for the Lattice Boltzmann Method", *Phys. Fluids* 8 (7) pp. 1788-1801.
- Maier, R., Kroll, D., Kutsovsky, Y., Davis, H. T., Bernard, R., (1997) "Simulation of Flow Through Bead Packs Using the Lattice Boltzmann Method" AHPCRC Preprint 97-034, Univ. of Minnesota.
- Martys, N. S., Hagedorn, J. G. and J. E. Devaney (2001) "Pore scale modeling of fluid transport using discrete boltzmann methods", *Materials Science of Concrete*, Ed. R. D. Hooten, M.D.A. Thomas, Jacques Marchand, James J. Beaudoin
- Martys, N. S., Shan, X., Chen, H., (1998) "Evaluation of external force term in the discrete boltzmann equation", *Phys. Rev. E*, Vol 58, No 5. pp. 6855-6857.
- Martys, N.,S., Hagedorn, J.,G., (2002) "Multiscale Modeling of Fluid Transport in Heterogenous Materials unisng Discrete Boltzmann Methods", *Materials and Structures*, Vol. 35, pp. 650-659.
- Masad, E., Al-Omari, A., (2004) "Three Dimensional Simulation of Fluid Flow in X-ray CT Images of Porous Media", *Int. J. Numer. Anal. Meth. Geomech.*, Vol. 28:1327–1360
- Masad, E., Birgisson, B., Al-Omari A., and Cooley A. (2004) "Analytical Derivation of Permeability and Numerical Simulation of Fluid Flow in Hot-Mix Asphalt", *Journal of Materials in Civil Engineering*, 16:5, pp.487.
- Masad, E., Birgisson, B., Al-Omari, A, Cooley, A., (2003) "Analysis of Permeability and Fluid Flow In Asphalt Mixes", 82nd Transportation Research Board Annual Meeting, CD-ROM.
- Masad, E., Muhuthan, B., Shashidar, N. and Harman, T. (1999) "Internal Structure Characterization of Asphalt Concrete using Image Analysis", *Journal of Computing in Civil Engineering*, Vol. 13-2, pp. 88-95.
- McCann, M., Anderson-Sprecher, R., Thomas, K., Huang, S. (2005) "Comparison of Moisture Damage in Hot Mix Asphalt Using Ultrasonic Accelerated Moisture Conditioning and Tensile Strength Test Results", 82nd Transportation Research Board Annual Meeting, CD-ROM.
- McDonald, D.A. (1974) *Blood Flow in Arteries*. Baltimore: Williams & Wilkins
- McNamara, G. and Zanetti, G. (1988) "Use of the Boltzmann equation to simulate lattice-gas automata", *Phys. Rev. Lett.*, Vol. 61, pp. 2332-2335.
- Mogawer, W.,S., Mallick, R.,B., Teto, M.,R., and Crockford, W.,C., (2002) "Evaluation of Permeability of Superpave Mixes", Report prepared for The New England Transportation Consortium. Project No. NETC 00-2, NETCR 34.

- Moore, P.J. (1979) “Determination of permeability anisotropy in a two-way permeameter”. *Geotechnical Testing Journal*, 2(3):167–169.
- Noble, D. R., Chen, S., Georgiadis, J. G., and Buckius, R. O. (1995). “A Consistent Hydrodynamic Boundary Condition for the Lattice Boltzmann Method”, *Physics of Fluids*, Vol. 7, No. 1, pp. 203-205.
- Panton, R. L., (1996), *Incompressible Flow, 2nd Ed.*, J. Wiley, New York.
- Papagiannakis, A. T., Amoah, N., and Taha, R. (1996) “Formulation of Viscoelastic Response of Pavements under Moving Dynamic Loads”, *Journal of Transportation Engineering*, Vol. 122, No. 2.
- Pilotti, M. (2003) “Viscous flow in three-dimensional reconstructed porous media”, *International Journal for Numerical and Analytical Methods in Geomechanics*, 27:633–649.
- Rothman, D.H. and Zaleski, S. (1998). “Lattice-Gas Model of Phase Separation: Interfaces, Phase Transitions, and Multiphase Flow”, *Rev. Mod., Phys.*, Vol. 66, No. 4, pp. 1471-1479.
- Sheng, P. and Zhou, M. Y. (1988) “Dynamic Permeability of Porous Media”, *Physical Review Letters*, Vol. 61, No 14.
- Skordos, P. A., (1993) “Initial and Boundary Conditions of the Lattice Boltzmann Method”, *Phys. Rev. E.*, 48, 4823.
- Succi S. (2001). “*The Lattice Boltzmann Equation: for Fluid Dynamics and Beyond*”, Series Numerical Mathematics and Scientific Computation, Oxford University Press., Oxford-New York.
- Tang, G. H., Tao, W. Q., and He, Y. L. (2004) “Lattice Boltzmann Method for Simulating Gas Flow in Microchannels”, *Int. J. of Mod. Phys.* Vol. 15, No 2 pp. 335-347.
- Walsh, J.,B., Brace, W.,F., (1984) “The Effect of Pressure in Porosity and the Transport Properties of Rock”, *Journal of Geophysical Research*, Vol. 89, No. B11, pp. 9425-9431.
- Wang J.C., Leung C.F., Chow Y.K. (2003) “Numerical solutions for flow in porous media”, *International Journal for Numerical and Analytical Methods in Geomechanics* 27:565–583.
- Yoshino, M., Matsuda, Y., Shao, C., (2004) “Comparison of Accuracy and Efficiency between the Lattice Boltzmann Method and the Finite Difference Method in Viscous/Thermal Fluid Flows”, *International Journal of Computational Fluid Dynamics*, Vol. 18 (4), pp. 333-345.
- Zhou, M., Y. and Sheng, P. (1989) “First-Principles Calculations of Dynamic Permeability in Porous Media”, *Physical Review B*, Vol. 39, No 16.

Zou, Q.S., He, X.Y. (1997) "On pressure and velocity boundary conditions for the lattice Boltzmann BGK model", *Physics of Fluids*, Vol. 9 No 6, pp. 1591-1598.